

IN 738 LC MICROSTRUCTURE OPTIMIZATION WITH HEAT TREATMENT
AND SIMULATION TO IMPROVE MECHANICAL PROPERTIES OF
TURBINE BLADES

A THESIS SUBMITTED TO
THE GRADUATE SCHOOL OF NATURAL AND APPLIED SCIENCES
OF
MIDDLE EAST TECHNICAL UNIVERSITY

BY

MUSTAFA TARIK BOYRAZ

IN PARTIAL FULFILLMENT OF THE REQUIREMENTS
FOR
THE DEGREE OF MASTER OF SCIENCE
IN
METALLURGICAL AND MATERIALS ENGINEERING

MAY 2018

Approval of the thesis:

**IN 738 LC MICROSTRUCTURE OPTIMIZATION WITH HEAT
TREATMENT AND SIMULATION TO IMPROVE MECHANICAL
PROPERTIES OF TURBINE BLADES**

submitted by **MUSTAFA TARIK BOYRAZ** in partial fulfillment of the requirements
for the degree of **Master of Science in Metallurgical and Materials Engineering
Department, Middle East Technical University** by,

Prof. Dr. Halil Kalıpçılar
Dean, Graduate School of **Natural and Applied Sciences**

Prof. Dr. C. Hakan Gür
Head of Department, **Metallurgical and Materials Engineering**

Assist. Prof. Dr. M. Bilge İmer
Supervisor, **Metallurgical and Materials Eng. Dept., METU**

Examining Committee Members:

Prof. Dr. Macit Özenbaş
Metallurgical and Materials Eng. Dept., METU

Assist. Prof. Dr. M. Bilge İmer
Metallurgical and Materials Eng. Dept., METU

Prof. Dr. Kadri Aydınol
Metallurgical and Materials Eng. Dept., METU

Assist. Prof. Dr. Mert Efe
Metallurgical and Materials Eng. Dept., METU

Assist. Prof. Dr. Caner Şimşir
Manufacturing Eng. Dept., Atılım University

Date: May 24, 2018

I hereby declare that all information in this document has been obtained and presented in accordance with academic rules and ethical conduct. I also declare that, as required by these rules and conduct, I have fully cited and referenced all material and results that are not original to this work.

Name, Last name :Mustafa Tarık Boyraz

Signature :

ABSTRACT

IN 738 LC MICROSTRUCTURE OPTIMIZATION WITH HEAT TREATMENT AND SIMULATION TO IMPROVE MECHANICAL PROPERTIES OF TURBINE BLADES

Boyraz, Mustafa Tarık

M.Sc., Department of Metallurgical and Materials Engineering

Supervisor: Assist. Prof. Dr. Bilge İmer

May, 2018, 226 pages

IN 738 LC is a Ni-based superalloy that is employed mostly in nozzle guide vanes and turbine blades in gas turbines. In these parts of gas turbines, material is exposed to high temperatures and the highly corrosive environment. Therefore, improvement in high temperature strength (yield strength, creep strength, tensile strength) and corrosion resistance are extremely important.

In this study, effect of heat treatment and aluminide coating parameters to IN 738 LC microstructure were investigated. Both experimental and simulation studies were performed to improve materials microstructure and optimize its yield strength. Microstructure evolution during heat treatments and aluminide coating was simulated using JMAT PRO software and simulation results were compared to experimental results. The experimental microstructure information obtained from aluminide coating and heat treatment results were used as input to a physical model that was formed to estimate yield strength of IN 738 LC samples with different microstructures. The result of this model was compared with experimental tensile test literature findings and

JMAT PRO yield strength estimations. Additionally, surface growth and diffusion during the aluminide coating were simulated using DICTRA software. The composition profile and coating thickness results of simulations were compared to experimental aluminide coating results. The purpose was to achieve a simulation model capable of estimating coating composition profile and thickness for given experimental conditions since experimental aluminide coating is a costly and time-consuming process.

Keywords: IN 738 LC, Ni-based superalloy, aluminide coating, heat treatment, DICTRA, JMATE PRO, microstructure characterization, simulation.

ÖZ

İN 738 LC TÜRBİN BİÇAKLARININ MEKANİK ÖZELLİKLERİNİN GELİŞTİRİLMESİ İÇİN ISIL İŞLEM VE SİMÜLASYONLA MİKROYAPI OPTİMİZASYONU

Boyraz, Mustafa Tarık

Yüksek Lisans, Metalurji ve Malzeme Mühendisliği Bölümü

Tez Yöneticisi: Assist. Prof. Dr. Bilge İmer

Mayıs 2018, 226 sayfa

İN 738 LC genel olarak karada yer alan gaz türbinlerinde türbin nozüllerinde ve türbin bıçaklarında kullanılan Ni bazlı bir süperalaşımdır. Gaz türbin motorunun bu bileşenlerinde sıklıkla kullanılan İN 738 LC yüksek sıcaklığa ve yüksek korozyona maruz kalmaktadır. Bu nedenle, bu malzemenin yüksek sıcaklık mukavemeti (akma dayanımı, sünme dayanımı, çekme dayanımı) ve korozyon direnci büyük önem taşımaktadır.

Bu çalışmada, ısıtıl işlemlerin ve alüminid kaplama parametrelerinin İN 738 LC mikroyapısına etkisi incelenmiştir. Simülasyon çalışmaları ve deneysel çalışmalar kullanılarak malzemenin mikroyapısı geliştirilmiş, akma dayanımı optimize edilmiştir. Isıl işlemler ve alüminid kaplama sırasında gerçekleşen mikroyapı değişimi JMAT PRO yazılımı kullanılarak simüle edilmiştir ve simülasyon sonuçları deney sonuçları ile karşılaştırılmıştır. Kaplama ve ısıtıl işlemlerden elde edilen deneysel mikroyapı bilgileri, farklı mikroyapılara sahip İN 738 LC örneklerinin akma dayanımını hesaplamak amacıyla oluşturulmuş bir fiziksel modele girdi olarak

kullanılmıştır. Bu modelin sonucu, deneysel çekme testi literatür sonuçları ve JMAT Pro yazılımı akma dayanımı tahminleri ile karşılaştırılmıştır. Bu çalışmalara ek olarak, aluminid kaplama işlemi sırasında gerçekleşen yüzey büyümesi ve difüzyon DICTRA yazılımı kullanılarak simüle edilmiştir. Simülasyon ve deneysel kompozisyon profili ve kaplama kalınlığı karşılaştırılmıştır. Amaç, deneysel aluminid kaplama maliyetli ve zaman alıcı bir işlem olduğundan, belirlenen deneysel koşullar için kaplama kompozisyonu profilini ve kalınlığını tahmin edebilen bir simülasyon modeli oluşturmaktır.

Anahtar Kelimeler: IN 738 LC, Ni bazlı süperalaşım, aluminid kaplama, ısıtıl işlem, DICTRA, JMATP PRO, mikroyapı karakterizasyonu, simülasyon.

ACKNOWLEDGEMENTS

First of all, I would like to express my sincere gratitude to Dr. Bilge İmer, for her support, patience, encouragement, and confidence on me from the very first day.

It has been my pleasure and honor to work and share with my colleagues Umutcan Ertürk, Ali Fırat Dinler, Seren Özer, Dođuhan Sarıtürk and Fırat Güler. Also, I am very grateful for their support and friendship during this study.

I want to thank TUBİTAK MAM, TÜBİTAK KAMAG, GURMETAL, SDM and EUAŞ for their contribution to this study. I also want to thank ONATUS and THERMOCALC company for their technical support.

Then, my heartiest thanks go to Yvonne Kreidl, for her endless support during this study.

My deepest gratitude goes to my parents for their endless support during this study as in the entire of my lifetime.

To my beloved family

TABLE OF CONTENTS

ABSTRACT	v
ÖZ	vii
ACKNOWLEDGEMENTS	ix
TABLE OF CONTENTS	xi
LIST OF TABLES	xvi
LIST OF FIGURES	xx
LIST OF ABBREVIATIONS.....	xxix

CHAPTERS

1. INTRODUCTION.....	1
1.1 General	1
1.2 Background Information and Literature Review	4
1.2.1 The Need for High Temperature Materials in Gas Turbines Blades ..	4
1.2.2 Introduction to Ni-based Superalloys	5
1.2.3 Metallurgy of Ni-Based Superalloys	11
1.2.3.1 Role of Alloying Elements.....	11
1.2.3.2 Phases Present in Ni-Based Superalloys	13
1.2.3.2.1 Gamma (γ) Matrix.....	13
1.2.3.2.2 Gamma Prime (γ') Precipitates.....	14
1.2.3.2.3 Topologically Close Packed Phases (TCP).....	18
1.2.4 Heat Treatments and Their Simulations	18
1.2.4.1 Hot Isostatic Pressing	18
1.2.4.2 Solutionizing	19

1.2.4.3 Aging	21
1.2.4.4 Heat Treatment Simulations	22
1.2.5 Diffusion Coatings and Their Simulations	24
1.2.6 Modeling of Yield Strength for Ni-Based Superalloys	28
1.2.6.1 Solid Solution Strengthening	28
1.2.6.2 Grain/Phase Boundary Strengthening	29
1.2.6.2.1 Grain Boundary Strengthening	29
1.2.6.2.2 Phase Boundary Strengthening	30
1.2.6.3 Precipitation Strengthening	31
1.3 Thesis Overview	34
2. ALUMINIDE COATING SURFACE GROWTH AND INTERDIFFUSION SIMULATIONS FOR INCONEL 738 LC	35
2.1 Introduction	35
2.2 Method	36
2.2.1 Simulation Method Optimization	37
2.2.2 Independent Growth Rate Estimation Method	42
2.3 Results and Discussion	45
2.3.1 Simulation Method Optimization Results	45
2.3.2 Independent Growth Rate Optimization Results	47
2.3.3 Independent Simulation for Hypothetical Growth Condition	55
2.4 Conclusion	58
3. EFFECT OF HEAT TREATMENT AND CVD COATING CONDITIONS ON IN 738 LC	61
3.1 Introduction	61
3.2 Experimental Procedure	62
3.2.1 Material	62
3.2.2 Experimental Setup	63

3.2.3	Simulation Method	64
3.2.4	Metallography and Characterization	65
3.2.4.1	Metallography	66
3.2.4.2	Characterization	67
3.2.4.2.1	Scanning Electron Microscopy	67
3.2.4.2.2	Electron Diffraction Spectroscopy Analysis	67
3.2.4.2.3	Hardness Testing	67
3.2.4.2.4	Grain Size and Dendrite Spacing Determination	69
3.2.4.2.5	Gamma Prime Size and Volume Fraction Determination	69
3.3	Heat Treatment Plan.....	70
3.4	Results and Discussion.....	75
3.4.1	Effect of Hot Isostatic Press to IN 738 LC Microstructure	75
3.4.2	Effect of Solutionizing to IN 738 LC Microstructure	78
3.4.2.1	Effect of Solutionizing Temperature.....	79
3.4.2.2	Effect of Solutionizing Time Cooling Rate	84
3.4.3	Effect of Varying Solutionizing Parameters in Combine with Varying Aluminide Coating Temperature	88
3.4.3.1	Effect of Varying Solutionizing Temperature in Combine with Varying Aluminide Coating Temperature.....	89
3.4.3.2	Effect Varying Solutionizing Time and Cooling Rate in Combine with Varying Aluminide Coating Temperature	97
3.4.4	Effect of HIP, Solutionizing, Varying Aluminide Coating Temperatures and Aging to Thick and Thin Samples	103
3.4.5	Microstructure Evolution Simulation Results	115

3.4.5.1 Microstructure Evolution Simulations for Varying Solutionizing Conditions and CVD Temperatures.....	116
3.4.5.2 Microstructure Evolution Simulations for Solutionizing, CVD at Varying Temperatures and Aging of Thick and Thin Samples.....	130
3.5 Effect of Heat Treatments and Aluminide Coating Temperature to Carbide Types.....	137
3.6 Secondary Dendrite Spacing	140
3.7 Conclusion.....	142
4. MODELLING OF YIELD STRENGTH FOR INCONEL 738 LC	147
4.1 Introduction	147
4.2 Solid Solution Strengthening	149
4.3 Phase/Grain Boundary Strengthening	152
4.3.1 Phase Boundary Strengthening	152
4.3.2 Grain Boundary Strengthening	154
4.3.2.1 Effect of Solutionizing Parameters in Combine with Varying Aluminide Coating Temperature	155
4.3.2.1.1 Effect of Varying Solutionizing Temperature in Combine with Varying Aluminide Coating Temperature.....	155
4.3.2.1.2 Effect of Varying Solutionizing Time and Cooling Rate in Combine with Varying Aluminide Coating Temperature	157
4.3.2.2 Effect of HIP, Solutionizing, Varying Aluminide Coating Temperatures and Aging to Grain Boundary Strengthening of Thick and Thin Samples	159
4.4 Precipitation Strengthening	162
4.4.1.1 Effect of Solutionizing Parameters in Combine with Varying Aluminide Coating Temperature	164
4.4.1.1.1 Effect of Varying Solutionizing Temperature in Combine with Varying Aluminide Coating Temperature.....	164

4.4.1.1.2 Effect of Varying Solutionizing Time and Cooling Rate in Combine with Varying Aluminide Coating Temperature	169
4.4.1.2 Effect of HIP, Solutionizing, Varying Aluminide Coating Temperatures and Aging to Precipitation Strengthening of Thick and Thin Samples	172
4.5 Total Yield Strength	176
4.5.1.1 Effect of Solutionizing Parameters in Combine with Varying Aluminide Coating Temperature	176
4.5.1.1.1 Effect of Varying Solutionizing Temperature in Combine with Varying Aluminide Coating Temperature	177
4.5.1.1.2 Effect of Varying Solutionizing Time and Cooling Rate in Combine with Varying Aluminide Coating Temperature	180
4.5.1.2 Effect of HIP, Solutionizing, Varying Aluminide Coating Temperatures and Aging to Total Yield Strength of Thick and Thin Samples	182
4.6 Yield Strength Simulation Comparison	186
4.7 Literature Comparison	192
4.8 Conclusion	195
5. FUTURE WORK	199
REFERENCES	201
APPENDICES	
A. DICTRA Simulation Commands for Aluminide Coating Simulation	213
B. Average Cooling Rates of Different Cooling Types Available in VAKSIS Vacuum Furnace	219
C. SEM Images and Composition Analysis Results of Carbides	220

LIST OF TABLES

Table 1.1: The Important Problems for Gas Turbine Applications [8, 9]	3
Table 1.2: Composition of Some Commercial Ni-Based Superalloys (wt. %) [17]. [XXXXXX] [XXXXXX]	8
Table 1.3: IN 738 LC Chemical Composition (wt. %) [21].....	9
Table 1.4: Functions of various in Ni-based superalloys [3, 20, 26].	12
Table 1.5: Solid Solution Contribution Constants for Alloying Elements in IN 738 LC [73].	29
Table 1.6: Strengthening Parameters Used in The Precipitation Strengthening.	33
Table 2.1: Nominal and Simulation (4 Elements) Composition of Substrate IN 738 LC (at. %).	41
Table 2.2: Nominal and Simulation (5 elements) Composition of Substrate IN 738 LC (at. %).	43
Table 2.3: Parameters of CVD Aluminide Coating.	45
Table 2.4: Parameters of Simulation.	45
Table 2.5: Aluminide Coating Experimental Parameters at Varying Temperatures..	47
Table 2.6: Aluminide Coating Experimental Parameters for Varying Time Periods.	48
Table 2.7: Simulation Parameters at Varying Temperatures.	48
Table 2.8: Simulation Parameters at Varying Time Periods.	48
Table 2.9: Coating Thickness Results of SEM-EDS Analysis and Coating Simulations at 950 °C, 1000 °C, 1050 °C and 1100°C.	52
Table 2.10: Coating Thickness Results of SEM-EDS Analysis and Coating Simulations for 4, 8 and 12 hours at 1100°C.....	53
Table 2.11: Hypothetical Experimental Parameters of Two Different Aluminide Coating Operation.	55
Table 2.12: Simulation Parameters of Two Different Aluminide Coating Operation.	56
Table 2.13: The Simulation Coating Thickness Results.	57

Table 2.14: The Experimental Coating Thickness Results.	58
Table 3.1: Microstructure Input Data of HIPed IN 738 LC.	65
Table 3.2: Chemical Composition of Etchants. [4, 91].....	66
Table 3.3: Heat Treatment and Aluminide Coating Plan for Different Sample Groups.	71
Table 3.4: Experiment Parameters of CVD Aluminide Coating Operations.	74
Table 3.5: γ' Size and Volume Fraction of As Cast and HIPed Samples.	77
Table 3.6: Hardness and Grain Size of As Cast and HIPed Samples.	78
Table 3.7: Parameters Used to Investigate Effect of Solutionizing Temperature.....	79
Table 3.8: Parameters Used to Investigate Effect of Solutionizing Time and Cooling Rate	84
Table 3.9: Parameters of Solutionizing and Coating at Varying Temperatures.	89
Table 3.10: Parameters of solutionizing for varying time periods and cooling rates, and coating at varying temperatures.	97
Table 3.11: Heat Treatment and Coating Parameters for Thick and Thin Samples	104
Table 3.12: The HIP, solutionizing and aging parameters applied to thick and thin samples.....	105
Table 3.13: The Parameters Used to Investigate Effect of Aging on Coated Thick and Thin Samples.....	112
Table 3.14: Heat Treatment and Coating Parameters for Thick and Thin Samples	116
Table 3.15: Parameters of Solutionizing at Varying Time and Cooling Rate, and CVD at Varying Temperatures.....	121
Table 3.16: Parameters of Solutionizing for Varying Time Periods and Cooling Rates, and CVD at Varying Temperatures.....	130
Table 3.17: Experiment Plan to Observe Effect of Solutionizing Time and Cooling Rate on Carbide Types	138
Table 3.18: Experiment Plan to Observe Effect of Solutionizing and CVD Temperature on Carbide Types	138
Table 3.19: Experiment Plan to Observe Effect of Aging (after CVD) on Carbide Types.....	138

Table 3.20: Experiment Plan to Observe Effect of Aging (No CVD applied) on Carbide Types	138
Table 3.21: Heat Treatment and Coating Conditions and Abbreviations.	140
Table 3.22: Secondary Dendrite Spacing and Phase Boundary Strengthening.....	140
Table 4.1: List of Abbreviations in Chapter 4.....	149
Table 4.2: IN 738 LC Solid Solution Constants and Calculated Contributions of Alloying Elements [73].	151
Table 4.3: Heat Treatment and Coating Conditions and Related Abbreviations.	153
Table 4.4:Secondary Dendrite Spacing and Phase Boundary Strengthening Results.	153
Table 4.5: Parameters Used to Investigate Effect of Solutionizing Temperature.	155
Table 4.6: Parameters of solutionizing for varying time periods and cooling rates, and CVD at varying temperatures.....	157
Table 4.7: Heat Treatment and Coating Parameters for Thick and Thin Samples...	159
Table 4.8: Strengthening Parameters Used in The Precipitation Hardening.....	163
Table 4.9: Parameters Used to Investigate Effect of Solutionizing Temperature.	164
Table 4.10: Parameters of solutionizing for varying time periods and cooling rates, and CVD at varying temperatures.....	169
Table 4.11: Heat Treatment and Coating Parameters for Thick and Thin Samples.	172
Table 4.12: Parameters Used to Investigate Effect of Solutionizing Temperature. .	177
Table 4.13: Post-solutionizing and post-coating total yield strength of samples that were solutionized and coated at different temperatures.	178
Table 4.14. Abbreviations and Related Definitions.	179
Table 4.15: Parameters of solutionizing for varying time periods and cooling rates, and CVD at varying temperatures.....	180
Table 4.16: Post-solutionizing and post-coating total yield strength of samples that are solutionized for different time periods, Ar or furnace cooled.	182
Table 4.17: Heat Treatment and Coating Parameters for Thick and Thin Samples.	183
Table 4.18: Calculated yield strength of as cast, HIPed, solutionized and aged thick and thin samples.	184

Table 4.19: Post-coating and post-aging total yield strength of thin and thick samples.	185
Table 4.20: Literature tensile test, yield strength model, and JMAT PRO calculation results [93].....	193

LIST OF FIGURES

Figure 1.1: Main components of gas turbine engine (GT13E2 Gas Turbine) [7].	3
Figure 1.2: Turkey's energy production shares by resources [11].	4
Figure 1.3: In a jet engine, the turbine part is made by Ni-based superalloys (red parts) [5].	6
Figure 1.4: Evolution of production methods of the Ni-based superalloys over about 60 years of period [15].	6
Figure 1.5: Cast turbine blades: a) Equiaxed, b) Directionally solidified (DS),	7
Figure 1.6: Conventional a) FCC and b) FCC_L12 [30].	14
Figure 1.7: Ni-Al binary phase diagram.	14
Figure 1.8 Uniformly distributed cuboidal γ' precipitates in IN 100, mag. 13625x [2].	15
Figure 1.9: Morphology of carbides [31].	16
Figure 1.10: Fine M23C6 and coarse MC grain boundary carbides in X-750, mag. 4900x [2].	17
Figure 1.11: Phase-Temperature profile of IN 738 LC calculated in JMAT PRO software.	20
Figure 1.12: Comparison of calculated and experimentally observed a) coarsening rate of various Ni-based superalloys and b) TTT diagram for the single crystal alloy RR2071 [50].	23
Figure 1.13: Comparison between calculated and experimental 0.2% proof stress of various Ni-based superalloys [50].	24
Figure 1.14: Relative oxidation and corrosion resistance of high temperature coating systems [14].	24
Figure 1.15: SEM image on a cross-section of aluminide coating and NiAl binary phase diagram.	25
Figure 1.16: Concentration profiles for IN 939-NiAl coating region. Solid lines are calculated. Symbols are experimental data [59].	27

Figure 1.17: Secondary dendrite arms in CMSX-4 single-crystal [82].	31
Figure 1.18: Configuration of dislocations and precipitates during cutting and bowing. Duplicated from Kozar et. al [78].	32
Figure 2.1: a) Scheme of Al surface growth and diffusion during CVD aluminide coating and SEM image of aluminide coating region.	36
Figure 2.2: Schematic of DICTRA diffusion simulation.	37
Figure 2.3: Schematic Al-substrate, β -NiAl-substrate diffusion couples and simultaneous surface growth and diffusion simulation model.	40
Figure 2.4: The schemes, thickness and composition of a) Al-substrate and b) β -NiAl-substrate diffusion couples, and c) surface growth and diffusion model.	42
Figure 2.5: Independent growth rate estimation flow chart.	43
Figure 2.6: SEM image and WDS composition analysis result of coating region.	44
Figure 2.7: Comparison of different aluminide coating simulation model results to SEM-EDS and EPMA-EDS results of the experimental aluminide coating.	46
Figure 2.8: Aluminide coating linear composition profile and DICTRA simulation results for different aluminide coating temperatures.	49
Figure 2.9: Aluminide coating linear composition profile and DICTRA simulation results for different aluminide coating times.	50
Figure 2.10: Simulation and experiment outer layer/inner layer ratio results at a) different coating temperatures and b) for different coating periods.	54
Figure 2.11: Calculated and iteratively simulation Al incorporation rates for samples a) coated at different temperatures and b) for different time periods.	55
Figure 2.12: The Simulation Results for Hypothetical Experimental Conditions	56
Figure 2.13: The Experimental Results for Hypothetical Experimental Conditions .	57
Figure 3.1: The scheme of heat treatments and coatings applied to IN 738 LC microstructure.	61
Figure 3.2: IN 738 LC SEM images of a) bimodal γ' precipitation and b) MC carbide [42].	62
Figure 3.3: IN 738 LC rotor blade cutting and label method.	63
Figure 3.4: Scheme of VAKSIS Vacuum Furnace	63
Figure 3.5: Cutting lines of an IN 738 LC sample.	66

Figure 3.6: Hardness testing locations on the sample.	68
Figure 3.7: Optic microscope and SEM image of IN 738 LC that shows macro hardness and micro hardness measurement area diameters respectively.	68
Figure 3.8: Photo of an IN 738 LC samples taken from middle section of a turbine blade and used for grain size measurement and secondary dendrite arm spacing measurement.....	69
Figure 3.9: Points SEM images were taken on the thick and thin sample.	70
Figure 3.10: SEM image and IMAGE J analyze result that calculates a number of γ' particles.	70
Figure 3.11: Location of samples used in each heat treatment group.	72
Figure 3.12: Sample cutting method.	72
Figure 3.13: Coating region SEM images of samples coated at 1000°C-20 hours, 1050 °C-16 hours and 1100 °C-12 hours.	74
Figure 3.14: The scheme of heat treatments and coatings applied to IN 738 LC microstructure.....	75
Figure 3.15: Location of samples that were used to study the effect of HIP.	76
Figure 3.16: Optic microscope images of IN 738 LC before and after HIP.	76
Figure 3.17: SEM images of as cast and HIPed samples.	77
Figure 3.18: The scheme of heat treatments and coatings applied to IN 738 LC microstructure.....	79
Figure 3.19: The location of samples that were solutionized in between 1080-1235°C for 2 hours.	79
Figure 3.20: SEM images of IN 738 LC samples after solutionizing at various temperatures between 1080°C-1235°C for 2 hours (Ar cooled-180°C/min).....	80
Figure 3.21: Primary and secondary γ' size and volume fraction of as cast, HIPed samples, and solutionized samples at various temperatures between 1080°C-1235°C with representative SEM images.....	81
Figure 3.22: Hardness of as cast, HIPed samples, and solutionized samples at various temperatures between 1080°C-1235°C.....	83
Figure 3.23: Grain size of as cast, HIPed samples, and solutionized samples at various temperatures between 1080°C-1235°C.....	83

Figure 3.24: The location of samples that were solutionized at 1120°C for 1, 2 and 4 hours using Ar (180°C/min) and furnace cooling (20°C/min).	84
Figure 3.25: SEM images, and primary and secondary γ' size and volume fraction after 1, 2 and 4 hours solutionizing time periods, at 1120°C and with Ar (180°C/min) or furnace cooling (20°C/min) rates.	85
Figure 3.26: Hardness of samples after 1, 2 and 4 hours solutionizing time periods, at 1120°C and with Ar (180°C/min) or furnace (20°C/min) cooling rates.....	86
Figure 3.27: Grain sizes of samples after 1, 2 and 4 hours solutionizing time periods, at 1120°C and with Ar (180°C/min) or furnace (20°C/min) cooling rates.....	86
Figure 3.28: The scheme of heat treatments and coatings applied to IN 738 LC microstructure.	88
Figure 3.29: The location of samples that were solutionized in between 1080-1235°C for 2 hours and aluminide coated.	89
Figure 3.30: Post-solutionizing and post-coating SEM images of samples that were solutionized at various temperatures between 1080°C-1235°C for 2 hours (Ar cooled-180°C/min).	90
Figure 3.31: Post-solutionizing and post-coating primary and secondary γ' sizes with some representative SEM images.	92
Figure 3.32: Post-solutionizing and post-coating primary and secondary γ' volume fractions with some representative SEM images.	93
Figure 3.33: Post-solutionizing and post-coating grain size of samples that were solutionized at various temperatures between 1080°C-1235°C.	95
Figure 3.34: Post-solutionizing and post-coating hardness of samples that were solutionized at various temperatures between 1080°C-1235°C.	96
Figure 3.35: The locations of samples that were solutionized at 1120°C for 1, 2 and 4 hours, and aluminide coated.....	97
Figure 3.36: Post-coating and post-solutionizing SEM images of samples.....	98
Figure 3.37: Post-solutionizing and post-coating primary and secondary γ' size of samples that were solutionized at 1120°C for 2 hours, Ar (180°C/min) or furnace cooled (20°C/min), and aluminide coated at 1000, 1050 and 1100°C temperatures..	99

Figure 3.38: Post-solutionizing and post-coating primary and secondary γ' volume fraction of samples that were solutionized at 1120°C for 2 hours, Ar (180°C/min) or furnace cooled (20°C/min), and aluminide coated at 1000, 1050 and 1100°C. temperatures.	100
Figure 3.39: Post-solutionizing and post-coating hardness of samples that were solutionized at 1120°C for 2 hours, Ar (180°C/min) or furnace cooled (20°C/min), and aluminide coated at 1000, 1050 and 1100°C.	101
Figure 3.40: Post-solutionizing and post-coating primary and secondary grain size of samples that were solutionized at 1120°C for 2 hours, Ar (180°C/min) or furnace cooled (20°C/min), and aluminide coated at 1000, 1050 and 1100°C.	101
Figure 3.41: The scheme of heat treatments and coatings applied to IN 738 LC microstructure.	104
Figure 3.42: The locations of as cast, HIPed, solutionized, coated and aged thick and thin samples.	105
Figure 3.43: SEM images of thick IN 738 LC sample after HIP, solutionizing, coating and aging.	106
Figure 3.44: SEM images of thin IN 738 LC sample after HIP, solutionizing, coating and aging.	107
Figure 3.45: γ' size and volume fraction of as cast, HIPed and solutionized thick and thin samples with SEM images.	109
Figure 3.46: Hardness of the of the as cast, HIPed, solutionized and aged thick and thin samples.	110
Figure 3.47: Grain size of the of the cast, HIPed, solutionized and aged thick and thin samples.	111
Figure 3.48: Primary and secondary γ' size and volume fraction of post-coating and post-aging thick and thin samples.	113
Figure 3.49: Hardness of post-coating and post-aging thick and thin samples.	114
Figure 3.50: Grain size of post-coating and post-aging thick and thin samples.	114
Figure 3.51: Experimental and JMAT PRO simulation results for primary and secondary γ' size	117

Figure 3.52: Experimental and JMAT PRO simulation results for primary and secondary γ' volume fraction.....	119
Figure 3.53: JMAT PRO simulation results for tertiary γ' size volume fraction. ...	120
Figure 3.54: Post-solutionizing and post-coating experiment and JMAT PRO simulation for primary and secondary γ' size results of samples solutionized for 1, 2 and 4 hours, and Ar cooled (180°C/min).	122
Figure 3.55: Experiment and JMAT PRO simulation results for primary and secondary γ' volume fractions.	123
Figure 3.56: JMAT PRO simulation results for tertiary γ' size and volume fraction of samples solutionized for 1,2 and 4 hours, and Ar cooled (180°C/min).	125
Figure 3.57: Post-solutionizing and post-coating experiment and JMAT PRO simulation for primary and secondary γ' size results of samples solutionized for 1, 2 and 4 hours, and furnace cooled (20°C/min).....	126
Figure 3.58: Post-solutionizing and post-coating experiment and JMAT PRO simulation for primary and secondary γ' volume fraction of samples solutionized for 1, 2 and 4 hours, and furnace cooled (20°C/min).....	127
Figure 3.59: Experiment and JMAT PRO simulation γ' size of post-coating and post-aging results for thick and thin samples.	131
Figure 3.60: Experiment and JMAT PRO simulation γ' volume fraction of post-coating and post-aging results for thick and thin samples.	133
Figure 3.61: JMAT PRO simulation γ' size and volume fraction of post-coating and post-aging thick and thin samples.	134
Figure 3.62: Experiment and JMAT PRO simulation γ' volume fraction of post-solutionizing and post-aging results for thick and thin samples.	135
Figure 3.63: Experiment (left) and JMAT PRO simulation (right) γ' volume fraction of post-solutionizing and post-aging results for thick and thin samples.....	136
Figure 3.64: Optic microscope images of samples with different heat treatment histories.	141
Figure 4.1: a) Yield strength calculation flow chart, b) SEM image, c) Optic Microscope Image.....	148

Figure 4.2: Composition change of γ -matrix depending on temperature calculated by JMAT PRO software.....	150
Figure 4.3: Solid solution contribution of alloying elements in γ -matrix of IN 738 LC depending on temperature (in equilibrium).....	151
Figure 4.4: The location of samples that were solutionized in between 1080-1235°C for 2 hours and aluminide coated.	156
Figure 4.5: Post-solutionizing and post-coating grain boundary strengthening of samples that were solutionized at different temperatures.	156
Figure 4.6: The location of samples that were solutionized at 1120°C for 1, 2 and 4 hours and aluminide coated.....	157
Figure 4.7: Post-coating grain boundary strengthening of samples that were solutionized for different time periods and Ar cooled.	158
Figure 4.8: Post-coating grain boundary strengthening of samples that were solutionized for different time periods and furnace cooled.....	158
Figure 4.9: The locations of thick and thin sample group.....	160
Figure 4.10: Grain boundary strengthening of the cast, HIPed, solutionized and aged thick and thin samples.	160
Figure 4.11: Grain boundary strengthening of post-coating and post-aging thick and thin samples.....	161
Figure 4.12: The location of samples that were solutionized in between 1080-1235°C for 2 hours and aluminide coated.	165
Figure 4.13: Primary γ' strengthening of post-solutionizing and post-coating samples.	165
Figure 4.14: Secondary γ' strengthening of post-solutionizing and post coating samples.	166
Figure 4.15: Total γ' strengthening of solutionized and post-coating samples.	166
Figure 4.16: The location of samples that were solutionized at 1120°C for 1, 2 and 4 hours and aluminide coated.....	169
Figure 4.17: Post-solutionizing and post-coating, primary and secondary γ' strengthening for samples Ar and furnace cooled.	170
Figure 4.18: The locations of thick and thin samples.	172

Figure 4.19: Primary, secondary and total γ' strengthening of the cast, HIPed and solutionized thick and thin samples.	173
Figure 4.20: Post-coating and post-aging primary and secondary γ' strengthening of thick and thin samples.	174
Figure 4.21: Post-coating and post-aging γ' derived yield strength of samples.	175
Figure 4.22: The location of samples that were solutionized in between 1080-1235°C for 2 hours and aluminide coated.	177
Figure 4.23: Post-solutionizing and post-coating total yield strength of samples that were solutionized and coated at different temperatures.	178
Figure 4.24: The location of samples that were solutionized at 1120°C for 1, 2 and 4 hours and aluminide coated.	180
Figure 4.25: Post-solutionizing and post-coating total yield strength of samples that are solutionized for different time periods and Ar cooled.	181
Figure 4.26: Post-solutionizing and post-coating total yield strength of samples that are solutionized for different time periods and furnace cooled.	181
Figure 4.27: The locations of as cast, HIPed, solutionized, coated and aged thick and thin samples.	183
Figure 4.28: Calculated yield strength of as cast, HIPed, solutionized and aged thick and thin samples.	184
Figure 4.29: Post-coating and post-aging total yield strength of thin and thick samples.	185
Figure 4.30: Yield strength estimation results of JMAT PRO and yield strength model for IN 738 LC samples solutionized at different temperatures.	187
Figure 4.31: JMAT PRO yield strength estimation and yield strength model results for IN 738 LC samples solutionized for different time periods followed by Ar or furnace cooling.	189
Figure 4.32: Yield strength estimation of JMAT PRO and yield strength model results for total yield strength of thick and thin IN 738 LC samples.	190
Figure 4.33: Yield strength model and JMAT PRO simulation yield strength estimation results for total yield strength of thick and thin IN 738 LC samples.	191

Figure 4.34: Literature tensile test (measured), yield strength model (calculated), and JMAT PRO calculation results. [93]	194
--	-----

LIST OF ABBREVIATIONS

CVD	Chemical Vapor Deposition
EDS	Energy Dispersive Spectroscopy
EPMA	Electron Probe Micro Analysis
FCC	Face Centered Cubic
HIP	Hot Isostatic Pressing
SEM	Scanning Electron Microscopy
G.P.	Gamma Prime
Ar C.	Argon Cooling
F.C.	Furnace Cooling
Γ_k^ϕ	Averaging Function
M_k^ϕ	Mobility of Component k
x_k^ϕ	Mole Fraction of Component k
J_k	Flux of Component k
V_m	Molar Volume of Component k
$\Delta \tilde{z}$	Time-dependent Spatial Coordinate
R	Gas Constant
T	Temperature
$\sigma_{y,s,i}$	Solid Solution Strengthening
β_i	Solid Solution Constant
x_i	Atomic Fraction
q	Concentration Exponent
p	Concentration Exponent
σ_D	Grain Boundary Strengthening

σ_0	Friction Stress
k_y	Hall-Petch Constant for Grain Boundary
D_D	Average Grain Size
σ_P	Phase Boundary Strengthening
k_d	Hall-Petch Constant for Dendrite
D_P	Average Secondary Dendrite Spacing
τ_p^{strong}	Strong Couple Precipitation Strengthening
τ_p^{weak}	Weak Couple Precipitation Strengthening
M	Taylor Equation Factor
T	Line Tension
f	Gamma Prime Volume Fraction
w	Elastic Repulsion
b	Burgers Vector
d	Average Gamma Prime Radius
γ_{APB}	Anti-phase Boundary Energy
ϕ	γ' Morphology Constant
μ	Shear Modulus
P.	Precipitation Strengthening
S.S.	Solid Solution Strengthening
G.B.	Grain Boundary Strengthening

CHAPTER 1

INTRODUCTION

1.1 General

In 1872, George Bailey Brayton introduced Brayton cycle and showed that increasing inlet temperature of a thermal system also increases its efficiency. This development led to the discovery of the steam turbine in the 19th century, that was followed by employment of gas turbines in the early 1900s [1]. It was soon understood that operations under high temperatures and progress of these new energy technologies were only possible with high temperature materials. This led to the introduction of superalloys and their employment in gas turbine engines.

The term “superalloys” was first used to describe a group of alloys developed for turbine engines and turbo superchargers in the 1930s. [2] These alloys are based on Group 8B elements and commonly consist of various combinations of Fe, Ni, Co, and Cr, as well as lesser amounts of W, Mo, Ta, Nb, Ti, and Al. The three major classes of super alloys are iron, cobalt, and nickel-based.

Iron-based superalloys are developed from austenitic stainless steels and strengthened by both solid solution and precipitation strengthening. The most important group of these alloys contain at least 25 percent Ni to stabilize FCC matrix phase; these type of alloys are called as nickel-iron-cobalt based superalloys. The precipitates of iron-based alloys are Ni_3Al (γ'), Ni_3Nb (γ'') and Ni_3Ti (η). [3, 4]

Cobalt-based superalloys are strengthened by solid solution hardening and carbide strengthening. Unlike the iron-based and nickel-based superalloys, no precipitates

exist to strengthen the material. These alloys show superior corrosion resistance, thermal fatigue resistance and weldability over nickel alloys. However, they have lower strength, ductility and fracture toughness than Ni-based super alloys. [3, 4, 5]

Ni-based superalloys are the most complex group of all superalloys. These alloys have highly stable FCC matrix that is strengthened by various processes. High temperature strength, surface stability, oxidation and corrosion resistance of Ni-based superalloys are readily improved by alloying with Cr and Al elements. Corrosion resistance of Ni-based Superalloys can be improved even further by high temperature coatings. Therefore, Ni-based superalloys are widely used for gas turbine blades.

The first appearance of simple turbines dates back to the time of ancient Greece. However, the gas turbines are relatively new in energy production history. Brown Boveri company developed the first gas turbine to produce electricity in Switzerland in 1939, and first gas turbine powered plane took off in Germany in 1940 using the gas turbine developed by Hans P. von Ohain [6].

Today, the gas turbines are used in several different models. Shaft power gas turbines are used in industrial applications and energy production to provide shaft power while jet engine gas turbines are used in military and commercial aviation to deliver thrust. Regardless of whether it is at sea, on land or in the air, the gas turbine operates in the same form, however depending on power output and operation environment, the design changes. Gas turbines can utilize a variety of fuels, including natural gas, fuel oils, and synthetic fuels.

A gas turbine basically compresses air and mixes it with fuel, which are then ignited together. Resulting gases are expanded through a turbine under high temperature and pressure. That turbine's shaft continues to rotate and drive the compressor, which is on the same shaft, and loops continues. The basic components of the gas turbine are shown in Figure 1.1.

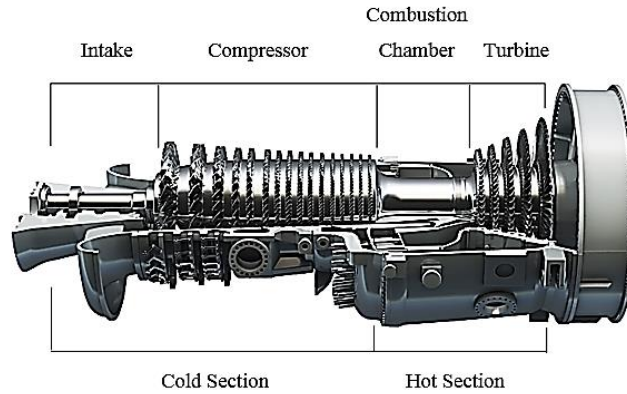


Figure 1.1: Main components of gas turbine engine (GT13E2 Gas Turbine) [7].

Gas turbine components must work under a variety of extreme stress, temperature, and corrosion conditions. Compressor blades operate at a comparably low temperature but a highly stressed condition. The combustor operates at a relatively high temperature and low-stress conditions. The turbine blades operate under high temperature and high stress, and additionally in extremely corrosive environment. The high temperature durability of turbine blade improves the lifetime and efficiency of gas turbine. Depending on the application type, the severity of problems in gas turbines changes greatly as shown in Table 1.1.

Table 1.1: The Important Problems for Gas Turbine Applications [8, 9]

	Oxidation	Hot Corrosion	Interdiffusion	Thermal Fatigue	Weight
Aircraft Engines	severe	moderate	severe	severe	severe
Land-Based Power Generators	moderate	severe	moderate	light	light
Marine Engines	moderate	severe	light	moderate	moderate

The first gas turbine was developed to produce electricity in Switzerland in 1939. However, first gas turbines were used in 1980s to produce electricity in Turkey [10].

Today, Turkey is one of the fastest growing energy markets in the world and it has been experiencing sharp demand growth in the energy sector in last years. Currently, almost 35% energy demand of Turkey is heavily met by natural gas and fuel oil as shown in Figure 1.2 [11]. A significant part of these resources is used in gas turbine based power plants to produce energy. Some of the power plants that have highest energy production capacity in Turkey are Enka Gebze, Enka Adapazarı, Bursa and Ambarlı power plants. [12, 10] Therefore, researchers about critical high temperature materials that are used in gas turbines such as turbine blades have critical importance to guarantee energy security of Turkey. [11]

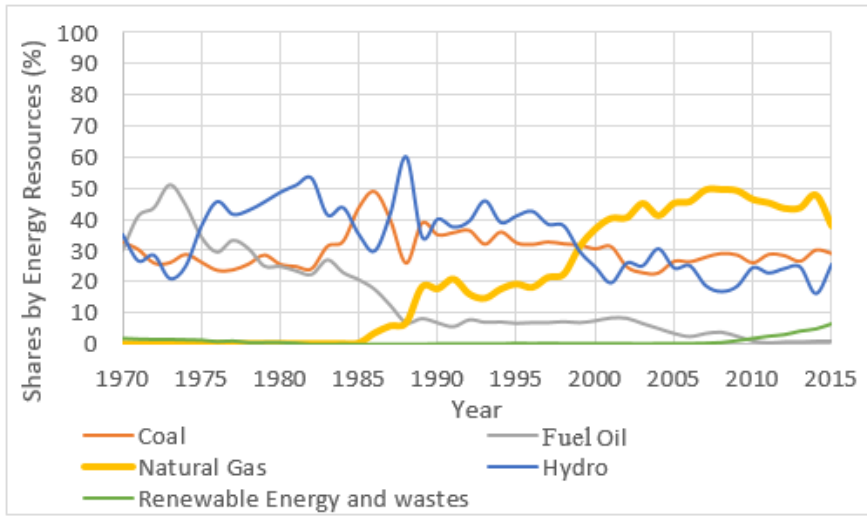


Figure 1.2: Turkey's energy production shares by resources [11].

1.2 Background Information and Literature Review

1.2.1 The Need for High Temperature Materials in Gas Turbines Blades

Gas turbines were first introduced during the Second World War. Since heat resistant steels and super alloys were not available, back then the efficiency of gas turbines was very low, and the necessity of this technology was discussable.

Wrought and cast iron were used in the earliest version of turbines in hot sections where operation temperature and pressure was relatively low. However, it was soon

understood that higher operating temperature is necessary to increase the corresponding efficiency. Low alloy steels were used as the first high temperature metallic materials in gas and steam turbines temperatures up to 550°C. The need for higher oxidation resistance resulted in the progress of stainless steel with high Cr contents. 9-12% Chromium steel allowed operation temperatures up to 600°C, however above this temperature creep strength of high Cr steel was quite insufficient [13].

The Ni-Cr alloys was developed early in 1900's and recognized with excellent oxidation resistance. The addition of small amounts of Al and Ti was found to be considerably increasing creep strength of Ni-Cr alloys in 1929. This mechanism provided the basis of the first Ni-based superalloy (Nimonic 80) in 1940. In 1960s, changes in Ni-based superalloy composition to increase creep resistance, resulted in degradation of corrosion resistance. Since then, application of protective coating become a general practice to improve corrosion resistance [13].

As the inventions in gas turbines progressed, different high temperature materials were developed through composition and microstructural modification. A brief list of these materials includes Ni-Cr alloys, Ni-based superalloys, Ti-based alloys, Co-based alloys, ceramic materials (silicon carbide, silicon nitride, glass ceramics, alumina, and zirconia), high temperature composite materials.

Due to insufficient dislocation mobility, poor ductility and incapability of plastic deformation, ceramic materials are utilized in stationary parts of gas turbines such as combustion chamber. However, the ceramic composites have been developed, suitable for turbine blades that are improved upon so called material drawbacks [13].

1.2.2 Introduction to Ni-based Superalloys

Ni-based superalloys have exceptional performance at high temperatures that usually combines high strength (creep, tensile, fatigue), toughness, ductility, and corrosion resistance. Due to these characteristic properties, Ni-based superalloys are heavily

employed in the production of gas turbine blades and discs at temperatures as shown in Figure 1.3, between 650°C-1150°C [14].

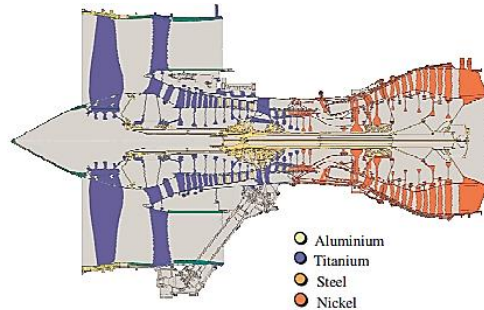


Figure 1.3: In a jet engine, the turbine part is made by Ni-based superalloys (red parts) [5].

Turbine blades are critical components in both aeronautical and stationary gas turbines. The engine performance is closely related to the capability of the turbine blade to withstand high temperature. The evolution of the high temperature capability of the Ni-based superalloy over about 60 years'' period is shown in Figure 1.4 [15].

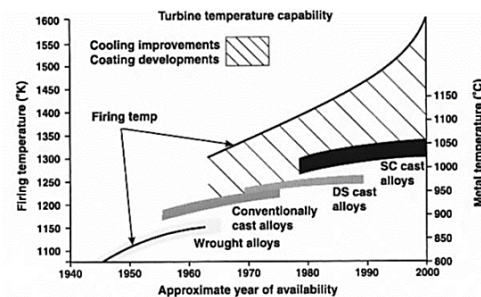


Figure 1.4: Evolution of production methods of the Ni-based superalloys over about 60 years of period [15].

As shown in Figure 1.4, wrought superalloys were used as turbine blades in the 1940s. Due to increased demand in aviation after 1955, conventionally cast superalloys took the place of the wrought superalloys. The conventional equiaxed casting process is widely used to create uniform grain structure along in all axes, since undesirable grain

sizes, shapes, and transition areas cause failure of turbine blades. These failures occur at grain boundaries during service rather than within the grains. Therefore, the full strength of the crystal itself cannot be used [15, 16]. The grain boundaries of this equiaxed microstructure were strengthened by carbon, boron and zirconium, hafnium [14]. The equiaxed microstructures is shown in Figure 1.5a [14].

In the 1960s, directionally solidified Ni-based superalloys were developed to improve the creep strength and ductility. In this method, columnar grains were aligned to the blade axis (most of the stress in the blade is in the direction of centrifugal force-along the length of the blade) and transversal grain boundaries were eliminated. The directionally solidified microstructure is shown in Figure 1.5b [14].

Around thirty years ago, 1st generation of single crystal (SC) alloys were developed by eliminating all the grain boundaries. This removed the necessity of using grain boundary strengthening elements such as zirconium, boron, and carbon. Additionally, creep resistance of blades was improved due to the absence of grain boundary sliding and lower vacancy condensation. The cast turbine blades made by these three techniques are given in Figure 1. 5c [14]. Compositions of some commercial Ni-based superalloys that are used in industry are given in Table 1.2 [17].

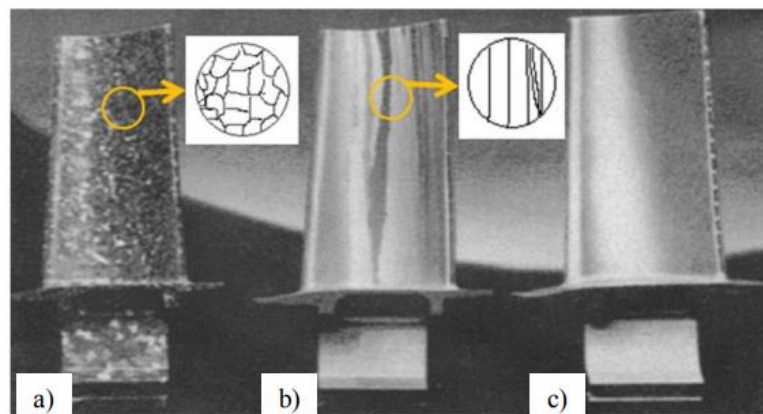


Figure 1.5: Cast turbine blades: a) Equiaxed, b) Directionally solidified (DS), c) Single crystal (SC) [14]

Table 1.2: Composition of Some Commercial Ni-Based Superalloys (wt. %) [17].

Alloy	Cr	Co	Mo	W	Ta	Re	Nb	Al	Ti	Hf	C	B	Y	Zr	Fe
Conventionally Cast Alloys															
IN 713 LC	12.0	-	4.5	-	-	-	2.0	5.9	0.6	-	0.05	0.01	-	0.10	-
Rene 80	14	9.5	4	4	-	-	-	3	5	-	0.17	0.02	-	0.03	-
Directionally Solidified Superalloys															
IN 792	12.6	9	1.9	4.3	4.3	-	-	3.4	.4	1	0.09	0.02	-	0.06	-
GTD 111	14	9.5	1.5	3.8	2.8	-	-	3.	4.9	-	0.1	0.01	-	-	-
First Generation Single Crystal Alloys															
Rene N4	9.8	7.5	1.5	6	4.8	-	0.5	4.2	3.5	0.15	0.05	-	-	-	-
CMSX3	8	5	0.6	8	6	-	-	5.6	1	0.1	-	-	-	-	-
Second Generation Single Crystal Alloys															
Rene N5	7	7.5	1.5	5	6.5	3	-	6.2	-	0.15	0.05	-	0.01	-	-
CMSX 4	6.5	9	0.6	6	6.5	3	-	5.6	1	0.1	-	-	-	-	-
Third Generation Single Crystal Alloys															
Rene N6	1.2	12.5	1.4	6.0	7.2	5.4	-	5.8	-	0.15	0.05	-	0.01	-	-
CMSX 10	2	3	0.4	5.0	8	6	0.1	5.7	0.2	0.03	-	-	-	-	-
Wrought Superalloys															
IN 718	19.0	-	3.0	-	-	-	5.1	0.5	0.9	-	-	0.02	-	-	18.5
UDIMET 500	17.5	16.5	4	-	-	-	-	2.9	-	-	-	0.01	-	-	-

IN 738 is one of the widely used conventionally cast Ni-based superalloy, developed and patented by Inconel Corporation in 1969 [18]. The alloy was specifically designed for land-based turbines rather than aircraft gas turbines to withstand high temperature corrosion/oxidation and stress environment [19]. The objective to design this alloy was to combine sulfidation and oxidation resistance of UDIMET 500 with high strength of IN 713 [20]. Composition of these alloys and other commercially available Ni-based superalloys are given in Table 1.2, specifically composition of IN 738 LC is given in Table 1.3.

GE used IN-738 as a first stage blade material from 1971 until 1984. Then it was replaced by GTD-111 (Table 1.2). It is now mostly used as a second and third stage material in gas turbines. IN 738 LC has an operational capability in high temperature hostile environment up to 950°C and melting range to 1230-1315°C [13, 21]. It has high (0.17 wt.% C) and low carbon versions where low carbon (0.11 wt.% C) shows better castability in large section sizes [21].

IN 738 LC has a unique design that combines phase stability, corrosion resistance and high temperature strength corresponding to perfectly balanced critical elements (Cr. Mo. Co. Al. W. and Ta) inside [22]. The chemical composition of IN 738 LC (low carbon) is given in Table 1.3 [21].

Table 1.3: IN 738 LC Chemical Composition (wt. %) [21].

Elements	Range	Nominal Composition
Ni	Balance	Balance (61)
Ti	3.20-3.70	3.4
Nb	0.6-1.1	3.4
Ta	1.5-2	1.75
C	0.09-0.13	0.11
Co	3-9	8.5
Cr	15.7-16.3	16
W	2.4-2.8	2.6
Mo	1.5-2	1.75
B	0.007-0.012	0.01
Zr	0.03-0.08	0.05
Al	3.20-3.70	3.4

In this study, IN 738 LC superalloy is used to manufacture third stage gas turbine rotor blade. The manufacturing process of these turbine blades consists of casting, different heat treatments (hot isostatic pressing, solutionizing and aging) and high temperature coating steps.

IN 738 LC structure is tend to form micro porosities during solidification that reduces the materials mechanical properties. Hot isostatic pressing (HIP) is a typical heat treatment that is performed after casting, at high temperature and high Ar pressure to eliminate these micro porosities and their detrimental effects.

Traditionally, two heat treatments are performed for IN 738 LC after the HIP operation is completed. First one is the “solutionizing” heat treatment to dissolve γ' and secondary carbides, to homogenize the microstructure, and to reduce the effects of elemental segregation. The second one is “aging” treatment to achieve maximum volume fraction and accordingly maximum strength facilitating to precipitation of γ' phase in the matrix. The cooling rate after these heat treatments is also critical to design and develop materials microstructure and mechanical properties. The high cooling rate is known to improve mechanical properties of the blade [23, 24].

Preferably after solutionizing, high temperature coatings are applied on IN 738 LC. Thermal barrier and bond coatings are widely used high temperature coatings for Ni-based superalloy gas turbine blades to reduce blade temperatures and to provide oxidation/corrosion resistance, thereby increasing lifetime. Bond coating is preferred for turbine blades with lower operation temperatures [25]. It can be performed by pack, above the pack, or chemical vapor deposition (CVD) methods. These coating operations are performed at high temperature for long time periods. Due to this reason, studying the effect of coating condition is important.

The details of heat treatment and aluminide coating operations is provided in following sections.

1.2.3 Metallurgy of Ni-Based Superalloys

Ni-based superalloys are usually multicomponent and multiphase alloys that have highly complicated microstructures. They constitute more than ten elements and these elements form a number of phases such as gamma (γ), γ' , γ'' , carbides (MC , $M_{23}C_6$, M_6C , and M_7C) and topologically closed pack (TCP) phases. All of these phases and alloying elements, influence characteristic properties of the superalloy. Thus, chemical composition and structure of alloy should be optimized accurately. In this section, roles of alloying elements and effects of the phases on superalloy properties are discussed.

1.2.3.1 Role of Alloying Elements

Ni-based superalloys usually constitute high amounts of nickel, chromium, cobalt, and low amounts of aluminum, titanium, tungsten, carbon, niobium and trace amounts of tramp elements (such as sulfur and oxygen). The properties of superalloy highly depend on the chemical composition of these contributing elements. A single element can be a major contributor or it can cause massive degradation in superalloys' properties depending on its chemical composition and the presence of phases. Therefore, it is important to control amounts of alloying elements in a superalloy precisely. Alloying elements are generally classified by the phases they form (γ' or γ'' formers, carbide formers, carbon nitride formers, etc.) or their beneficial/detrimental effects (oxidation/corrosion resistants, grain boundary refiners, embrittlement increasers, etc.) Roles of alloying elements widely used in Ni-based superalloys are given in Table 1.4 [3, 20, 26].

Solid solution formers provide strength to the matrix via interacting and blocking dislocation movements. These elements cause lattice distortions and limit slip of dislocations. Jena and Chatuverdi stated that solutes that are having high hardening coefficients and reasonable solid solubility should also improve the creep strength [27].

The effects of residual elements in Ni-based superalloys are investigated by Sinha et. al. Tramp elements found to be segregating to grain boundaries and reduce creep resistance, ductility and stress rupture properties. However, trace elements (B, Mg, Y, Zr, Cr) added in ppm (part per million) level sometimes found to be beneficial for high temperature performance and hot workability [28].

Table 1.4: Functions of various in Ni-based superalloys [3, 20, 26].

Effect		Element
Solid solution strengtheners		Co, Cr, Fe, Mo, W, Ta, Re
High temperature strength		Ni, Nb, C, Co, Mo, W
γ' formers $\text{Ni}_3(\text{Al,Ti})$		Al, Ti
Carbide Formers	MC	Ta, Ti, Mo, Nb, Hf
	M_{23}C_6	Cr
	M_6C	Mo, W, Nb
	M_7C_3	Cr
Carbionitrides: $\text{M}(\text{CN})$		C, N
Raises γ' solvus temperature and melting Point of γ matrix		Co
Hardening precipitates and/or intermetallics		Al, Ti, Nb
Oxidation resistance		Ni, Al, Cr, Y, La, Ce, Si, Co, Mo
Hot corrosion resistance		La, Th
Sulfidation resistance		Cr, Co, Si
Increases rupture strength		B
Grain boundary refiners		B, C, Zr, Hf
Adherence of oxide layer		Rare earth elements
Causes embrittlement by grain boundary segregation		S, P, Si

Ni, Al, Ti and Nb form γ' - Ni_3X phase in Ni-based superalloys. Since these alloys strength derives from γ' - Ni_3X phase, the formation of these precipitates are crucial.

Carbides are classified by their morphology and chemical composition. Depending on their morphology and distribution, they may have both detrimental and favorable effects. Fine sized carbides formed along grain boundaries can prevent grain boundary sliding and dislocation, thus improving creep resistance and rupture strength. On the

other hand, continuous chain of carbides formed along grain boundaries may facilitate crack propagation [3, 29].

Corrosion, oxidation and sulfidation resistant elements can also be called surface stabilizers. These elements prevent material degradation in aggressive environments. Ni, Al, Cr, Y, La, Ce, Si, Co, Mo, Ti and Nb elements are called surface stabilizers. [3, 20, 26, 29].

Presence of B, C, Zr and Hf elements are known to contribute grain boundary strengthening [27].

1.2.3.2 Phases Present in Ni-Based Superalloys

Ni-based superalloys are the most complex alloy type because of their dynamic chemical structure. They are multicomponent and multiphase alloying systems. The microstructure of Ni-based superalloys consists of γ matrix phase, γ' precipitate phase (γ' : $\text{Ni}_3(\text{Al, Ti, Nb})$), metal carbide phases (MC, M_{23}C_6 , M_7C_3 , M_6C) and some minor other phases such as borides and TCP phases. In this section, structure and constitution of the major phases present in Ni-based superalloys are summarized.

1.2.3.2.1 Gamma (γ) Matrix

The continuous FCC- γ matrix phase consists of primarily Ni and solid solution elements such as Co, Cr, Fe, Mo, W, Ta, and Re. The strengthened γ matrix can withstand with most severe temperature and time conditions. It shows high phase stability due to its almost filled third (d) electron shell [3].

Typically, addition of Co, Cr, and Al to γ matrix is favorable. Co is increasing alloys melting temperature [20]. A reasonable level of Cr is important for corrosion resistance. An excessive level of Cr is found to decrease the strength of the material [29]. Also, Cr_2O_3 formed on the surface of the material limits the inward diffusion of oxygen, nitrogen, and sulfur. A similar effect is displayed by Al_2O_3 formed on the surface that provides resistance against further oxidation in the material. [3]

1.2.3.2.2 Gamma Prime (γ') Precipitates

γ' -Ni₃Al precipitation is the major strengthening mechanism of Ni-based superalloys. 60% of the aluminum inside γ' can be substituted by Ti and/or Nb. [3] This phase coherently precipitates in matrix and it has FCC_L12 crystal structure. In FCC_L12, corners and faces are occupied by a different type of atoms as shown in Figure 1.6. [1]

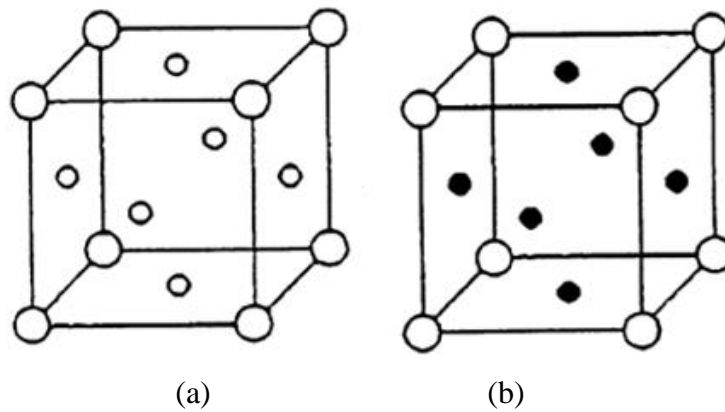


Figure 1.6: Conventional a) FCC and b) FCC_L12 [30].

The precipitate Ni₃Al (γ') has a narrow range as can be seen in Ni-Al binary phase diagram given in Figure 1.7.

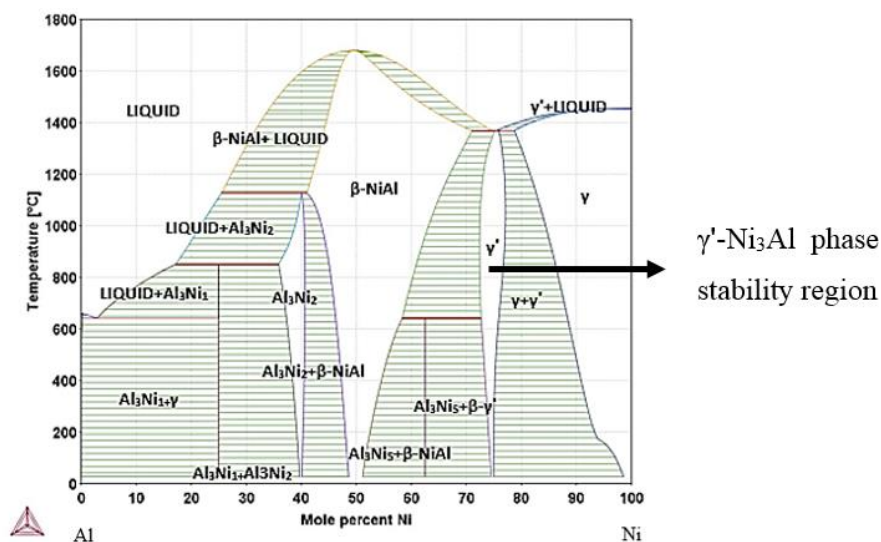


Figure 1.7: Ni-Al binary phase diagram.

The shape of the γ' precipitate depends on the mismatch between γ -matrix and γ' precipitate. Increasing the mismatch result with the transformation of spheroidal to cuboidal, then cuboidal to plate like morphology [3]. SEM image of uniformly distributed cuboidal γ' precipitates is shown in Figure 1.8 [2].

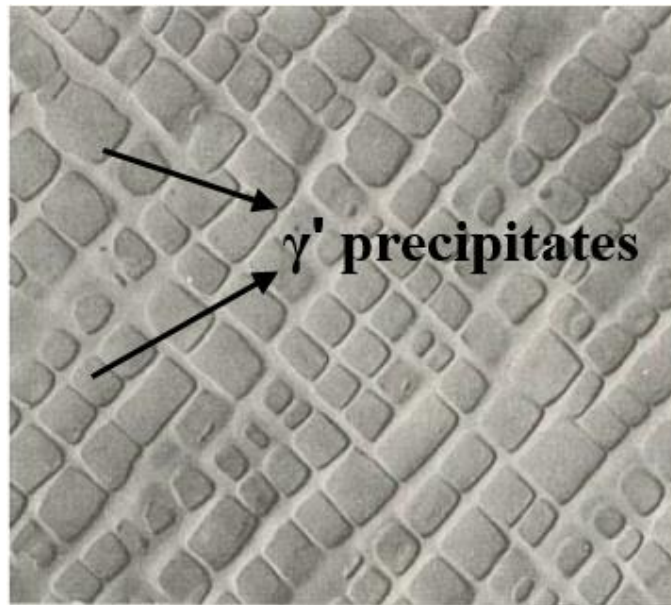


Figure 1.8: Uniformly distributed cuboidal γ' precipitates in IN 100, mag. 13625x [2].

γ' particles in matrix limit dislocation movements and enhance the high temperature strength of material [31]. This can be controlled by amount and distribution of γ' precipitates. Considering γ' is the main strengthening mechanism of Ni-based superalloys, the amount of this phase is highly important. This phase is dispersed at the points that Al, Nb and Ti presence is higher than the solubility limit of the matrix.

Carbides & Borides

Carbon (amount of 0.02 to 0.2 weight percent) and reactive elements combined, forms carbide phases in Ni-based superalloys [2]. Depending on their distribution and morphology they can be detrimental and beneficial to materials properties. MC, $M_{23}C_6$, M_7C_3 and M_6C are the common carbide types where M represents metals such as Ti, Ta, Nb, Mo, W and Cr. Figure 1.9 shows common shapes of carbides formed in Ni-based superalloys [31].

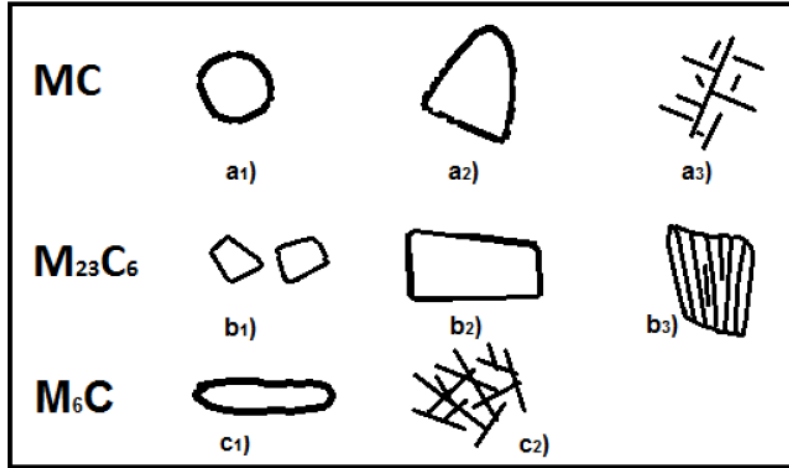
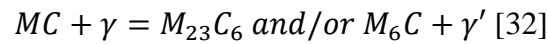


Figure 1.9: Morphology of carbides [31].

MC type of carbides are formed during solidification as coarse and random particles in transgranular, intergranular positions and between dendrites [3]. Fine MC carbides that are segregated at matrix or grain boundaries strengthens the alloy and ties up elements that promote unstable phase formations during heat treatments or service [32]. These carbides are very stable at low temperatures [33]. However, they degenerate at high temperatures and transforms into more stable $M_{23}C_6$ and M_6C carbides at 760-980°C and 815-980°C, respectively [32]. This transformation can be described as:



$M_{23}C_6$ carbides are relatively smaller and more irregularly shaped compared to MC carbides. Finely shaped and distributed $M_{23}C_6$ carbides at grain boundaries can limit dislocation movement and increase rupture strength [3]. However, chain and film like carbide particles might facilitate crack propagation that causes failure [3, 29]. Additionally, the formation of $M_{23}C_6$ carbides causes a significant decrease of Cr in the matrix that can weaken the corrosion resistance of alloy [34, 35]. Examples of MC and $M_{23}C_6$ carbides are shown in Figure 1.10 on SEM image [2].

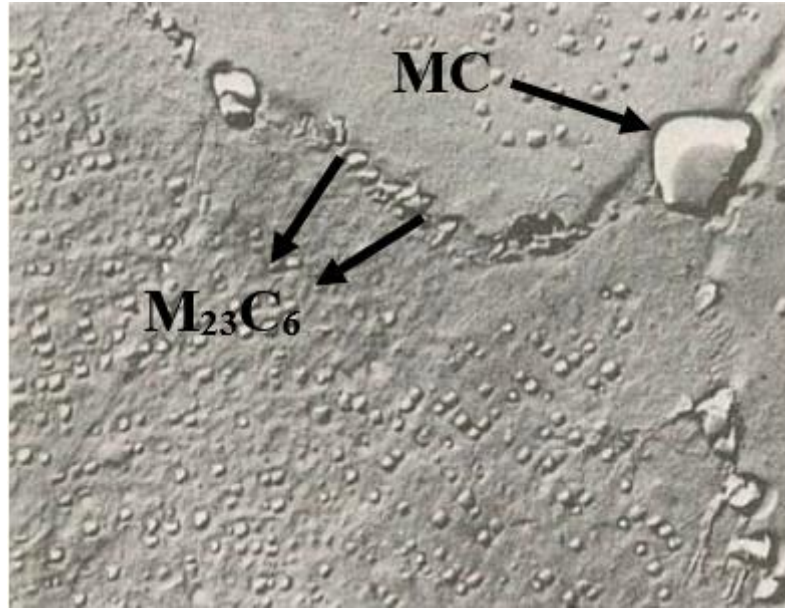
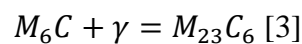


Figure 1.10: Fine $M_{23}C_6$ and coarse MC grain boundary carbides in X-750, mag. 4900x [2].

M_6C type carbide is more stable than $M_{23}C_6$. It is formed when Cr is replaced by Mo and/or W. This carbide is commonly encountered when the amount of these two elements is more than 6-8% of alloy composition. It is commercially important for grain size controlling. It can transform into $M_{23}C_6$ with a long time exposure to heat treatment as described below [3].



M_7C_3 is not a common carbide in superalloys. It presents mostly in Co-based superalloys and rarely in Ni-based superalloys as blocky shaped in grain boundaries. It can take the formation of Cr_7C_3 [3].

Borides are formed due to the low solubility of B in γ matrix phase [32]. Similar to carbides they act as a dislocation barrier, thus they increase creep resistance and rupture strength of superalloys. They are blocky to half-moon shaped hard particles [3]. M_3B_2 and M_5B_3 boride types are generally encountered in Ni-based superalloys [32].

1.2.3.2.3 Topologically Close Packed Phases (TCP)

Topologically close packed (TCP) phases form during heat treatment or more likely, during service. Specifically, they form when the alloy composition is not balanced and controlled properly. Distinctively, the presence of high amount BCC transition metals (Cr, Ta, Nb, Mo, and W) promotes TCP phase formation. Ni-based superalloys commonly have μ -(Fe,Co)₇(Mo,W)₆, σ -(Fe, Mo)_x(Ni,Co)_y and Laves (Fe,Cr,Mn,Si)₂(Mo,Ti,Nb) TCP phases that are mostly plate or needle like shaped [3]. Since μ has similar crystal structure to M₆C and σ has a similar structure to M₂₃C₆, they are known to nucleate on these secondary carbides [4]. TCP phases are known to be detrimental to material properties because of two reasons. They are (specifically σ -phase) known to degrade ductility and creep rupture strength properties of superalloys because of their extreme hardness [2, 3, 31]. Secondly, they are known to deplete strengthening elements around their formation regions in the matrix. This could cause the lack of solid solution elements in the matrix such as Mo, Co, and W. Additionally since they are also retrieving Cr from the matrix during their formation process, they promote weakened corrosion resistant spots on materials surface [2, 31].

1.2.4 Heat Treatments and Their Simulations

Ni-based superalloys are specifically designed to be utilized in high temperature applications. The microstructure and mechanical properties of these materials can be related to their manufacturing process. One of these manufacturing processes is heat treatment which consists of hot isostatic pressing, solutionizing followed by a single or double step of aging.

1.2.4.1 Hot Isostatic Pressing

Discontinuities of IN 738 LC in interdendritic areas such as porosities form during the solidification and weaken the mechanical properties which eventually degrading creep resistance and ductility of material. Hot isostatic press is a widely used method to eliminate these micro porosities and their detrimental effects. An additional benefit of

HIP is increasing materials' homogeneity. Basically, HIPing process involves subjecting the material to combined effects of high temperature and isostatic gaseous pressure.

The studies in the literature show that internal porosities and their detrimental effects on cast IN 738 LC could be eliminated by HIP operation at about 1200°C and 100 MPa. HIP duration time has been varies between 2 to 5 hours depending on the initial microstructure [36, 37, 38, 39, 40].

Saeed Farahany et. al proved that HIP is more effective when it is applied before solutionizing and aging treatment than after for IN 738 LC. Application of HIP at 1200°C for 2 hours under 120 MPa followed by secondary heat treatments provided better creep strength, hardness and ductility compared to IN 738 LC samples heat treated and afterward HIPed [36].

Due to high temperature and long durations of HIP operations γ' morphology in microstructure changes. Saeed Farahany et. al also found that HIP causes coarsening of primary γ' particles and making them less coherent with the matrix. Wangyao et al. reported that smaller γ' particles dissolve into the matrix during HIP operation, decreasing total γ' volume fraction [40]. Due to necessity of recovering from these detrimental changes that occur on IN 738 LC microstructure during HIP, especially on γ' morphology, secondary heat treatments (solutionizing and aging) are necessary.

1.2.4.2 Solutionizing

Several studies had been carried out in the literature regarding the solutionizing operation of IN 738 LC in between 1090-1235°C for 1 to 4 hours with different cooling rates [20, 41, 42].

Generally, Ni-based superalloys are solutionized over their γ' solvus temperature to have complete dissolution and provide maximum γ' volume fraction. However, the high solutionizing temperature to dissolve all γ' particles is not an option for IN 738 LC due to incipient melting [41]. Therefore, mostly subsolvus solution temperature is

used that results in incomplete dissolution of primary γ' and non-stoichiometric secondary and tertiary γ' particles. Equilibrium weight fractions of γ , γ' and liquid phases in IN 738 LC are calculated in JMAT PRO software as shown in Figure 1.11.

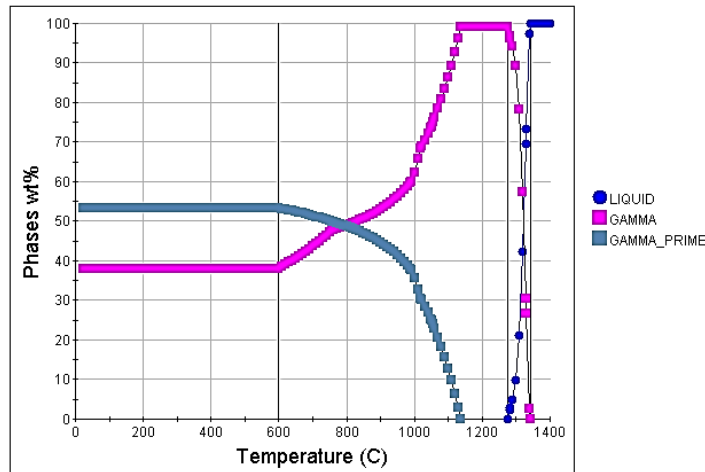


Figure 1.11: Phase-Temperature profile of IN 738 LC calculated in JMAT PRO software.

The predicted solvus temperature is calculated to be 1137°C while commercially recommended solution heat treatment is 1120°C for IN 738 LC, which is a subsolvus temperature. [20] Ho-Seob Yun et. al and Jeong Min Kim et. al performed partial solutionizing at 1120°C for 2 hours in their studies and found a bimodal microstructure with coarse cuboidal primary and fine secondary γ' particles. They also used 1200°C as solutionizing temperature for 2 hours that formed a unimodal fine γ' particles in the microstructure [42, 43].

Anurag Thakur used solutionizing temperatures at 1120, 1150 1175 and 1225°C. Highest γ' size was achieved at 1150°C and temperature increase over 1150°C resulted in decrease of γ' size and decrease in γ' volume fraction due to bimodal to unimodal structure transformation [20]. Besides γ' particles, there are also MC carbides in IN 738 LC microstructure. Due to a melting point above 1525°C, they just partly dissolve during solutionizing. [43].

Solutionizing time has been used in a range of 1 to 4 hours for IN 738 LC in the literature [36, 43]. The commercially recommended heat treatment period is 2 hours at 1120°C for IN 738 LC [20]. However, Saeed Farahany showed that 1 hour solutionizing treatment is enough to have desired bimodal final microstructure at the same solutionizing temperature [36].

Jeong Min Kim proved that increasing solutionizing time of IN 738 LC from 2 to 4 hours at 1200°C, increases γ' size and decreases γ' volume fraction. It was also reported that 4 hours solutionizing heat treatment caused coarsening of γ' particles in IN 738 LC [43].

The commercially recommended IN 738 LC cooling type is air cooling after at 1120°C for 2 hours [20]. Behrouzghaemi et. al has the leading work focused on the influence of cooling rate on IN 738 LC γ' microstructural properties. It was reported that at low cooling rates precipitate growth occurs in a more stable manner; increasing cooling rate also increases γ' size, however, doesn't change the γ' density greatly [41].

Contrarily, a similar work has been performed by Guzman et. al, reporting that increasing cooling rate decreased both primary and secondary γ' sizes after solutionizing at 1120°C for 2 hours [44]. This result can also be supported by Ho-Seob Yun's study that investigates the effect of cooling rate on secondary γ' precipitates [42]. Bagoury et. al reported that increasing cooling rate decreases the volume fraction of γ' particles which was expected due to smaller γ' particles obtained at higher cooling rates [45].

1.2.4.3 Aging

Aging is commercially recommended to be performed after 1120°C-2 hours (air cooling) solutionizing, at 845°C for 24 hours (air cooling) to provide further γ' precipitation and increase γ' volume fraction of IN 738 LC [20]. Ho-Seob Yun performed these heat treatment conditions and obtained a final bimodal microstructure with coarse cuboidal primary and fine secondary precipitates [43].

Anurag Thakur used different aging time periods between 8 to 72 hours at 845 °C and reported that increasing aging time increases both primary and secondary γ' size. It was reported that 8, 24 and 72 hours aging at 845°C achieves, 392, 425 and 482 μm primary and 65, 96, and 112 μm secondary γ' sizes respectively [20].

Panyawat Wangyao et. al applied two stage aging that consists of primary and secondary precipitate agings. Primary aging was applied at 925 °C and 1055°C for 1 hour while secondary was applied at 845°C for 20 hours. It was reported that additional primary aging step provided higher volume fraction and uniform distribution of γ' particles compared to single step aging at 845°C for 20 hours [39].

There are aging studies performed for also longer time periods in literature to obtain the effect of operation condition to microstructure. Hoffelner performed aging of IN 738 LC at 788°C and 871°C for 1000-20000 hours range and obtained that increasing aging temperature and time also increases primary and secondary γ' sizes, changing the morphology of the larger γ' particles from blocky to spherical. It was also reported that exposure to long time aging causes detrimental TCP- σ formation in microstructure [46].

Shargi performed aging at the same temperature for 750, 1500, 3000 hours. It was reported that when aging time was increased volume fraction of primary γ' increases while secondary γ' decreases. Additionally, it was reported that samples at early aging stages performed better yield strength than later stages [47].

1.2.4.4 Heat Treatment Simulations

CALPHAD (Computer Coupling of Phase Diagrams and Thermochemistry) is a widely used method to perform thermodynamic and kinetic calculations for Ni-based superalloys based on theoretic models and experimentally formed databases [48]. The use of this method has become quite widespread through the development of the software JMAT PRO. There are various studies in literature calculating phase-

temperature profile, solidification behavior, mechanical properties of Ni-based superalloys using JMAT PRO software [49, 50, 51].

The heat treatment module of JMAT PRO can be used to estimate γ' size and microstructure evolution during heat treatments. This evolution is dictated by three mechanisms included in JMAT PRO; precipitation, coarsening and dissolution of γ' . The accuracy of this module is proved by N. Saunders et. al for coarsening of γ' in various Ni-based superalloys and TTT and CCT diagrams as shown in Figure 1.12 [50].

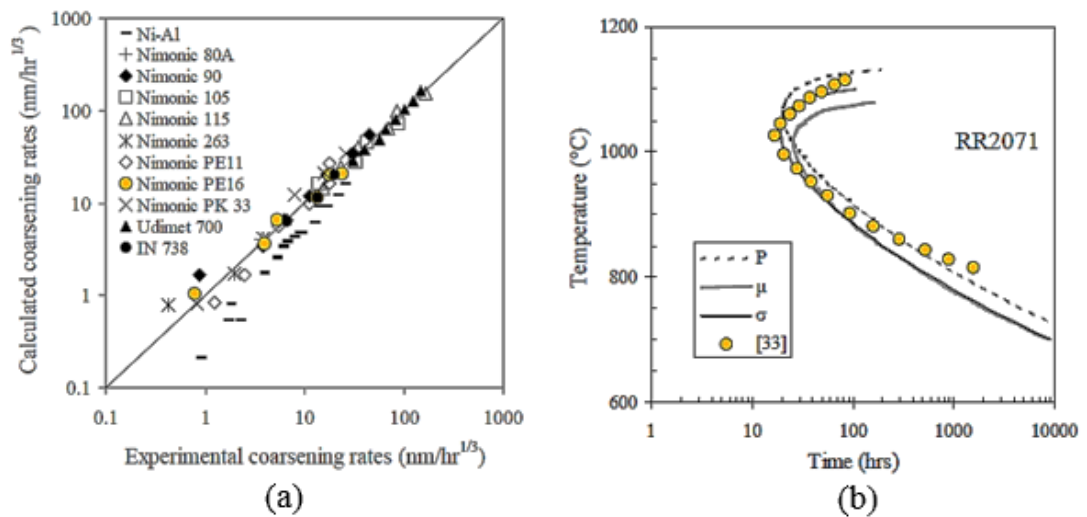


Figure 1.12: Comparison of calculated and experimentally observed a) coarsening rate of various Ni-based superalloys and b) TTT diagram for the single crystal alloy RR2071 [50].

N. Saunder also calculated 0.2% proof stress using JMAT PRO for various Ni-based superalloys and compatible results were found with experimental results as shown in Figure 1.13 [50].

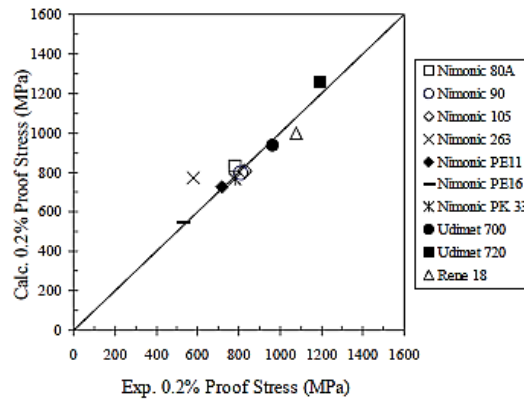


Figure 1.13: Comparison between calculated and experimental 0.2% proof stress of various Ni-based superalloys [50].

1.2.5 Diffusion Coatings and Their Simulations

Ni-based gas turbine blades operate in very aggressive corroding and oxidizing environment that can consume substrate material at an extremely rapid rate. Consequently, turbine blades' load carrying capacity is decreased, accordingly lifetime is limited. Therefore, Al and Cr rich protective coatings applied to Ni-based substrate surface as shown in Figure 1.14 [25]. These coatings can be classified as given in relative to their oxidation and corrosion resistance [14].

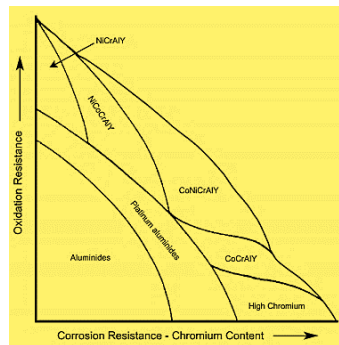


Figure 1.14: Relative oxidation and corrosion resistance of high temperature coating systems [14].

Diffusion (aluminide) and overlay (MCrAlY) coatings are two main types of protective coating [52]. Diffusion aluminide coatings have been widely used as

protective coatings on gas turbine blades made of nickel superalloys since the 1960s [53]. There are three main processes, by which the aluminide coating can be formed. These are the pack, above the pack, and chemical vapor deposition (CVD) processes [25].

Chemical vapor deposition is a process where one or more volatile precursors are transported via the vapor phase to the reaction chamber, where they decompose on a heated substrate to create high quality, high-performance solid material from a gaseous phase. The CVD system has some advantages over pack and above the pack process. Main advantage of CVD is its ability to control process parameters., thereby growth rate and coating microstructure. Additionally, CVD coating provides more homogenous and clean coatings in complex geometries such as cooling channels. Simultaneous deposition of reactive and alloying elements is also possible with Al to substrate surface.

Aluminide coatings are based on the β -NiAl phase that is formed on the surface of the substrate as shown in Figure 1.15. This phase has high oxidation and corrosion resistance, high melting point around 1638°C, and wide stable range around stoichiometric point which makes it desirable. Between outer β -NiAl layer and substrate, interdiffusion zone (IDZ) forms by precipitation of substrate alloying elements due to their low solubility in β -NiAl.

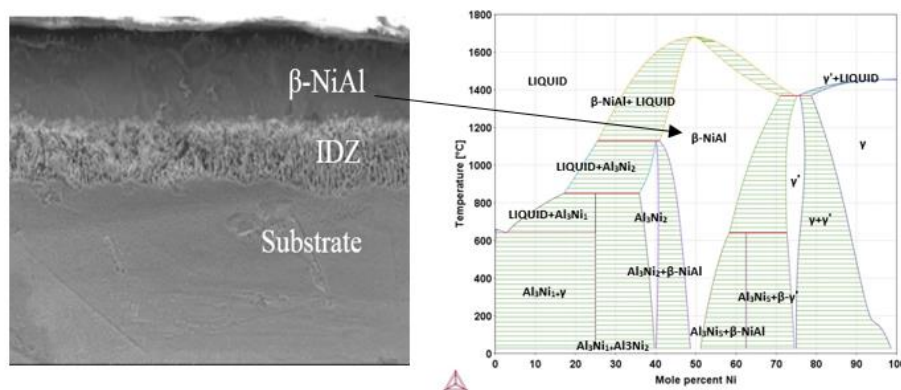


Figure 1.15: SEM image on a cross-section of aluminide coating and NiAl binary phase diagram.

Aluminide coating is a complex multicomponent and multiphase operation, making the continuous experimental coating operations a time-consuming and costly task. Thus, computational thermodynamic and kinetic calculations are used to accelerate the research and reduce the cost.

Computational thermodynamics and kinetics calculations are based on the concept of Gibbs energy and mobility. Today multicomponent databases exist for material systems including both thermodynamic and kinetic data. These databases have been collected from experimental data using the CALPHAD method, which has been discussed extensively in the literature [48]. The development of databases and a suitable software to calculate phase equilibria started in the 1950's and computational thermodynamics are nowadays applied in many fields of materials science [54]. Generally they can be divided into equilibrium calculations and diffusion simulations, which also consider kinetic effects.

Since coating operations are controlled by diffusion processes, thermodynamic and kinetic data including a model for high temperature material behavior is necessary. A suitable software package to treat such diffusion controlled system is DICTRA which was developed in the 1990's. The application of this software for turbine materials started in 1996, when Saunders developed a thermodynamic database for Ni-based superalloys [55]. However, the capability to perform diffusion calculations was achieved after a multicomponent diffusion mobility database for Ni-based superalloys was developed by Campbell in 2001 [56]. Since then, some successful thermodynamic and kinetic calculations for Ni-based superalloys and coating operations have been published with using DICTRA.

Campbell performed one of the key studies by assessing mobility of γ' and BCC_B2 (β -NiAl) phases in the Ni–Al–Cr system in 2007, since these elements and phases are characteristic properties of a Ni-based diffusion couples and coating systems. Validation of these assessments was proved by performing both simulation and experiment of B2-B2, γ - γ' and γ -B2 phase diffusion couples [57]. Based on Ni-Al-

Cr ternary system, Kaisheng Wu simulated $\gamma+\beta-\gamma$ and $\gamma+\beta-\gamma+\gamma$ diffusion couples to study MCrAlY coating system and found a reasonable agreement of interdiffusion behavior with experimental results [58]. Engström et. al have recently simulated the interdiffusion occurring between NiAl coating and IN 939 superalloy substrate. Compatible experiment and simulation concentration profile results of this study are given in Figure 1.17 [59].

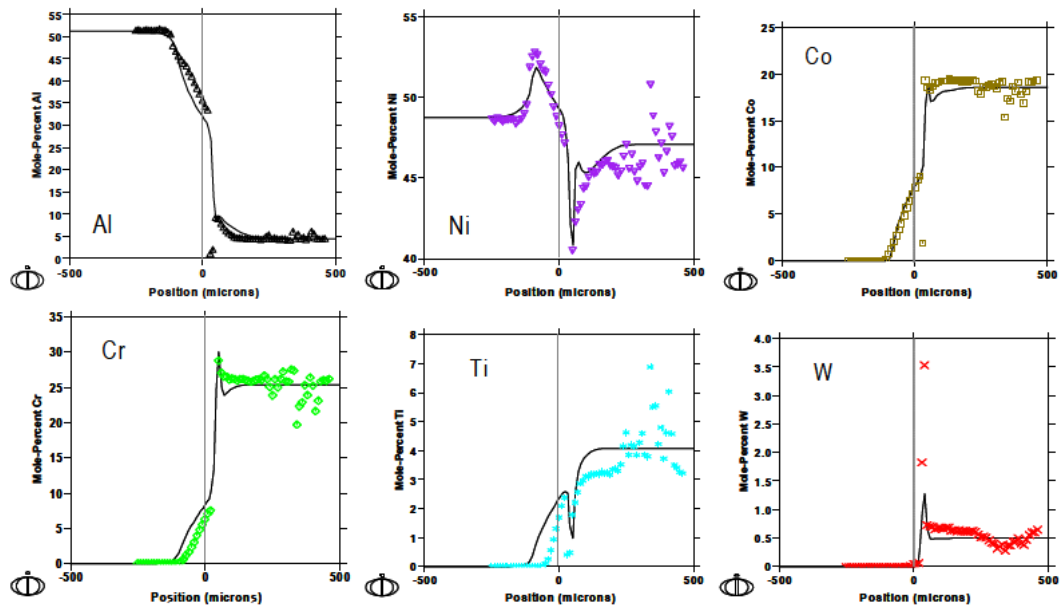


Figure 1.16: Concentration profiles for IN 939-NiAl coating region. Solid lines are calculated. Symbols are experimental data [59].

Also, evolution of diffusion coating on aging or service like conditions are simulated in the literature by using DICTRA. Dahl and J. Hald studied the evolution of MCrAlY applied IN 738 superalloy surface isothermally heat treated up to 875°C, 925°C or 950°C for 12000 hours [60]. Kang Yuan et. al also studied MCrAlY coating applied IN 792 behavior aged for different times at 900°C, 1000°C and 1100°C [61]. The results of both simulation studies captured the main microstructural features and predicted the phase-transformations occurring at the interface observed.

1.2.6 Modeling of Yield Strength for Ni-Based Superalloys

The turbine blades see the most aggressive conditions in the engine. Because of the high temperatures involved turbine blades are manufactured from Ni-based alloys. It is the only material that retains sufficient integrity at high temperature with an exceptional combination of strength, toughness, and resistance to degradation. This outstanding strength of the Ni-based material is derived from three parameters; solid solution, grain/phase boundary strengthening and precipitation strengthening mechanisms.

1.2.6.1 Solid Solution Strengthening

Solid solution strengthening derives from solute interactions with dislocations in the material's matrix. These solutes strengthen the material by introducing atomic diameter differences, elastic interactions, modulus interactions, electrical interactions, and short-range/long-range order interactions [62, 63].

The γ -FCC nickel matrix provides high solubility for many solid solution strengthening elements because of its nearly filled 3d electron shell electronic structure. These solid solution strengtheners include W, Mo, Cr, Co, Ta, Ti and Al [20, 62, 64]. Addition of these elements increases yield strength of the material since each solute atom acts as frictional obstacles for dislocation slips. There is a common equation described that is reviewed by Butt to calculate the contribution of solid solution to yield strength as given below [65].

$$\sigma_{y,s,i} = \beta_i C_i^p \quad (\text{Eq. 1.1})$$

In this equation, β_i is a strengthening constant, C_i^p is the concentration of solute i while p is a constant that varies between 1/2 and 1 [66]. $\sigma_{y,s,i}$ defines yield strength due to solid solution. Labusch [67], Nabarro [68] and Galindo [69] used p as 2/3 while Felthman proposed as a value of 1/2 for various alloys [70].

Gypen and Deruyttere expanded the simple Hall-Petch approach to integrating solid solution contribution of various alloying elements in multicomponent systems as given below where $q = 3/2$ and $p = 2/3$. [71, 72].

$$\sigma_{y,s,i} = (\sum(\beta_i x_i^p)^q)^{1/q} \text{ [71, 72] (Eq. 1.2)}$$

Gypen and Deruyttere's results showed that p is a concentration used as $2/3$ provides better compatibility than 1 and $1/2$ with experimental results for FCC structure [72]. Solid solution contribution constant β_i is related to lattice and modulus misfit of element i in Ni matrix. Mishima et. al defined β_i experimentally for binary Ni-X systems, with X being an alloying element from the transition metal group [73]. β_i constants for alloying elements are given below taken from Mishima et. al's study are given below [73].

Table 1.5: Solid Solution Contribution Constants for Alloying Elements in IN 738 LC [73].

Elements	β_i (MPa At.Fraction ^{-1/2})
Ni	Matrix
Ti	775,00
Nb	1183,00
Ta	1191,00
C	1061,00
Co	39,40
Cr	337,00
W	977,00
Mo	1015,00
B	Ignored
Zr	2359,00
Al	225

1.2.6.2 Grain/Phase Boundary Strengthening

1.2.6.2.1 Grain Boundary Strengthening

Grain act as barriers for dislocation movement, and contribute, together to yield strength. Decreasing grain size increases the number of neighboring grains; more grain

boundaries create more barriers against dislocation movement, increasing the amount of stress necessary to move dislocation across a grain boundary. Thus, there is an inverse relationship between yield strength and grain size that relationship was explained in the 50s by Hall and expanded by Petch as given below [74, 75].

$$\sigma_D = \sigma_0 + \frac{k_y}{\sqrt{D_D}} \quad [76] \quad (\text{Eq. 1.3})$$

In this equation, σ_D is grain boundary strengthening, σ_0 is friction stress of matrix, k_y is Hall-Petch constant, and D_D is mean grain size of samples. Hall-Petch constant is experimentally estimated to be between 700-750 MPa $\mu\text{m}^{1/2}$ for Ni-based superalloys in various studies [77, 78]. Kozar et. al used 750 MPa $\mu\text{m}^{1/2}$ for calculation of IN 100 grain boundary strengthening [78]. Since it's in the same family of superalloys with IN 738 LC and it has a similar chemical composition distribution, 750 MPa $\mu\text{m}^{1/2}$ is used as Hall Petch constant in our calculations.

γ phase has a friction stress that inhibits the dislocation movement. Thompson defined this friction stress for pure Ni as $\sigma_0=21.8$ MPa. [79] Since γ -matrix phase contains a high amount of Ni in IN 738 LC superalloy this value is accepted for simplification.

The Hall–Petch relation between the yield stress of polycrystalline metals and the grain size is known to be used for over a grain size range from 20 nm to hundreds of micrometers which is a valid range for our calculations [80].

1.2.6.2.2 Phase Boundary Strengthening

Dendrite arm spacing is one of the microstructural characteristic that has an effect on mechanical properties of materials. It was reported that dendrite arm spacing is determined by process parameters such as thermal gradient and solidification rate [81]. Additionally, the dendrite arm spacing can change during heat treatments or dendrites can dissolve into matrix and disappear. A SEM image of secondary dendrites in CMSX-4 single crystal superalloy is shown in Figure 1.17 [82].

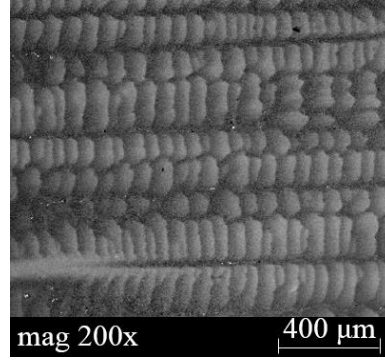


Figure 1.17: Secondary dendrite arms in CMSX-4 single-crystal [82].

The Hall-Petch is used to describe the yield strength variation due to change in dendrite spacing. The equation is given below.

$$\sigma_P = \frac{k_d}{\sqrt{D_P}} \text{ [83, 84] (Eq. 1.4)}$$

In this equation, k_d is Hall-Petch constant and D_P is dendrite arm spacing. k_d is accepted as $230 \text{ MPa } \mu\text{m}^{1/2}$ which is reported by Z. C. Cordero et. Al for pure Ni [85].

1.2.6.3 Precipitation Strengthening

It is well known that most effective way to strengthen the matrix of a Ni-based superalloy is precipitation strengthening mechanism, where strength is related to volume fraction, size, morphology, and distribution of γ' and carbide (MC and $M_{23}C_6$) precipitates. Carbide volume fraction of IN 738 LC was measured to be below 3 %. Therefore, effect of MC carbide to yield strength was not calculated in this study.

Modeling of γ' strengthening has been the subject of studies since the 70s [69]. There is a limited number of physically based models in superalloys with multimodal γ' structure. Kozar et. al used partially modified weak coupling model and found a good prediction for sub solvus heat treatment conditions [78]. Jackson and Reed, and subsequently Collins and Stone have employed the classic weak and strong pair models to predict yield strength of Udimet 720Li and RR1000, respectively and achieved compatible yield strength results with experiments [86, 87]. The purpose of

these studies was to find the optimum heat treatment conditions leading microstructure that provides highest yield strength. There is a common view that this can be achieved by examining the interaction of dislocation pairs between small (weak pair coupling) and large (strong pair coupling) γ' particles [86, 87].

When the γ' particles are too small, dislocations cut through them. On the contrary, case when particles are large and too strong to be cut through, dislocation bowing (Orowan strengthening) occurs. Maximum strength can be achieved if precipitates can resist cutting and are too close to allow dislocation bypassing. The radius that maximum strength is achieved is also called as “critical radius” that can be calculated by the given formula below for Ni-based superalloys.

$$d_{critical} = \frac{\mu b^2}{\gamma_{APB}} [69] \quad (\text{Eq. 1.5})$$

In this formula, b is Burgers vector, μ is shear modulus, γ_{APB} is anti-phase boundary energy. When γ' size d is lower than critical radius $d_{critical}$ weak coupling, in contrary case strong coupling is dictated as shown in Figure 1.18.

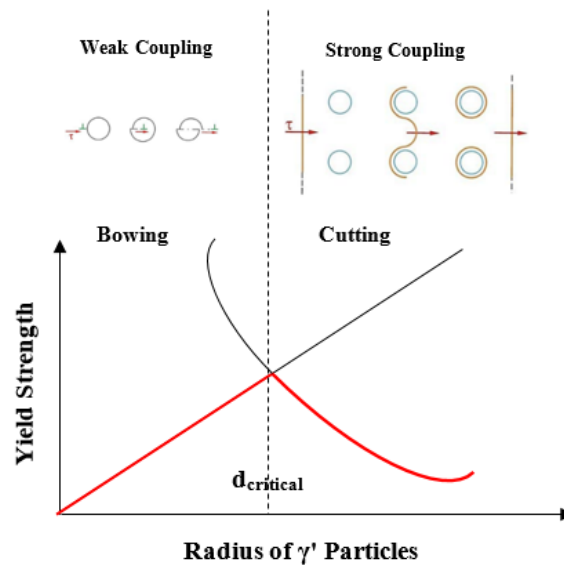


Figure 1.18: Configuration of dislocations and precipitates during cutting and bowing. Duplicated from Kozar et. al [78].

The yield strength formula for strong and weak couples are given below.

$$\tau_p^{strong} = 1.72M \frac{Tf^{1/2}w}{2bd} \left(1.28 \frac{d\gamma_{APB}}{wT} \right)^{1/2}] [86] \quad (\text{Eq. 1.6})$$

$$\tau_p^{weak} = M \frac{\gamma_{APB}}{2b} \left[\phi \left(\frac{\gamma_{APB}fd}{\tau} \right)^{1/2} - f \right] [86] \quad (\text{Eq. 1.7})$$

In these formula, M is Taylor equation factor, f is γ' volume fraction, w is elastic repulsion which is order of unity. [86] f volume fraction and d radius of γ' particles which were obtained from experimental work. ϕ is a constant depending on the morphology of γ' particles. For spherical particles $\phi = 0.72$ [86]. T is line tension expressed by the formula given below.

$$T = \frac{\mu b^2}{2} [86] \quad (\text{Eq. 1.8})$$

All the constants taken from the literature that were used to calculate yield strength and their reference numbers are given in Table 1.6.

Table 1.6: Strengthening Parameters Used in The Precipitation Strengthening.

Parameters	Values	References
γ_{APB}	0.17 J/m ²	[20]
b	0.249 nm	[88]
μ_{Ni}	80 GPa	[89]
M	3	[90]

1.3 Thesis Overview

The main objective of this study is to create an independent simulation model to perform aluminide coating simulations that is capable of estimating thickness and composition profile of coating applied on IN 738 LC turbine blade substrate and optimize microstructure of IN 738 LC turbine blade using heat treatment and simulations to improve mechanical properties.

Chapter 2 covers aluminide coating surface growth and the interdiffusion simulation that was performed by diffusion based modeling in DICTRA on IN 738 LC surface. An independent simulation model in DICTRA was formed to estimate aluminide coating thickness and composition profile for given experimental conditions. Simulation results of the composition distribution of coating region were compared with experimental aluminide coating results obtained by a colleague and graduate student Umutcan Ertürk.

Chapter 3 involves the microstructure optimization studies of IN 738 LC. The effect of hot isostatic pressing, solutionizing and aging to IN 738 LC microstructure was studied. Additionally, the effect of aluminide coating conditions on IN 738 LC microstructure was investigated. Microstructure evolution simulations were performed using JMAT PRO for experimental heat treatment and aluminide coating operations. Simulation results were compared with experimental results.

In Chapter 4, the yield strength of IN 738 LC was modeled based on solid solution, grain/phase boundary and gamma prime strengthening mechanisms for the samples that have different heat treatment history and microstructure. The results were compared with tensile test results of IN 738 LC found in literature and yield strength estimations of JMAT PRO.

Chapter 5 contains the future studies that lack in the literature and expected to provide promising results in both simulation and experimental studies of Ni-based superalloys.

CHAPTER 2

ALUMINIDE COATING SURFACE GROWTH AND INTERDIFFUSION SIMULATIONS FOR INCONEL 738 LC

2.1 Introduction

In this chapter, surface growth and interdiffusion during aluminide coating process is simulated using DICTRA software at the same conditions of aluminide coating experiments performed using chemical vapor deposition method (CVD) on IN 738 LC substrate surface. A colleague and graduate student Umutcan Ertürk performed the experimental aluminide coatings used in this study.

In CVD process there are two rates competing each other. These are interdiffusion (between substrate and Al deposited on substrate surface) and Al incorporation rates, used to maximize growth rate and β -NiAl/interdiffusion (IDZ) zone thickness ratio (Figure 2.1). An increase in the interdiffusion rate results increase in the interdiffusion zone thickness and an increase in the Al incorporation rate results increase in the β -NiAl zone thickness. Optimization of this process is time, money and energy consuming considering each growth takes at least takes 17 hours. The purpose of creating a simulation was to predict composition profile and thickness of aluminide coating for hypothetical conditions independent from experiments, thereby reduce time, money and energy used in experiments.

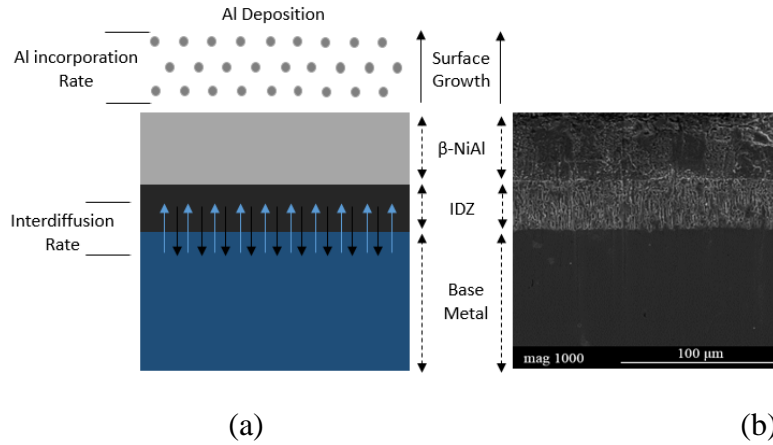


Figure 2.1: a) Scheme of Al surface growth and diffusion during CVD aluminide coating and SEM image of aluminide coating region.

In order to be independent from experimental process, multiple number of growth experiments with various conditions, and their characterization results (SEM-EDS, WDS-EPMA) were used to find related growth rates. After sufficient of growth rate experiments input pair, growth rate was educationally estimated for hypothetical experimental conditions.

2.2 Method

Simulation method optimization and independent growth rate estimations methods were followed to create a simulation that can estimate coating thickness and composition profile. The command list used for the simulation is given in Appendix A.

In the Appendix A, the code lines in between 1 to 15 represents definition of the system including databases, the code lines in between 16 to 21 represents definition of temperature, the code lines in between 22 to 28 represents definition of base metal thickness and number of grid points, the code lines in between 29 to 96 represents phases and compositions, the code lines in between 97 to 102 represents simulation time and the code lines starting from 102 till the end represents the definition of boundary condition and some further settings.

2.2.1 Simulation Method Optimization

DICTRA is a suitable software package to solve diffusion controlled phase transformations. It is connected to CALPHAD (Computer Coupling of Phase Diagrams and Thermochemistry) based THERMOCALC software, which provides all necessary thermodynamic data. The thermodynamic database used in this study was “Ni-based superalloys database (TCNI8)”, and the kinetic database was “Ni-alloys mobility database (MOBNI4)”.

The basic of DICTRA program can be described as follows. Initially, experimental and simulation parameters defined for the software with associated kinetic and thermodynamic databases. Initial composition, time, temperature and pressure were defined for the system. Then, a “region” can be set up with a distribution of linear or geometric nodes for numerical calculations. In each node, DICTRA stores the local composition and corresponding thermodynamic and kinetic parameters. A boundary condition needs to be defined for the “region” such as “FIX FLUX” condition to provide growth rate (Al incorporation rate) on a surface. The basic schematic of how DICTRA use these databases and how diffusion simulation works is given in Figure 2.2 and explained further in following pages.

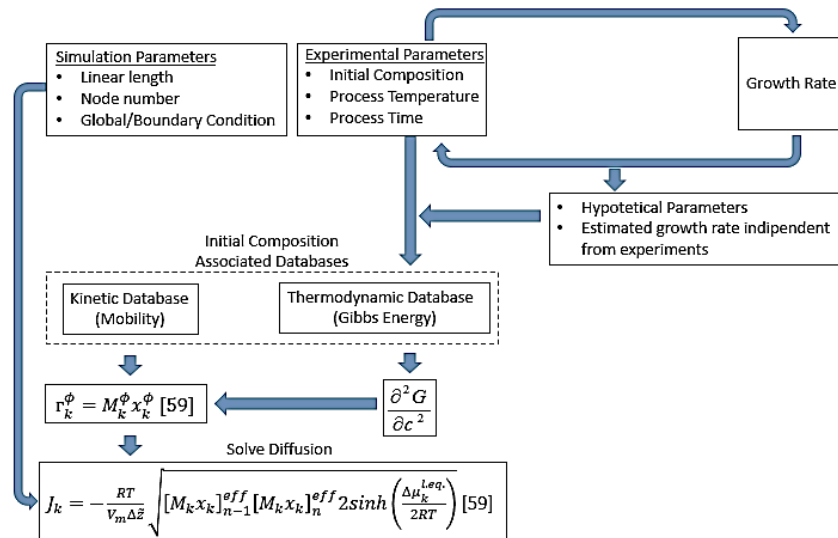


Figure 2.2: Schematic of DICTRA diffusion simulation.

As explained in previous section, after calculated growth rates were related to experiment parameters, growth rate was estimated for given hypothetical condition independent from experiment

In order to perform multiphase and multicomponent simulations, the problem is transformed into a single-phase problem by a homogenization procedure: it is assumed that equilibrium holds locally, i.e. in a small volume element the chemical potentials, phase fractions and phase compositions and are given by the equilibrium corresponding to the local temperature, pressure and composition. This local equilibrium assumption is essentially the same for all models suggested for 1D multiphase simulations. The local kinetic properties are found by choosing a suitable "averaging function", r_k^ϕ as given below where M_k^ϕ and x_k^ϕ are the mobility and mole fraction of component k , respectively.

$$r_k^\phi = M_k^\phi x_k^\phi \quad [59] \quad (\text{Eq. 2.1})$$

DICTRA uses homogenization model automatically when a spheroid phase is entered to configured system. This is useful when long-range diffusion through a multiphase mixture is simulated, under the assumption that local equilibrium exists at each node. This way, the homogenization model can be used when calculating a moving boundary problem.

The simulations presented in this thesis have been performed using homogenization model, in which a diffusion flux of species k , J_k , is calculated in a lattice fixed frame of reference using the "averaging function" as given in Eq. 2.2.

$$J_k = -\frac{RT}{V_m \Delta \tilde{z}} \sqrt{[M_k x_k]_{n-1}^{eff} [M_k x_k]_n^{eff} 2 \sinh\left(\frac{\Delta \mu_k^{l.eq.}}{2RT}\right)} \quad [59] \quad (\text{Equation 2.2})$$

In Eq. 2.2, V_m is the molar volume, which is assumed as constant for substitutional species and zero for interstitial species. $\Delta \tilde{z}$ is a time-dependent spatial coordinate defined in the lattice-fixed frame of reference that can be related to the ordinary time-

dependent spatial coordinate z , by keeping track of the velocity with which the lattice- and number-fixed frames of reference move with respect to each other. R and T represents gas constant and temperature, respectively.

The number-fixed frame of reference is determined by the condition that the number of atoms on each side of a reference plane stays constant. With this above assumption for the molar volume, then the number- and volume-fixed frames of reference are identical. Thus, the fluxes are calculated in a lattice-fixed frame of reference, but the resulting concentration fields are mapped to number fixed frame of reference.

Furthermore, in Eq. 2.2 $[M_k x_k]_{n-1}^{eff}$ is a “effective” kinetic property on plane/source $n-1$ that is calculated by combining the product of atomic mobility for species k with its fraction for the phases present on that plane/source.

$\mu_k^{l.eq.}$ in Eq. 2.2 is the chemical potential for species k under local equilibrium conditions. A locally minimized Gibbs energy is assumed in this model, as is also the case for the disperse diffusion model. This means that the local phase fractions, phase compositions etc. can be obtained by performing an equilibrium calculation with the local composition.

For the calculation presented in this thesis, the upper Wiener bound [59] or “Rule of Mixtures” has been used including the equation given below.

$$[M_k x_k]^{eff} = \sum f^i [M_k x_k]^i \quad [59] \quad (\text{Eq. 2.3})$$

In Eq. 2.3, f_i is fraction of phase i . The summation in Eq. 2.3 is taken over all phases that are to be included, i.e. in our case γ , β and γ' phase.

The assumptions made to perform the simulations using DICTRA software are given below.

- Local equilibrium is established in each volume element at each time-step in the calculation.

- Molar volume of all substitutional elements is constant and equal.
- Matrix phases are present as continuous layers.

The pressure value used in simulation was changed in between 1 to 10 atm to see effect of pressure on coating composition profile and thickness. But, the pressure change didn't affect any of these parameters. This was expected since solid state diffusion occurs between substrate and coating in simulation. Therefore, the pressure parameter in simulations accepted as a constant atmospheric pressure.

In literature, DICTRA is usually used for simulation of diffusion couples to investigate coating operations. Diffusion couples are preferred as β -NiAl-substrate or Al-substrate to observe interdiffusion between substrate and coating that leads to a complicated microstructure [55, 58, 49]. However, during CVD aluminide coating process, there is a continuous Al deposition instead of a bulk diffusion couple with a certain thickness, which leads to continuous surface growth on substrate surface.

At best of author's knowledge, simulations that perform both interdiffusion and surface growth during aluminide coating process are not available in literature and studies performed in this thesis to achieve that is a leading work. The schematics of diffusion couples and simultaneous surface growth and diffusion model are given in Figure 2.3.

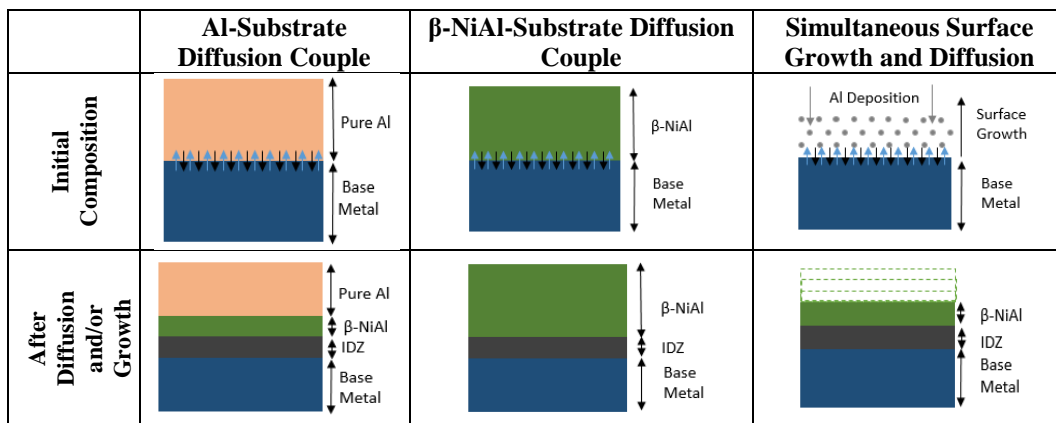


Figure 2.3: Schematic Al-substrate, β -NiAl-substrate diffusion couples and simultaneous surface growth and diffusion simulation model.

The models given in Figure 2.3 were simulated at the same experimental conditions. The results of these simulation models were compared to experimental CVD aluminide coating region composition analysis results. The composition of experimental coating region was determined by using coating energy dispersive X-Ray spectroscopy and wavelength dispersive spectroscopy methods. After the best simulation model was chosen, multiple number of experiments were performed to pair the experimental parameters to growth rates. Then estimated growth rate was simulated for randomly given hypothetical experimental conditions.

In simulation method optimization, four elements of IN 738 LC, Ni, Al, Cr and Co are used to define IN 738 LC substrate composition as shown in Table 2.1 to simplify the simulation. These elements were preferred due to the majority of phases (γ matrix and γ' precipitate) they form in microstructure and composition profile of substrate IN 738 LC and aluminide coating. Depending on compositions of these four elements in the substrate, coating and interdiffusion region, γ -FCC_L12#1, γ' -FCC_L12#2, BCC_B2#1, β -NiAl-BCC_B2#2, LIQUID phases were defined to DICTRA. Time and temperature parameters were also used as input.

Table 2.1: Nominal and Simulation (4 Elements) Composition of Substrate IN 738 LC (at. %).

Elements	Nominal Composition	Composition Range	Simulation Composition
Ni	Balance	Balance	Balance
Ti	4.04	3.8-4.39	4.18
Nb	0.55	0.37-0.67	-
Ta	0.55	0.47-0.63	-
C	0.52	0.43-0.62	-
Co	8.2	2.89-8.68	8.87
Cr	17.49	17.16-17.81	18.92
W	0.8	0.74-0.87	-
Mo	1.04	0.89-1.18	-
B	0.05	0.04-0.06	-
Zr	0.03	0.02-0.05	-
Al	7.16	6.74-7.79	7.75

The composition and thickness of Al-substrate and β -NiAl-substrate diffusion couples, and surface growth and diffusion model are given in Figure 2.4.

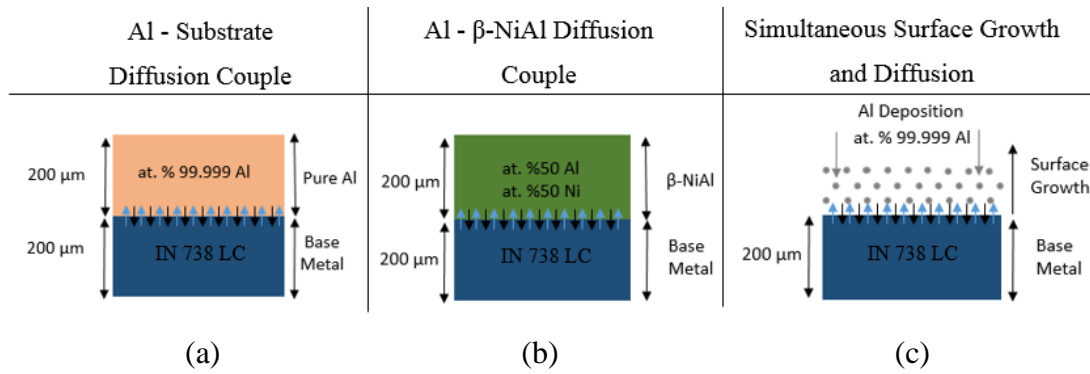


Figure 2.4: The schemes, thickness and composition of a) Al-substrate and b) β -NiAl-substrate diffusion couples, and c) surface growth and diffusion model.

Substrate thickness was assumed as 200 μm since substrate thicknesses higher than this value changed the composition profile hardly and higher substrate thicknesses increased simulation time considerably due to increase in number of node points. After simulation models were compared with experimental results, simultaneous surface growth and diffusion model was found to be best model to estimate coating thickness and composition profile. Optimization of necessary growth rate data input for this model is given in next section.

2.2.2 Independent Growth Rate Estimation Method

After Al-substrate, β -NiAl substrate diffusion couples, and simultaneous surface growth and diffusion model results were compared with experimental results, simultaneous surface growth and diffusion model's results found to be promising. To provide necessary growth rate (Al incorporation rate) to simulations independent from experiments, multiple numbers of growth experiments with various conditions, and their characterization results were used to find related growth rates for different experimental parameters. After calculated growth rates were related to experiment parameters, growth rate was estimated for a given hypothetical condition independent from experiment as shown in Figure 2.5. Then CVD aluminide coating experiments were performed for simulated hypothetical conditions and results were compared to see accuracy of estimated growth rate.

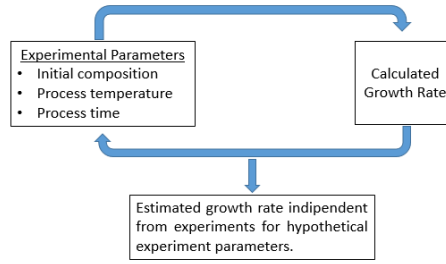


Figure 2.5: Independent growth rate estimation flow chart.

In growth rate optimization process number of elements used in simulations were increased to five. Ni, Al, Cr, Co and Ti to define IN 738 LC substrate composition as shown in Table 2.2 to simplify the simulation. The reason of the increase in number of defined elements compared to simulation optimization model was to define more elements from IN 738 LC into simulation to improve compatibility of simulation to experimental condition. Ti was added to system as fifth element due to its high composition in γ' phase in IN 738 LC. However, more than five elements decreased the simulation time and efficiency greatly.

Table 2.2: Nominal and Simulation (5 elements) Composition of Substrate IN 738 LC (at. %).

Elements	Nominal Composition	Composition Range	Simulation Composition
Ni	Balance	Balance	Balance
Ti	4.04	3.8-4.39	4.18
Nb	0.55	0.37-0.67	-
Ta	0.55	0.47-0.63	-
C	0.52	0.43-0.62	-
Co	8.2	2.89-8.68	8.5
Cr	17.49	17.16-17.81	18.13
W	0.8	0.74-0.87	-
Mo	1.04	0.89-1.18	-
B	0.05	0.04-0.06	-
Zr	0.03	0.02-0.05	-
Al	7.16	6.74-7.79	7.43

The Ni, Al, Cr, Co and Ti elements were preferred due to the majority of phases (γ matrix and γ' precipitate) they form in microstructure and composition profile of substrate IN 738 LC and aluminide coating. Depending on compositions of these four elements in the substrate, coating and interdiffusion region, γ -FCC_L12#1, γ' -

FCC_L12#2, BCC_B2#1, β -NiAl-BCC_B2#2, BCT_D022, LIQUID and NI3TI_D024 phases were defined to DICTRA in independent growth rate estimation studies. However, the simulations performed at 1000, 1050 and 1100°C showed a miscibility gap. Due to this reason, an additional BCC#3 phase was added to the system for simulations performed at these temperatures. Each “#” shows a different composition of that phase formed by different elements. Simulation temperature, time and substrate thickness were also used as input to simulation. Substrate thickness was assumed as 200 μm since substrate thicknesses higher than this value changed the composition profile hardly and higher substrate thicknesses increased simulation time considerably due to increase in number of node points. Time and temperature parameters were also used as input.

In order to measure growth rate (Al incorporation rate), the total coating thickness was multiplied with the average Al at. % of the total coating (including β -NiAl and IDZ) region as shown in Figure 2.6. The molar volume fraction of elements were not considered since DICTRA assumes that all substitutional elements have the same molar volume in all phases. The necessary coating composition was determined from WDS results and coating thickness was determined from SEM images of coating region.

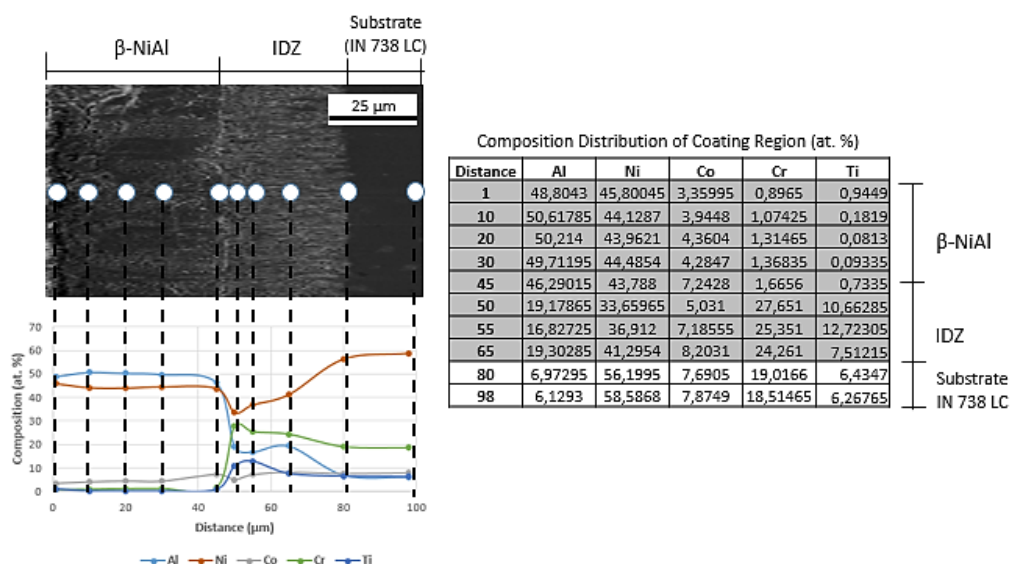


Figure 2.6: SEM image and WDS composition analysis result of coating region.

After sufficient of growth rate results related to experiment conditions, growth rate was educationally estimated for hypothetical experimental conditions.

2.3 Results and Discussion

Optimization simulation method and growth rate estimation results and discussions are given in this section.

2.3.1 Simulation Method Optimization Results

In literature, DICTRA is usually used for simulation of β -NiAl-substrate and Al-substrate diffusion couples to investigate coating operations. [55, 58, 49]. However, during CVD aluminide coating process, there is a continuous Al deposition instead of a bulk diffusion couple with a certain thickness, which leads to continuous surface growth on substrate surface. To obtain a simulation model that estimates coating thickness and composition profile prior to deposition, NiAl-substrate, Al-substrate diffusion couples and surface growth and diffusion simulations were performed at the same parameters of an aluminide coating experiment. The parameters of aluminide coating experiment is given in Table 2.3

Table 2.3: Parameters of CVD Aluminide Coating.

Temperature (°C)	Time (h)	Pressure (mbar)	HCl Flow (sccm)	H ₂ Flow (sccm)	HCl : H ₂	Ar Flow (sccm)	HCl:Ar	Internal Trays (gr)
1050	4	100	125	1000	1:8	250	1:2	Al-Cr 50/50 wt. %

The simulation parameters for NiAl-substrate, Al-substrate diffusion couples and surface growth and diffusion simulations are given in Table 2.4

Table 2.4: Parameters of Simulation.

Temperature (°C)	Time (h)	Base Metal Thickness (μm)	Node Number
1050	4	200	100

The schemes of these simulation models, and comparison of experimental and different diffusion simulation model results are given in Figure 2.7.

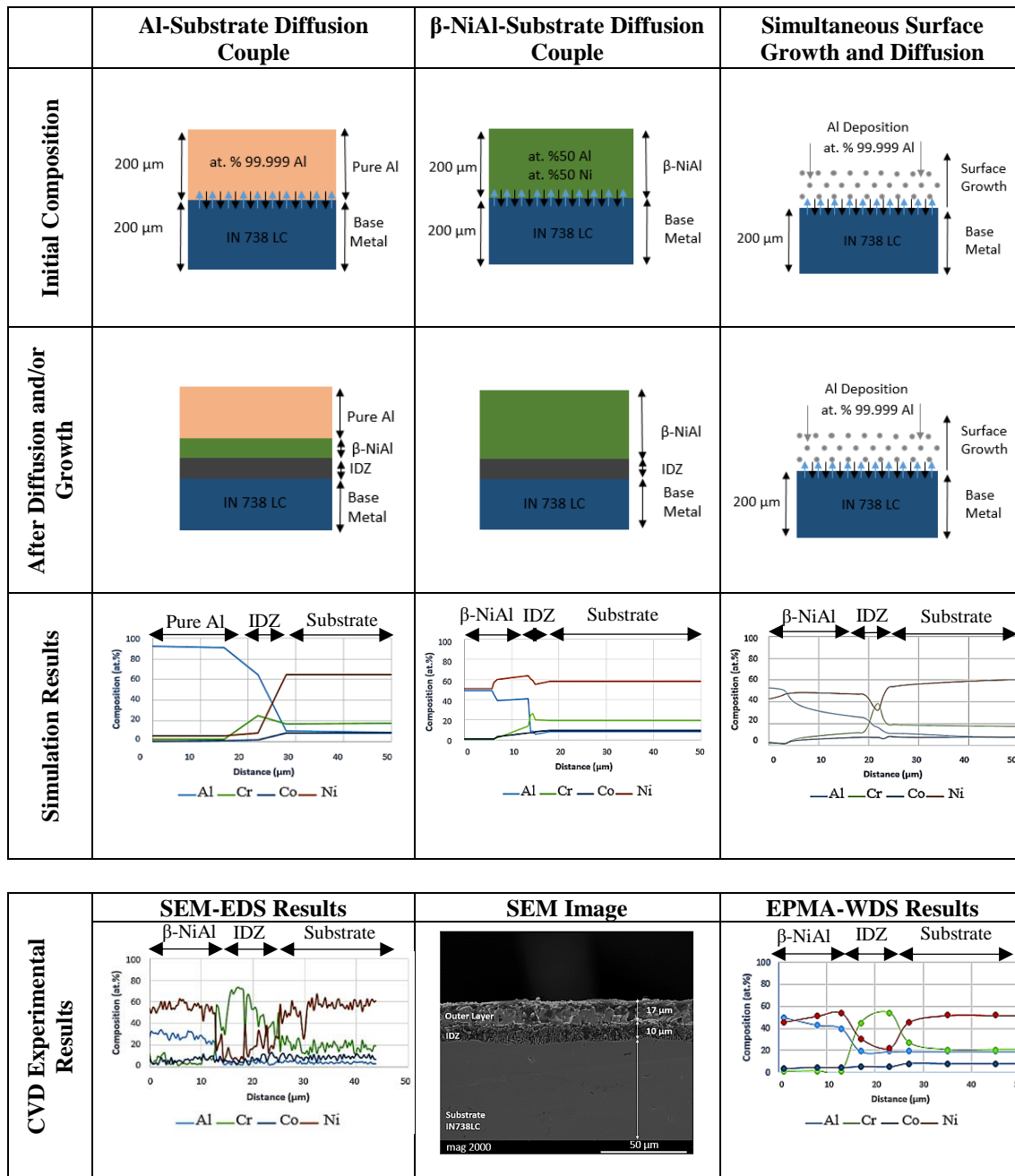


Figure 2.7: Comparison of different aluminide coating simulation model results to SEM-EDS and EPMA-EDS results of the experimental aluminide coating.

Al-substrate and β -NiAl substrate diffusion model results failed to estimate coating thickness and composition profile of experimental CVD aluminide coating. However, simultaneous surface growth and diffusion model showed good compatibility with

experimental coating thickness and composition except the inter diffusion zone (IDZ) thickness and Cr composition. This model needs an Al (incorporation rate) growth rate input to simulate surface growth and diffusion simultaneously. Therefore, growth rate needed to be calculated, optimized and related to performed experimental conditions. After enough experiment parameters pair with growth rate, it was educationally estimated and simulated for given hypothetical parameters.

2.3.2 Independent Growth Rate Optimization Results

The different simulation models were used to simulate the simultaneous surface growth and diffusion in previous section. Surface growth and diffusion model showed better compatibility with experimental results than Al-substrate and β -NiAl substrate diffusion models. This model uses the growth rate (Al flux rate) as input. Two groups of experiments simulated using DICTRA software to find related growth rates for different experiment parameters as given in Table 2.5 and Table 2.6. The first experiment group given in Table 2.5 was performed at varying temperatures 950, 1000, 1050 and 1100°C for 4 hours. The second experiment group given in Table 2.6 was performed at 1100°C for varying time periods 4, 8 and 12 hours. Time and temperature were chosen as varying parameters since these two parameters of experiment are common parameters with simulation and they have a considerable influence on coating structure. Other experimental parameters were kept as constant.

Table 2.5: Aluminide Coating Experimental Parameters at Varying Temperatures.

Temperature (°C)	Time (h)	Pressure (mbar)	HCl Flow (sccm)	H2 Flow (sccm)	HCl : H2	Ar Flow (sccm)	HCl:Ar	Internal Trays (gr)
950	4	100	125	1000	1:8	250	1:2	Al-Cr 50/50 wt. %
1000	4	100	125	1000	1:8	250	1:2	Al-Cr 50/50 wt. %
1050	4	100	125	1000	1:8	250	1:2	Al-Cr 50/50 wt. %
1100	4	100	125	1000	1:8	250	1:2	Al-Cr 50/50 wt. %

Table 2.6: Aluminide Coating Experimental Parameters for Varying Time Periods.

Temperature (°C)	Time (h)	Pressure (mbar)	HCl Flow (sccm)	H2 Flow (sccm)	HCl : H2	Ar Flow (sccm)	HCl:Ar	Internal Trays (gr)
1100	4	100	125	1000	1:8	250	1:2	Al-Cr 50/50 wt. %
1100	8	100	125	1000	1:8	250	1:2	Al-Cr 50/50 wt. %
1100	12	100	125	1000	1:8	250	1:2	Al-Cr 50/50 wt. %

The simulation parameters used to simulate the experiments given in Table 2.5 and 2.6, are given in Table 2.7 and 2.8.

Table 2.7: Simulation Parameters at Varying Temperatures.

Temperature (°C)	Time (h)	Al Growth ($\mu\text{m}/\text{h}$)	Base Metal Thickness (μm)	Node Number
950	4	1.40	200	100
1000	4	1.31	200	100
1050	4	2.36	200	100
1100	4	3.94	200	100

Table 2.8: Simulation Parameters at Varying Time Periods.

Temperature (°C)	Time (h)	Al Growth ($\mu\text{m}/\text{h}$)	Base Metal Thickness (μm)	Node Number
1100	4	3.94	200	100
1100	8	5.58	200	100
1100	12	6.66	200	100

The comparison of simulation results with SEM images of analyzed coated regions and linear composition analyze results (SEM-EDS, EPMA-WDS) are given in Figure 2.8 for samples coated at 1000, 1050 and 1100°C for 4 hours, and for samples coated at 1100°C for 4, 8, 12 hours in Figure 2.9.

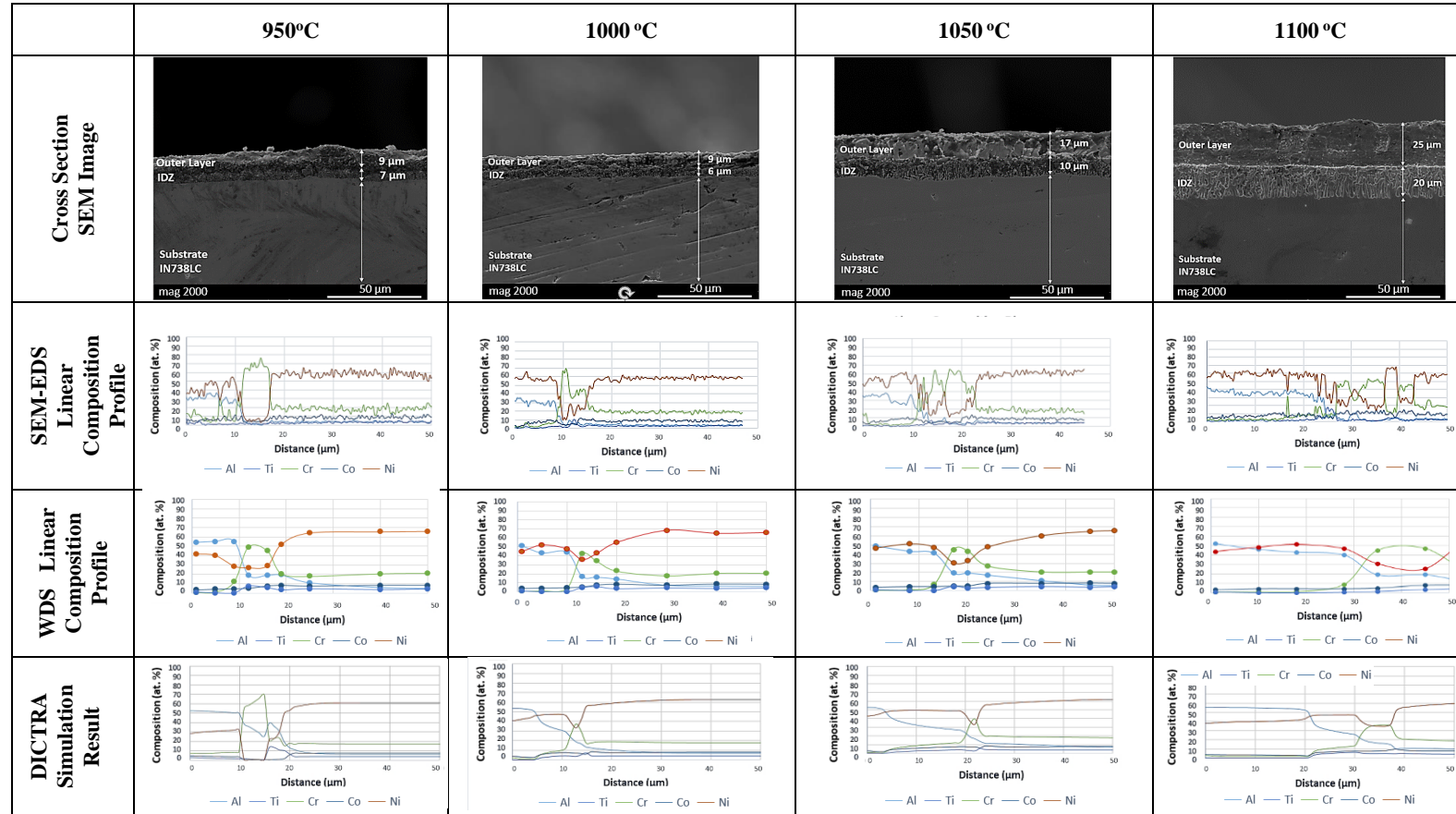


Figure 2.8: Aluminide coating linear composition profile and DICTRA simulation results for different aluminide coating temperatures.

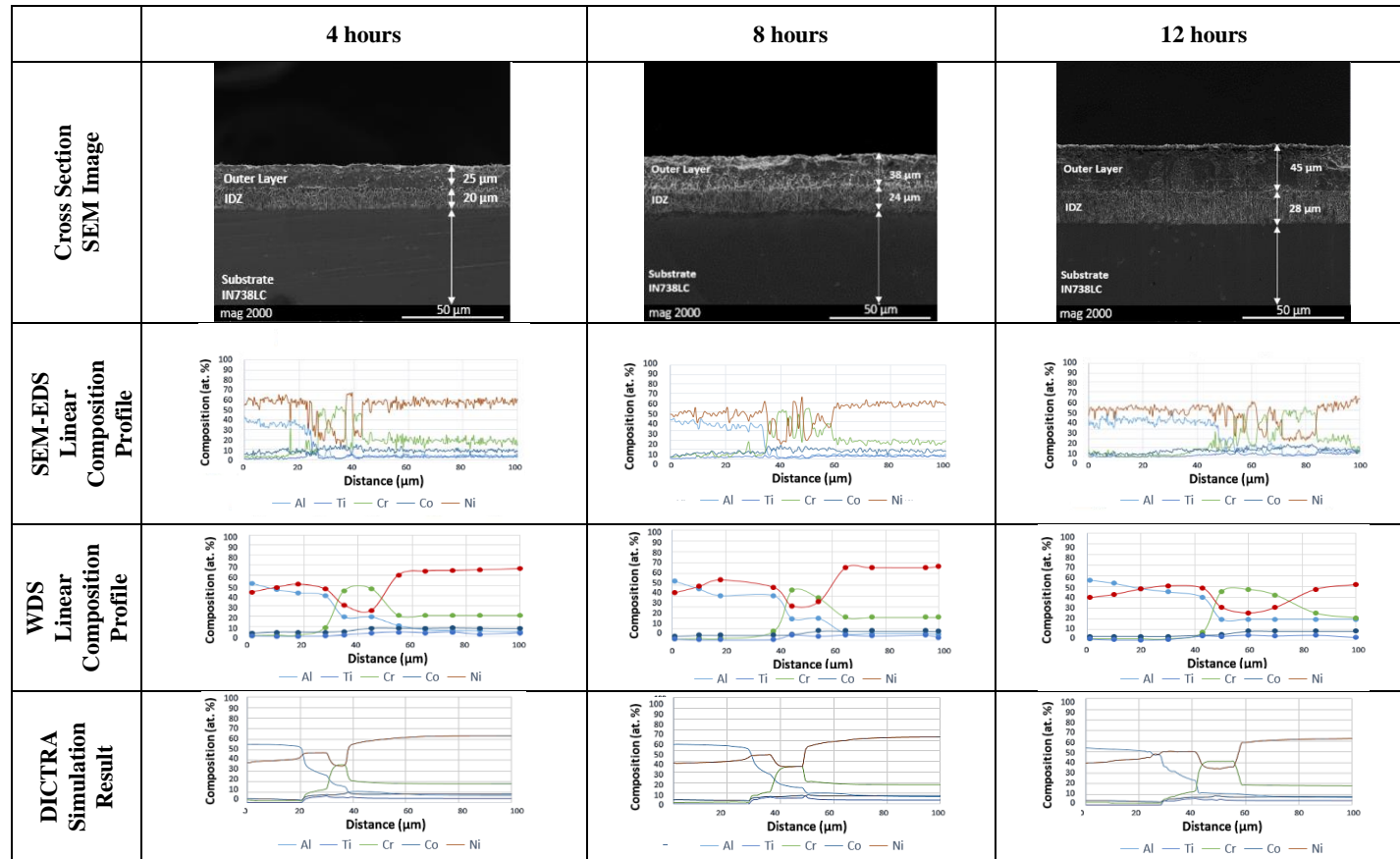


Figure 2.9: Aluminide coating linear composition profile and DICTRA simulation results for different aluminide coating times.

Before comparison of simulations to experimental results, SEM-EDS and EPMA-WDS results were compared. SEM-EDS is usually used for qualitative compositional analysis while EPMA-WDS is used for quantitative compositional analysis due higher accuracy and resolution of this method. It was found that in the outer layer of coating (β -NiAl region), EDS results (500 ms for each point) provided 10-15 at. % lower Al content than WDS results. The composition profile of inner layer coating found to be relatively similar for both analyze methods. Additionally, thicknesses of the outer and the inner layer of coatings were found to be compatible with both linear composition analyze methods.

Composition distribution results of simulations that were performed at 950, 1000, 1050 and 1100°C for 4 hours were compared with SEM-EDS and EPMA-WDS results of in Figure 2.8. The diffusion simulation performed at 950°C for 4 hours shows similarity to both SEM-EDS and EPMA-WDS characterization results. The inner layer (inter diffusion zone) of coating shows similarity to SEM-EDS results due to higher Cr composition obtained in this method. However, outer layer found composition found to be similar to EPMA-WDS results due to higher Al composition obtained in this characterization method.

As shown in Figure 2.8, the outer layer composition profile results of simulations that were coated at 1000, 1050 and 1100°C for 4 hours shows more similarity to WDS results that have Al rich region close to the coating surface. Since SEM-EDS results show higher composition profile of Ni than Al in the outer layer of coating similarity with simulations couldn't be acquired with this composition analyze method. Simulation results showed up to 15 at. % lower Cr rate in the inner layer of the coating compared to SEM-EDS and EPMA-WDS results for the same coating samples. The gap between simulation and experimental inner coating layer Cr composition found to be slightly increasing when coating temperature was increased.

The composition profile of simulations performed at 1100°C for 4, 8 and 12 hours are given in Figure 2.9. These simulation results showed more similarity to EPMA-WDS results since EPMA-WDS results show an Al rich region close to coating surface.

However, SEM-EDS results showed higher composition of Ni than Al in the outer layer of coating. The thickness of this Al rich region showed a slight increase when coating time was increased shown in simulation and WDS results. Simulation results showed up to 15 at. % lower Cr rate in the inner layer of the coating when it is compared to SEM-EDS and EPMA-WDS results. The gap between simulation and experimental inner coating layer Cr composition found to be slightly increasing when coating time was increased.

As shown in Figure 2.9, the Cr in inner layer was diffused to the outer layer of coating at the amount of less than 10 at. % and up to 10 μm at the coatings applied at 1100°C for 4, 8 and 12 hours. Increasing simulation time also increased the diffusion of Cr into the outer layer of coating slightly. This Cr diffusion to the outer layer of coating did not occur remarkably at simulations performed at lower temperatures than 1100°C. This could be due to increased diffusion coefficient of Cr in $\beta\text{-NiAl}$ when the coating temperature was increased. Similar Cr profile is seen at SEM-EDS results of coatings applied at 1100°C for 4, 8 and 12 hours as given in Figure 2.8. Experimental and simulation coating thickness results of samples coated at 950, 1000, 1050, and 1100°C for 4 hours and coated at 1100°C for 4, 8, and 12 hours are given in Table 2.9 and 2.10 respectively.

Table 2.9: Coating Thickness Results of SEM-EDS Analysis and Coating Simulations at 950 °C, 1000 °C, 1050 °C and 1100°C.

Experimental Results				
Temperature (°C)	$\beta\text{-NiAl}$ Thickness (μm)	IDZ Thickness (μm)	Total Thickness (μm)	$\beta\text{-NiAl}/\text{IDZ}$
950	9	7	16	1.28
1000	9	6	15	1.50
1050	17	10	27	1.70
1100	25	20	45	1.25
Simulation Results				
Temperature (°C)	$\beta\text{-NiAl}$ Thickness (μm)	IDZ Thickness (μm)	Total Thickness (μm)	$\beta\text{-NiAl}/\text{IDZ}$
950	9	6	15	1.50
1000	11	7	18	1.57
1050	18	8	26	2.25
1100	26	12	37	2.16

Table 2.10: Coating Thickness Results of SEM-EDS Analysis and Coating Simulations for 4, 8 and 12 hours at 1100°C.

Experimental Results				
Time (hour)	β -NiAl Thickness (μm)	IDZ Thickness (μm)	Total Thickness (μm)	β -NiAl/IDZ
4	25	20	45	1.25
8	38	24	62	1.58
12	45	28	73	1.61
Simulation Results				
Temperature (hour)	β -NiAl Thickness (μm)	IDZ Thickness (μm)	Total Thickness (μm)	β -NiAl/IDZ
4	26	12	37	2.16
8	37	14	51	2.64
12	42	17	69	2.47

The simulation β -NiAl thicknesses were found to be similar to experimental results. However, the inner layer thicknesses of coating were found to be considerably lower than experimental results for all simulations. Increasing coating temperature or time increased the gap between simulation and experimental inner coating thicknesses. A similar trend was seen for inner layer Cr composition as mentioned before. Since Cr accumulation is lower in simulation results, inner layer coating thickness was found to be also lower. This could be due to some experimental conditions that were not considered and/or assumed differently while simulating surface growth and diffusion during aluminide coating. One of this condition is the limited number of elements used in DICTRA to simplify simulations. Ignored elements in the simulation could affect the amount of Cr accumulation under the outer layer of coating. The second reason of this error could be the linearly defined Al incorporation rate against time. In experimental conditions, Al incorporation rate follows the parabolic law. Another problem could be an error in kinetic and thermodynamic databases, affecting the Cr diffusion during coating.

Table 2.9 and 2.10 also shows outer layer/inner layer ratio (β -NiAl/inter diffusion zone) of simulation and experimental results. Due to lower thickness of inner layer

obtained in simulations, this ratio was also estimated to be higher in simulation results. However, the trend of this ratio against time and temperature found to be relatively similar as shown in Figure 2.10.

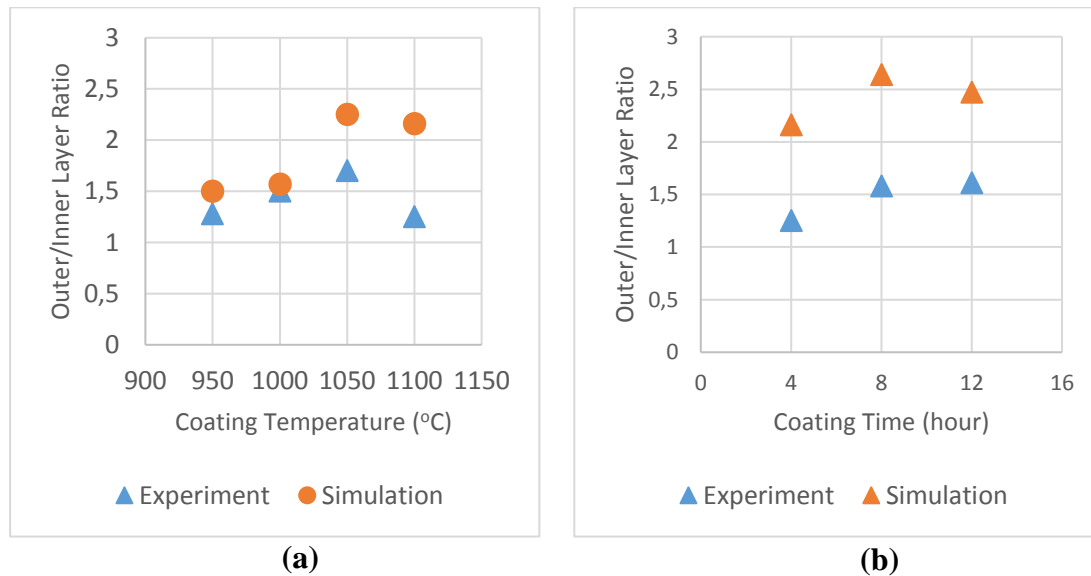


Figure 2.10: Simulation and experiment outer layer/inner layer ratio results at a) different coating temperatures and b) for different coating periods.

Calculated Al incorporation rates were iteratively changed slightly to achieve the same coating thickness with experimental results. The simulated and calculated incorporation rates are given in Figure 2.11 for the experimental groups given in Table 2.5 and 2.6. Calculated Al rates achieved higher coating thicknesses than experiment results except the coating performed at 950°C. Despite the fact that calculated and simulated Al incorporation rates were slightly different, similar trends were obtained for the change in Al incorporation rate against time and temperature.

Al incorporation rate primarily depends on coating temperature. Increasing coating temperature from 950°C to 1100°C increased calculated Al incorporation rate almost two times higher as shown in Figure 2.11. This is due to higher diffusion coefficient of Al to substrate at higher temperatures that allowed higher Al incorporation to IN 738 LC substrate surface. Time has a relatively lower effect on Al incorporation rate than temperature. Increasing time increases the total amount of Al deposited on the

substrate surface. Due to this reason Al incorporation rate is increased slightly as shown in Figure 2.11.

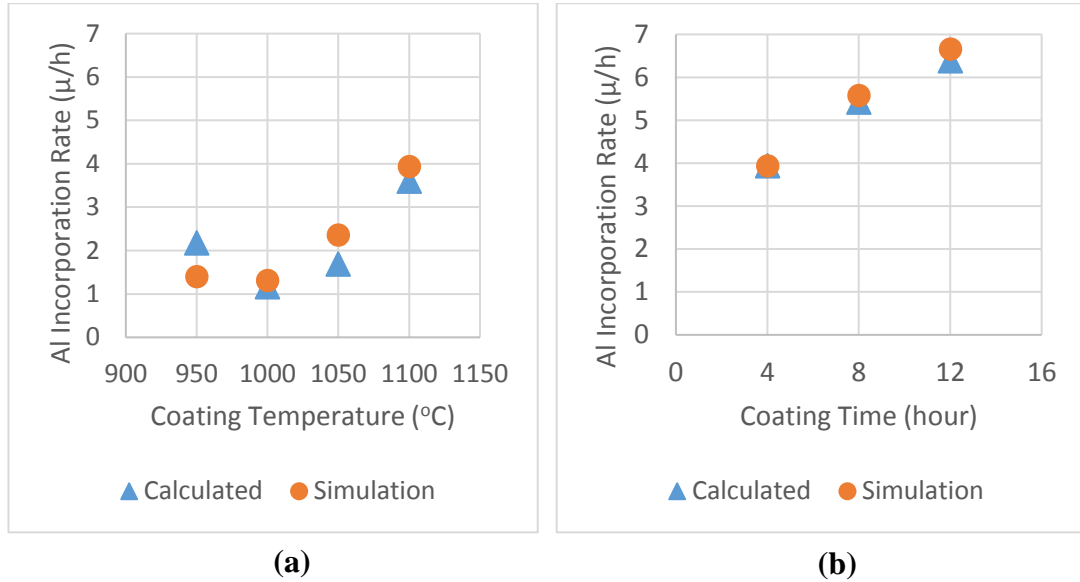


Figure 2.11: Calculated and iteratively simulation Al incorporation rates for samples a) coated at different temperatures and b) for different time periods.

2.3.3 Independent Simulation for Hypothetical Growth Condition

After Al incorporation rates were determined for related heat treatment parameters, Al incorporation rate estimation was performed for hypothetical experiment parameters independent from experiments. Two independent simulations were performed to estimate coating thickness and composition profile for given coating experimental conditions. Experimental parameters of these two hypothetical condition are given in Table 2.11.

Table 2.11: Hypothetical Experimental Parameters of Two Different Aluminide Coating Operation.

Aluminide Coating Number	Temperature (°C)	Time (h)	Pressure (mbar)	HCl Flow (sccm)	H ₂ Flow (sccm)	HCl : H ₂	Ar Flow (sccm)	HCl:Ar	Internal Trays (gr)
#1	1050	4	50	125	1000	1:8	250	1:2	Al-Cr 50/50 wt. %
#2	1050	4	100	500	1000	1:8	1000	1:2	Al-Cr 50/50 wt. %

The first experiment given in Table 2.11 was performed at the same conditions with the experiment performed at 1050°C in Table 2.5 except the pressure that was decreased to 50 mbar. The second experiment given in Table 2.11 was performed at the same conditions with the experiment performed at 1050°C in Table 2.5 except the HCl flow that was increased to 500 sccm. Based on the group of experiments that was performed to relate the growth rate to experimental parameters, decreasing pressure to 50 mbar at 1050°C and increases total coating thickness 18% while increasing HCl flow to 500 sccm decreases the total coating thickness 11% when other parameters were kept constant. Based on these results, the Al incorporation rate that was used for the experiments performed at 1050°C in Table 2.8 was increased 18% and decreased 11% respectively to simulate these two experimental conditions. The simulation conditions used to simulate hypothetical experimental conditions (Table 2.11) is given in Table 2.12.

Table 2.12: Simulation Parameters of Two Different Aluminide Coating Operation.

Aluminide Coating Number	Temperature (°C)	Time (h)	Al Growth (μm/h)	Base Metal Thickness (μm)	Node Number
#1	1050	4	2.78	200	100
#2	1050	4	2.62	200	100

The simulation results for composition profile of coating region are given in Figure 2.12.

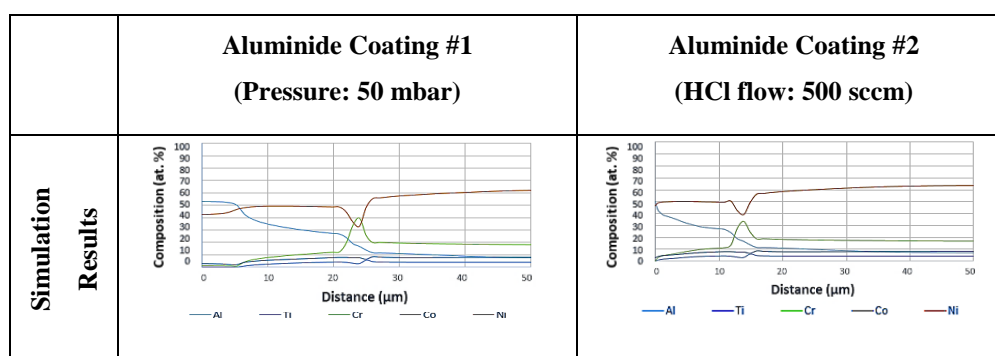


Figure 2.12: The Simulation Results for Hypothetical Experimental Conditions

The simulation results for coating thickness are given in Table 2.13.

Table 2.13: The Simulation Coating Thickness Results.

Simulation Results					
Aluminide Coating Number	Al Growth ($\mu\text{m/h}$)	β -NiAl Thickness (μm)	IDZ Thickness (μm)	Total Thickness (μm)	β -NiAl/IDZ
#1	2.78	22	7	28	3.14
#2	2.62	13	5	19	2.6

After the simulation results are obtained for hypothetical conditions, aluminide coatings were performed at the same conditions using chemical vapor deposition method to investigate accuracy of simulation results. The SEM images of coating region and EDS and WDS composition analysis results are given in Figure 2.13.

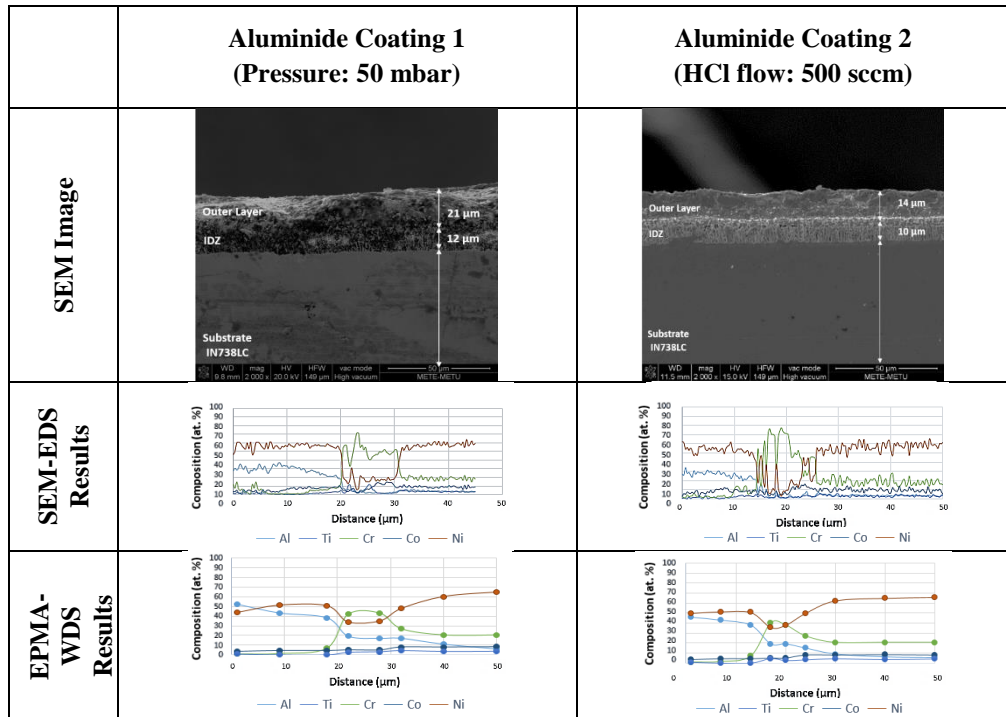


Figure 2.13: The Experimental Results for Hypothetical Experimental Conditions

The experimental results for coating thickness are given in Table 2.14.

Table 2.14: The Experimental Coating Thickness Results.

Experimental Results				
Aluminide Coating Number	β -NiAl Thickness (μm)	IDZ Thickness (μm)	Total Thickness (μm)	β -NiAl/IDZ
#1	21	12	33	2
#2	14	10	24	1.4

As shown in Figure 2.12 and 2.13, and Table 2.13 and 2.14, simulation and experimental results showed similar composition profiles and similar coating thicknesses. Similar to previous simulation results, these two simulations estimated β -NiAl composition profile and thickness relatively better than inner layer composition profile and thickness. The inner layer thickness and Cr composition were again estimated to be lower than experimental results. Correspondingly, the total coating thickness and β -NiAl/IDZ ratio found to be higher than experiments as shown in Table 2.13 and 2.14. However, the simulations still achieved relatively successful results independent of experiments.

2.4 Conclusion

In this chapter, diffusion between substrate and coating, and surface growth during aluminide coating application by CVD method on IN 738 LC was simulated for various coating time and temperatures. The conclusions obtained in this chapter are given below.

- Results of the Al substrate, β -NiAl-substrate and, diffusion and surface growth models were compared with experimental results. The most compatible results were achieved using diffusion and surface growth simulation model.
- Since “FIX FLUX” boundary condition was defined in software, an Al incorporation rate calculation was necessary to perform. Calculated Al incorporation rates were iteratively changed slightly to achieve the same coating thickness with experimental results. A similar trend between iteratively

simulated and calculated Al incorporation rates were found for different aluminide coating time and temperature.

- SEM-EDS and EPMA-WDS composition analyze results of coating region were compared. EPMA-WDS results showed higher Al composition at the outer layer of the coating up to 15 at. %.
- Simulation results were found to be closer to EPMA-WDS results that show higher Al composition at the outer layer of the coating for all samples.
- Outer layer thickness and composition profile were more successfully estimated than inner layer thickness and composition profile in DICTRA simulation results.
- The thickness of the inner layer of the coating was found to be lower than EPMA-EDS and SEM-EDS results up to almost 40 in simulations and Cr composition was found to be lower up to 15 at. % Increasing coating time and temperature found to be increasing these errors.
- Outer layer/inner layer rate was found to be higher in simulations than experimental results due to lower inner layer obtained in simulations. However, the trend of this ratio against coating time and temperature was found to be similar.
- After a trend was obtained between simulations and experiments, simulations were performed independent of experimental results. The Al incorporation rate was calculated for random experimental aluminide coating parameters. As a result, the independent simulation results provided satisfactory estimations of coating thickness and composition profile.

CHAPTER 3

EFFECT OF HEAT TREATMENT AND CVD COATING CONDITIONS ON IN 738 LC

3.1 Introduction

In this chapter, both experimental and simulation studies were performed to optimize and improve IN 738 LC microstructure. The effects varying solutionizing, CVD aluminide coating and aging parameters to IN 738 LC microstructure were studied. γ' size and volume fraction, hardness, grain size measurement and dendrite size measurement results are given for before and after heat treatments and aluminide coating. The heat treatments and aluminide coating process that were performed to improve and optimize IN 738 LC microstructure are shown in Figure 3.1.

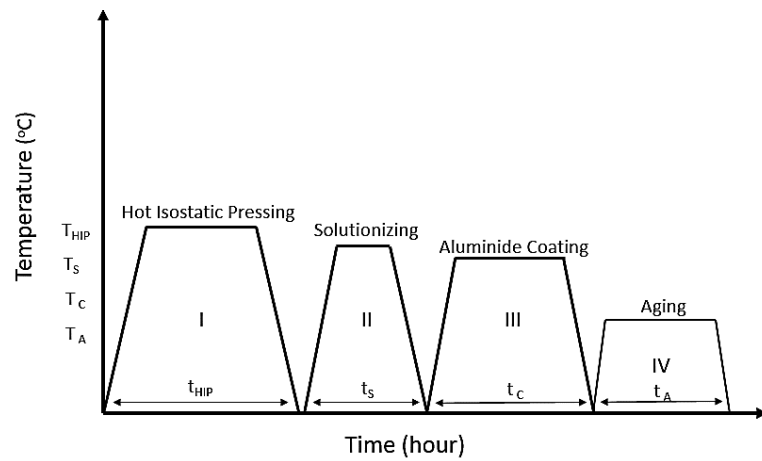


Figure 3.1: The scheme of heat treatments and coatings applied to IN 738 LC microstructure.

As shown in Figure 3.1, there are four steps applied to IN 738 LC after casting. At the end of these four steps, the purpose was to achieve a bimodal γ' precipitation and finely

shaped MC carbides as shown in Figure 3.2 that are known to provide highest mechanical properties for this material. [42]

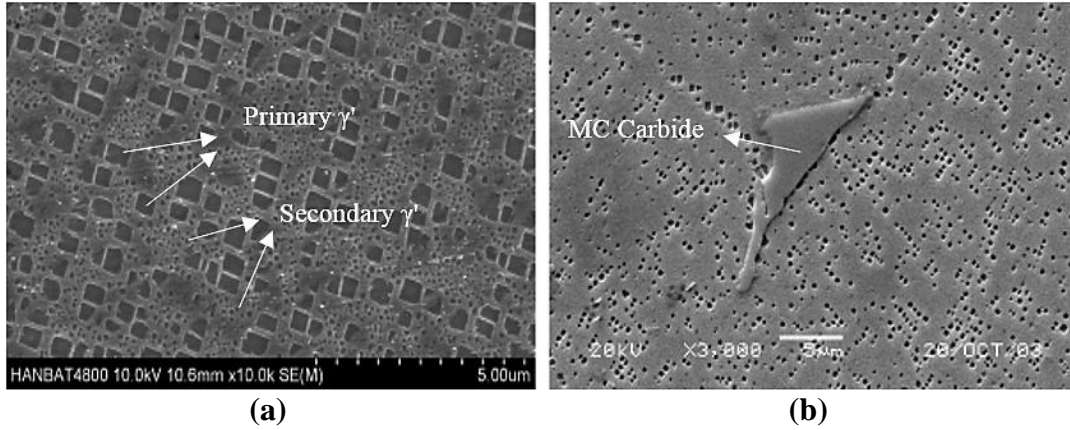


Figure 3.2: IN 738 LC SEM images of a) bimodal γ' precipitation and b) MC carbide [42].

3.2 Experimental Procedure

The information about the material, experimental setup, metallography and characterization methods are given in this section.

3.2.1 Material

In this study, IN 738 LC was used to manufacture third stage gas turbine rotor blade as a base material. Conventional equiaxed investment casting was performed to cast polycrystalline IN 738 LC rotor blade. Then the blade was cut to prepare 2x2 cm samples by electrical discharge machining and labeled by using laser marking as shown in Figure 3.3 Then samples were hot isostatic pressed (HIPed) at 1200°C for 10 hours under 150 MPa pressure to remove micro porosities that form during solidification.

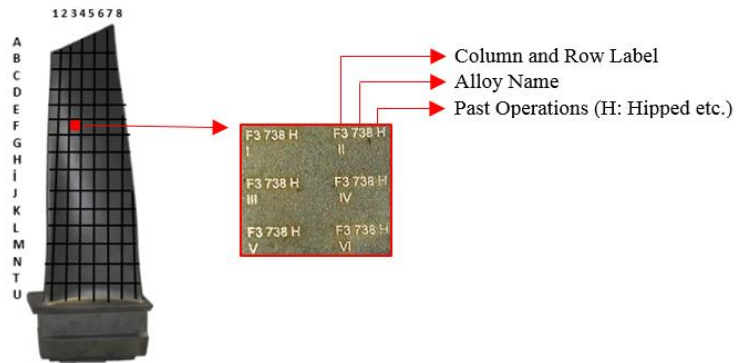


Figure 3.3: IN 738 LC rotor blade cutting and label method.

3.2.2 Experimental Setup

In this study, solutionizing and aging operations were carried out at different conditions in VAKSIS vacuum furnace that consist of pumps, molybdenum heaters, and cooling units as shown in Figure 3.4.

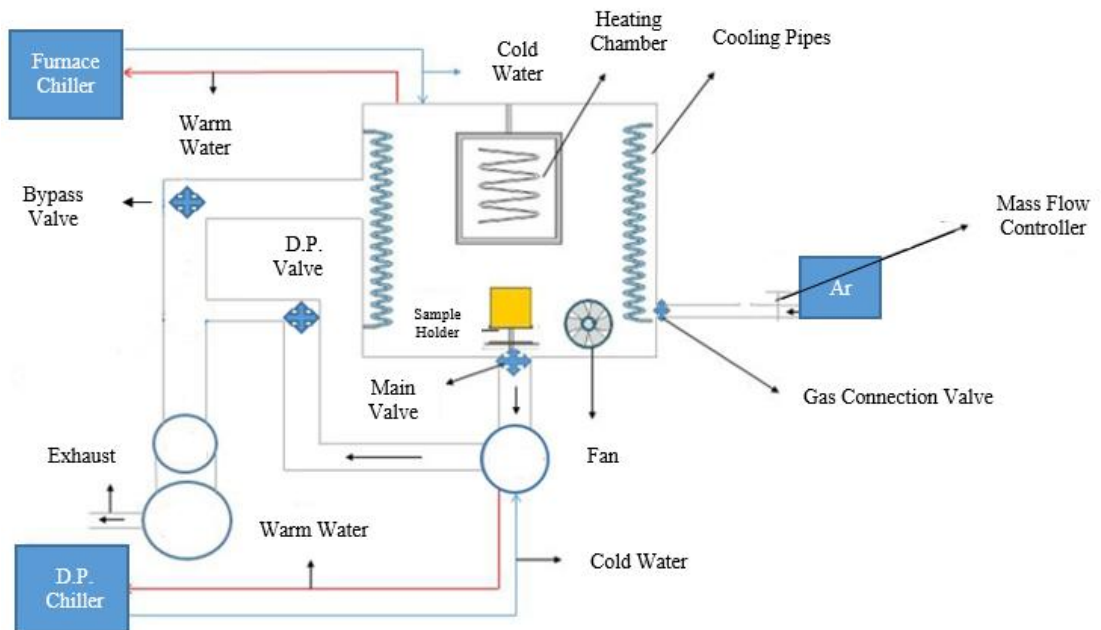


Figure 3.4: Scheme of VAKSIS Vacuum Furnace

Three pumps of VAKSIS vacuum furnace working simultaneously achieved 10^{-5} Torr vacuum environment during heat treatments and heaters were capable of heating

furnace up to 1350°C. Outer and inner chambers existed for better insulation and higher efficiency of the furnace. Samples were placed in holder in the outer chamber and carried to inside chamber by a pneumatic elevator. Two thermocouples existed in inner chamber to measure temperature. One was attached to upper wall of inner chamber, and another one was attached to holder near to samples. The one on holder was used for tracking temperature of heat treatment. Ar cooling and furnace cooling methods were available as cooling types. Ar cooling method was used by pumping Ar to inside of chamber up to 4500 sccm and increasing its circulation by a fan. The cooling curves of Ar and furnace cooling are given in Appendix B. The average cooling rates of these methods were measured as 180°C/min and 20°C/min, respectively. In this experimental setup, solutionizing and aging heat treatments were performed at various temperatures, time periods and cooling rates.

Additionally, HIP operation was conducted in a high pressure furnace, and aluminide coating was performed at “ATL Archer Tecnicoat” chemical vapor deposition system.

3.2.3 Simulation Method

JMAT PRO software was used to simulate microstructure evolution during various heat treatments and aluminide coating. IN 738 LC composition, grain size, γ' size and cooling rate were used as input to heat treatment module of software. Microstructure evolution during solutionizing, aluminide coating and aging were simulated using the microstructure data of HIPed both thick samples taken from middle section of the blade (average thickness 18.25 mm in range of 17.7-18.5 mm) and thin samples were taken from leading edge of the blade (average thickness 8.5 mm in range of 8.2-9.1 mm). Initial microstructure (HIPed microstructure) solutionizing temperature and cooling rate, coating temperature and period, aging temperature and period were provided as input to JMAT PRO simulation. Estimated γ' size, volume fraction and yield strength values were JMAT PRO's outputs. Estimated microstructure data was compared in this chapter with experimental results. Estimated yield strength data was compared with the yield strength model results and literature tensile test findings in

Chapter 4. The microstructure data of HIPed IN 738 LC samples that were used as simulation input is given in Table 3.1.

Table 3.1: Microstructure Input Data of HIPed IN 738 LC.

γ' Size (nm)		Grain Size (μm)		Cooling Rate ($^{\circ}\text{C}/\text{min}$)	
Thick Sample (18.25 mm)	Thin Sample (8.25 mm)	Thick Sample (18.25 mm)	Thin Sample (8.25 mm)	Ar Cooling ($^{\circ}\text{C}/\text{min}$)	Furnace Cooling ($^{\circ}\text{C}/\text{min}$)
351	325	2846	692	180	20

The γ' size and grain size measurement methods for the results given in Table 3.1, are given under section 3.2.4.2.4 Grain Size and Dendrite Spacing Determination and 3.2.4.2.5 Gamma Prime Size and Volume Fraction Determination. The further information about cooling rate is provided in section 3.2.2 Experimental Setup and Appendix A.

Solutionizing temperature and cooling rate, aluminide coating temperature and time period, aging temperature and time period were entered as input to JMAT PRO. However, JMAT PRO was not capable of simulating the effect of solutionizing time to microstructure, since the software assumes a certain time period for solutionizing that achieves an equilibrium state of microstructure. Furthermore, the cooling rates after aluminide coating and aging were not entered to JMAT PRO since the software was not able to simulate these parameters. However, during comparison of experimental and JMAT PRO results, it is assumed that the experiments and the JMAT PRO simulations were performed at the same conditions.

3.2.4 Metallography and Characterization

All the samples were exposed to conventional metallographic sample preparation. Various characterization methods were used to investigate the effect of heat treatments and aluminide coating parameters to IN 738 LC microstructure.

3.2.4.1 Metallography

Before and after heat treatment and aluminide coating operations, the IN 738 LC samples were prepared for microstructural analysis. The metallographic preparation consisted of steps given below.

- Casting, HIP, solutionizing, coating, and aging were a continuous operations chain. Before next process was performed, one of the six parts of IN 738 LC sample was left behind to compare before and after of a heat treatment or coating. Therefore, samples were cut by aggressive cutting method on the dashed lines as shown in Figure 3.5.

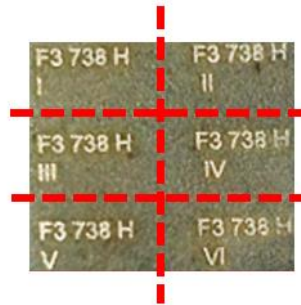


Figure 3.5: Cutting lines of an IN 738 LC sample.

- Samples were grinded by 60, 220, 400, 800 and 1200 μm papers and polished by 3 and 1 μm diamond suspension.
- Before characterization, samples were etched with etchant 1 for microstructure analyze in scanning electron microscopy and etchant 2 for grain size measurement using immersion method. The chemical compositions of these etchants are given below.

Table 3.2: Chemical Composition of Etchants. [4, 91]

Etchant 1	4gCuSO ₄ +20cc+HCl+20ccH ₂ O [91]
Etchant 2	33% HNO ₃ +33% CH ₃ COOH +33H ₂ O+1% HF [4]

3.2.4.2 Characterization

Scanning electron microscopy (SEM), electron diffraction spectroscopy (EDS), hardness testing, and grain size determination were the methods used to characterize IN 738 LC samples before and after heat treatments and aluminide coating.

3.2.4.2.1 Scanning Electron Microscopy

The microstructural characterization was conducted in “FEI Nova Nano 430 Scanning Electron Microscope” in free-field mode. The images were taken with an integrated software at different magnifications. SEM images were used for γ' and carbide volume fraction and size measurements.

3.2.4.2.2 Electron Diffraction Spectroscopy Analysis

EDS (Energy Dispersive X-Ray Spectroscopy) studies were performed using “EDAX SSD Apollo10 Detector” and “EDAX Genesis Version 6.0 Analysis Software” adapted to “FEI Scanning Electron Microscope (SEM)”.

Composition analyzes with electron diffraction spectroscopy was conducted. Line scans and mapping were used to see whether detected elements can be related to the carbides.

3.2.4.2.3 Hardness Testing

Micro and macro hardness testing were performed to see whether there was a change of hardness in heat treated and coated samples. “SHIMADZU HMV-G Series Micro Vickers Hardness Tester” was used under 9.807 N load for micro hardness testing while “WILSON Macro Hardness Tester” was used to conduct macro hardness testing under 150 kg load. At least five measurements were performed for each sample, and average value was determined as shown in Figure 3.6.

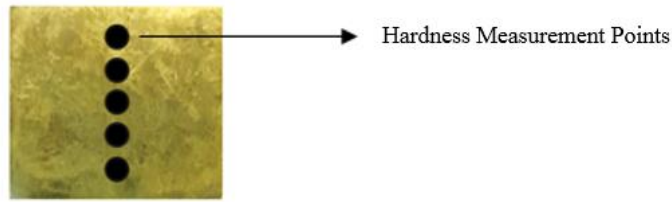


Figure 3.6: Hardness testing locations on the sample.

After the initial measurements were performed, considerably higher standard deviation was obtained for micro hardness results than macro hardness results taken from the same IN 738 LC sample. This was expected since the average diameter of the micro hardness measurement area found to be 20 μm while macro hardness measurement area found to be 745 μm . These diameters compared to an optic microscope image and a SEM image as shown in Figure 3.7.

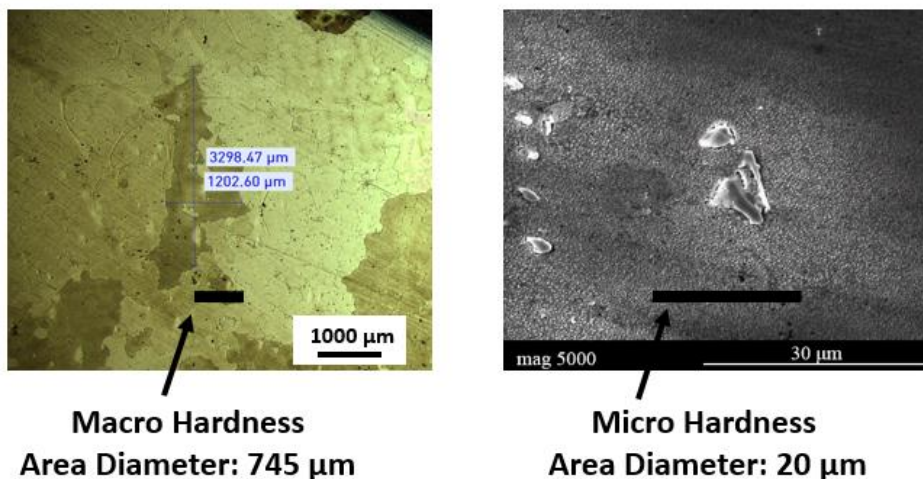


Figure 3.7: Optic microscope and SEM image of IN 738 LC that shows macro hardness and micro hardness measurement area diameters respectively.

As shown in Figure 3.7, micro hardness measurement area diameters are almost similar to a carbide diameter in IN 738 LC. During micro hardness measurement, particles such as carbides might affect the micro hardness measurement result greatly.

Macro hardness is measured from a much bigger surface area that contains high volume of the matrix. Due to this reason, macro hardness measurements achieved

better precision and accuracy. Therefore, macro hardness measurement was performed for all samples instead of micro hardness measurements.

3.2.4.2.4 Grain Size and Dendrite Spacing Determination

Grain size and secondary dendrite arm spacing is determined using photos of samples taken by high resolution cameras. Since the surface areas of samples were less than 4 cm², only three measurements were able to be taken from minimum four grains, each asymmetric grain pivotted by a center.

IMAGE J software was used to measure average grain size in three different directions as shown in Figure 3.8. Average secondary dendrite arm spacing was found using 20 measurements taken from each sample by using IMAGE J software as in Figure 3.8.

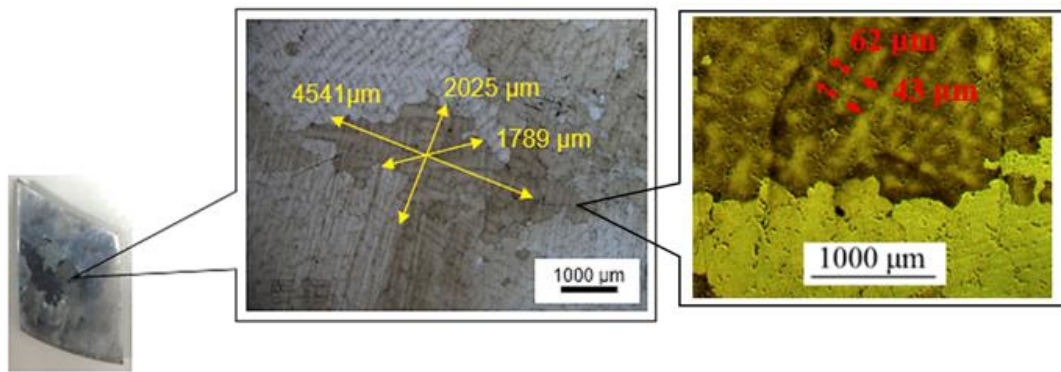


Figure 3.8: Photo of an IN 738 LC samples taken from middle section of a turbine blade and used for grain size measurement and secondary dendrite arm spacing measurement.

3.2.4.2.5 Gamma Prime Size and Volume Fraction Determination

Gamma prime (γ') volume fraction and particle size were calculated using 5 different SEM images taken from thick IN 738 LC samples and 3 different SEM images taken from thin IN 738 LC samples as shown in Figure 3.9.

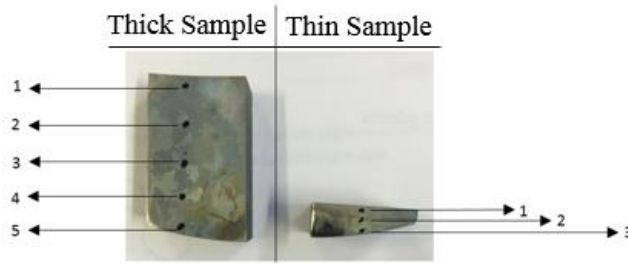


Figure 3.9: Points SEM images were taken on the thick and thin sample.

The SEM images were taken from different depth from cast surface. Primary and secondary γ' particles were counted from SEM images using IMAGE J software as shown in Figure 3.10.

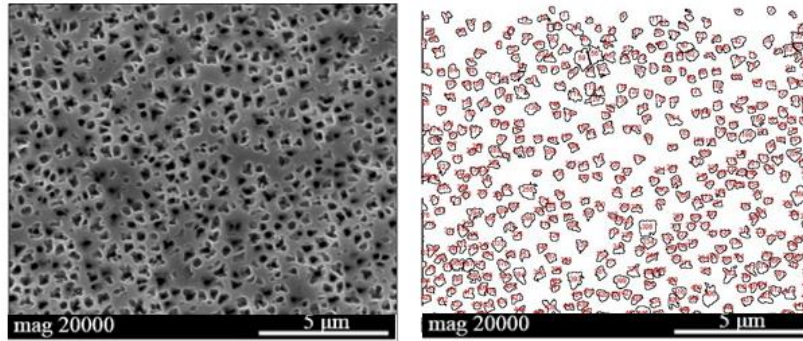


Figure 3.10: SEM image and IMAGE J analyze result that calculates a number of γ' particles.

Secondary γ' size range was determined to be at least 60% lower than primary γ' size range. These particles were counted separately using IMAGE J software. Calculated area fractions were used to calculate volume fraction of both primary and secondary γ' particles by assuming the particle shapes are square or sphere. 15 measurements were taken from each SEM image to obtain average primary and secondary γ' particle sizes.

3.3 Heat Treatment Plan

Several heat treatments and aluminide coating experiments were performed at various conditions for IN 738 LC samples. Different experiment groups were formed as shown in Table 3.3.

All the samples used in A, B and C experiment groups were HIPed at 1200°C for 10 hours under 150 MPa pressure. Effect of HIP to IN 738 LC was also investigated individually in this chapter.

Table 3.3: Heat Treatment and Aluminide Coating Plan for Different Sample Groups.

Heat Treatment Group Name	Solutionizing Parameters		Coating Parameters			Aging Parameters
			1	2	3	
GROUP A	2h-Ar C. (180°C/min)	1080°C-	1000 °C-20h-F.C. (7°C/min)	1050 °C-16h-F.C. (7°C/min)	1100 °C-12h-F.C. (7°C/min)	No aging
		1100 °C)				
		1120 °C				
		1150 °C				
		1180 °C				
		1200 °C				
		1235 °C				
GROUP B	1120 °C-1h	Ar C. (180°C/min)	1000 °C-20h-F.C. (7°C/min)	1050 °C-16h F.C. (7°C/min)	1100 °C-12h-F.C. (7°C/min)	
		F.C. (20°C/min)				
	1120 °C-2h	Ar C. (180°C/min)				
		F.C. (20°C/min)				
	1120 °C-4h	Ar C. (180°C/min)				
		F.C. (20°C/min)				
GROUP C	1120 °C-2h-Ar C. (180°C/min)		1000 °C-20h-F.C. (7°C/min)	1050 °C-20h-F.C (7°C/min)	1100 °C-20h-F.C (7°C/min)	845 °C-24h-Ar.C. (180°C/min)
			No coating applied.			

The location of samples used in each experiment group is shown in Figure 3.10. Sample group W was used in heat treatment group A and sample group X was used in heat treatment group B. Sample group Y and Z were used in heat treatment group C.

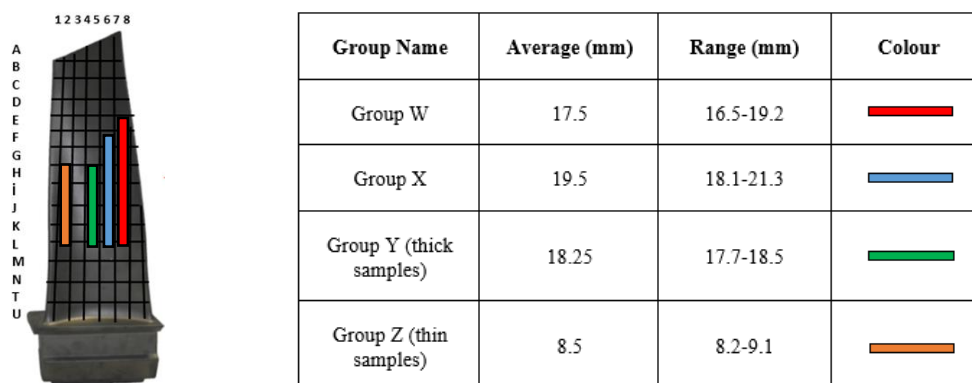


Figure 3.11: Location of samples used in each heat treatment group.

After the solutionizing operation, samples were cut by aggressive cutting method, and each piece of sample was used as shown in Figure 3.12.



Figure 3.12: Sample cutting method.

Details of each experiment group are given below.

Group A: 7 IN 738 LC samples were used in Group A with the average thickness of 17.5 mm and in the range of 16.5-19.2 mm. The samples at this group were solutionized at different heat treatment temperatures 1080, 1100, 1120, 1150, 1200 and 1235 °C for 2 hours, and Ar cooled (180°C/min). Then, each sample was cut as shown in Figure 3.12 and each piece was coated at different conditions given as 1000°C-20 hours, 1050°C-16 hours and 1100°C-12 hours (furnace cooled-7°C/min).

Microstructure characterizations of samples were performed before and after solutionizing and aluminide coating.

Group B: 6 IN 738 LC samples were used in Group B with the average thickness of 19.5 mm in the range of 18.1-21.3 mm. The samples at this group were solutionized at 1120°C for 1, 2 and 4 hours using both Ar (180°C/min) and furnace cooling (20°C/min). Then, each sample was cut as shown in Figure 3.12 and each piece was coated at different conditions given as 1000°C-20 hours, 1050°C-16 hours and 1100°C-12 hours (furnace cooled-7°C/min). Microstructure characterization of samples was performed before and after solutionizing and aluminide coating.

Group C: 8 IN 738 LC samples were used in Group C. 4 of them were taken from the thick middle section part (average thickness 18.25 mm and in range of 17.7-18.5 mm) while the other 4 were taken from thin leading edge (average thickness 8.5 mm and in range of 8.2-9.1 mm) of the IN 738 LC rotor blade. The samples in this group were solutionized at 1120°C for 2 hours, and Ar (180°C/min) cooled. Then, samples were grouped by 2, including one thick and one thin sample in each group. 3 groups were used in coating experiments, and each group was coated at different conditions given as 1000°C-20 hours, 1050°C-16 hours and 1100°C-12 hours. No coating was applied to the 4. group. Finally, both coated and uncoated samples were aged at 845°C for 24 hours and Ar cooled (180°C/min).

Samples solutionized at various temperatures for different time periods and with different cooling rates were all coated at 1000°C-20 hours, 1050°C-16 hours and 1100°C-12 hours by using chemical vapor deposition method to investigate microstructure evolution during aluminide coating. The purpose of performing coating operations at 1000°C-20 hours, 1050°C-16 hours and 1100°C-12 hours was to achieve same coating thickness at different coating temperatures. Since coating thickness is proportional to coating temperature, coating operations with lower temperature were performed for longer time durations. The other experimental parameters were constant for all three coating operations as given in Table 3.4.

Table 3.4: Experiment Parameters of CVD Aluminide Coating Operations.

Temperature (°C)	Time (hour)	Pressure (mbar)	HCl Flow (sccm)	H ₂ Flow (sccm)	HCl:H ₂ Flow Rate	Ar Flow (sccm)	HCl:Ar Flow Rate
1100	12	100	125	250	1:2	250	1:2
1050	16	100	125	250	1:2	250	1:2
1000	20	100	125	250	1:2	250	1:2

Coating region SEM images of samples coated at 1000°C-20 hours, 1050 °C-16 hours, and 1100 °C-12 hours, and thicknesses of coating outer layer (β -NiAl zone) and the inner layer (interdiffusion zone-IDZ) are given in Figure 3.13.

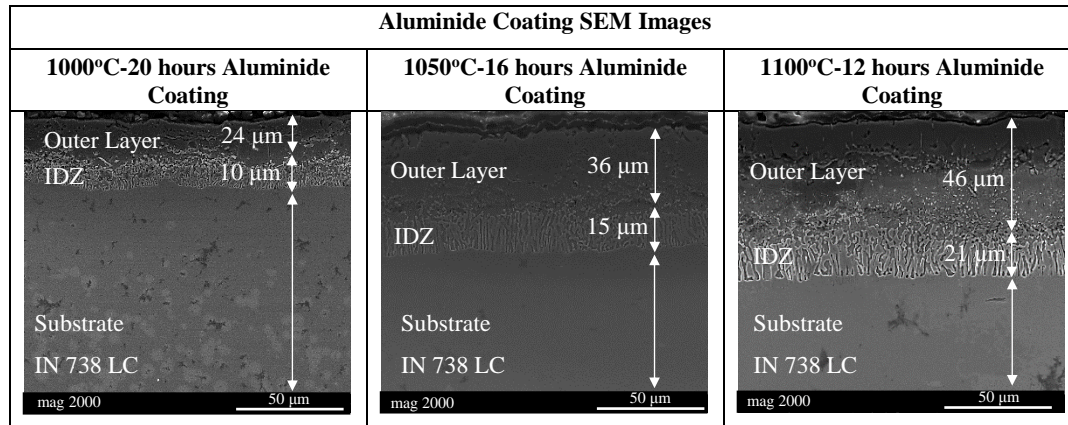


Figure 3.13: Coating region SEM images of samples coated at 1000°C-20 hours, 1050 °C-16 hours and 1100 °C-12 hours.

As it is shown in Figure 3.13, the coating thickness achieved at 1100°C for 12 hours is twice as big as at 1000°C for 20 hours. Although longer time periods were used for lower coating temperatures, same coating thickness for three different conditions was not achieved. The desired coating thickness was at least 70 μ m. 1100°C-12 hours aluminide coating achieved this thickness. However, the coatings performed at 1000°C-20 hours and 1050°C-16 hours couldn't achieve 70 μ m. The time periods of these two coatings were not kept longer since a CVD aluminide coating over 20 hours is not desirable, and a dramatic microstructure change was not expected for coatings performed for longer time periods than 20 hours.

3.4 Results and Discussion

The response of IN 738 LC microstructure to hot isostatic pressing, solutionizing, coating and aging is presented with some varying experimental parameters in this section. γ' and carbide characterizations, grain size, and hardness measurements were performed before and after heat treatments and aluminide coating to track microstructural change during these processes. JMAT PRO microstructure evolution simulations were performed, and simulation results were compared with microstructural findings of experiments.

3.4.1 Effect of Hot Isostatic Press to IN 738 LC Microstructure

Hot isostatic press was applied to IN 738 LC samples at 1200°C for 10 hours under 150 MPa pressure. It is the first heat treatment applied to IN 738 LC microstructure as shown in Figure 3.14.

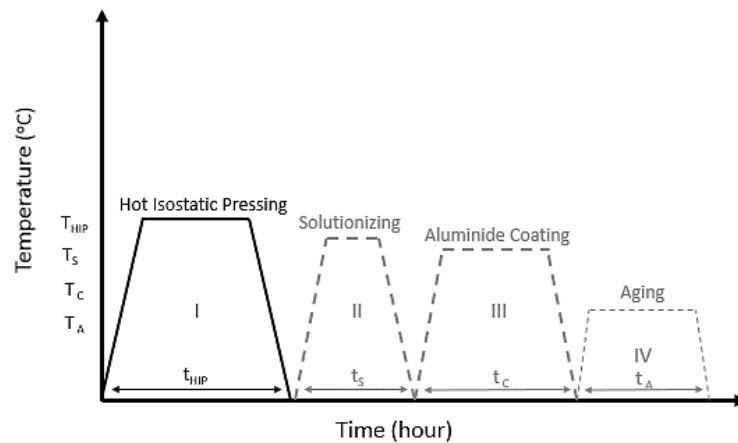


Figure 3.14: The scheme of heat treatments and coatings applied to IN 738 LC microstructure.

Effect of HIP to IN 738 LC microstructure was investigated comparing the microstructures of two HIPed and two cast samples with similar thicknesses. The sample locations are shown on IN 738 LC turbine blade in Figure 3.15.

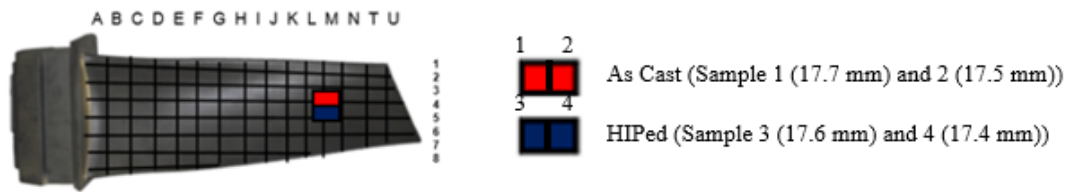


Figure 3.15: Location of samples that were used to study the effect of HIP.

Since the primary reason to apply HIP is decreasing the number of cavities, initially density of porosity was investigated as shown in Figure 3.16. Size and density of porosities decreased similarly to literature findings after HIP operation. [36, 37, 38, 39, 40] However, there are still some porosities left at smaller scales, that shows similar characteristics to gas pores. J.C. Beddoes and W. Wallace also reported that HIP operation for IN 738 samples at 1200°C under 100 MPa pressure failed to close all porosities [37].

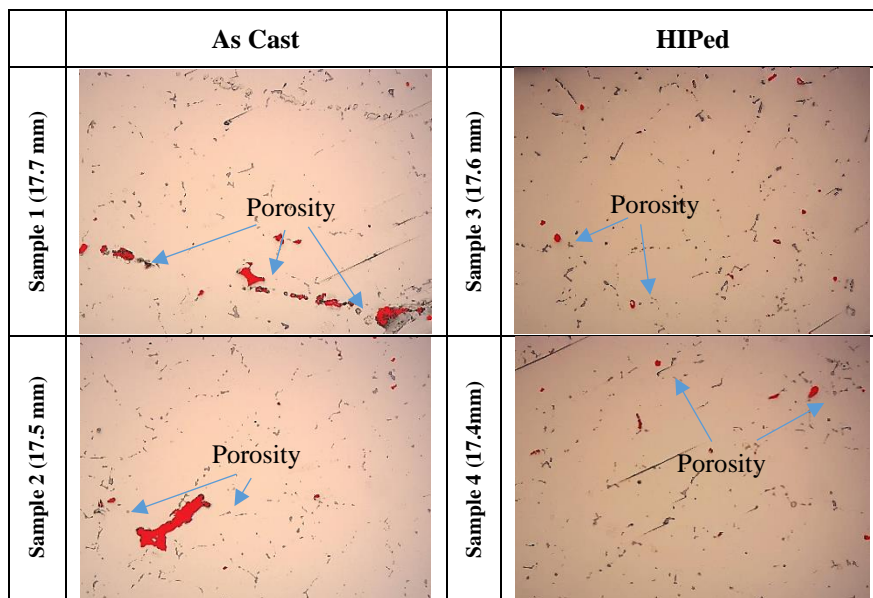


Figure 3.16: Optic microscope images of IN 738 LC before and after HIP.

SEM images of as cast two samples were compared with HIPed samples (with similar thicknesses) as shown in Figure 3.17. Average γ' size and volume measurement of these samples are given in Table 3.18. Similar to Saed Farahany et. al's results, during HIP primary γ' its size was increased about 25 nm due to coarsening. [36] Secondary

γ' is dissolved into the matrix as Wanygao et. al reported during HIP. [38] Due to the disappearance of secondary γ' after HIP, total γ' volume fraction was decreased as given in Table 3.5. To recover from these detrimental effects of HIP, secondary heat treatments (solutionizing and aging) were applied to IN 738 LC samples.

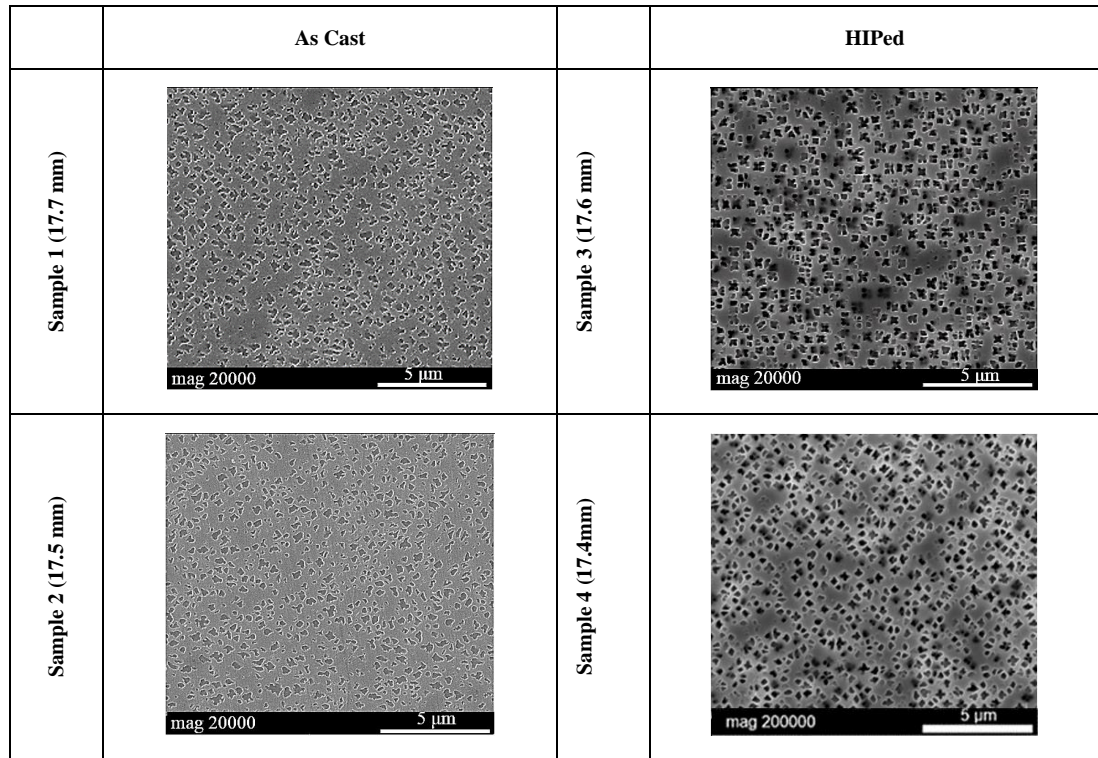


Figure 3.17: SEM images of as cast and HIPed samples.

Table 3.5: γ' Size and Volume Fraction of As Cast and HIPed Samples.

	As Cast					HIPed			
	Primary		Secondary			Primary		Secondary	
	Size (nm)	Volume Fraction	Size (nm)	Volume Fraction		Size (nm)	V.F.	Size (nm)	Volume Fraction
Sample 1 (17.7 mm)	332	0.37	108	0.11	Sample 3 (17.6 mm)	359	0.44	-	-
Sample 2 (17.5 mm)	321	0.32	96	0.14	Sample 4 (17.5 mm)	342	0.38	-	-

Hardness and grain size measurement results of samples are given in Table 3.6. Hardness is directly proportional to γ' volume and inversely proportional to γ' size.

Post-HIP microstructure showed lower hardness than as cast samples due to dissolution of secondary γ' particles that decreased total γ' volume fraction.

Table 3.6: Hardness and Grain Size of As Cast and HIPed Samples.

Hardness (HRC)				Grain Size (μm)			
Sample #	As Cast	Sample #	HIPed	Sample #	As Cast	Sample #	HIPed
Sample 1 (17.7 mm)	46	Sample 3 (17.6 mm)	41	Sample 1 (17.7 mm)	2442	Sample 3 (17.6 mm)	2617
Sample 2 (17.5 mm)	44	Sample 4 (17.4 mm)	43	Sample 2 (17.5 mm)	2722	Sample 4 (17.4 mm)	3075

IN 738 LC generally has coarse grain. The HIPing temperature for IN 738 LC is generally preferred above the γ' and $\text{M}_{23}\text{C}_6/\text{M}_6\text{C}$ solvus temperature but preferably below the MC solvus temperature since MC carbides prevent rapid grain growth. Rapid grain growth provides less area to form carbides, that results in film like carbide chains that are detrimental for mechanical properties of the material. Additionally, the larger the grain, the lower the grain strengthening of material. Koul et. al reported that rapid grain growth in IN 738 LC starts at 1225°C [92]. As shown in Table 3.6, there was a slight increase in grain size after HIP at 1200°C for 10 hours under 150 MPa pressure.

3.4.2 Effect of Solutionizing to IN 738 LC Microstructure

Effects of solutionizing time, temperature and cooling rate to IN 738 LC were investigated in this section. Solutionizing is the second heat treatment applied to IN 738 LC as shown in Figure 3.18.

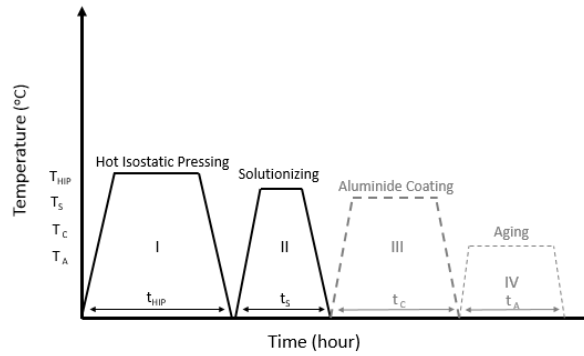


Figure 3.18: The scheme of heat treatments and coatings applied to IN 738 LC microstructure.

3.4.2.1 Effect of Solutionizing Temperature

Various solutionizing heat treatment temperatures (Table 3.3-Group A) were applied to HIPed IN 738 LC samples to investigate the effect of solutionizing temperature on microstructure. The solutionizing temperature was changed in between 1080-1235°C and other parameters were kept constant as shown in Table 3.7

Table 3.7: Parameters Used to Investigate Effect of Solutionizing Temperature.

HIP Condition		Solutionizing Conditions	
Temperature (°C)	1200	Temperature (°C)	1080, 1100, 1120, 1150, 1180, 1200, 1235
Time (h)	10	Time (h)	2
Pressure (MPa)	150	Cooling Type and Rate (°C/min)	Ar Cooling-180

The location of samples used in these solutionizing heat treatments is shown on IN 738 LC rotor blade in Figure 3.19.

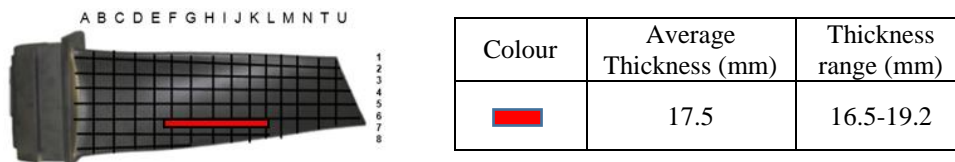


Figure 3.19: The location of samples that were solutionized in between 1080-1235°C for 2 hours.

The representative SEM images of each sample after solutionizing is given in Figure 3.20.

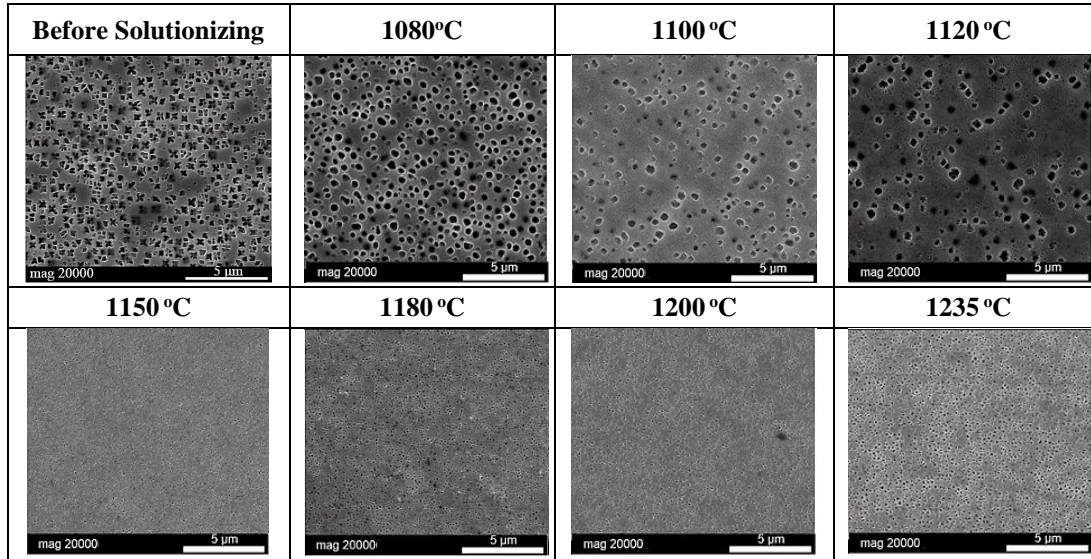


Figure 3.20: SEM images of IN 738 LC samples after solutionizing at various temperatures between 1080°C-1235°C for 2 hours (Ar cooled-180°C/min).

As it is shown in Figure 3.20, bimodal γ' structure was found after solutionizing performed at 1080, 1100 and 1120°C while the unimodal structure was found at 1150, 1180, 1200 and 1235°C.

Primary γ' found to be cuboidal and secondary γ' found to be spherical after solutionizing at 1100 and 1120°C. Both primary and secondary γ' found to be spherical solutionizing at 1080°C. However, it is possible to see the beginning of primary γ' shape transformation from spherical to square at 1080°C solutionizing temperature. Solutionizings at 1150, 1180, 1200 and 1235°C resulted with only spherical unimodal γ' particles.

Primary and secondary γ' size and volume fraction of the as cast, HIPed samples, and samples solutionized between 1080-1235°C for 2 hours and Ar cooled (180°C/min) are given in Figure 3.21.

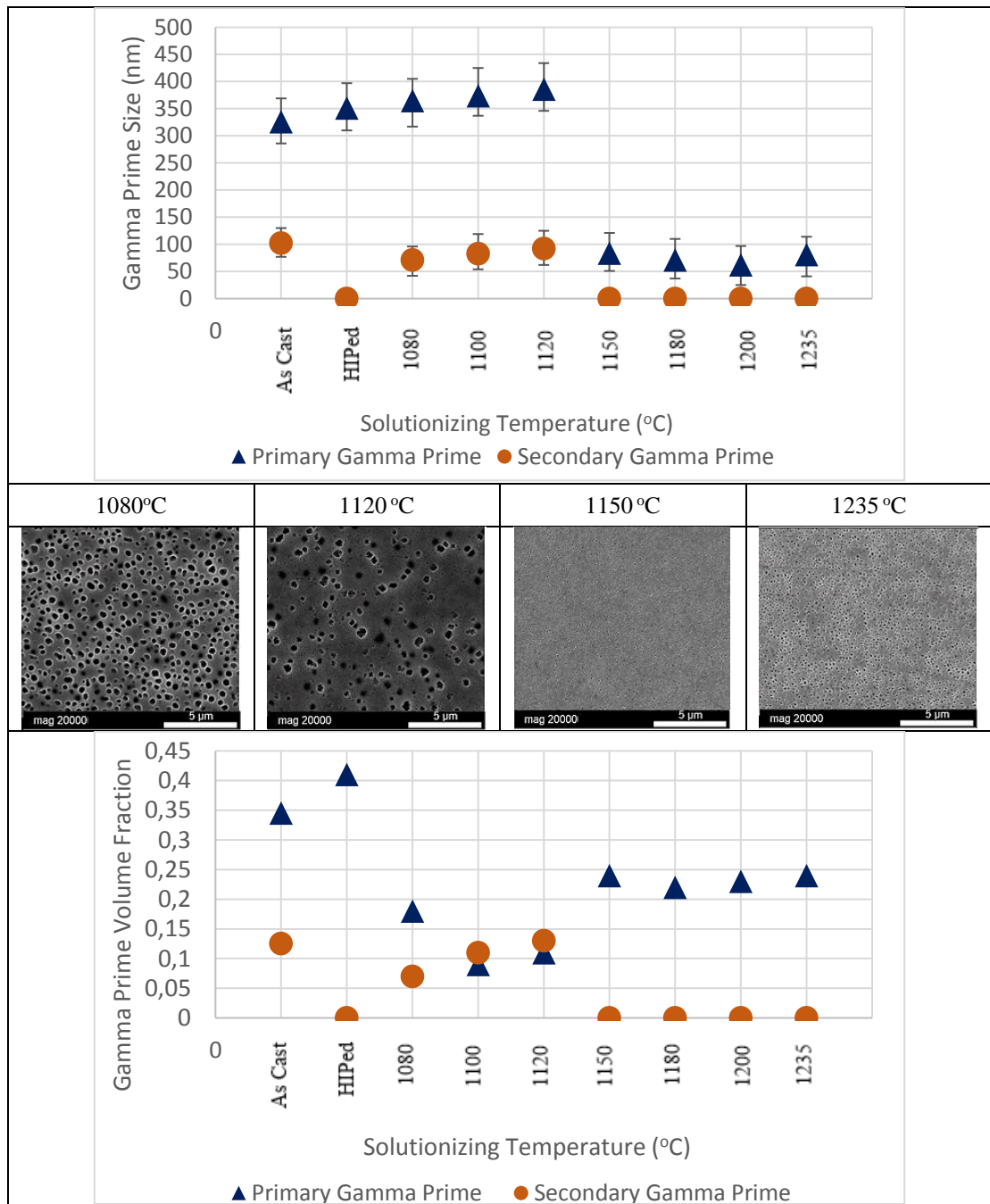


Figure 3.21: Primary and secondary γ' size and volume fraction of as cast, HIPed samples, and solutionized samples at various temperatures between 1080°C-1235°C with representative SEM images.

The 1080°C solutionizing temperature found to be too low even for partial solutionizing. It only decreased γ' volume fraction slightly since γ' didn't dissolve into the matrix at this temperature. However, γ' shape was changed into a sphere due to the increase in γ - γ' mismatch and corner-dissolution of the γ' particles during heat treatment.

The solutionizing at 1100 and 1120°C acquired bimodal microstructure with a fine dispersion of secondary γ' precipitates. However, slightly bigger primary and secondary γ' were obtained at 1120°C. A similar bimodal microstructure was found by Yun et. al and Jeong Min Kim et. al after the same solutionizing conditions performed at this temperature [42, 43]. Solutionizing temperatures at 1150°C and above acquired increased dissolution of γ' particles and formation of unimodal γ' microstructure. However, Anurag Thakur found bimodal microstructure at 1150°C and obtained unimodal structure at 1175°C for IN 738 [20]. This could be due to a different initial microstructure solutionized or the different type of furnaces used to perform solutionizing studies.

Highest bimodal volume fraction was achieved at 1120°C. Above 1150°C increasing temperature resulted in stable unimodal γ' size and volume fraction. As shown in Figure 3.21 secondary γ' fraction is higher than primary for solutionizings performed only at 1100°C and 1120°C which is an advantage since homogeneously distributed smaller γ' particles provide higher yield strengthening.

Hardness measurement results of as cast, HIPed samples and samples solutionized between 1080-1235°C for 2 hours and Ar cooled are given in Figure 3.22.

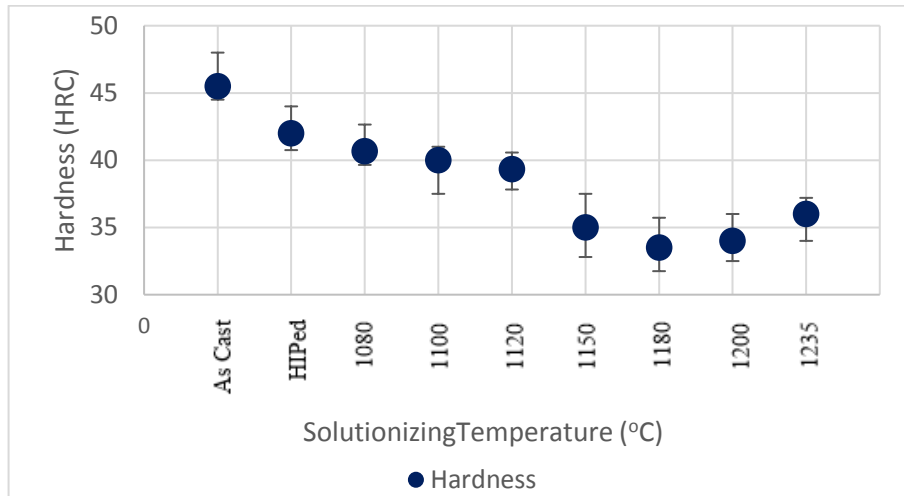


Figure 3.22: Hardness of as cast, HIPed samples, and solutionized samples at various temperatures between 1080°C-1235°C.

The hardness results were found to be similar to Anurag Thakur's results; higher solutionizing temperatures provided lower hardness due to softening effect of primary γ' disappearance and slight decrease in total γ' volume fraction at temperatures above 1150°C [20].

Grain size measurement results of as cast, HIPed samples and samples solutionized between 1080-1235°C for 2 hours and Ar cooled are given in Figure 3.23.

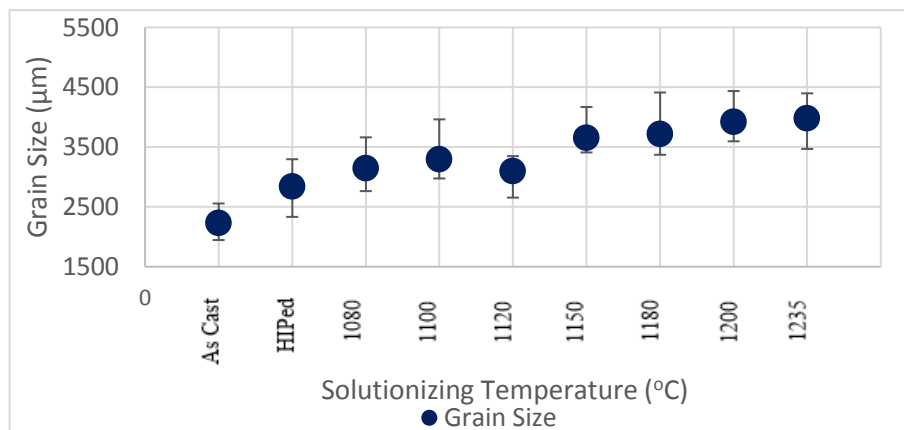


Figure 3.23: Grain size of as cast, HIPed samples, and solutionized samples at various temperatures between 1080°C-1235°C.

The result shows that there was two considerable increase in grain size during solutionizing heat treatments. The first one was during HIP operation due to high temperature and long period of this process, at 1200°C for 10 hours under 150 MPa.

The second considerable increase occurred where materials microstructure changes from bimodal to unimodal in between 1120-1150°C solutionizing temperature range. This was expected due to the disappearance of coarse primary γ' particles that block the movement of grain boundaries above 1120°C. This effect was also seen in studies of Koul and Castiio and Anurag Thakur [20, 38].

3.4.2.2 Effect of Solutionizing Time Cooling Rate

Solutionizing treatments at varying conditions was applied to HIPed IN 738 LC samples to see the effect of solutionizing time and cooling rate on IN 738 LC microstructure. The experimental parameters used for this purpose are given in Table 3.8.

Table 3.8: Parameters Used to Investigate Effect of Solutionizing Time and Cooling Rate

HIP Condition		Solutionizing Conditions	
Temperature (°C)	1200	Temperature (°C)	1120
Time (h)	10	Time (h)	1, 2, 4
Pressure (MPa)	150	Cooling Type and Rate (°C/min)	Ar Cooling-180 Furnace Cooling-20

The location of used samples on IN 738 LC rotor blade is given in Figure 3.24.

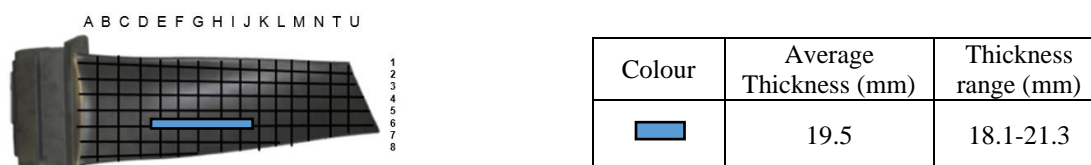


Figure 3.24: The location of samples that were solutionized at 1120°C for 1, 2 and 4 hours using Ar (180°C/min) and furnace cooling (20°C/min).

The representative post-solutionizing SEM images, and γ' size and volume fraction of each sample are given in Figure 3.25.

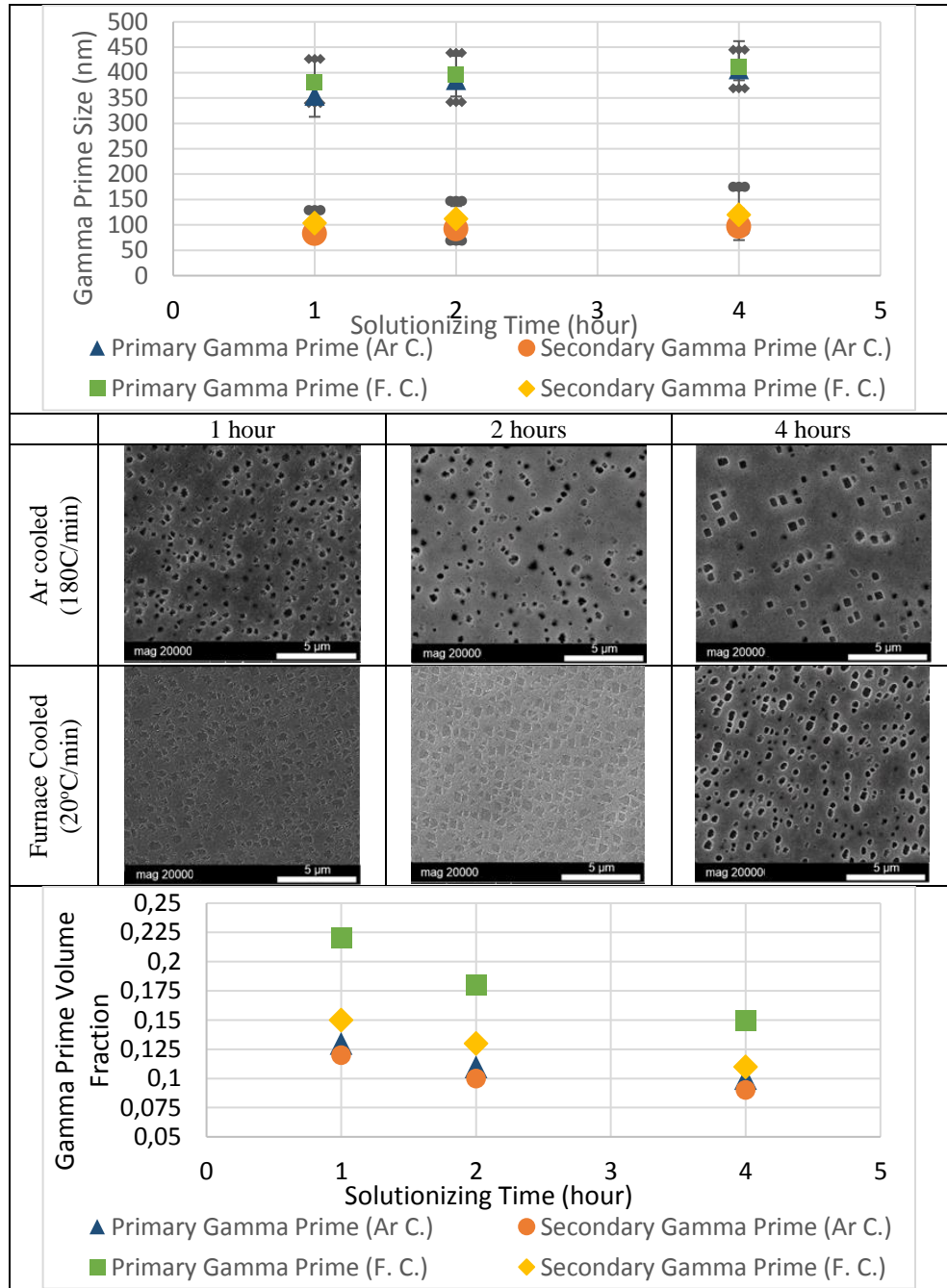


Figure 3.25: SEM images, and primary and secondary γ' size and volume fraction after 1, 2 and 4 hours solutionizing time periods, at 1120°C and with Ar (180°C/min) or furnace cooling (20°C/min) rates.

Hardness and grain size measurement results are given in Figure 3.26 and Figure 3.27.

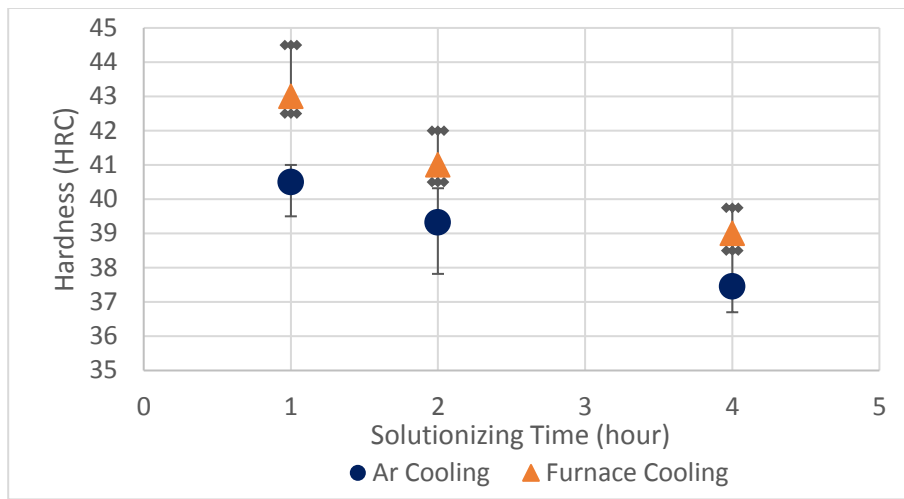


Figure 3.26: Hardness of samples after 1, 2 and 4 hours solutionizing time periods, at 1120°C and with Ar (180°C/min) or furnace (20°C/min) cooling rates.

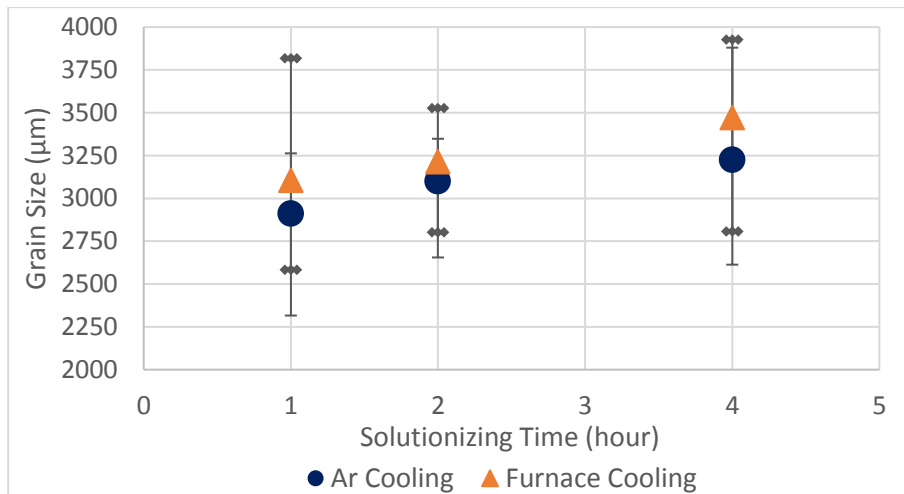


Figure 3.27: Grain sizes of samples after 1, 2 and 4 hours solutionizing time periods, at 1120°C and with Ar (180°C/min) or furnace (20°C/min) cooling rates.

Effect of Solutionizing Time

As it can be seen in Figure 3.25, precipitation and coalescence of primary γ' were not completed for solutionizings performed for 1 hour and γ' particles were coarsened when the solutionizing time was increased similar to Jeong-Min Kim et. al's studies [43].

The γ' size and volume fraction are given in Figure 3.25. Increasing solutionizing time slightly increased the γ' size and decreased the γ' volume fraction. This trend was also seen in Jeong Min Kim's studies with IN 738 LC [43]. Main decrease in γ' volume fraction was seen when the solutionizing time was increased from 1 to 2 hours rather than 2 to 4 hours.

Hardness and grain size of samples that were solutionized for different time periods and cooling rates are given in Figure 3.26 and 3.27. Increasing solutionizing time decreased γ' volume fraction and increased γ' sizes. Therefore, increasing solutionizing time decreased the measured hardness. The increase in solutionizing time resulted in increase in grain sizes as shown in Figure 3.27, since grain size is proportional to solutionizing time.

Similar trends were seen for samples against solutionizing time either they are furnace or Ar cooled. Effect of cooling rate after solutionizing to IN 738 LC was discussed in next section.

Effect of Solutionizing Cooling Rate

As it can be seen in Figure 3.25, Ar cooling achieved higher γ - γ' mismatch resulting in the cuboidal primary and spherical secondary γ' shapes while furnace cooling achieved irregularly shaped primary and secondary γ' particles. Only the furnace cooling used after 4 hours of solutionizing achieved relatively finer shaped primary γ' particles. This could be due to longer solutionizing time period resulted in increase of γ - γ' mismatch.

Effect of solutionizing time and cooling rate to γ' size and volume fraction are given in Figure 3.26 in previous section. Similar to Guzman et. al's findings, higher cooling rate achieved finely shaped smaller primary and secondary γ' particle sizes and lower total volume fraction of γ' [44]. In contrary, these findings were different in Behrouzghaemi et. al's findings that reports higher cooling rates achieved higher γ' size [41].

Hardness and grain size of samples that were solutionized for different time periods and cooling rates are given in Figure 3.26 and 3.27 in the previous section. Similar to Anurag Thakur's findings, furnace cooling achieved higher hardness values than Ar cooling. This is due to higher γ' volume fraction in microstructure of furnace cooled samples [20]. Grain sizes were found to be higher for furnace cooling samples due to longer time that furnace cooling provided during cooling.

3.4.3 Effect of Varying Solutionizing Parameters in Combine with Varying Aluminide Coating Temperature

The samples solutionized at various temperatures, times and cooling rates (Table 3.7 and Table 3.8) were all aluminide coated at 1000°C-20 hours, 1050°C-16 hours and 1100 °C-12 hours (furnace cooled (7°C/min) using chemical vapor deposition method. Aluminide coating is the third process applied to IN 738 LC as shown in Figure 3.28.

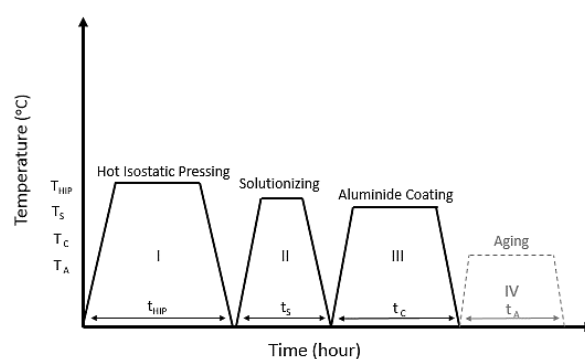


Figure 3.28: The scheme of heat treatments and coatings applied to IN 738 LC microstructure.

The response of the IN 738 LC microstructure to aluminide coating was greatly different depending on initial microstructure that was formed by solutionizing conditions. Therefore, the effect of aluminide coating to IN 738 LC microstructure was investigated separately for each different solutionizing sample group.

3.4.3.1 Effect of Varying Solutionizing Temperature in Combine with Varying Aluminide Coating Temperature

The post-coating microstructure is directly affected from the initial microstructure that was formed by solutionizing applied before aluminide coating operation. The samples solutionized at different temperatures (Table 3.7) were coated at three different conditions as given in Table 3.9.

Table 3.9: Parameters of Solutionizing and Coating at Varying Temperatures.

HIP Condition		Solutionizing Conditions		Aluminide Coating Conditions
Temperature (°C)	1200	Temperature (°C)	1080, 1100, 1120, 1150, 1180, 1200, 1235	1000 °C-20 hours 1050 °C-16 hours 1100 °C-12 hours (Furnace Cooling-7°C/min)
Time (h)	10	Time (h)	2	
Pressure (MPa)	150	Cooling Type and Rate (°C/min)	Ar Cooling-180	

The location of used samples on IN 738 LC rotor blade is shown in Figure 3.29.

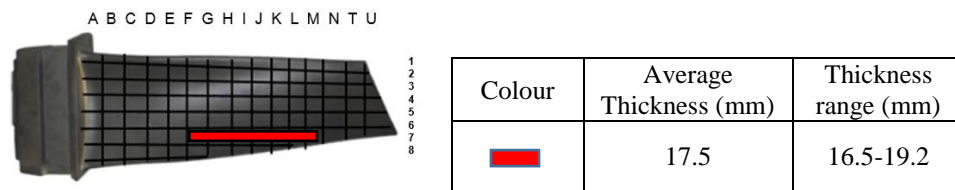


Figure 3.29: The location of samples that were solutionized in between 1080-1235°C for 2 hours and aluminide coated.

The post-solutionizing and post-coating SEM images of IN 738 LC samples that were solutionized and coated at different temperatures are given in Figure 3.30.

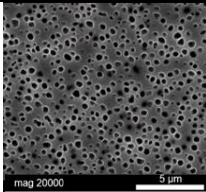
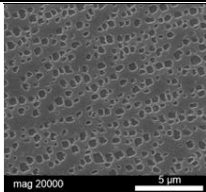
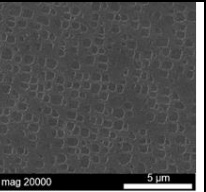
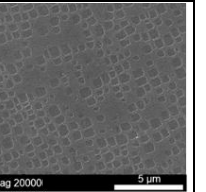
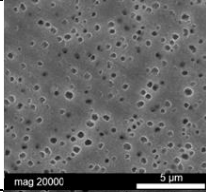
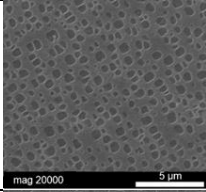
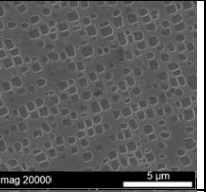
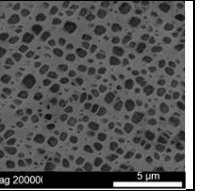
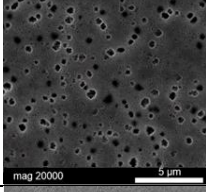
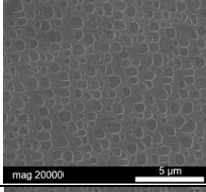
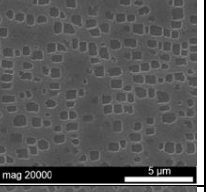
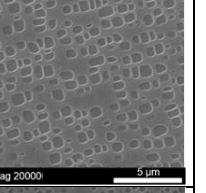
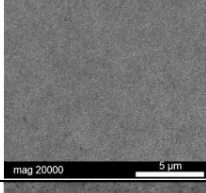
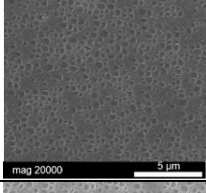
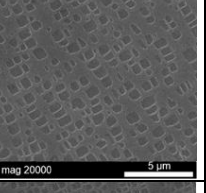
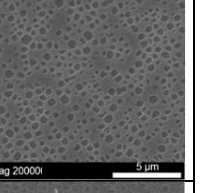
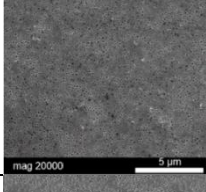
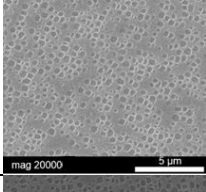
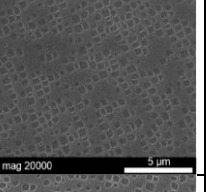
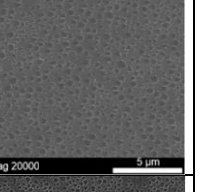
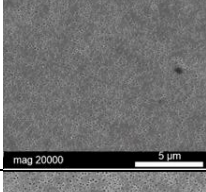
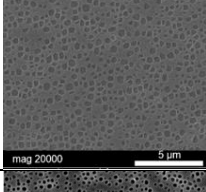
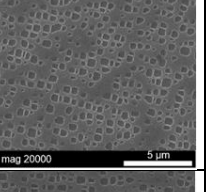
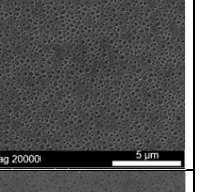
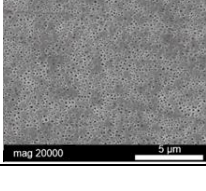
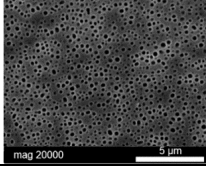
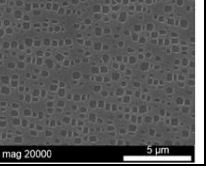
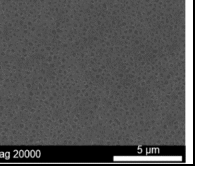
	Before Coating (Post-Solutionizing) SEM Images	Coating Conditions and Post-Coating SEM Images		
		1000°C-20 hours- F.C. (7°C/min)	1050°C-16 hours- F.C. (7°C/min)	1100°C-12 hours- F.C. (7°C/min)
1080°C				
1100°C				
1120°C				
1150°C				
1180°C				
1200°C				
1235°C				

Figure 3.30: Post-solutionizing and post-coating SEM images of samples that were solutionized at various temperatures between 1080°C-1235°C for 2 hours (Ar cooled-180°C/min).

As it is shown in Figure 3.30, the samples solutionized at 1080, 1100 and 1120°C, showed bimodal microstructure after all coating operations.

The sample solutionized at 1150°C and coated at 1050°C-16 hours also showed bimodal structure. However, the other samples that were solutionized at 1150, 1180, 1200 and 1235°C showed unimodal microstructure after all coating operations. Post-coating bimodal microstructures showed cuboidal primary and spherical secondary γ' profile while post-coating unimodal microstructures showed both cuboidal and spherical γ' particles.

Post-coating primary and secondary γ' sizes are given in Figure 3.31 and volume fractions are given Figure 3.32.

Increasing solutionizing temperature between 1080-1120°C, increased primary and secondary γ' size in post-coating microstructures. However, above 1120°C, increasing solutionizing temperature decreased post-coating primary γ' particle sizes due to bimodal to unimodal structure transformation.

Highest primary γ' size was achieved after coating applied at 1100°C-12 hours for the samples that were solutionized below 1150°C (bimodal region) while at 1150°C and above solutionizing temperatures (unimodal region), highest γ' was achieved after coating at 1050°C-16 hours. Based on these results, it was obtained that bimodal microstructures increase their size greatly after coating applied at 1100°C-12 hours while unimodal structures increase it only slightly. This could be due to different behavior of coarsening mechanism for γ' particles with different sizes and structures at temperatures close to solutionizing.

In post-coating microstructures of the samples solutionized above 1120°C, only secondary γ' particle is achieved at 1150°C solutionizing followed by 1050°C-16 hours coating. This could be due to high primary γ' size achieved in this sample that allows the secondary γ' determination that was precipitated at lower sizes.

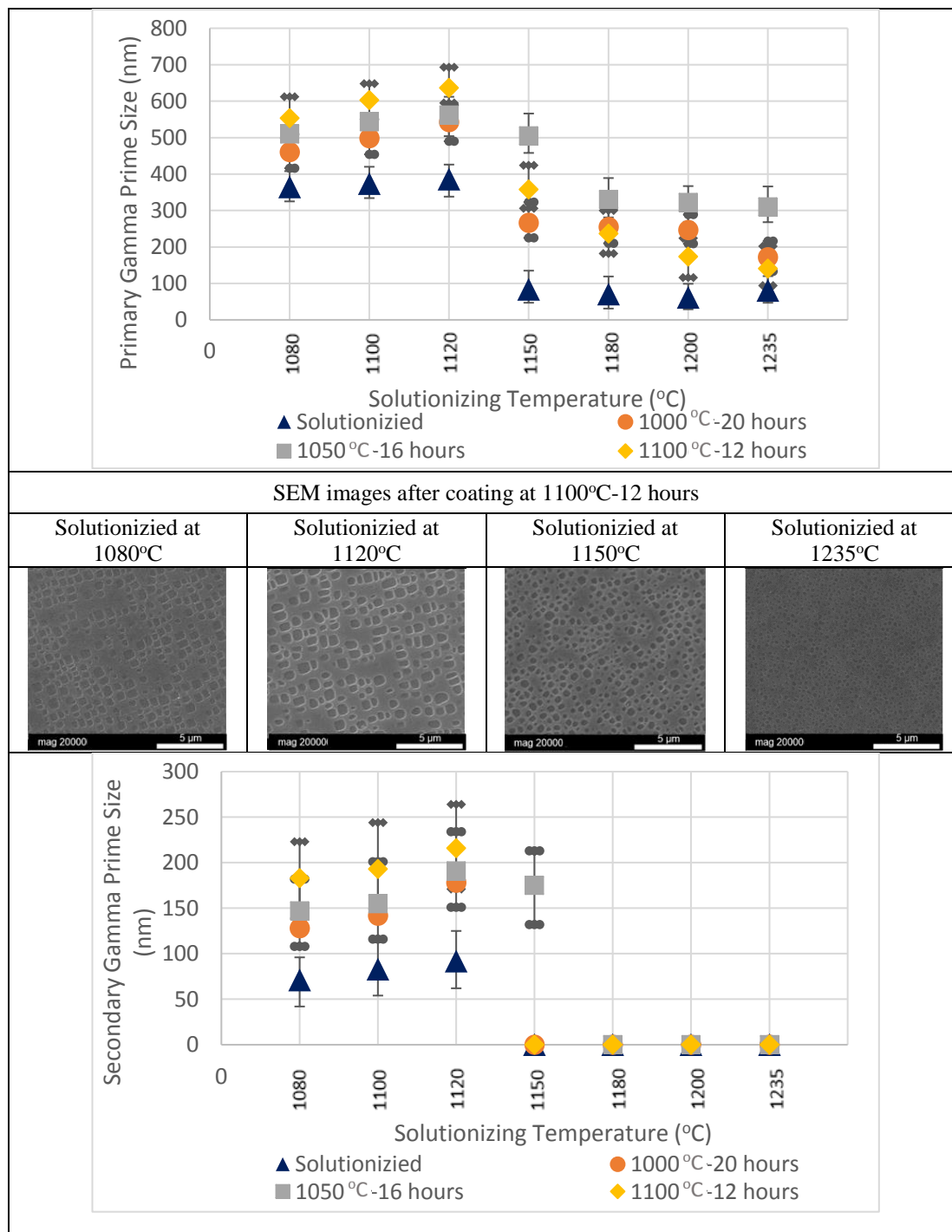


Figure 3.31: Post-solutionizing and post-coating primary and secondary γ' sizes with some representative SEM images.

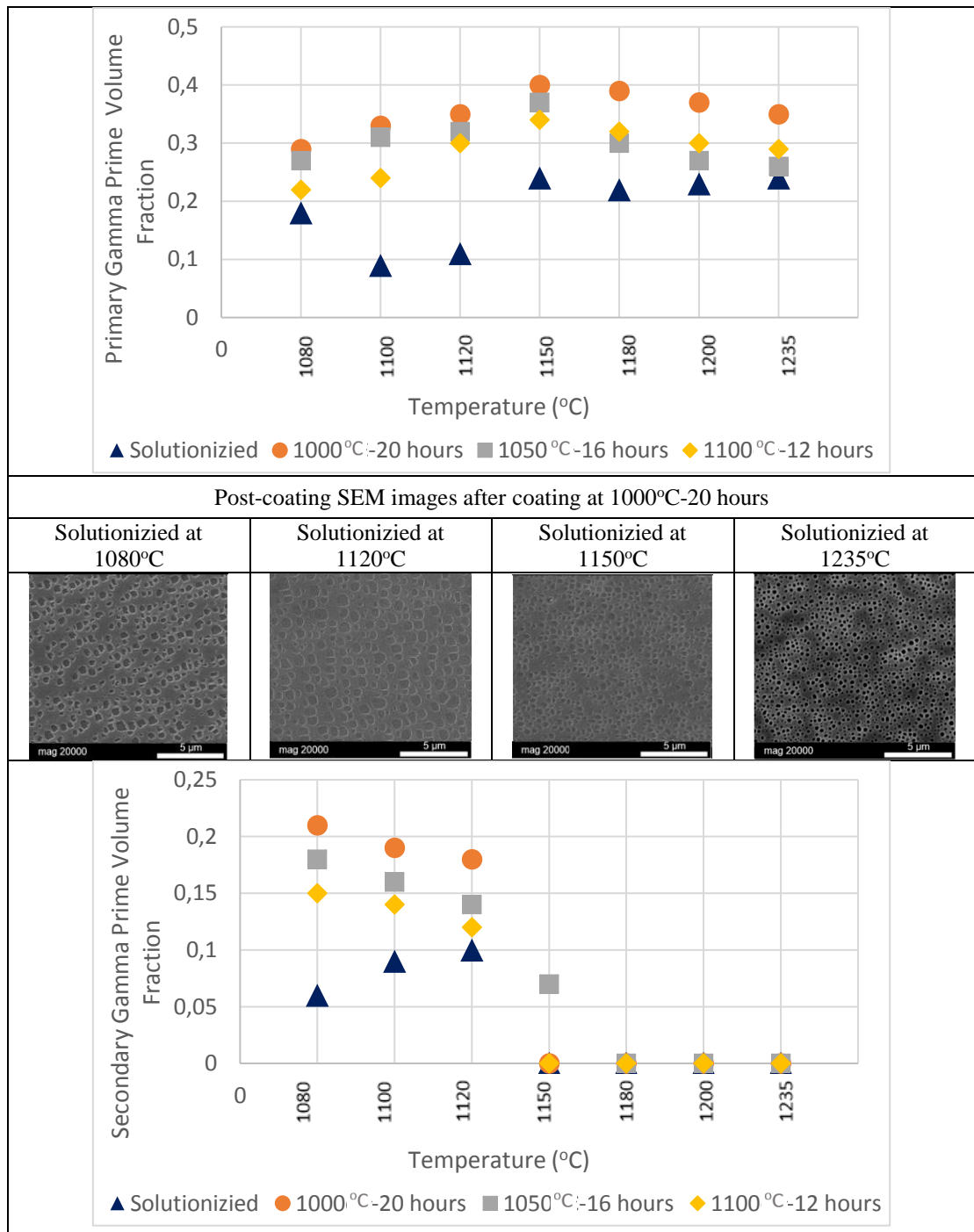


Figure 3.32: Post-solutionizing and post-coating primary and secondary γ' volume fractions with some representative SEM images.

As shown in Figure 3.32, highest primary and secondary γ' volume fraction was achieved after coating at 1000°C-20 hours, followed by 1050°C-16 hours and 1100°C-12 hours respectively for the samples that were solutionized below 1150°C (in the bimodal region).

Above 1150°C solutionizing temperature (in unimodal region), highest primary γ' volume fraction was achieved after coating at 1000°C-20 hours followed by 1100°C-12 hours and 1050°C-16 hours respectively. This is due to higher γ' size and higher area of PFZ (particle free zone) achieved after the coating performed at 1050°C-16 hours in the unimodal region.

Primary post-coating γ' volume fraction was slightly higher for samples solutionized above 1150°C than below this temperature. In bimodal region (solutionized below 1150°C), total γ' volume fraction was derived from both primary and secondary γ' particles. However, in unimodal region (solutionized above 1150°C), total γ' was derived from only primary γ' particles. Since there were no secondary γ' particles in this region, primary γ' volume fraction found to be higher.

The post-coating samples solutionized below 1150°C showed higher total γ' volume fraction due to existence and volume fraction contribution of secondary γ' particles below this temperature.

Post-coating hardness measurement results of samples that were solutionized at different temperatures are given in Figure 3.33.

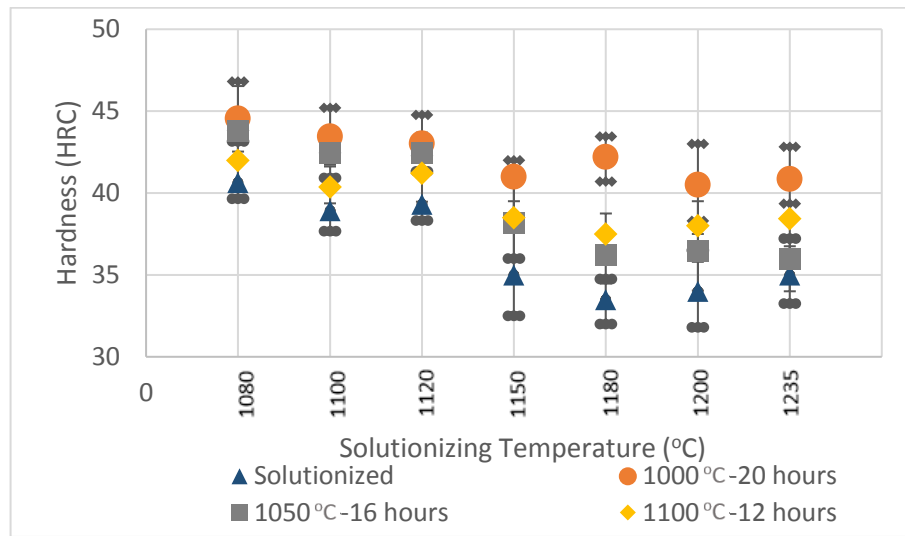


Figure 3.33: Post-solutionizing and post-coating grain size of samples that were solutionized at various temperatures between 1080°C-1235°C.

Post-coating microstructures showed higher hardness than post-solutionizing due to increased γ' volume fraction after aluminide coating. Highest hardness was achieved after the coating at 1000°C-20 hours, followed by 1050°C-16 hours and 1100°C-12 hours respectively for the samples solutionized below 1150°C (bimodal region), due to decreasing γ' volume fraction in the same order.

The highest post-coating hardness of samples achieved after aluminate coating applied at 1000°C-20 hours, followed by 1100°C-12 hours and 1050°C-16 hours for the samples solutionized above 1150°C (unimodal region).

1100°C-12 hours post-coating sample showed most similar microstructure to post-solutionizing. However, it had slightly higher γ' volume fraction. Therefore, the post-coating hardness of this coating parameter measured to be slightly higher than post-solutionizing.

The post-coating microstructure of 1050°C-16 hours condition showed higher γ' size and lower γ' volume fraction than 1100°C-12 hours coating that caused even lower hardness values to be measured for 1050°C-16 hours post-coating microstructure.

Post-coating grain size of samples that are solutionized at different temperatures are given in Figure 3.34.

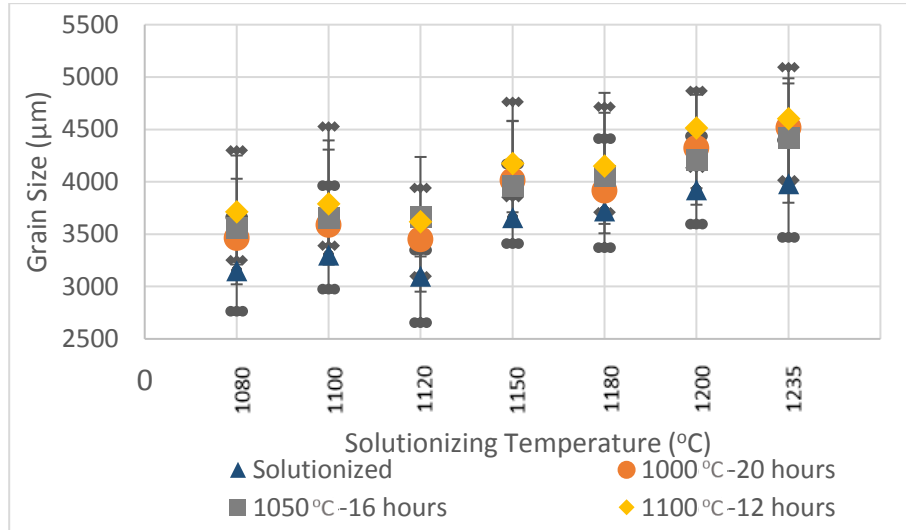


Figure 3.34: Post-solutionizing and post-coating hardness of samples that were solutionized at various temperatures between 1080°C-1235°C.

The grain size of post-coating samples solutionized below 1120°C found to be lower than the samples solutionized above this temperature. The main increase in post-coating grain size was achieved above 1120°C solutionizing temperature due to the disappearance of primary γ' particles. Primary γ' is known to pin the grain boundaries and disappearance of this particle known to cause rapid grain growth. This effect was mentioned in Koul and Castillo's and Anurag Thakur's studies. [20, 38]

Highest post-coating grain size was obtained after the coating operation applied at 1100°C-12 hours, followed by 1050°C-16 hours and 1000°C-20 hours respectively. However, there are few exceptions as shown in Figure 3.34. Since high temperature was balanced by low time period of aluminide coating process, the grain sizes were measured to be quite close the each other.

3.4.3.2 Effect Varying Solutionizing Time and Cooling Rate in Combine with Varying Aluminide Coating Temperature

The post-coating microstructure is directly affected from the initial microstructure that is formed by solutionizing applied before coating operation. The samples solutionized for varying time periods and with different cooling rates (Table 3.8) were coated at three different conditions as given in Table 3.10.

Table 3.10: Parameters of solutionizing for varying time periods and cooling rates, and coating at varying temperatures.

HIP Condition		Solutionizing Conditions		Aluminide Coating Conditions
Temperature (°C)	1200	Temperature (°C)	1120	1000 °C-20 hours 1050 °C-16 hours 1100 °C-12 hours (Furnace Cooling-7°C/min)
Time (h)	10	Time (h)	1, 2, 4	
Pressure (MPa)	150	Cooling Type and Rate (°C/min)	Ar Cooling-180 Furnace Cooling-20	

The location of used samples on IN 738 LC rotor blade is shown in Figure 3.35.

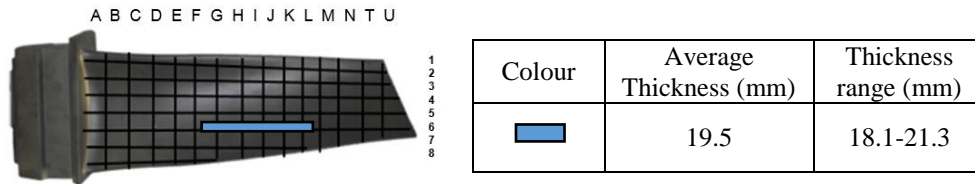


Figure 3.35: The locations of samples that were solutionized at 1120°C for 1, 2 and 4 hours, and aluminide coated.

The post-solutionizing and post-coating SEM images of these samples are shown in Figure 3.36. The samples solutionized at 1120°C for 1, 2 and 4 hours followed by Ar (180°C/min) and furnace (20°C/min) cooling showed bimodal γ' microstructure in their post-coating condition similar to their post-solutionizing microstructures. The effect of solutionizing cooling rate and time period to post-coating was investigated under different subtitles at the end of characterization results.

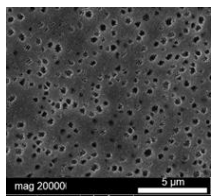
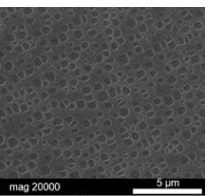
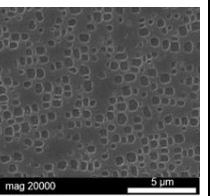
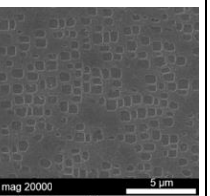
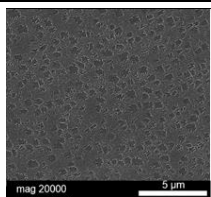
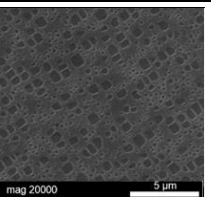
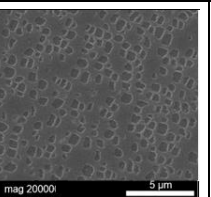
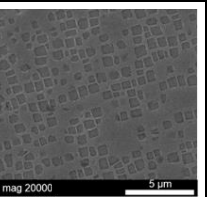
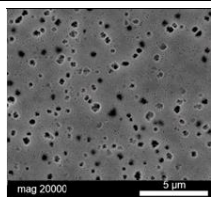
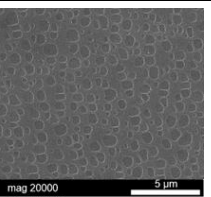
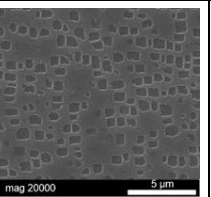
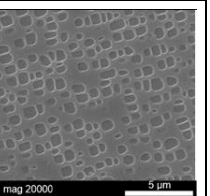
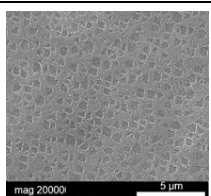
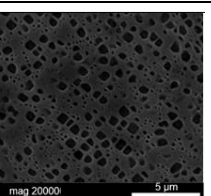
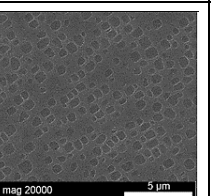
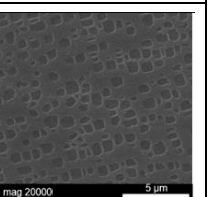
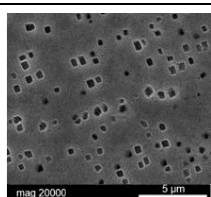
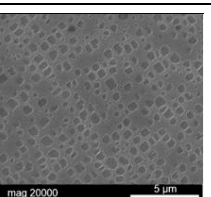
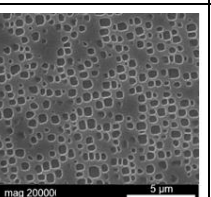
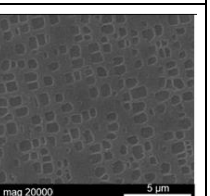
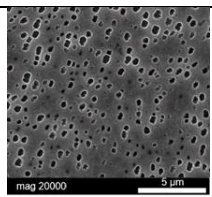
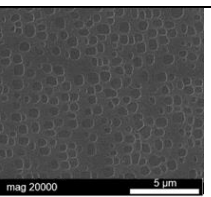
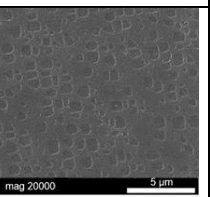
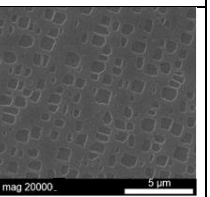
		Before Coating (Post-Solutionizing) SEM Images	Coating Conditions and Post-Coating SEM Images		
			1000°C-20 hours-F.C. (7°C/min)	1050°C-16 hours-F.C. (7°C/min)	1100°C-12 hours-F.C. (7°C/min)
1 hour	Ar C. (180°C/min)				
	F.C. (20°C/min)				
2 hours	Ar C. (180°C/min)				
	F.C. (20°C/min)				
4 hours	Ar C. (180°C/min)				
	F.C. (20°C/min)				

Figure 3.36: Post-coating and post-solutionizing SEM images of samples that were solutionized for 1, 2 and 4 hours, Ar or furnace cooled.

Post-solutionizing and post-coating primary and secondary γ' size, and volume fractions of these samples are given in Figure 3.37 and 3.38 respectively.

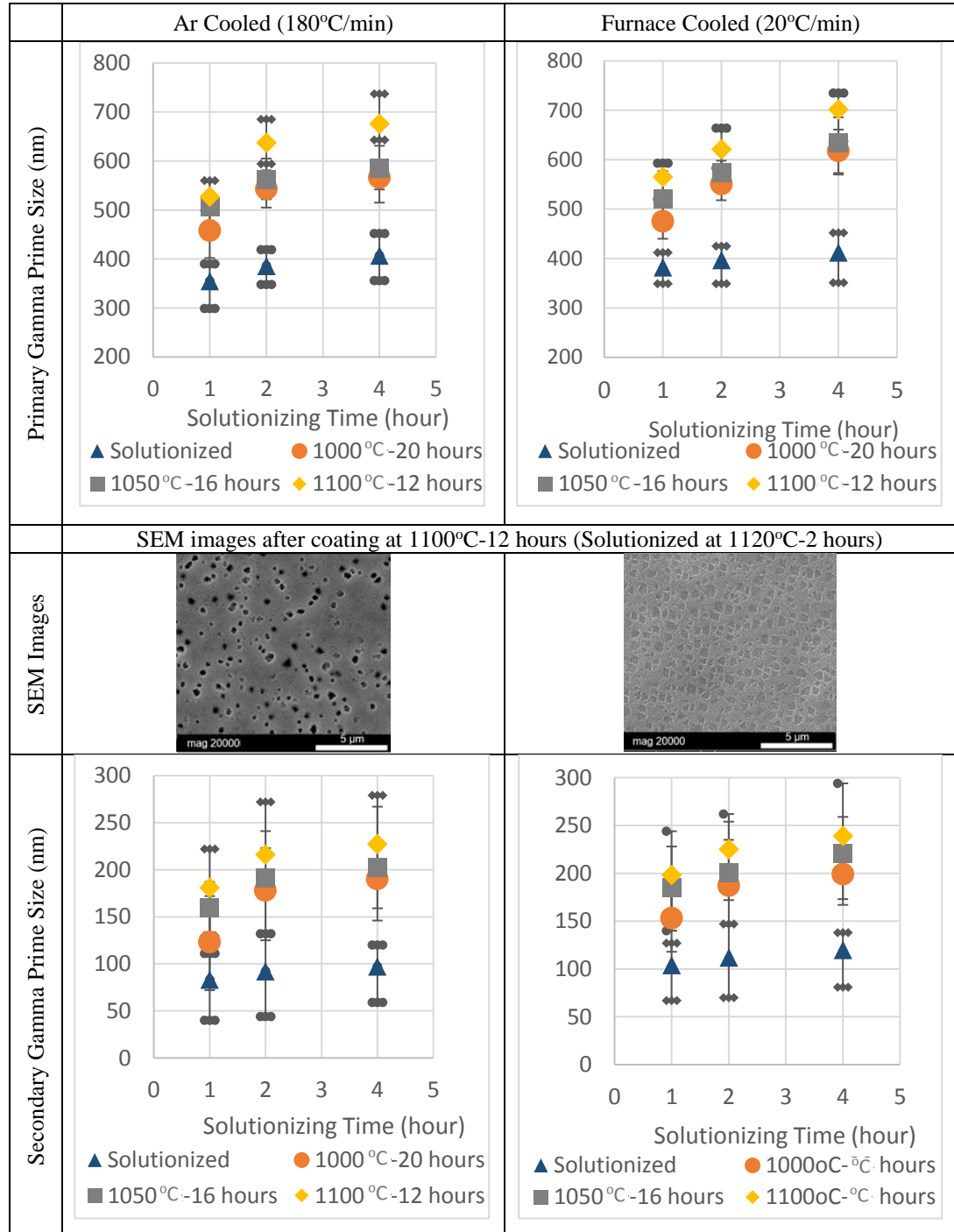


Figure 3.37: Post-solutionizing and post-coating primary and secondary γ' size of samples that were solutionized at 1120°C for 2 hours, Ar (180°C/min) or furnace cooled (20°C/min), and aluminide coated at 1000, 1050 and 1100°C temperatures.

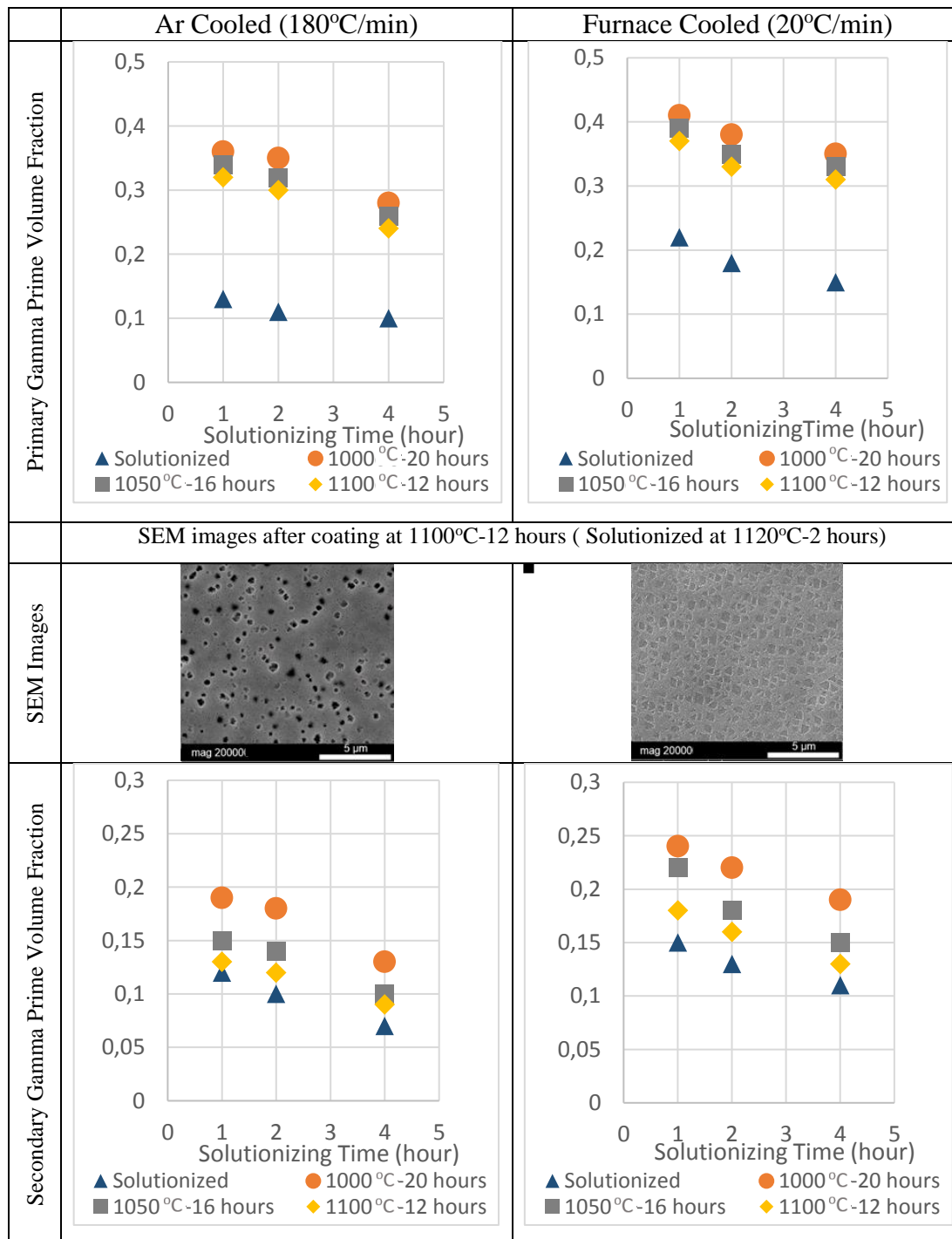


Figure 3.38: Post-solutionizing and post-coating primary and secondary γ' volume fraction of samples that were solutionized at 1120°C for 2 hours, Ar (180°C/min) or furnace cooled (20°C/min), and aluminide coated at 1000, 1050 and 1100°C.

Post-solutionizing and post-coating hardness and grain size γ' size of these samples are given in Figure 3.39 and 3.40 respectively.

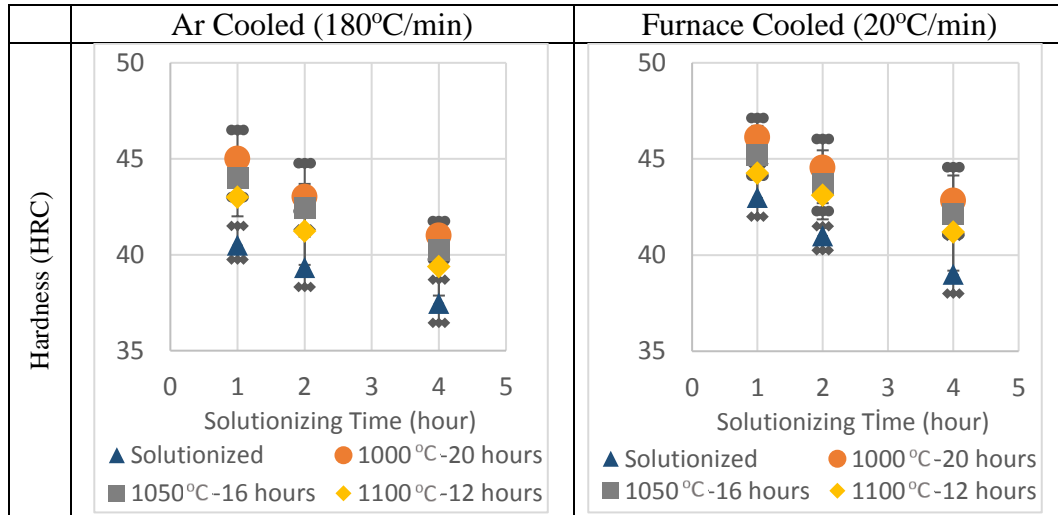


Figure 3.39: Post-solutionizing and post-coating hardness of samples that were solutionized at 1120°C for 2 hours, Ar (180°C/min) or furnace cooled (20°C/min), and aluminide coated at 1000, 1050 and 1100°C.

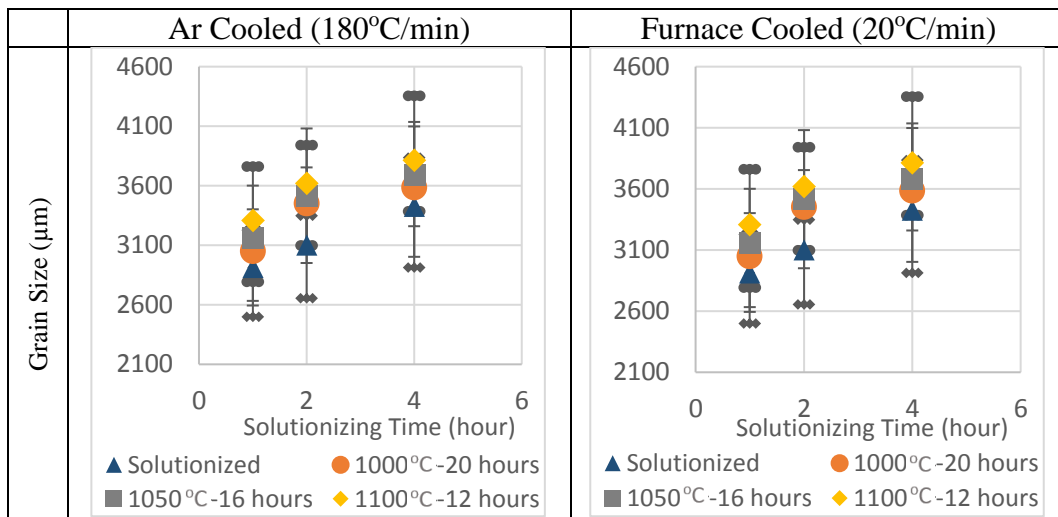


Figure 3.40: Post-solutionizing and post-coating primary and secondary grain size of samples that were solutionized at 1120°C for 2 hours, Ar (180°C/min) or furnace cooled (20°C/min), and aluminide coated at 1000, 1050 and 1100°C.

Effect of Solutionizing Time

The increase in solutionizing time period resulted in increased primary and secondary γ' sizes in post-solutionizing and accordingly post-coating microstructures (Figure 3.37). This is due to longer coarsening time provided for γ' particles.

Increasing solutionizing time decreased primary and secondary γ' volume fraction in post-solutionizing and accordingly post-coating microstructures. The increase in solutionizing time also increased the amount of γ' particles dissolved in the matrix. Therefore, PFZ area was increased and γ' volume fraction was decreased at longer solutionizing times (Figure 3.38).

Increasing solutionizing time in both Ar and furnace cooled samples decreased post-solutionizing and post-coating hardness due to decreasing γ' volume fraction and increasing γ' size in their microstructure.

Hence, the grain size is proportional to heat treatment time period, increase in solutionizing time resulted in increase of grain sizes.

Effect of Cooling Rate

The samples Ar cooled after solutionizing had lower γ' size and volume fraction than furnace cooled samples in their post-solutionizing and post-coating microstructures (Figure 3.37 and 3.38). Furnace cooling allowed longer period of time for precipitation and growth (coarsening) compared to Ar cooling. Therefore, γ' volume fraction was found to be higher for furnace cooled samples after solutionizing and accordingly coating.

Samples that were furnace cooled after solutionizing showed higher hardness than Ar cooled samples in their post-solutionizing and post-coating microstructures. This was expected due to higher γ' volume fraction of furnace cooled samples compared to Ar cooled samples.

Furnace cooled samples achieved slightly higher grain size since it allows a longer period of time to increase in grain size during cooling.

Effect of Coating Temperature

Highest primary and secondary γ' size was achieved after coating applied at 1100°C-12 hours, followed by 1050°C-16 hours and 1000°C-20 hours. Highest primary and secondary γ' volume fraction was achieved after coating applied at 1000°C-20 hours, followed by 1050°C-16 hours and 1100°C-12 hours. Increase in coating temperature resulted in increase of γ' coarsening and decrease of γ' precipitation.

Highest post-coating hardness was obtained after coating performed at 1000°C-20 hours, followed by 1050°C-16 hours and 1100°C-12 hours respectively. This was expected since increasing coating temperature increased γ' size and decreased γ' volume fraction.

Highest post-coating grain size was found after coating performed at 1100°C-12 hours, followed by 1050°C-16 hours and 1000°C-20 hours. However, results were pretty close to each other since higher coating temperature was balanced with shorter time period.

3.4.4 Effect of HIP, Solutionizing, Varying Aluminide Coating Temperatures and Aging to Thick and Thin Samples

In this section, the purpose was to investigate the respond of thick and thin samples' microstructure against heat treatments and aluminide coatings. Additionally, effect of aging was studied on coated and uncoated samples. Aging is the fourth and last process applied to IN 738 LC samples as shown in Figure 3.41.

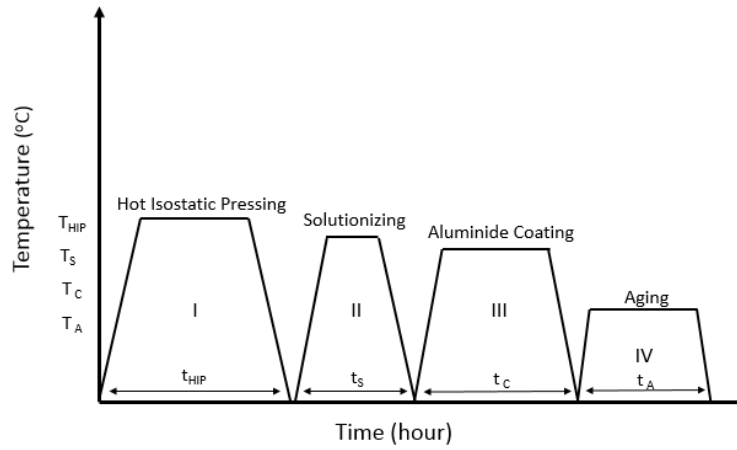


Figure 3.41: The scheme of heat treatments and coatings applied to IN 738 LC microstructure.

IN 738 LC samples that were taken from thick middle section (in range of 17.7-18.5 mm, average 18.25 mm) and thin leading edge of the turbine blade (in range of 8.2-9.1 mm, average 8.5 mm) were HIPed, solutionized coated and aged at given conditions in Table 3.11.

Table 3.11: Heat Treatment and Coating Parameters for Thick and Thin Samples

HIP Condition		Solutionizing Conditions		Aluminide Coating Conditions	Aging Condition
Temperature (°C)	1200	Temperature (°C)	1120	1000 °C-20 hours 1050 °C-16 hours 1100 °C-12 hours (Furnace Cooling-7°C/min)	845 °C-24 hours
Time (h)	10	Time (h)	2		
Pressure (MPa)	150	Cooling Type and Rate (°C/min)	Ar Cooling-180		

One thick and one thin sample were left uncoated and directly aged to investigate the effect of aging on uncoated IN 738 LC samples.

The locations of samples used in this experiment group is shown in Figure 3.42.

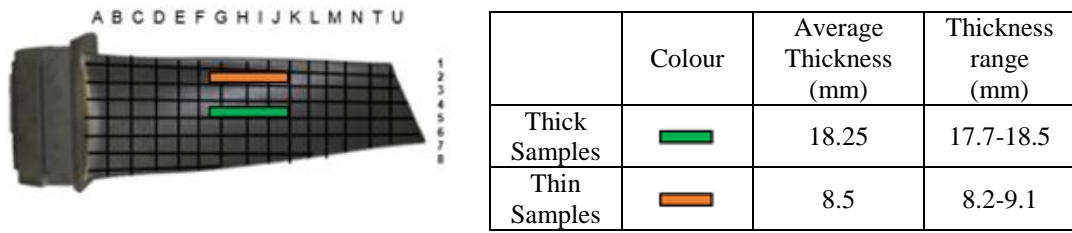


Figure 3.42: The locations of as cast, HIPed, solutionized, coated and aged thick and thin samples.

The effect of HIP, solutionizing and aging was investigated as first at the given parameters in Table 3.12. No coating was applied to these samples.

Table 3.12: The HIP, solutionizing and aging parameters applied to thick and thin samples.

HIP Condition		Solutionizing Conditions		Aluminide Coating Conditions	Aging Conditions
Temperature (°C)	1200	Temperature (°C)	1120	No Coating	845 °C-24 hours
Time (h)	10	Time (h)	2		
Pressure (MPa)	150	Cooling Type and Rate (°C/min)	Ar Cooling-180		

The SEM images of as cast, HIPed, solutionized, coated and aged thin and thick samples are given in Figure 3.43 and Figure 3.44.

As shown in Figure 3.43 and 3.44, bimodal microstructures were achieved in cast, post-solutionizing, post-coating and post-aging microstructures of both thick and thin samples. However, in the post-HIP microstructure, smaller sized secondary γ' were dissolved into the matrix and accordingly unimodal structure was obtained for both thick and thin samples.

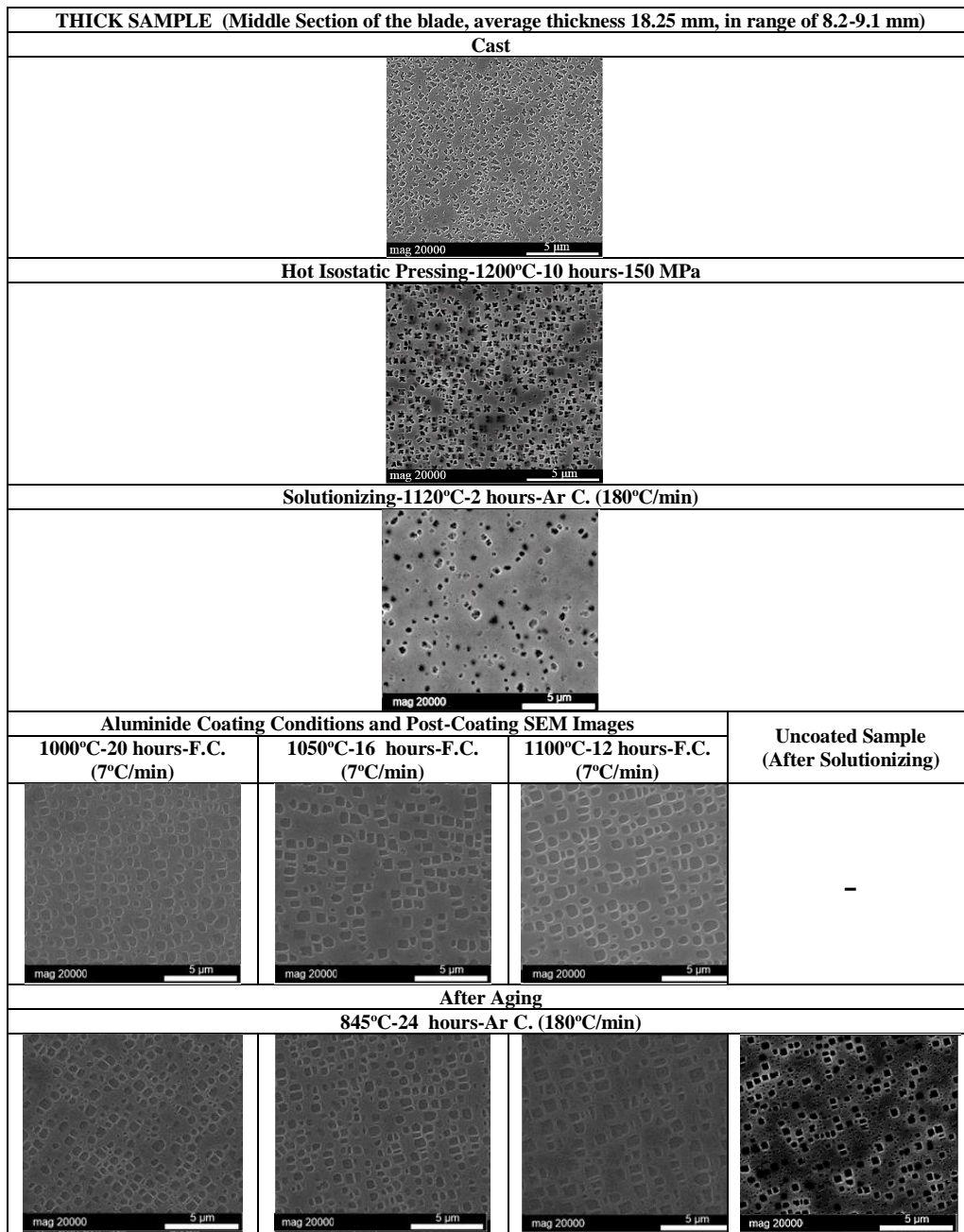


Figure 3.43: SEM images of thick IN 738 LC sample after HIP, solutionizing, coating and aging.

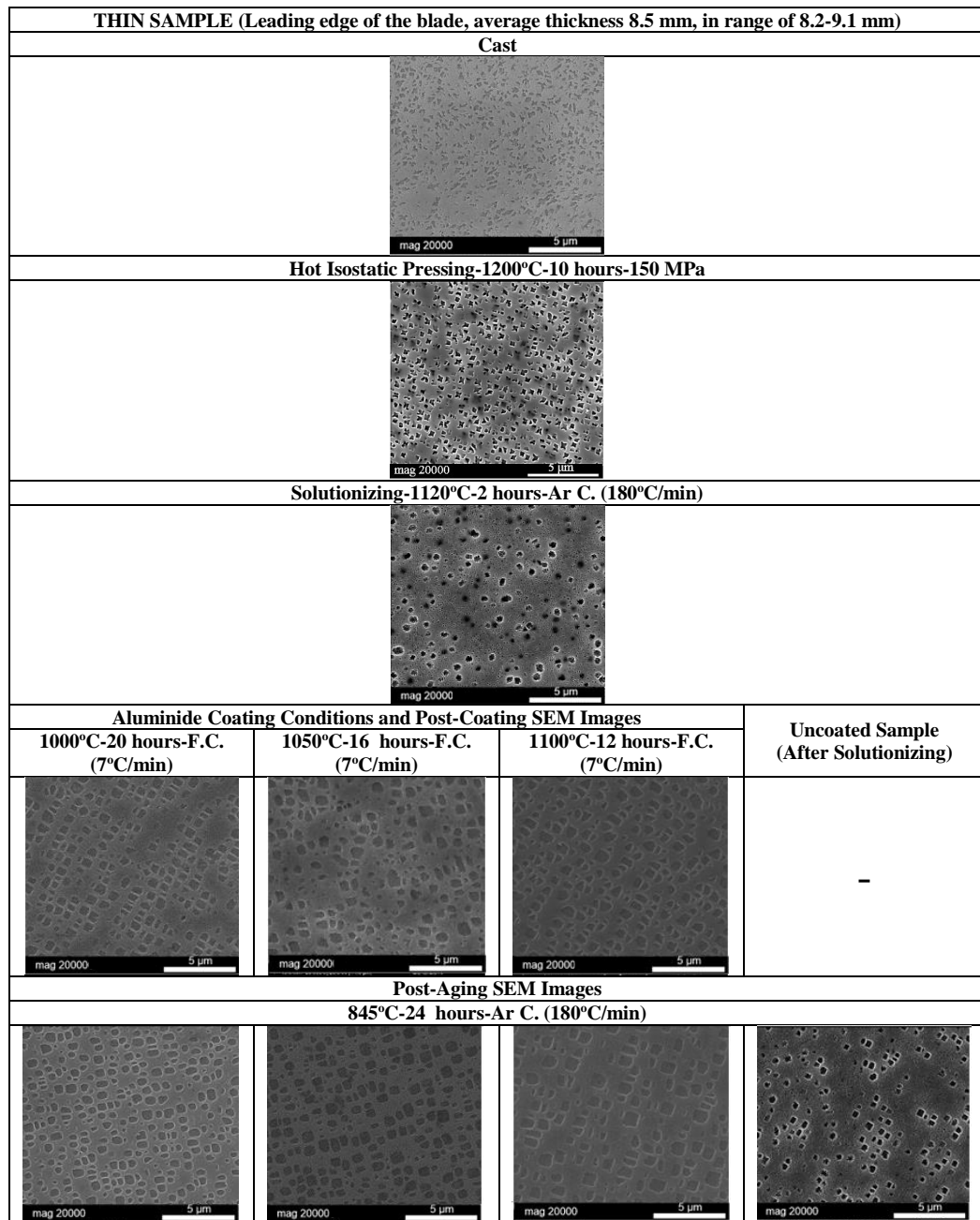


Figure 3.44: SEM images of thin IN 738 LC sample after HIP, solutionizing, coating and aging.

The as cast, solutionized, HIPed and aged samples γ' size and volume fraction are given in Figure 3.45.

HIP increased primary γ' size and volume fraction and dissolved secondary γ' particles in the matrix. The disappearance of secondary γ' particles is detrimental for material's strength. Solutionizing allowed the secondary γ' precipitation again while decreasing the primary γ' volume fraction sharply due to the dissolution of these particles.

Aging increased the both primary and secondary γ' sizes and volume fractions. After aging primary and secondary particles achieved similar volume fractions. Cuboidal primary and spheroidal secondary particles were formed in post-aging microstructure of both thick and thin samples.

The thick sample had slightly higher primary and secondary γ' size and volume fraction than thin sample due to slower cooling of thick sample after casting. Naturally, slower cooling for the thick sample was also seen after HIP, solutionizing, coating and aging. Due to these reasons, thick sample showed slightly higher primary and secondary γ' size and volume fraction than the thin sample.

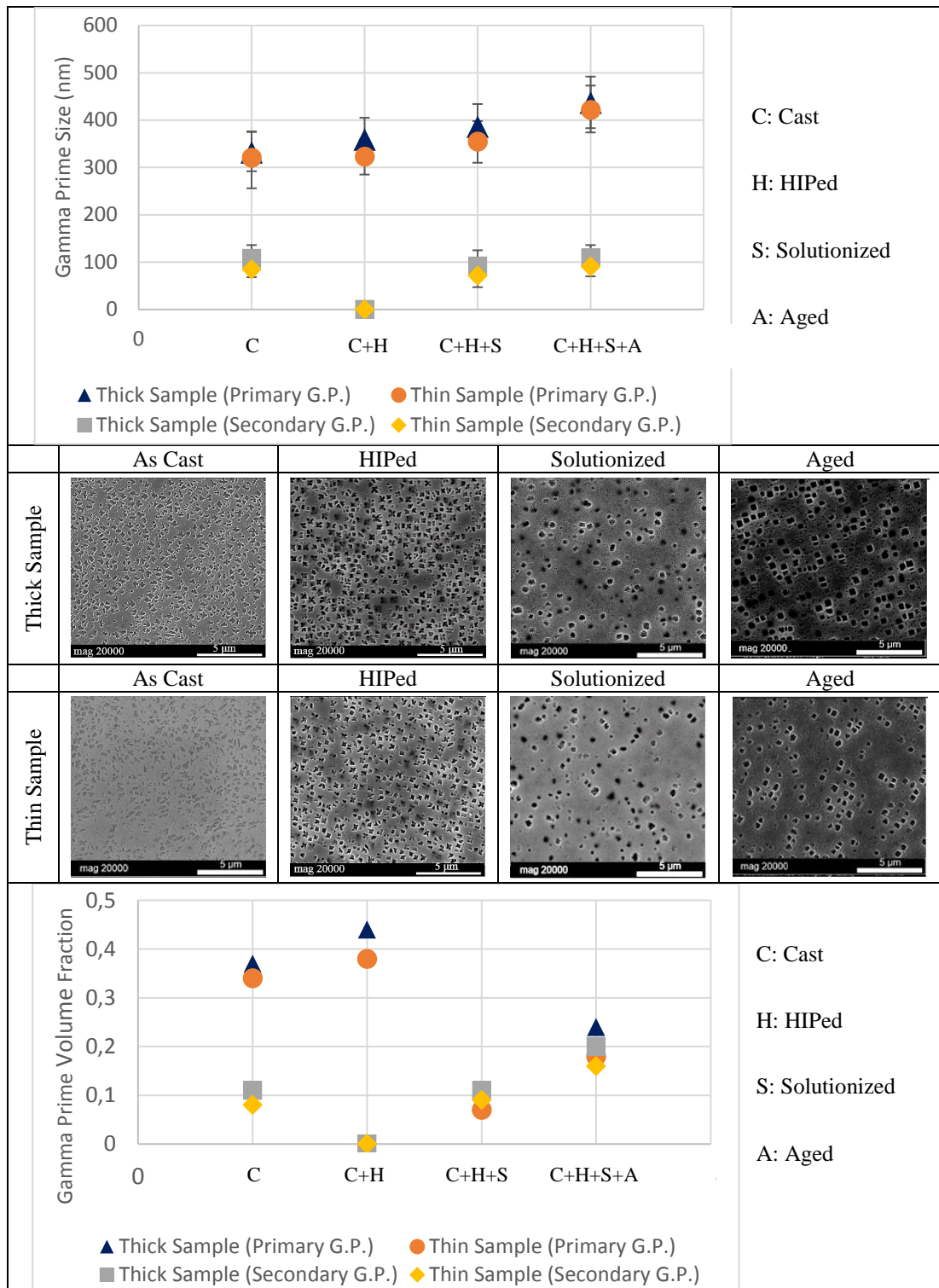


Figure 3.45: γ' size and volume fraction of as cast, HIPed and solutionized thick and thin samples with SEM images.

The hardness measurement results for as cast, HIPed, solutionized and aged thick and thin IN 738 LC samples are given in Figure 3.46.

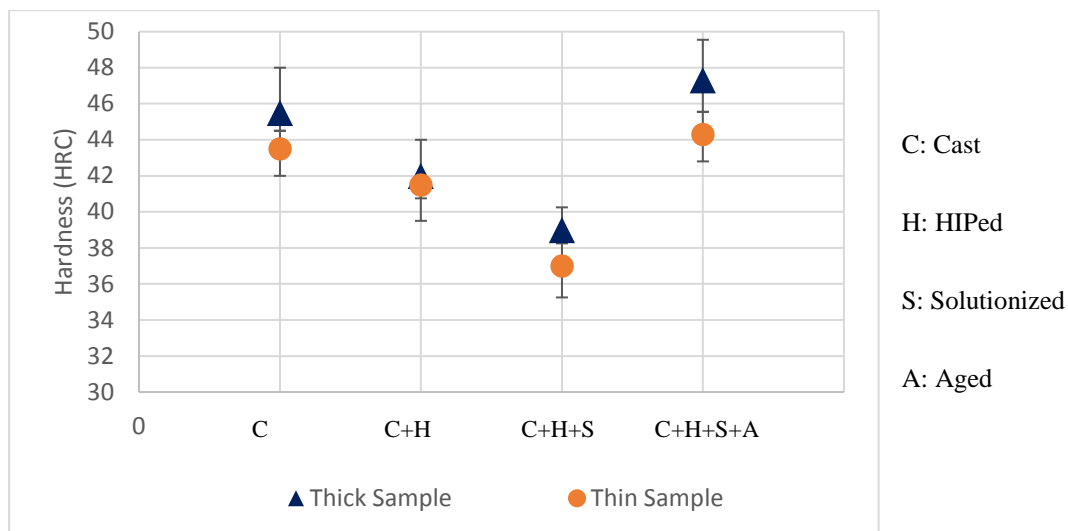


Figure 3.46: Hardness of the of the as cast, HIPed, solutionized and aged thick and thin samples.

HIP decreased the hardness due to the dissolution of secondary γ' particles to the matrix. Solutionizing decreased the hardness further due to partially dissolved primary γ' particles that decreased the volume fraction of primary γ' . After aging the samples achieved their higher hardness values due to highest γ' volume fraction obtained after this process.

The hardness of thick sample that was taken from middle section of the blade showed slightly higher hardness than the thin sample that was taken from leading edge of the turbine blade. This was expected due to higher γ' volume fraction that was provided by the slower cooling rate of the thick sample. This trend was also seen after casting, HIP, solutionizing and aging.

The grain size measurement results for as cast, HIPed and solutionized both thick and thin IN 738 LC samples are given in Figure 3.47.

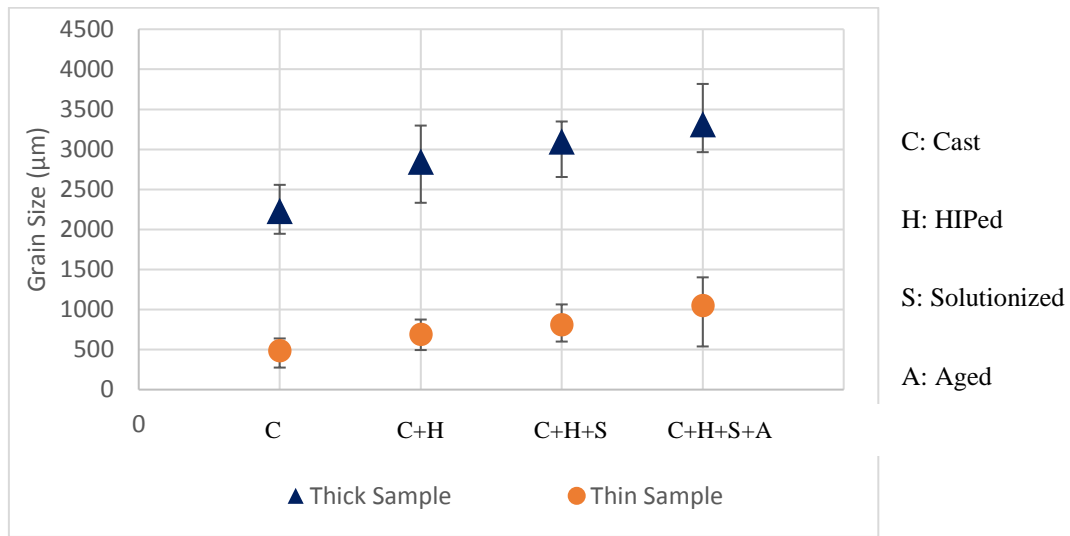


Figure 3.47: Grain size of the of the cast, HIPed, solutionized and aged thick and thin samples.

Grain size was increased after HIP, solutionizing compared to cast microstructure. However, the grain size increase during HIP (1200°C-10 hours) was slightly higher since it was performed at a higher temperature and longer period than solutionizing (1120°C-2 hours). Moreover, since γ' was totally dissolved at HIP temperature and partially dissolved in solutionizing temperature, primary γ' particles kept their existence during partial solutionizing. Due to this reason pinning effect of primary γ' particles against grain boundary movements blocked the rapid grain growth that was mentioned in studies of Koul and Castiio and Anurag Thakur's studies [20, 38]. Aging only slightly increased grain size. This could be due to lower temperature of aging (845°C-24 hours).

The grain size of the thick sample obtained to be almost 3 times higher than thin sample due to inhomogeneous cooling mainly occurred after casting of the turbine blade. This trend also continued for post-HIP, post-solutionizing and post-aging microstructures. The grain size of thin samples measured to be below 1000 μm while grain size of the thick sample measured to be above 2000 μm for as cast, solutionized, coated and aged samples.

The effect of HIP, solutionizing and aging was investigated in previous pages to uncoated samples. To investigate effect of aging to coated thick and thin samples, the experiment parameters given in Table 3.13 were used.

Table 3.13: The Parameters Used to Investigate Effect of Aging on Coated Thick and Thin Samples

HIP Condition		Solutionizing Conditions		Aluminide Coating Conditions	Aging Conditions
Temperature (°C)	1200	Temperature (°C)	1120	1000 °C-20 hours 1050 °C-16 hours 1100 °C-12 hours (Furnace Cooling-7°C/min)	845 °C-24 hours
Time (h)	10	Time (h)	2		
Pressure (MPa)	150	Cooling Type and Rate (°C/min)	Ar Cooling-180		

Post-coating and post-aging γ' size and volume fraction measurement results are given in Figure 3.48.

Highest post-coating γ' volume fraction was achieved at 1000°C-20 hours that was followed by 1050°C-16 hours and 1100°C-12 hours for both thick and thin samples. Highest post-coating γ' size was achieved at 1100°C-12 hours that was followed by 1050°C-16 hours and 1000°C-20 hours for both thick and thin samples. A similar trend was seen in the post-aging microstructure of samples.

Aging has not affected the post-coating microstructure of samples dramatically since coating operations performed for more than 10 hours at temperatures above 950°C acted as aging or primary high temperature aging. Only a slight increase was obtained in both γ' size and volume fraction after aging. γ' size and volume fraction showed similar trends for both thick and thin samples in post-coating and post-aging microstructures. However, they were found to be slightly higher for the thick sample than thin sample due to slower cooling of thick sample mainly after casting, following heat treatments and coating.

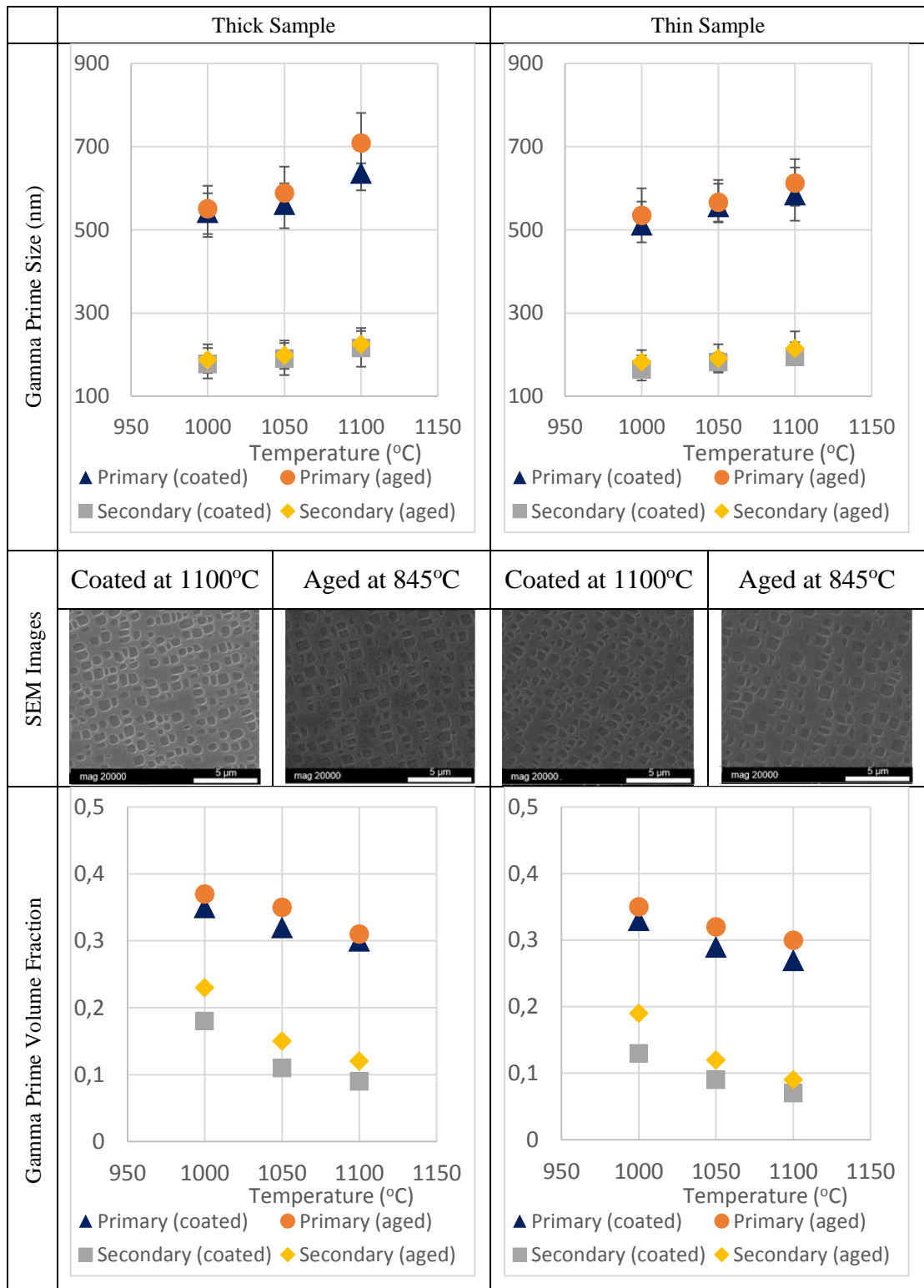


Figure 3.48: Primary and secondary γ' size and volume fraction of post-coating and post-aging thick and thin samples.

The hardness measurement results are given for post-coating and post-aging microstructures of thick and thin samples in Figure 3.49.

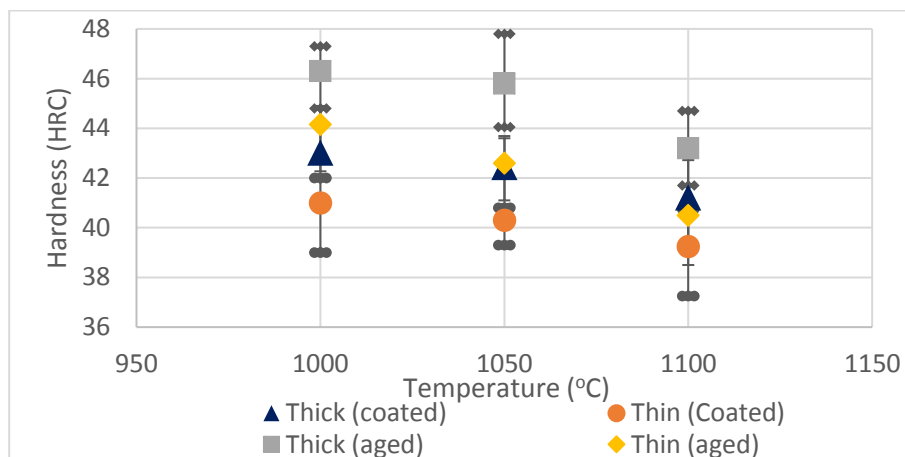


Figure 3.49: Hardness of post-coating and post-aging thick and thin samples.

The increase in coating temperature resulted in a decrease of measured hardness. This was expected since increasing coating temperature decreased γ' volume fraction and sizes. The thin sample showed slightly lower hardness than thick sample due to its lower γ' volume fraction. Both samples hardness was slightly increased after aging due to a minor increase in γ' volume fraction.

The grain size measurement results are given for post-coating and post-aging microstructures of thick and thin samples in Figure 3.50.

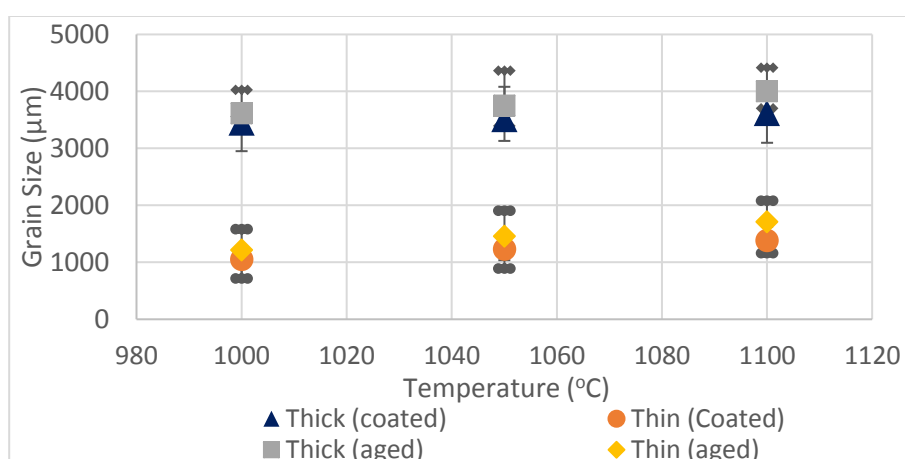


Figure 3.50: Grain size of post-coating and post-aging thick and thin samples.

The increase in coating temperature resulted in higher grain sizes. However, grain size was measured to pretty similar since higher coating temperature was balanced with shorter time period.

Aging has increased grain size slightly for all coated samples proving low temperature can be effective on grain size if enough time is given. The post-coating and post-aging grain sizes of thick and thin samples found to be quite different since the grain size difference derived from inhomogeneous cooling after casting as mentioned before. However, the grain size of both samples followed the same trend against varying coating parameters and aging.

The increase in γ' size, volume fraction, hardness, and grain size of the samples that were only solutionized found to be higher than the increase in the γ' size, volume fraction, hardness and grain size of the samples that were both solutionized and coated, before aging was applied.

Aging has not affected the microstructure of coated samples dramatically since coating operations applied for long durations at high temperatures, acted as aging or primary high temperature aging. Consequently, coating decreased the effect of aging on IN 738 LC samples.

3.4.5 Microstructure Evolution Simulation Results

JMAT PRO software was used to perform microstructure evolution simulations during solutionizing, coating and aging. Since the software was able to perform maximum three consecutive processes, hot isostatic pressing was not simulated. Simulations were only performed for solutionizing, aluminide coating and aging, using post-HIP microstructure as the initial microstructure. All simulation results were compared with experimental measurement results that are given in this chapter.

3.4.5.1 Microstructure Evolution Simulations for Varying Solutionizing Conditions and CVD Temperatures.

Comparison of Simulation and Experimental Results at Varying Solutionizing Temperature in Combine with Varying CVD Temperature

Experiment and simulation results for thick and thin samples solutionized and coated at varying coating temperatures are compared in this section. Only solutionizing and coating conditions that are given in Table 3.14 were simulated. HIPed microstructure was used as input to simulations.

Table 3.14: Heat Treatment and Coating Parameters for Thick and Thin Samples

HIP Condition		Solutionizing Conditions		CVD Conditions
Temperature (°C)	1200	Temperature (°C)	1080, 1100, 1120, 1150, 1180, 1200, 1235	1000 °C-20 hours 1050 °C-16 hours 1100 °C-12 hours (Furnace Cooling-7°C/min)
Time (h)	10	Time (h)	2	
Pressure (MPa)	150	Cooling Type and Rate (°C/min)	Ar Cooling-180	

Experiment and JMAT PRO simulation of primary and secondary post-solutionizing and post-coating γ' size results for samples that were solutionized and coated at different temperatures are given in Figure 3.51.

Simulation of samples solutionized at 1080°C and 1100°C followed by CVD at 1100°C-20 hours couldn't be performed since solutionizing temperatures were lower than or equal to CVD temperature and JMAT PRO didn't allow such a condition.

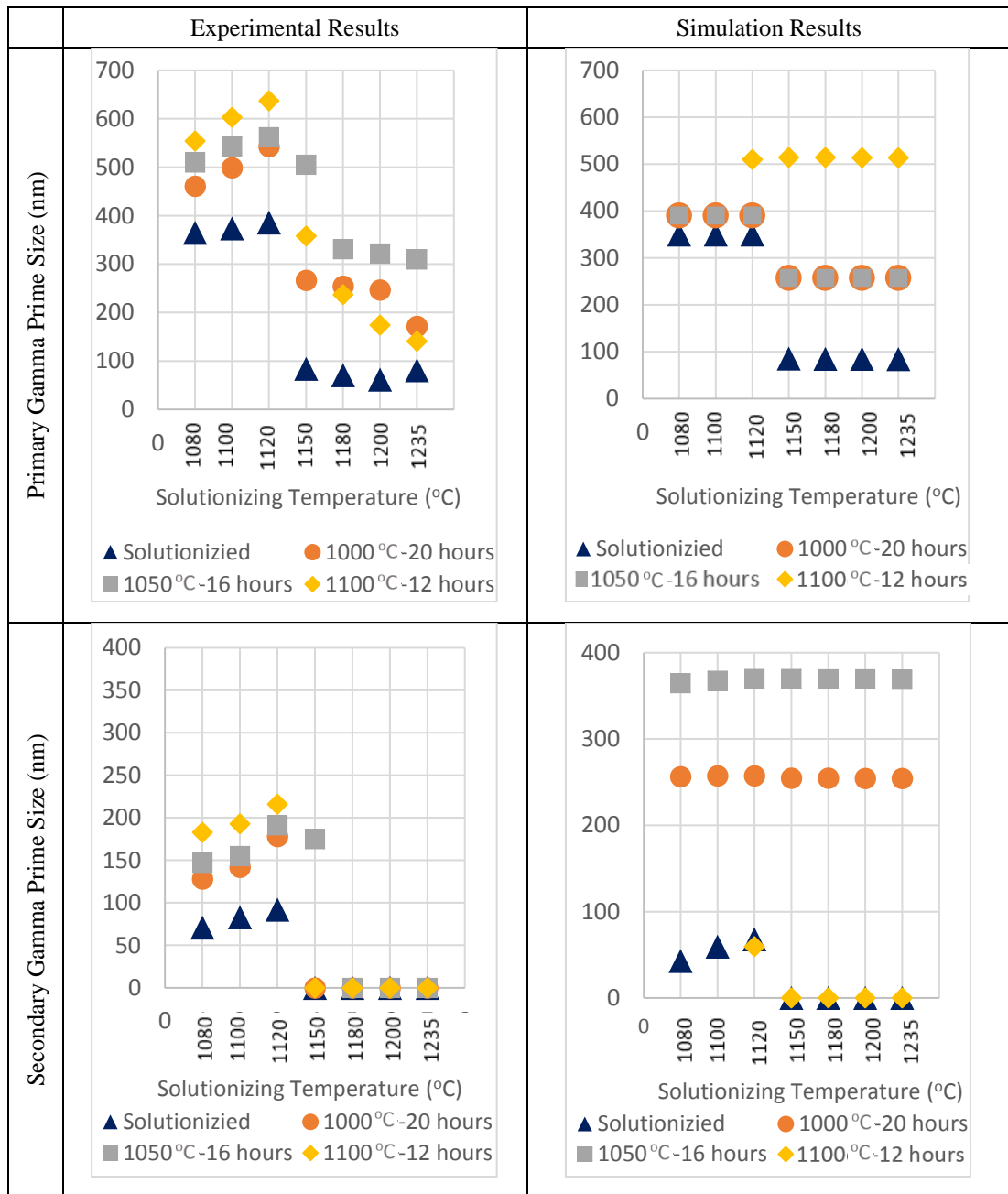


Figure 3.51: Experimental and JMAT PRO simulation results for primary and secondary γ' size .

As shown in Figure 3.51, post-solutionizing primary and secondary γ' size was found to be quite compatible with simulation results. Two obvious different regions were seen below 1150°C solutionizing temperature and above this temperature. This is due to bimodal to unimodal temperature transformation in between 1120-1150°C solutionizing temperatures in experimental results. However, this temperature range also promoted trimodal to bimodal γ' transformation in JMAT PRO results.

In post-coating microstructures, primary γ' size trend found to be similar for coatings performed at 1000°C-20 hours and 1050°C-16 hours. However, the γ' size results in these coating conditions found to be insensitive to solutionizing temperature except the increase in γ' size when the temperature was increased from 1120°C to 1150°C. The available simulation results for post-coating microstructure of 1100°C-20 hours condition was significantly higher than experimental results.

Secondary γ' sizes of post-solutionizing microstructure were found to be similar for simulation and experiment results.

The available simulation data on secondary γ' size of post-coating microstructure performed at 1100°C-12 hours found to be similar to experimental results. However, coatings simulated at 1000°C-20 hours and 1050°C-16 hours provided considerably higher secondary γ' size in simulation results than experimental results.

The samples solutionized above 1120°C and coated at 1100°C-12 hours didn't show secondary γ' structure since the unimodal structure was obtained in both experimental and simulation results in these conditions.

Experiment and JMAT PRO simulation of primary and secondary post-solutionizing and post-coating γ' volume fraction results for samples that were solutionized and coated at different temperatures are given in Figure 3.52.

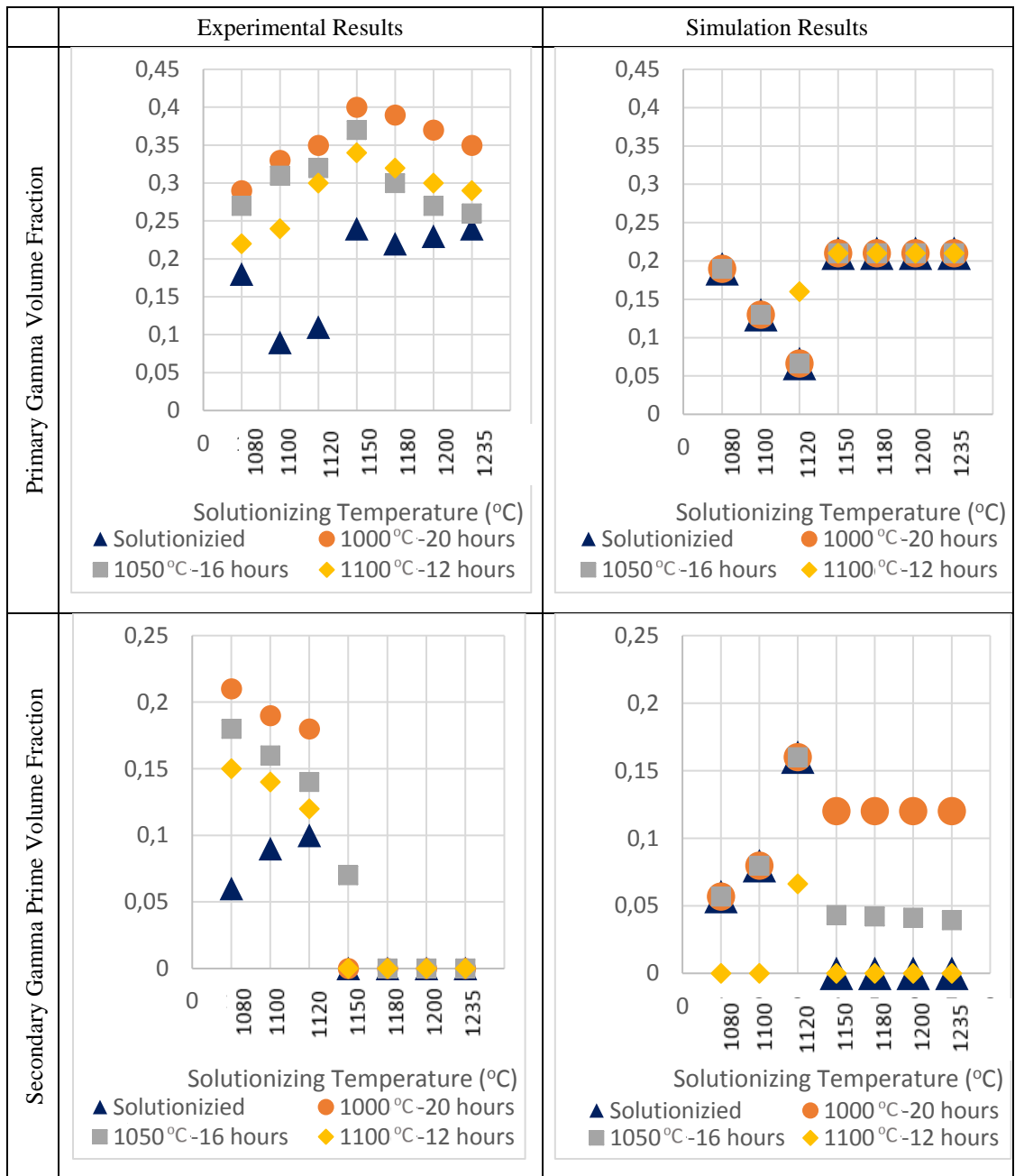


Figure 3.52: Experimental and JMAT PRO simulation results for primary and secondary γ' volume fraction.

As shown in Figure 3.52, both primary and secondary γ' volume fraction trend was found to be similar to simulation results for post-solutionizing microstructure. The only remarkable difference was obtained after solutionizing at 1120°C. Simulation results also show that secondary γ' volume fraction shows a sharper increase in this temperature than experimental results.

In JMAT PRO simulations, CVD conditions didn't affect primary γ' volume fraction significantly and different coating conditions provided similar primary γ' volume fraction. However, in experiment results, a sharp increase was obtained after CVD process applied to solutionized samples. Post-coating secondary γ' volume fraction found to be quite similar to post-solutionizing in simulation results below 1150°C. But, secondary γ' volume fraction obtained in post-coating microstructures was significantly higher than post-solutionizing in experimental results below 1150°C. Above this temperature, simulations show secondary γ' existence while experiment results showed that structure was unimodal and secondary γ' particles did not exist. Moreover, JMAT simulations showed tertiary γ' existence with size and volume fraction given in Figure 3.53 for post-coating microstructures.

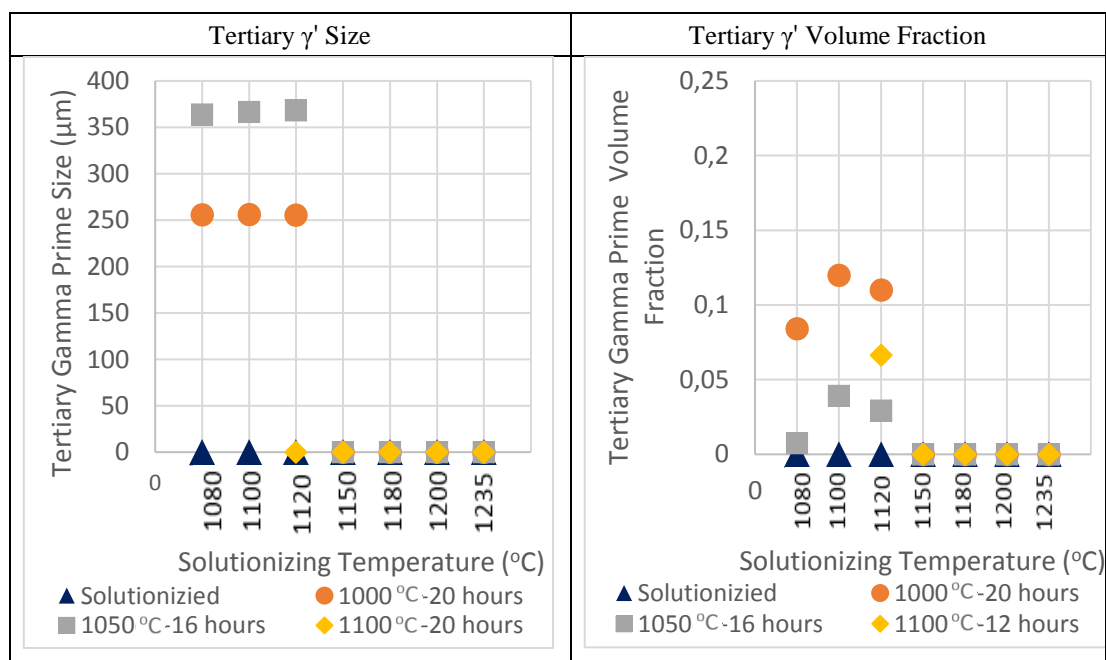


Figure 3.53: JMAT PRO simulation results for tertiary γ' size volume fraction.

Tertiary γ' particles existed only for the post-coating samples that were solutionized below 1150°C. Tertiary γ' particles were not found in post-coating microstructures in experimental results. There is a noticeable point that tertiary γ' size was only slightly lower than secondary γ' size obtained by simulations.

Comparison of Simulation and Experimental Results at Varying Solutionizing Time and Cooling Rate in Combine with Varying CVD Temperature

A group of simulations was performed with the same conditions with experiments to see the effect of solutionizing time and cooling rate at given conditions in Table 3.15.

Table 3.15: Parameters of Solutionizing at Varying Time and Cooling Rate, and CVD at Varying Temperatures.

HIP Condition		Solutionizing Conditions		CVD Conditions
Temperature (°C)	1200	Temperature (°C)	1120	1000 °C-20 hours 1050 °C-16 hours 1100 °C-12 hours (Furnace Cooling-7°C/min)
Time (h)	10	Time (h)	1, 2, 4	
Pressure (MPa)	150	Cooling Type and Rate (°C/min)	Ar Cooling-180 Furnace Cooling-20	

Simulation of samples that were solutionized for different time periods couldn't be performed since JMAT PRO is not able to perform solutionizing for different time periods. The software assumes that microstructure is in equilibrium at a stated solutionizing temperature and enough time was given for this achieve equilibrium condition. So, post-solutionizing condition for 1, 2 and 4 hours assumed to be equal and due to this reason not only post-solutionizing conditions but also post-coating conditions for samples that were solutionized 1, 2 and 4 hours obtained to be same in JMAT PRO results. However, the effect of cooling rate was simulated successfully in JMAT PRO.

Comparison of Simulation and Experiment Results at Varying Solutionizing Time of Ar Cooled Samples (180°C/min) in Combine with Varying CVD Temperature

Post-solutionizing and post-coating, simulation and experiment, primary and secondary γ' size and volume fraction of Ar cooled (180°C/min) samples are given in Figure 3.54 and Figure 3.55.

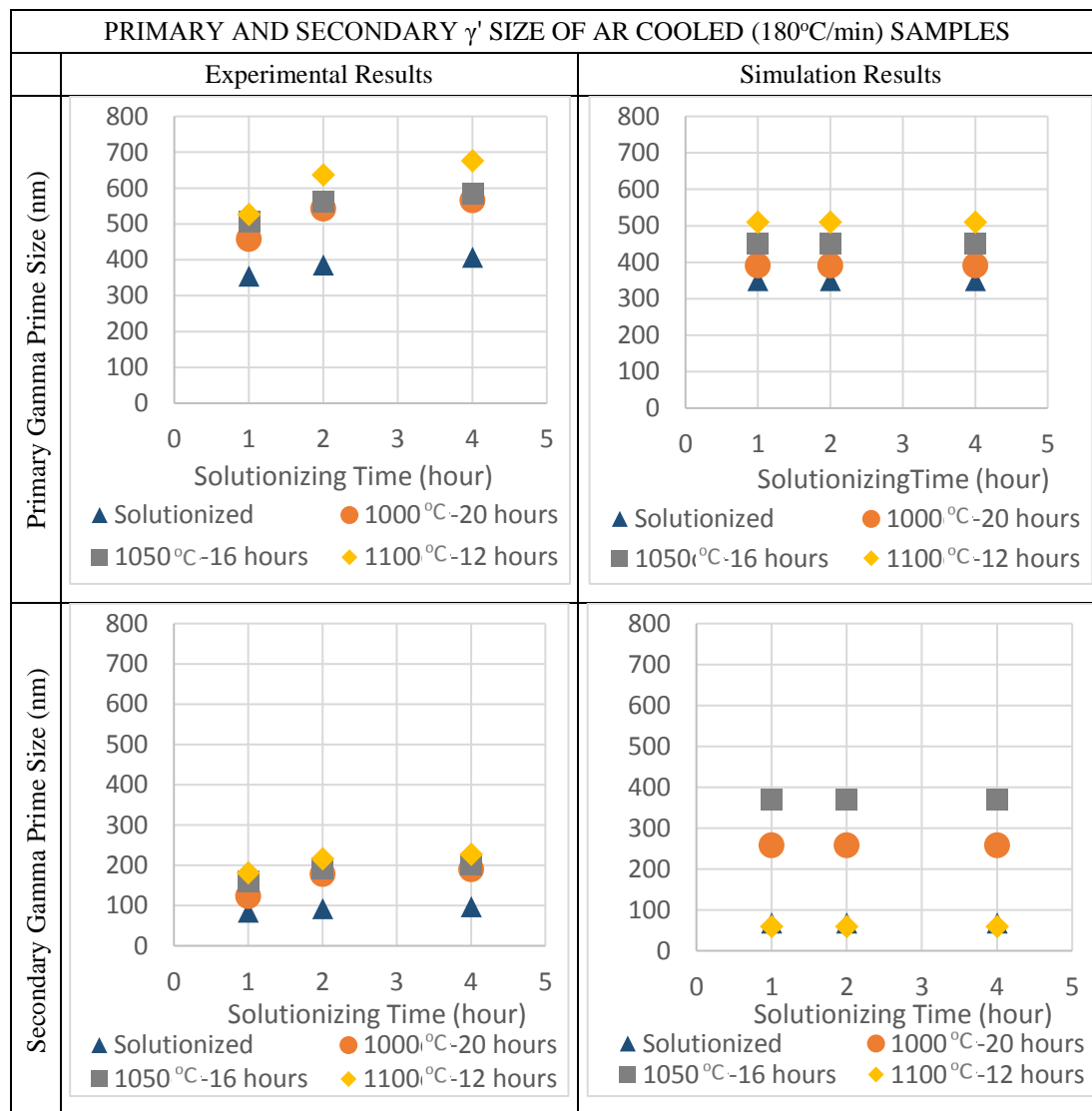


Figure 3.54: Post-solutionizing and post-coating experiment and JMAT PRO simulation for primary and secondary γ' size results of samples solutionized for 1, 2 and 4 hours, and Ar cooled (180°C/min).

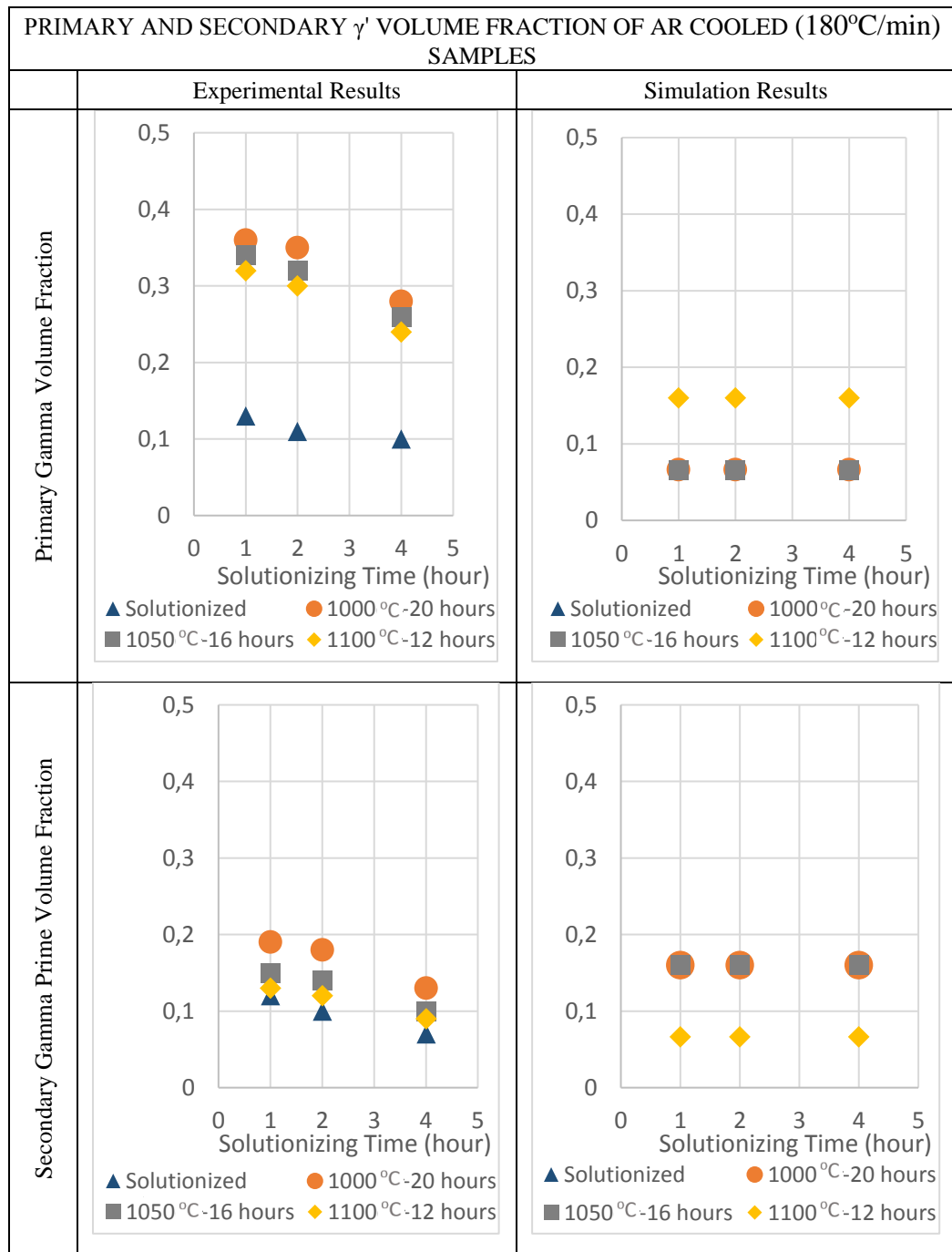


Figure 3.55: Experiment and JMAT PRO simulation results for primary and secondary γ' volume fractions.

Post-solutionizing primary γ' size results of samples solutionized for 1 hour were found to be similar to simulation results. The simulation could be obtaining equilibrium around 1 hour solutionizing time. Highest primary γ' size was obtained after coating at 1000°C-20 hours, followed by 1050 °C-16 hours and 1100 °C-12 hours in both simulation and heat treatment experiment results.

The same γ' size trend was obtained for secondary γ' size against different coating conditions in both experiment and simulation results except the coating at 1100°C-12 hours. The size of secondary γ' after coating at 1100°C-12 hours found to be equal to post-solutionizing secondary γ' size in simulation results. This could be due to simulated high coating temperature close to solutionizing temperature of IN 738 LC. However, 1100°C-12 hours coating provided highest secondary γ' size in experiments. In general, the post-coating secondary γ' sizes were slightly higher than post-solutionizing in experimental results.

Simulation results show that post-solutionizing and samples coated at 1000°C-20 and 1050 °C-16 hours exactly same primary and secondary γ' volume fraction for Ar cooled samples. Secondary γ' volume fraction after coating at 1100°C-12 hours found lower than post-solutionizing condition while the primary γ' volume fraction found to be higher than post solutionizing condition in simulation results.

Primary γ' volume fraction of experiment results was found to be significantly higher than simulation results. Secondary γ' volume fraction estimations values by JMAT PRO were relatively found to be more similar to experimental results. However, the trend of secondary γ' volume fraction against coating conditions were quite different for experiment and simulation results.

Highest primary and secondary γ' volume fraction was obtained after coating at 1000°C-20 hours, followed by 1050 °C-16 hours and 1100 °C-12 hours in experimental results. However, highest primary γ' volume fraction was obtained at 1100 °C-12 hours while highest secondary volume fraction was obtained at 1050 °C-16 hours and 1000 °C-20 hours equally in simulation results.

The JMAT PRO simulation estimated a tertiary γ' existence after coatings performed at 1000°C-20 hours and 1050 °C-16 hours which was not obtained in experimental results. The size of these tertiary particles was only slightly lower than the secondary particles. Tertiary γ' size was higher, and γ' volume fraction was lower after the CVD performed at 1050 °C-16 hours, compared to results of 1000°C-20 hours condition.

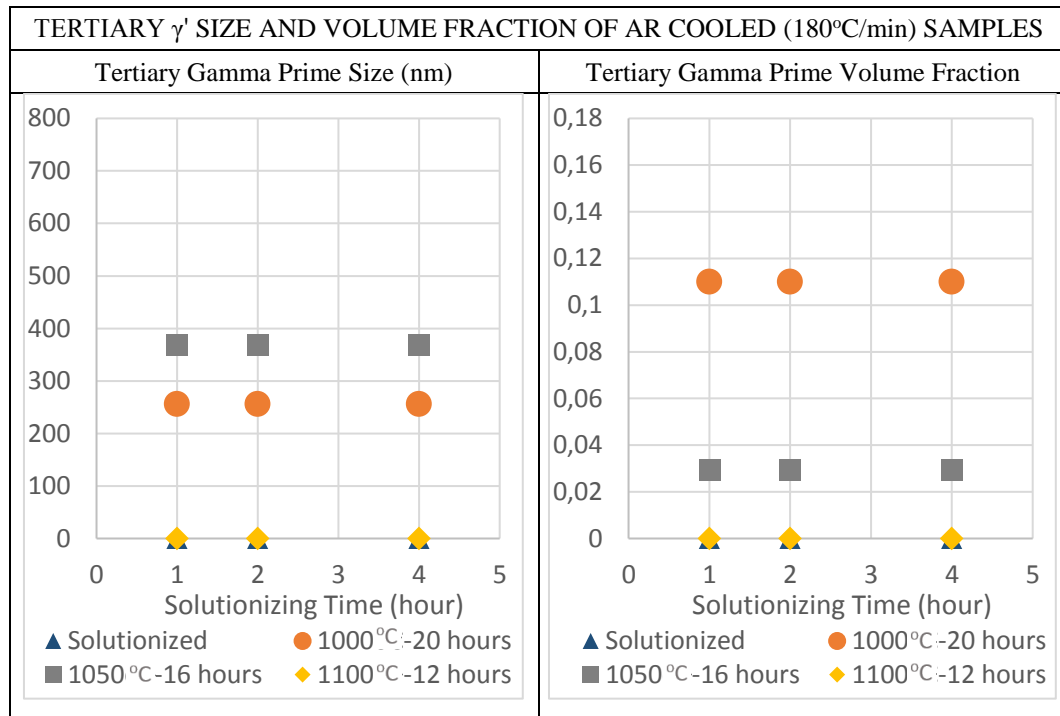


Figure 3.56: JMAT PRO simulation results for tertiary γ' size and volume fraction of samples solutionized for 1,2 and 4 hours, and Ar cooled (180°C/min).

Comparison of Simulation and Experiment Results at Varying Solutionizing Time of Furnace Cooled Samples (20°C/min) in Combine with Varying CVD Temperature

Post-solutionizing and post-coating, simulation and experiment, primary and secondary γ' size and volume fraction of furnace cooled (20°C/min) samples are given in Figure 3.57 and 3.58. JMAT PRO didn't estimate tertiary γ' particles existence for furnace cooled samples. Also, tertiary γ' particles didn't exist in experimental results of furnace cooled samples.

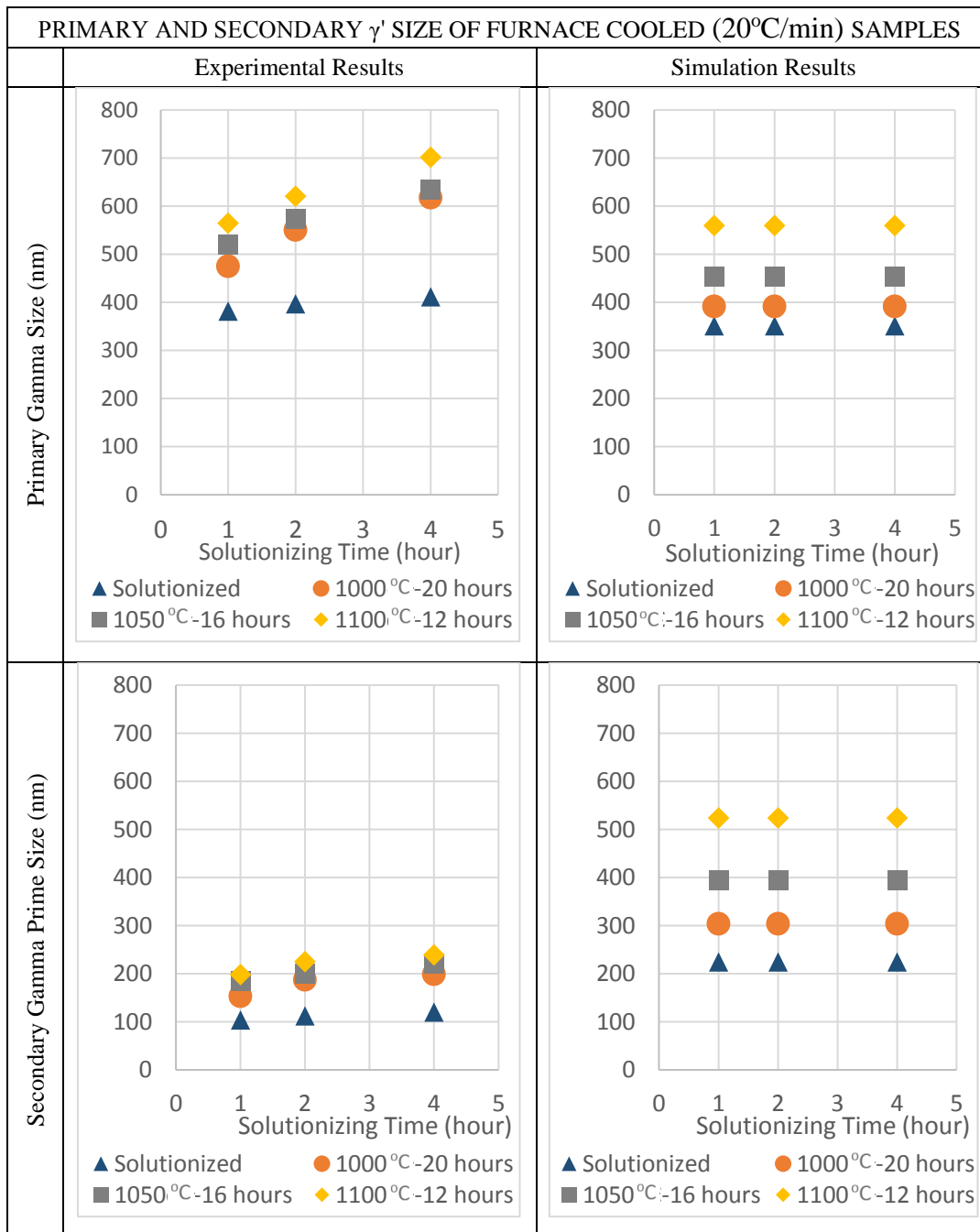


Figure 3.57: Post-solutionizing and post-coating experiment and JMAT PRO simulation for primary and secondary γ' size results of samples solutionized for 1, 2 and 4 hours, and furnace cooled (20°C/min).

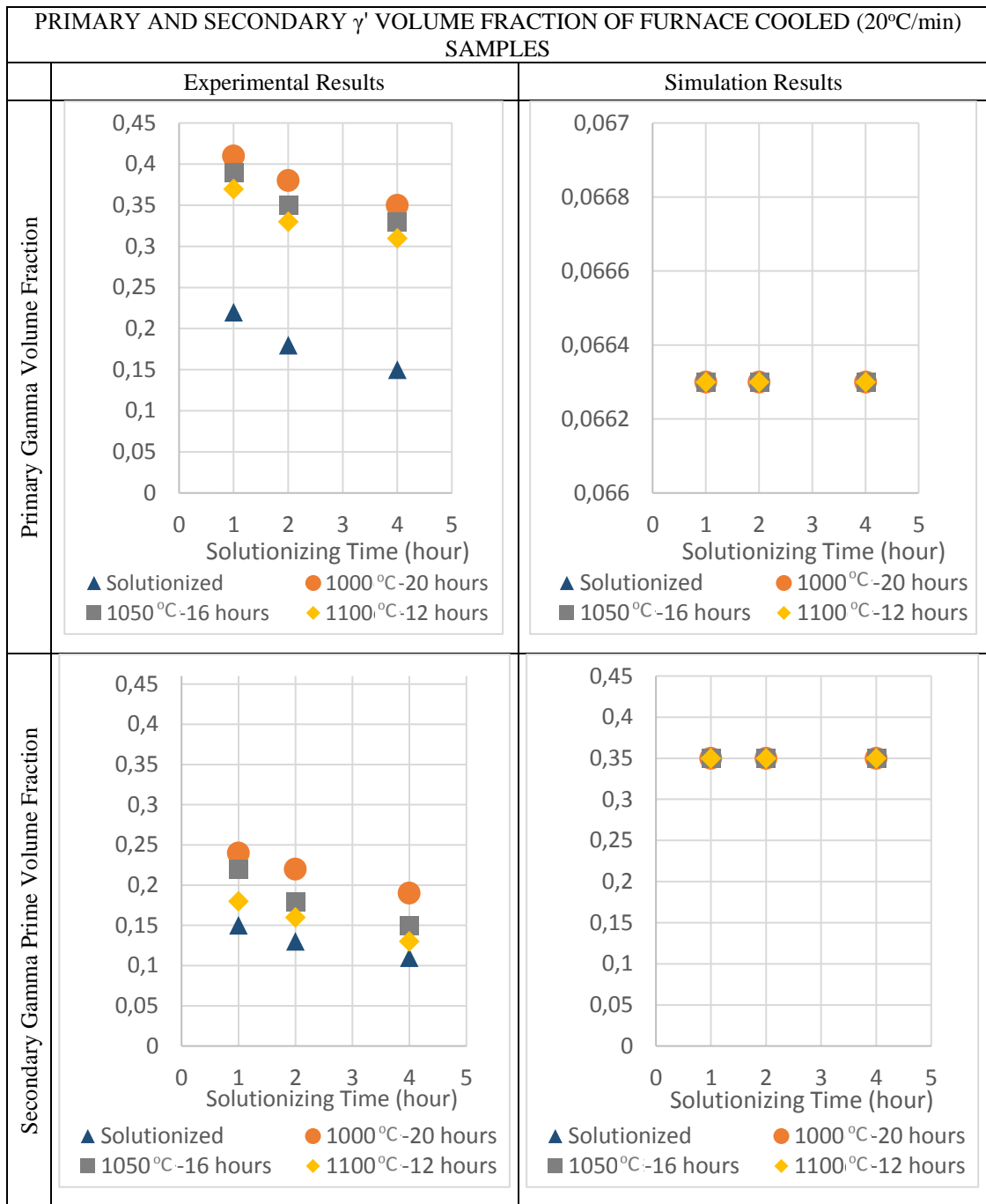


Figure 3.58: Post-solutionizing and post-coating experiment and JMAT PRO simulation for primary and secondary γ' volume fraction of samples solutionized for 1, 2 and 4 hours, and furnace cooled (20°C/min).

Post-solutionizing γ' size results of samples (furnace cooled) that were solutionized for 1 hours closer to simulation results (Figure 3.57). Considering the same equilibrium condition was assumed for different solutionizing times, the simulation could be obtaining equilibrium around 1 hour solutionizing time.

The post-solutionizing and post-coating primary γ' size result of simulations found to be closer to experimental primary γ' size results. However, simulation estimated post-solutionizing and post-coating secondary γ' sizes are considerably higher than experimental results (Figure 3.57).

Highest primary and secondary γ' size was obtained after coating at 1000°C-20 hours, followed by 1050 °C-16 hours and 1100 °C-12 hours in both simulation and heat treatment results (Figure 3.57).

JMAT PRO estimated a lower volume fraction of primary γ' particles compared to experimental results while it was found to be vice versa for secondary γ' particles. Additionally, software estimated a constant primary and secondary γ' volume fraction for post-solutionizing and various post-coating conditions. In furnace cooling condition, different CVD parameters didn't affect the γ' volume fractions; it only affected γ' sizes (Figure 3.57 and 3.58).

Primary γ' volume fraction of the post-coating and post-solutionizing microstructure was found to be less than 0.1 (Figure 3.58) in simulation results. This result was not expected. The possible reason for this will be explained in next section since the reason of this result could be the cooling rate.

Comparison of Simulation and Experiment Results Based on Varying Cooling Rate in Combine with CVD Temperature

Furnace cooling achieved higher primary and secondary post-solutionizing and post-coating γ' size and volume fraction in experimental results (Figure 3.57 and 3.58). Simulation results also showed that furnace cooling achieved higher primary and secondary γ' size than Ar cooling. But, simulations showed that primary γ' volume

fraction of furnace cooled sample is lower than Ar cooled sample (which is not expected), and secondary γ' volume of furnace cooled sample is higher than Ar cooled sample.

Primary γ' volume fractions of the post-coating and post-solutionizing microstructure of furnace cooled samples were found to be less than 0.1. This cooling method increased both primary and secondary γ' size slightly. However, the simulation decreased primary γ' volume fraction and increased secondary γ' volume fraction dramatically. It is believed that the decrease in primary γ' volume fraction occurred due to the dissolution of this particles during solutionizing and increase in secondary γ' volume fraction occurred due to precipitation during cooling in the simulation. After all, even these reasons are not enough to explain a primary γ' volume fraction less than 0.1. In experimental results furnace cooling achieved primary γ' volume fraction higher than 0.3.

Both Ar and furnace cooled post-solutionizing microstructures didn't show any tertiary γ' existence in simulation results. However, the samples Ar cooled after solutionizing had tertiary γ' particles after CVD performed at 1000°C-20 hours and 1050 °C-16 hours. Furnace cooled samples had no tertiary γ' particles in their post-coating microstructures. During furnace cooling applied after solutionizing, most of the dissolved γ' in the matrix was precipitated. However, since Ar cooling didn't allow a long period of time to precipitation, there were still potential dissolved γ' in matrix ready to precipitate in matrix after solutionizing. Therefore, a part of dissolved γ' in the matrix was reprecipitated after CVD. It is believed that this could be the reason of this behavior in the simulation. But, tertiary γ' particles were not seen in any post-solutionizing and post-coating experimental results.

3.4.5.2 Microstructure Evolution Simulations for Solutionizing, CVD at Varying Temperatures and Aging of Thick and Thin Samples.

A group of simulations was performed at the same conditions with experiments to see the effect of solutionizing, varying CVD temperatures and aging to thick and thin samples' microstructures at given conditions in Table 3.16. Additionally, one thick and one thin sample was left uncoated to see the effect of aging on uncoated samples. The only difference of thick and thin samples for JMAT PRO simulation was their initial (HIPed) γ' and grain sizes.

Table 3.16: Parameters of Solutionizing for Varying Time Periods and Cooling Rates, and CVD at Varying Temperatures.

HIP Condition		Solutionizing Conditions		CVD Conditions	Aging Condition
Temperature (°C)	1200	Temperature (°C)	1120	1000 °C-20 hours 1050 °C-16 hours 1100 °C-12 hours (Furnace Cooling- 7°C/min)	845 °C-24 hours
Time (h)	10	Time (h)	2		
Pressure (MPa)	150	Cooling Type and Rate (°C/min)	Ar Cooling-180		

Simulation and experiment results for primary and secondary γ' size for the coated and aged samples are given in Figure 3.59.

Primary and secondary γ' sizes of both post-coating and post-aging microstructures found to be similar to each other in simulation results for thick and thin samples. Thick samples showed higher primary and secondary γ' sizes in post-coating and post-aging microstructures due to higher γ' size provided for the thick sample as an initial condition in the simulation except one condition. Only difference in simulation results for thick and thin samples' γ' size was obtained at 1100°C-12 hours CVD process. Thick sample showed lower secondary γ' size than thin sample after coating at this condition. This could be due to different initial γ' sizes used as input for thick and thin sample, and the CVD temperature close to partial solutionizing temperature (1120°C).

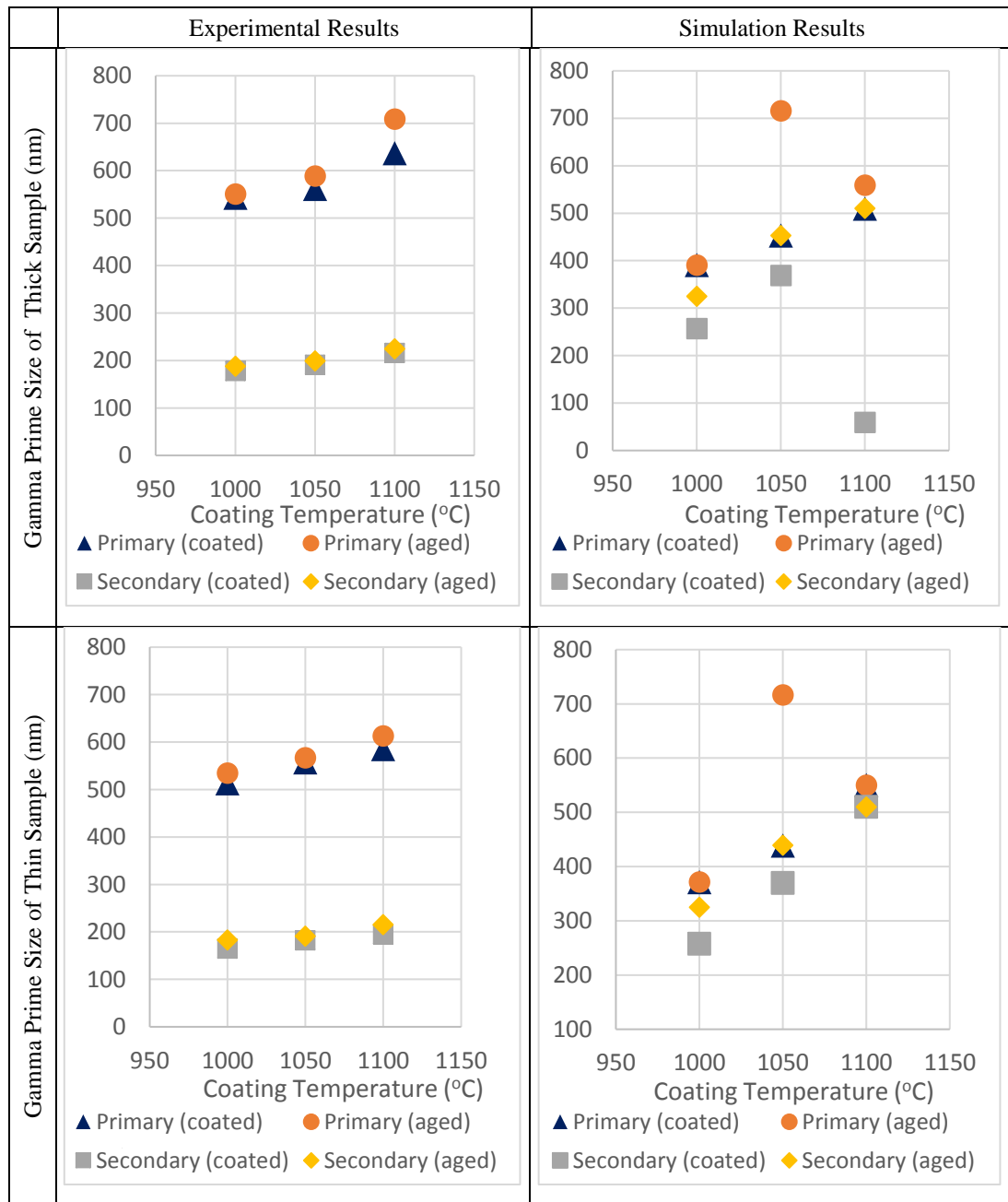


Figure 3.59: Experiment and JMAT PRO simulation γ' size of post-coating and post-aging results for thick and thin samples.

Primary γ' sizes of post-coating and post-aging found to be higher than simulation results except the CVD performed at 1050°C-16 hours for both thick and thin samples. Secondary γ' sizes of post-coating and post-aging found to be lower than simulation results except the CVD applied to the thin sample at 1100 °C-12 hours. Except the CVD performed at 1050°C-16 hours for both thick and thin samples and 1100 °C-12 hours for thin sample, similar trends were found for γ' size against CVD temperature between simulations and experiments.

Aging increased primary γ' sizes slightly for thin and thick samples in experiment results. Similar trend was seen in simulations except the thick and thin samples that were coated at 1050°C-16 hours and thin sample that was coated at 1100 °C-12 hours.

Simulation and experiment results for primary and secondary γ' volume fraction for the coated and aged samples are given in Figure 3.60.

Aging increased primary and secondary γ' volume fraction of post-coating microstructures slightly in experiments. However, in simulations, different results were obtained. Compared to post-coating condition, only primary γ' volume fraction increase was obtained after aging of the sample that was coated at 1050°C 16 hours in simulations for both thick and thin samples due to high γ' size obtained at this coating parameters as shown in Figure 3.59 and Figure 3.60.

Aging increased secondary γ' volume fraction for thick sample coated at 1000°C-20 hours and 1100°C-12 hours while for thin sample coated at 1000°C-20 hours. Aging decreased secondary γ' fraction of both thick and thin samples coated at 1050°C-16 hours in simulation results. A difference between thick and thin samples was obtained at 1100°C-12 hours aluminide coating operation in simulation results. Thin sample kept its secondary γ' volume fraction almost constant coating temperature is increased from 1050°C to 1100°C while thick sample decreased its secondary γ' volume fraction at during same condition change. However, after aging, the samples coated at 1100°C achieved almost the same volume fraction which was not expected. This different behavior could be due to initially provided different γ' sizes to simulation for thick and thin samples

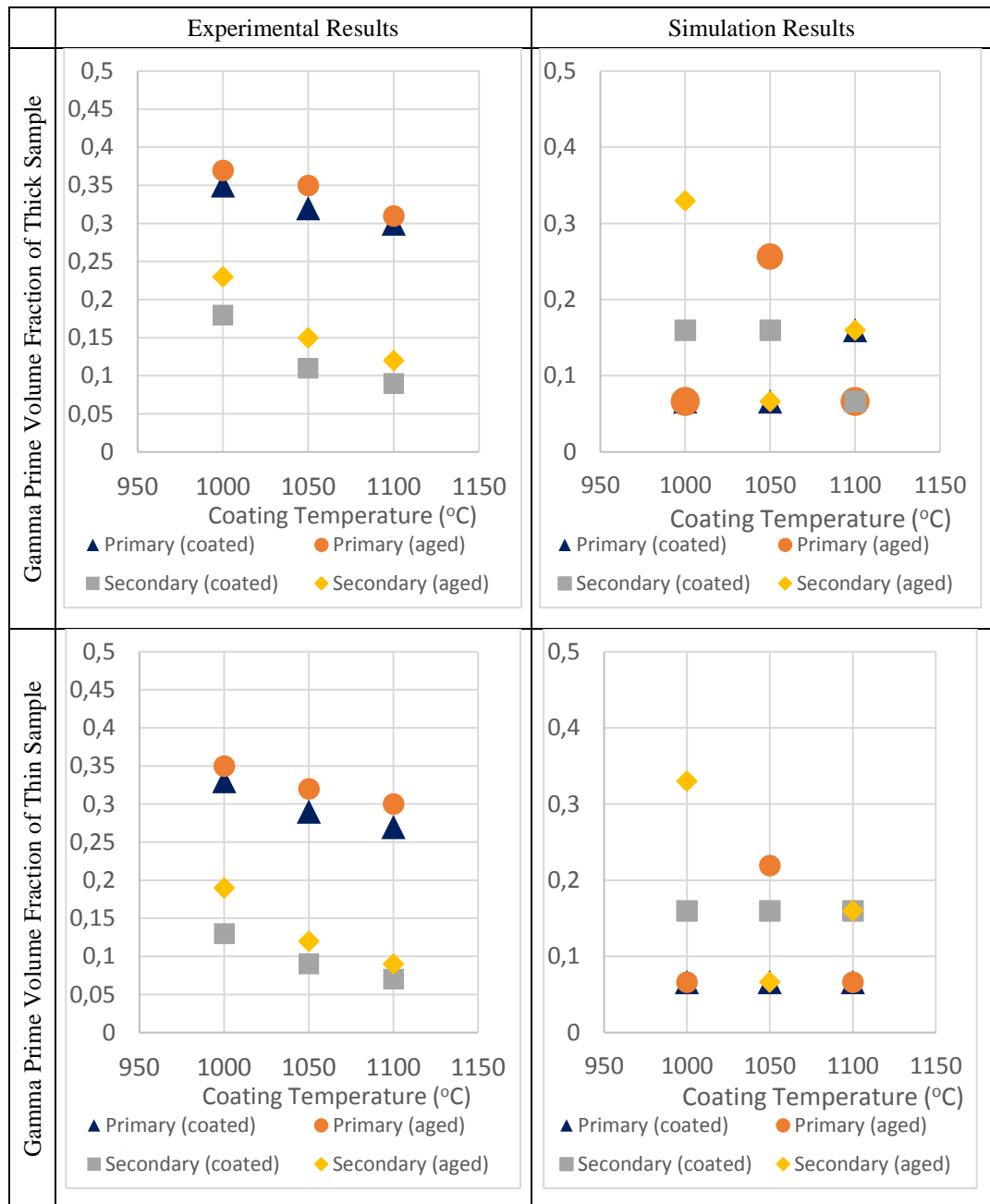


Figure 3.60: Experiment and JMAT PRO simulation γ' volume fraction of post-coating and post-aging results for thick and thin samples.

Tertiary γ' was obtained the same for both thick and thin samples in JMAT PRO simulation results for post-coating and post-aging microstructures. However,

experimentally tertiary γ' particles were not found. Tertiary γ' size and volume fraction simulation results are given in Figure 3.61.

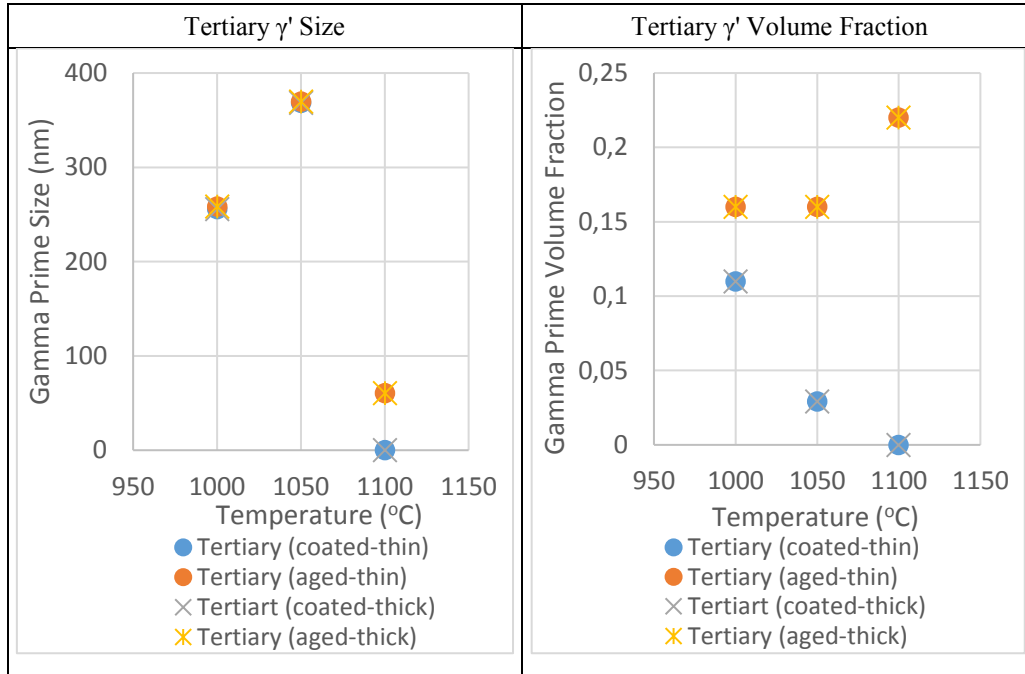


Figure 3.61: JMAT PRO simulation γ' size and volume fraction of post-coating and post-aging thick and thin samples.

As shown in Figure 3.61, aging caused only a slight increase in the size of tertiary γ' particles. The main increase was seen in volume fraction of tertiary γ' particles. The size and volume fraction of tertiary γ' particles were found to be identical for thick and thin samples despite the fact that different initial γ' size used as input to software for thick and thin samples.

Experimental and JMAT PRO simulation primary and secondary γ' size and volume fraction results for thick and thin samples that were solutionized and directly aged (no coating applied) are given in Figure 3.62.

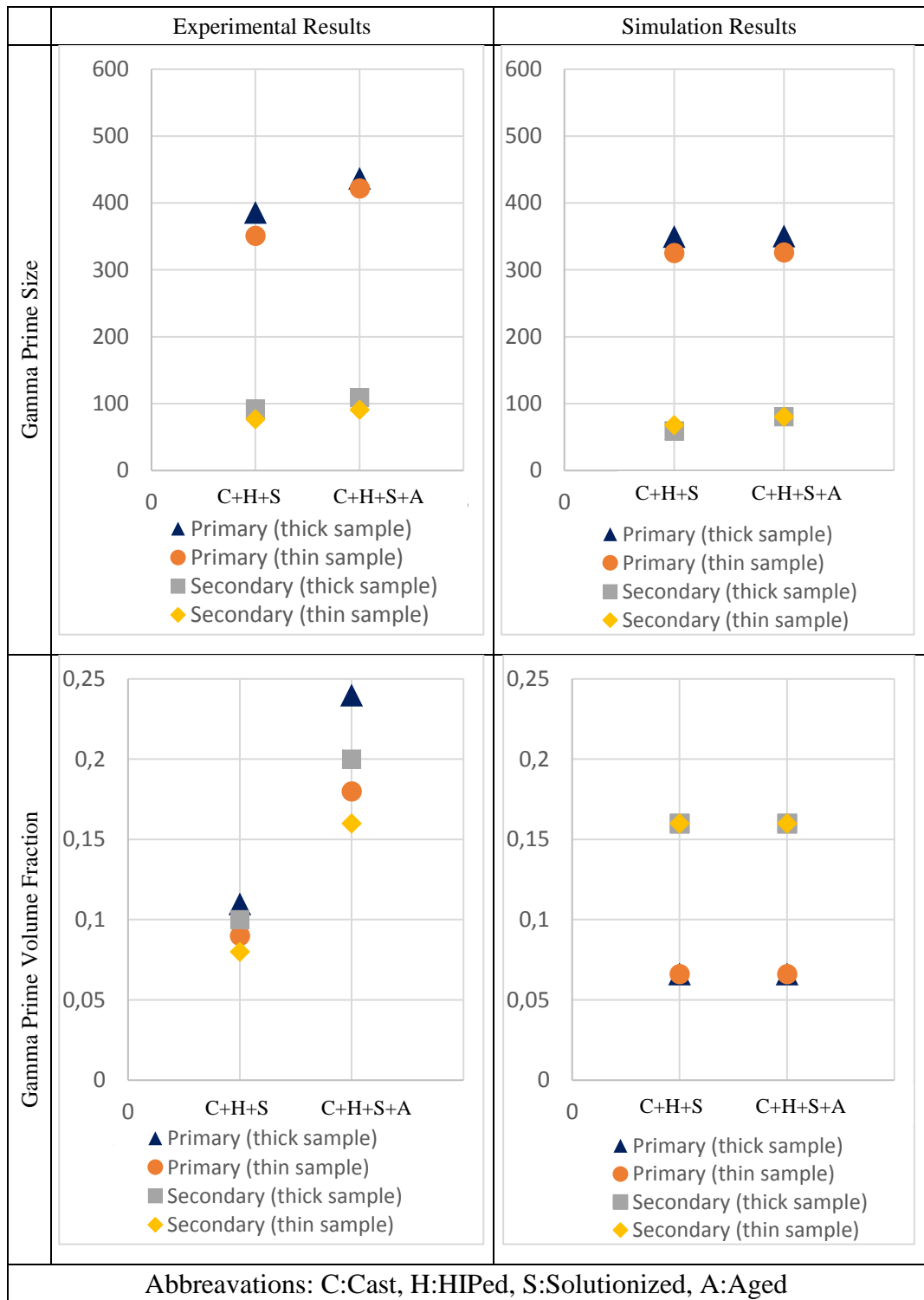


Figure 3.62: Experiment and JMAT PRO simulation γ' volume fraction of post-solutionizing and post-aging results for thick and thin samples.

Primary and secondary γ' size found to be similar in post-solutionizing and post-aging. However, experiments showed slightly higher increase in primary γ' size after aging than a coating. Aging didn't change primary and secondary volume fraction in simulation results. However, experiment results showed a sharp increase for both.

The reason for constant primary and secondary γ' volume fraction obtained in simulation results could be the tertiary γ' size estimated to be formed by simulation in during aging. The tertiary γ' size and volume fraction are given for post-solutionizing and post-aging conditions in Figure 3.63. The post-solutionizing condition had zero tertiary γ' particles. It is clear that simulation formed a tertiary γ' size during aging with a volume fraction over 20% instead of increasing primary and secondary γ' volume fraction. Thick and thin samples showed identical results for tertiary γ' profile in the post-aging microstructure.

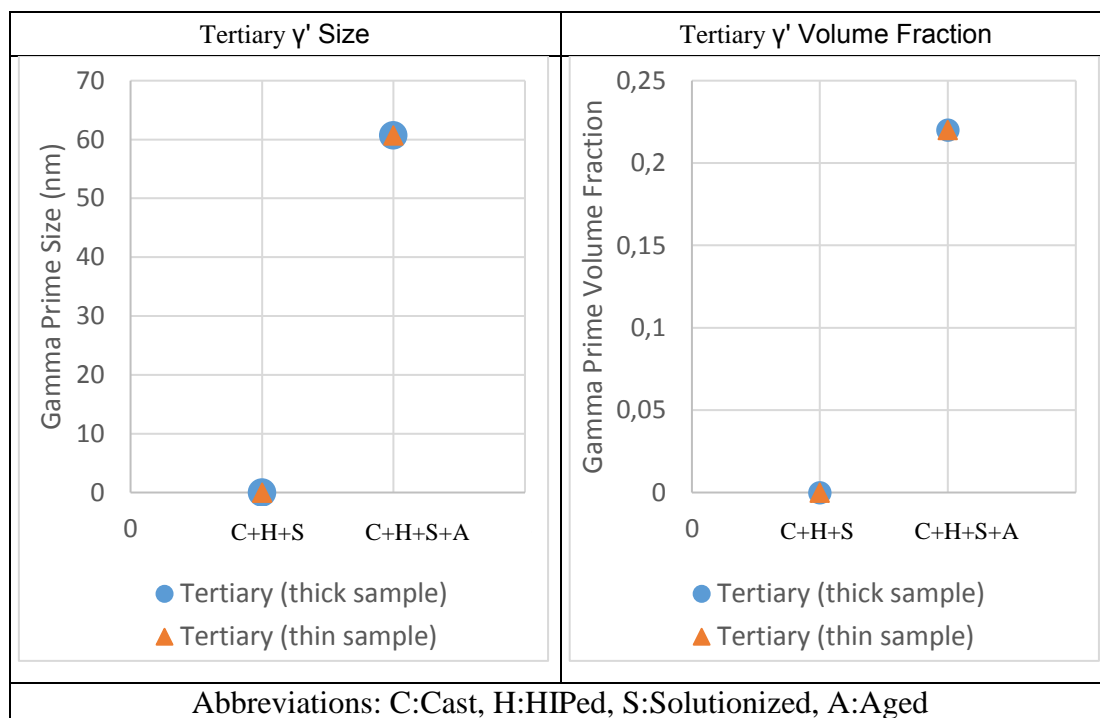


Figure 3.63: Experiment (left) and JMAT PRO simulation (right) γ' volume fraction of post-solutionizing and post-aging results for thick and thin samples.

3.5 Effect of Heat Treatments and Aluminide Coating Temperature to Carbide Types

Line scans and mapping were performed using electron diffraction spectroscopy to see whether detected elements can be related to the carbides. Group of samples for carbide type determination were relatively kept small. However, all experimental parameters that is expected to affect carbide types were considered.

Typically, MC type of carbides is formed during solidification as coarse and random particles in transgranular, intergranular positions and between dendrites of IN 738 LC. [3, 44] Fine MC carbides that are segregated at matrix or grain boundaries strengthens the alloy and ties up elements that promote instable phase formations during heat treatments or service. [32] These carbides are very stable at low temperatures. [33] Due to melting point above 1525°C, they just partly dissolve during solutionizing. [43] However, MC carbide degenerate at high temperatures and transforms into more stable $M_{23}C_6$ at 760-980°C and 815-980°C, respectively. [32] Formation of $M_{23}C_6$ carbides causes a significant decrease of Cr in the matrix that can weaken the corrosion resistance of the alloy. [3, 29]

MC carbides are known to be Ta, Ti, Mo, Nb rich while $M_{23}C_6$ carbides are Cr rich. Therefore, specifically, composition analyze of these elements were performed. As a cast, solutionized, coated and aged samples showed discretely shaped carbides that were Ta, Ti, Mo, Nb rich which defines them as MC carbides. Cr rich $M_{23}C_6$ carbides were not found as expected as expected. $M_{23}C_6$ carbides precipitate during long service times mostly.

The main motivation for analyzing carbides was to determine if the carbide types were detrimental or beneficial to material. Initially as cast and HIPed samples carbide types were investigated. The other investigated parameters are given in Table 3.19-3.20. The shaded areas show the investigated conditions and unshaded areas show the process history of samples.

Table 3.17: Experiment Plan to Observe Effect of Solutionizing Time and Cooling Rate on Carbide Types

HIP Condition		Solutionizing Conditions	
Temperature (°C)	1200	Temperature (°C)	1120
Time (h)	10	Time (h)	1, 2, 4
Pressure (MPa)	150	Cooling Type and Rate (°C/min)	Ar Cooling-180 Furnace Cooling

Table 3.18: Experiment Plan to Observe Effect of Solutionizing and CVD Temperature on Carbide Types

HIP Condition		Solutionizing Conditions		CVD Conditions
Temperature (°C)	1200	Temperature (°C)	1120, 1200	1000 °C-20 hours 1050 °C-16 hours 1100 °C-12 hours (Furnace Cooling- 7°C/min)
Time (h)	10	Time (h)	2	
Pressure (MPa)	150	Cooling Type and Rate (°C/min)	Ar Cooling-180	

Table 3.19: Experiment Plan to Observe Effect of Aging (after CVD) on Carbide Types.

HIP Condition		Solutionizing Conditions		CVD Conditions	Aging Condition
Temperature (°C)	1200	Temperature (°C)	1120	1000 °C-20 hours 1050 °C-16 hours 1100 °C-12 hours (Furnace Cooling- 7°C/min)	845 °C-24 hours
Time (h)	10	Time (h)	2		
Pressure (MPa)	150	Cooling Type and Rate (°C/min)	Ar Cooling-180		

Table 3.20: Experiment Plan to Observe Effect of Aging (No CVD applied) on Carbide Types

HIP Condition		Solutionizing Conditions		Aging Condition
Temperature (°C)	1200	Temperature (°C)	1120	845 °C-24 hours
Time (h)	10	Time (h)	2	
Pressure (MPa)	150	Cooling Type and Rate (°C/min)	Ar Cooling-180	

Multiple carbide analysis performed for each sample. The representative line scan and mapping composition analysis results are given in Appendix C.

As cast structure showed Ti, Nb and Ta rich MC carbides distributed in intergranular spaces. It was obtained that application of HIP is decreasing the Ti, Nb, and Ta considerably in the chemical composition of MC carbides. This could be due to high temperature and long period of HIP (1200°C-10 hours) that is increasing the diffusion between the matrix and MC carbide.

The amount of Ti, Nb, and Ta elements were slightly increased after solutionizing applied at 1120°C and 1200°C for 2 hours. There was no considerable change of carbide composition when solutionizing temperature was increased.

Increasing solutionizing time or cooling rate did not change carbide composition profile greatly. However, carbide sizes were found to be higher for furnace cooled samples than Ar cooled samples.

The coating applied at 1100°C-12 hours resulted in lower Ti, Nb, and Ta elements in MC carbides when it is compared to 1000°C-20 hours and 1050°C-16 hours. This could be due to higher coating temperature that increased the diffusion between MC carbide and matrix.

The sample that was directly (no coating applied with CVD) aged after solutionizing showed similar carbide composition profile to samples coated prior to aging.

The MC carbides were found to be discreetly shaped and mostly located in intergranular spaces of all samples rather than grain boundaries.

3.6 Secondary Dendrite Spacing

Secondary dendrite arm spacing was measured for a group of samples with different microstructures and heat treatment histories. The method of dendrite spacing measurement was given in section 3.2.4.2.5 Grain Size and Dendrite Spacing Determination. Relatively smaller group of experiment was used for this study. The purpose was to see the change in secondary dendrite arm spacing depending on heat treatment conditions. A group abbreviations were used in this section for different heat treatments as explained in Table 3.21.

Table 3.21: Heat Treatment and Coating Conditions and Abbreviations.

Processes	Conditions	Abbreviations
Hipped	1200°C-10 h-150 MPa	H
Solutionized	1120°C-2 h-Ar C. (180°C/min)	S
Coating 1	1000°C-20 h-F. C. (7°C/min)	C1
Coating 2	1050°C-16 h-F. C. (7°C/min)	C2
Coating 3	1100°C-12 h-F. C. (7°C/min)	C3
Aging	845°C-24 h-Ar. C. (180°C/min)	A

The optic microscope images of HIPed, solutionized, coated and aged samples are given in optic microscope images in Figure 3.64. Heat treatments and CVD processes increased the secondary dendrite arm spacing. The results of secondary dendrite arm spacing are given in Table 3.22. Only conditions dendrites were dissolved into matrix were H+S+C3 and H+S+C3+A. This could be expected due to high temperature CVD process applied at 1100°C-12 hours at these processes.

Table 3.22: Secondary Dendrite Spacing and Phase Boundary Strengthening

Processes	Secondary Dendrite Spacing (μm)
H	67
H+S	59
H+S+A	102
H+S+C1	86
H+S+C2	107
H+S+C3	-
H+S+C1+A	125
H+S+C2+A	129
H+S+C3+A	-

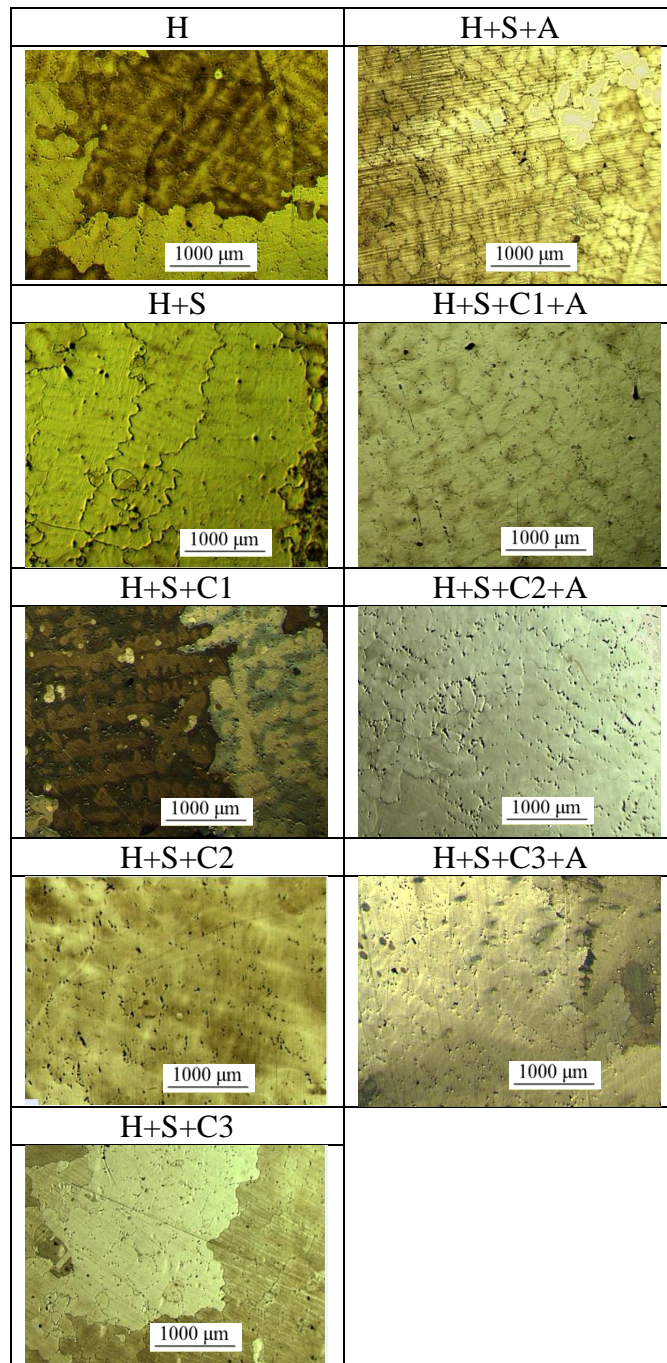


Figure 3.64: Optic microscope images of samples with different heat treatment histories.

3.7 Conclusion

This chapter has dealt with the effect of hot isostatic pressing, aluminide coating, solutionizing and aging to IN 738 LC microstructure. γ' size and volume fraction determination, carbide analysis, hardness and grain size measurements were performed. Beside experimental studies, JMAT PRO software was used to simulate microstructure evolution during these operations. The conclusions of these studies are listed as given below.

- The HIP operation was performed to close porosities that were formed during solidification of IN 738 LC at 1200°C-10 hours under 150 MPa. Porosities were partly closed during HIP, and grain sizes of samples were increased due to its high temperature and long period. However, HIP caused detrimental results in microstructure such as the disappearance of primary γ' particles and a decrease of total γ' volume fraction. Hardness was decreased due to these reasons. To recover from these detrimental results, solutionizing and aging were performed. HIP increased grain size of samples due to its high temperature and long period.
- Solutionizings were performed at various temperatures in between 1080-1235°C for 2 hours, and Ar cooled environment to see the effect of solutionizing temperature to γ' profile. The bimodal structure was obtained at solutionizing temperatures below 1150°C, above this temperature, unimodal structure was achieved. Highest γ' size and volume fraction were achieved after solutionizing at 1120°C. Increasing solutionizing temperature increased grain size and decreased hardness due to lower γ' volume fraction obtained at higher solutionizing temperatures.
- Solutionizings were performed at 1120°C in for 1, 2 and 4 hours in Ar furnace cooled environments. Increasing solutionizing time provided higher γ' size and lower γ' volume fraction that decreased the hardness of samples. Additionally, solutionizing time and grain size of samples found to be proportional.

- Furnace cooling promoted more γ' precipitation and growth than Ar cooling, increasing both γ' size and volume fraction. However, Ar cooling achieved finely shaped primary cubic γ' particles while furnace cooling results showed disorderly shaped γ' particles. Hardness was measured to be higher for samples that were furnace cooled due to higher γ' volume fraction in their microstructure. Furnace cooling also allowed higher grain size formation compared to Ar cooling.
- The aluminide coating operation was applied to all the samples that were solutionized at various temperatures, times and cooling rates. The coating operation was performed at 1000°C-20 hours, 1050°C-16 hours and 1100 °C-12 hours. The purpose of using these experimental conditions was to achieve same coating thickness at different temperatures. However, same coating thickness was not achieved. Highest coating thickness was achieved at 1100 °C-12 hours followed by 1000°C-20 hours, 1050°C-16 hours respectively.
- Effect of aluminide coatings to IN 738 LC microstructure was investigated. The coating applied at 1100 °C-12 hours provided the highest γ' size for samples solutionized below 1150°C (bimodal region) while samples solutionized above this temperature (unimodal region) achieved highest γ' size after coating at 1050°C-16 hours. Highest γ' volume fraction was achieved after 1000°C-20 hours coating. These results show that higher coating thickness-lower coating period promoted an increase in precipitate size while lower coating temperature-higher coating period promoted an increase in volume fraction of samples. Additionally, experimental conditions that provide highest γ' size and volume fraction might differ from bimodal structure to unimodal structure. Increasing coating temperature increased grain size while hardness was measured to be higher for coatings performed at lower temperatures due to higher γ' volume fraction in their microstructure.

- The effect of aging that was performed at 845°-24 hours-Ar cooled, to samples that were already coated, was found to be limited. The aging only increased γ' size and volume fraction of these samples slightly. However, aging increased γ' volume fraction of the samples that were only solutionized dramatically. These results show that coating operation acted as a main or primary high temperature aging that increased γ' size and volume fraction, and decreased the effect of aging applied afterward. This was expected due to high temperature and long period of aluminide coating operation. Aging was found to slightly increasing both hardness and grain size of samples that were coated. Uncoated samples showed relatively more considerable changes of grain size and hardness after aging.
- A group of thick and thin samples that were taken from middle section and leading edge of the blade to see effect of sample thickness on microstructure. These samples were HIPed, solutionized, coated and aged. Additionally, as cast microstructures of these samples were investigated. Due to inhomogeneous cooling after casting thin sample showed significantly lower γ' size and volume fraction, since leading edge cooled much faster of the blade. Due to same reason thin sample showed significantly lower grain size, slightly lower γ' volume fraction, and hardness. This trend was also seen in post-HIPed, post-solutionizing, post-coating and post-aging microstructures.
- Increasing aluminide coating temperature increased the γ' size and decreased the γ' volume fraction. Additionally, increasing aluminide coating temperature decreased the necessary coating period to achieve a certain coating thickness. An aluminide coating temperature that satisfies necessary coating thickness and desired bimodal high volume fraction γ' phase is necessary. The aluminide coating at 1100°C is not advised since this coating temperature increased γ' sizes and decreased γ' volume fraction dramatically. The aluminide coating at 1000°C provided high volume fraction of γ' and lower γ' sizes. However, this coating temperature only achieved 34 μm of coating thickness after 20 hours which is not a reasonable coating time period and thickness. Therefore 1050 °C

is advised as coating temperature to provide both necessary coating thickness over 50 μm and desired bimodal microstructure as given Figure 3.2 in Chapter 3. Solutionizing performed at 1120°C-2 hours (Ar cooled-180°C/min) before aluminide coating performed at 1050°C, found to be effecting post-coating microstructure positively since it achieved finely shaped bimodal highest γ' volume fraction in the post-solutionizing and accordingly post-coating microstructure. Although aging at 845°C-24 hours performed after aluminide coating only slightly improved the microstructure, application of aging process still found to be beneficial since aging helps the stabilization of microstructure due to aging temperature similar to third stage gas turbine blade service temperature.

- JMAT PRO simulations were performed to estimate γ' size and volume fraction after solutionizing and aging. Post- solutionizing results were found to be more compatible with experiments than post-coating and post-aging results. In general, the simulation results were not satisfactory except the few characteristic results estimated that were similar to experimental results.
- Only Ta, Ti, Mo and Nb rich discrete MC carbides were obtained in as cast, HIPed, solutionized, coated and aged samples and carbides were mostly located in intergranular spaces.

CHAPTER 4

MODELLING OF YIELD STRENGTH FOR INCONEL 738 LC

4.1 Introduction

The aim of the previous chapter was to improve and optimize microstructure of IN 738 LC with heat treatments. In this chapter, the microstructure characterization results obtained in Chapter 3 were used as input to estimate yield strength of IN 738 LC samples with different microstructures and heat treatment histories (Figure 4.1). The ultimate purpose was to obtain the microstructures that would outturn highest yield strengths and optimize consecutive heat treatments and chemical vapor deposition processes.

Three major yield strength contributors; solid solution, grain/phase boundary and precipitation strengthening, were calculated to find total yield strength. The results of calculated yield strength were compared with yield strength estimation of JMAT PRO and yield strength measurements obtained from literature as shown in Figure 4.1a. Figure 4.1b shows microstructure, carbides and gamma primes that provides precipitation strengthening. Figure 4.1c shows macrostructure, dendrites and grains that provides grain/phase boundary strengthening.

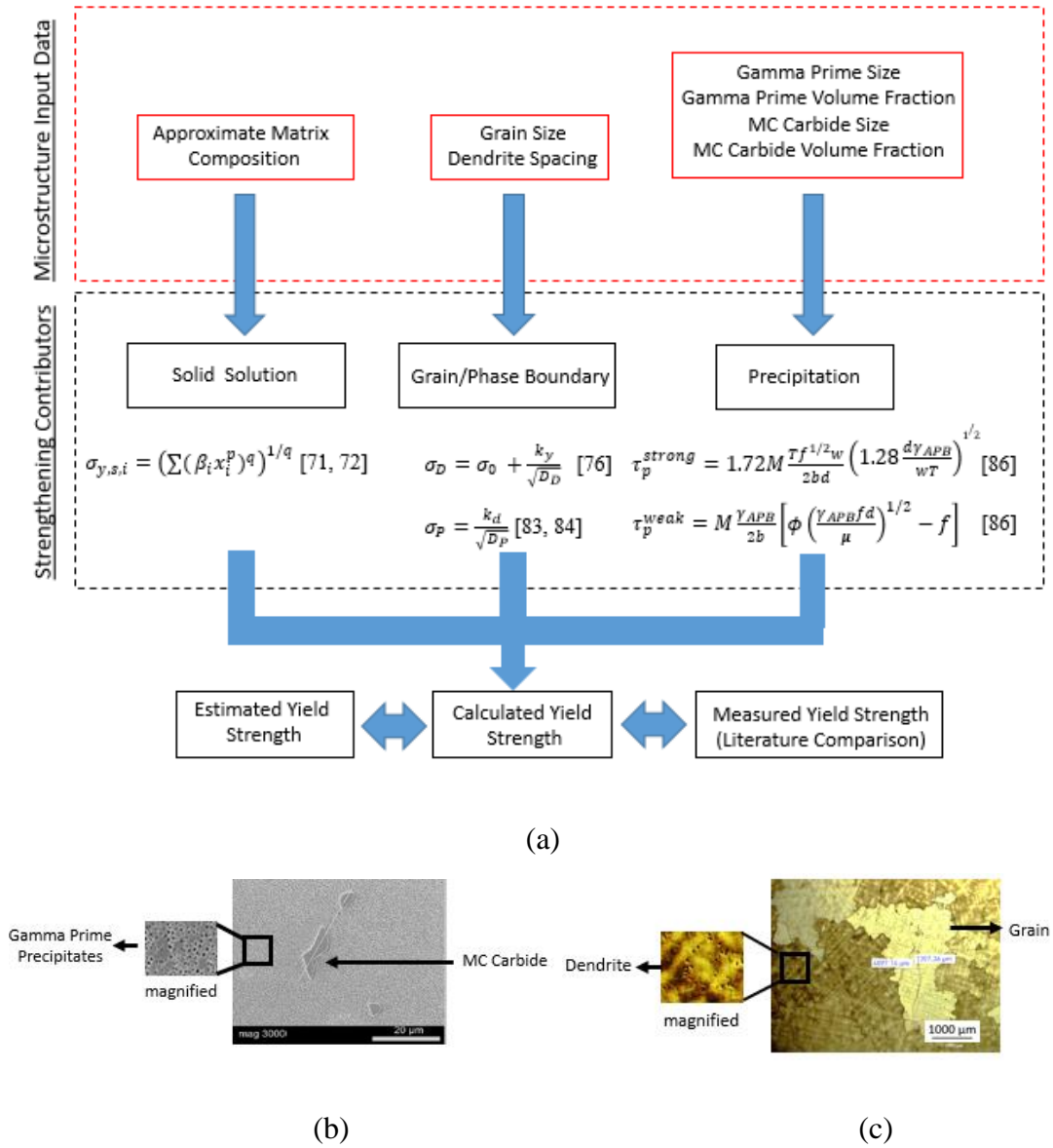


Figure 4.1: a) Yield strength calculation flow chart, b) SEM image, c) Optic Microscope Image.

Table 4.1 shows abbreviations that are used in Figure 4.1a and Chapter 4 as given below.

Table 4.1: List of Abbreviations in Chapter 4.

Symbols	Definition
$\sigma_{y,s,i}$	Solid solution strengthening
β_i	Solid solution constant
x_i	Atomic fraction
p and q	Concentration exponents
σ_D	Grain boundary strengthening
σ_0	Friction stress
k_y	Hall-Petch constant for grain boundary
D_D	Average grain size
σ_P	Phase boundary strengthening
k_d	Hall-Petch constant for dendrite
D_P	Average secondary dendrite spacing
τ_p^{strong}	Strong couple precipitation strengthening
τ_p^{weak}	Weak couple precipitation strengthening
M	Taylor equation factor
T	Line tension
f	γ' volume fraction
w	Elastic repulsion
b	Burgers vector
d	Average γ' radius
γ_{APB}	Anti-phase boundary energy
ϕ	γ' morphology constant
μ	Shear modulus

4.2 Solid Solution Strengthening

A slightly modified Hall-Petch equation was used for calculation of solid solution strengthening mechanism for IN 738 LC based on the equation given below. [71, 72]

$$\sigma_{y,s,i} = \left(\sum (\beta_i x_i^p)^q \right)^{1/q} [71, 72] \quad (\text{Eq. 1.9})$$

In this equation, $\sigma_{y,s,i}$ is solid solution strengthening, p and q are concentration exponents where $p = 2/3$ and $q = 3/2$. β_i is a solid solution constant that was calculated for different alloying elements in binary systems Ni-X, with X being an element from the transition metal group by Mishima et. al [73]. x_i^p is the atomic fraction of each solid solution element in γ -matrix since the solid solution strengthening mostly occurs in the matrix phase. Composition change of γ -matrix

depending on temperature was calculated in JMAT PRO software in equilibrium condition as given in Figure 4.2.

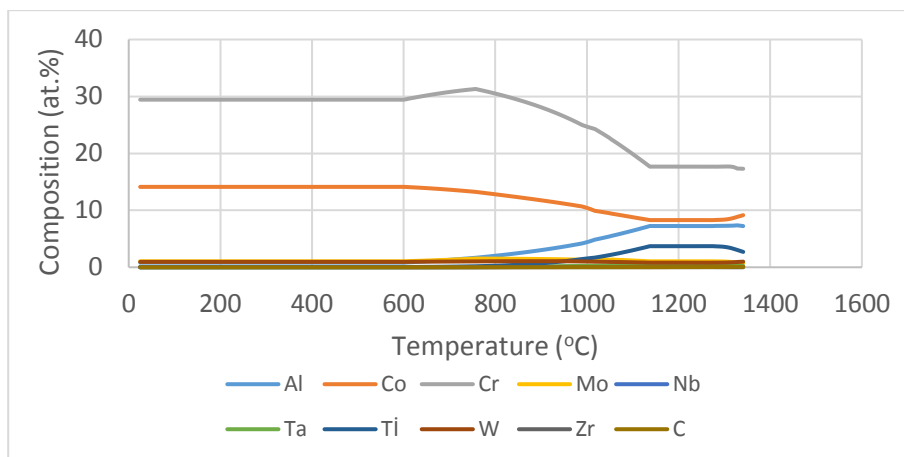


Figure 4.2: Composition change of γ -matrix depending on temperature calculated by JMAT PRO software.

As shown in Figure 4.2, Cr, Co, Al and Ti has the highest composition in γ -matrix independent of temperature. However, the composition fraction of Cr and Co is decreasing and the compositions of Al, Ti and Nb are increasing when the temperature is increased over 600°C. This could be due to dissolution Al, Ti and Nb rich γ' -Ni₃(Al, Ti, Nb) precipitates to the matrix. However, this simulation is valid for thermodynamic equilibrium condition. In the experimental condition, during cooling of IN 738 LC samples, γ' particles reprecipitate and grow by retrieving Al, Nb and Ti from the γ -matrix.

Below 600°C, composition of γ -matrix showed constant composition profile in JMAT PRO results (Figure 4.2). JMAT PRO γ -matrix composition below 600°C was used as constant γ -matrix composition for all samples with different heat treatment histories for the solid solution strengthening calculations. Strengthening β_i coefficients, atomic fraction calculated by JMAT PRO for below 600°C, and calculated solid solution contributions of each element in γ -matrix are given in Table 4.2 [73]. Total solid

solution contribution was calculated to be 273 MPa for IN 738 LC at room temperature composition.

Table 4.2: IN 738 LC Solid Solution Constants and Calculated Contributions of Alloying Elements [73].

Elements	β_i (MPa At.Fraction ^{-1/2})	x_i^p	$(\beta_i x_i^p)^{1/q}$ (MPa)
Ni	Balance element.	5.36×10^{-1}	Balance element.
Ti	775	4.88×10^{-4}	4.80
Nb	1183	6.26×10^{-5}	1.87
Ta	1191	1.22×10^{-4}	2.93
C	1061	1.21×10^{-6}	0.12
Co	39.40	1.41×10^{-1}	10.68
Cr	337	2.94×10^{-1}	149.12
W	977	9.46×10^{-3}	43.71
Mo	1015	1.05×10^{-2}	48.68
B	Ignored.	2.74×10^{-8}	Ignored.
Zr	2359	2.31×10^{-5}	1.92
Al	225	8.18×10^{-3}	9.14
Total Solid Solution Strengthening			273.00

The β_i coefficients given in Table 4.2 and composition profile given in Figure 4.2 for equilibrium condition were used to calculate the change of solid solution strengthening against temperature as shown in Figure 4.3.

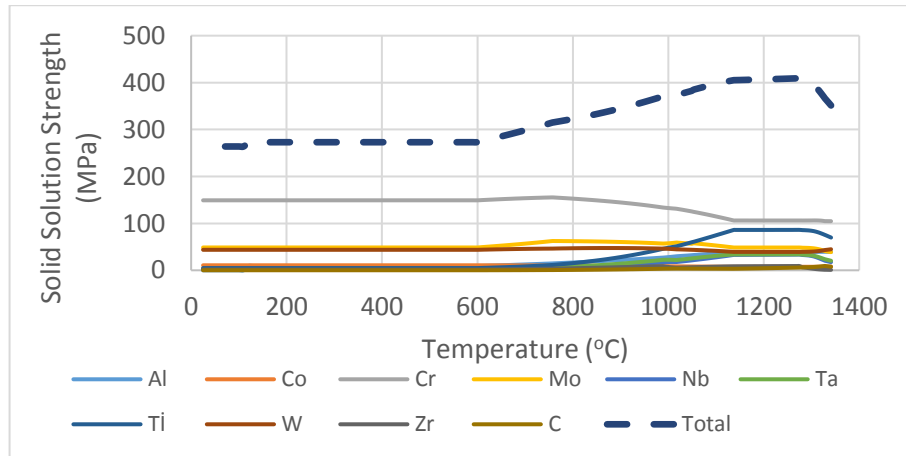


Figure 4.3: Solid solution contribution of alloying elements in γ -matrix of IN 738 LC depending on temperature (in equilibrium).

Highest solid solution contribution was acquired from Co, Mo, Cr and W for IN 738 LC matrix below 1000°C. Above 1000°C solid solution contribution of Ti showed a sharp increase due to dissolution of γ' -Ni₃(Al, Ti, Nb) particles. Solid solution contribution increase of Al and Nb were relatively lower since Al has lower solid solution strengthening constant and Nb has considerably lower composition (Table 4.2).

The assumption of using the constant composition below 600°C (Figure 4.2) for solid solution strengthening contributions of all samples with different microstructures, is accepted as an approach for simplification of calculations.

4.3 Phase/Grain Boundary Strengthening

Phase (dendrite boundaries) and grain boundary strengthening mechanisms contribute together to yield strength of the material. Grain boundaries and dendrites act as barriers against dislocations and block their movement. Therefore, grain size and dendrite spacing are important parameters to improve yield strength.

4.3.1 Phase Boundary Strengthening

Phase boundary strengthening was calculated by using secondary dendrite spacing. The Hall-Petch equation was used for this calculation.

$$\sigma_P = \frac{k_d}{\sqrt{D_P}} [83, 84] \text{ (Eq. 1.11)}$$

In this equation, k_d is Hall-Petch constant. D_P is dendrite arm spacing that was measured using the method given under section 3.2.4.2.4 Grain Size and Dendrite Spacing Determination. k_d is accepted as 230 MPa $\mu\text{m}^{1/2}$ which is reported by Z. C. Cordero et. Al for pure Ni [85]. The experimental group investigated in this study was relatively small. The conditions and abbreviations of applied processes and their results are given in Table 4.3 and Table 4.4.

Table 4.3: Heat Treatment and Coating Conditions and Related Abbreviations.

Processes	Conditions	Abbreviations
Hipped	1200°C-10 h-150 MPa	H
Solutionized	1120°C-2 h-Ar C. (180°C/min)	S
Coating 1	1000°C-20 h-F. C. (7°C/min)	C1
Coating 2	1050°C-16 h-F. C. (7°C/min)	C2
Coating 3	1100°C-12 h-F. C. (7°C/min)	C3
Aging	845°C-24 h-Ar. C. (180°C/min)	A

Table 4.4: Secondary Dendrite Spacing and Phase Boundary Strengthening Results.

Processes	Secondary Dendrite Spacing	Phase Boundary Strengthening
H	67	28,1
H+S	59	29,9
H+S+A	102	22,8
H+S+C1	86	24,8
H+S+C2	107	22,2
H+S+C3	-	-
H+S+C1+A	125	20,6
H+S+C2+A	129	20,3
H+S+C3+A	-	-

As show in Table 4.4, application of heat treatments and CVD process decreased the phase boundary strengthening due to increase in secondary arm spacing. The phase boundary strengthening increased the yield strength in between 20-30 MPa.

The phase boundary strengthening could not be calculated for H+S+C3, and H+S+C3+A. This is due to dissolution of secondary dendrite arms into matrix during CVD process applied at 1100°C-12 hours. This could be due to high coating temperature that allows the dissolution of secondary dendrite arm spacing at extended growth times.

Phase boundary strengthening was not considered in during total yield strength calculation since it has a relatively small effect on calculation of total yield strength.

4.3.2 Grain Boundary Strengthening

Grain boundaries block the dislocation movements and contribute together with the friction stress, to the yield strength of the γ -matrix. The inverse relationship between grain size and yield strength is explained by Hall-Petch equation as given below [76].

$$\sigma_D = \sigma_0 + \frac{k_y}{\sqrt{D_D}} \quad [76] \quad (\text{Eq. 1.10})$$

In this equation, σ_D is grain boundary strengthening, σ_0 is friction stress and k_y is Hall-Petch constant for grain boundaries. Kozar et. al used $750 \text{ MPa } \mu\text{m}^{1/2}$ as Hall-Petch constant for calculation of IN 100 grain boundary strengthening [78]. Since it's in the same family of superalloys with IN 738 LC and it has a similar chemical distribution, $750 \text{ MPa } \mu\text{m}^{1/2}$ was used as Hall-Petch constant in our calculations. Friction stress was accepted as $\sigma_0 = 21.8 \text{ MPa}$ for γ -matrix [79]. D_D is average grain size that was measured for each sample as mentioned under section 3.2.4.2.4 Grain Size and Dendrite Spacing Determination.

Due to the coarse grain size of IN 738 LC blade (over $2000 \mu\text{m}$ in thick parts, $500 \mu\text{m}$ thin parts), the grain boundary strengthening contribution was found to be below 50 MPa , and grain boundary showed just a slight change before and after heat treatments and CVD aluminide coatings.

Average grain boundary strengthening of cast and HIPed IN 738 LC samples (average thickness 17.6 mm) found to be 37.68 MPa and 35.86 MPa respectively. Due to grain size increase during HIP operation, grain boundary strengthening was slightly decreased.

Effect of solutionizing, coating and aging to IN 738 LC yield strength is investigated in following sections. All related microstructures were given in Chapter 3.

4.3.2.1 Effect of Solutionizing Parameters in Combine with Varying Aluminide Coating Temperature

The samples solutionized at various temperatures, times and cooling rates were all aluminide coated at 1000°C-20 hours, 1050°C-16 hours and 1100 °C-12 hours (furnace cooled 7°C/min) using chemical vapor deposition method.

CVD conditions changed the microstructure differently depending on initial microstructure that was formed by solutionizing conditions. Therefore, the effect of solutionizing in combined with CVD to grain boundary strengthening was investigated separately for solutionizing temperature, time and cooling rate variables.

4.3.2.1.1 Effect of Varying Solutionizing Temperature in Combine with Varying Aluminide Coating Temperature

HIPed IN 738 LC samples were solutionized at various temperatures to investigate the effect of solutionizing temperature on grain boundary strengthening. The solutionizing temperature was changed in between 1080-1235°C and other parameters were kept constant as shown in Table 4.5 The varying parameters are shown with darker background.

Table 4.5: Parameters Used to Investigate Effect of Solutionizing Temperature.

HIP Condition		Solutionizing Conditions		Aluminide Coating Conditions
Temperature (°C)	1200	Temperature (°C)	1080, 1100, 1120, 1150, 1180, 1200, 1235	1000 °C-20 hours 1050 °C-16 hours 1100 °C-12 hours (Furnace Cooling-7°C/min)
Time (h)	10	Time (h)	2	
Pressure (MPa)	150	Cooling Type and Rate (°C/min)	Ar Cooling-180	

The location of samples used in these heat treatments and CVD processes are given in Figure 4.4.



Figure 4.4: The location of samples that were solutionized in between 1080-1235°C for 2 hours and aluminide coated.

Post-solutionizing and post-coating grain boundary strengthening calculations of these samples are given in Figure 4.5.

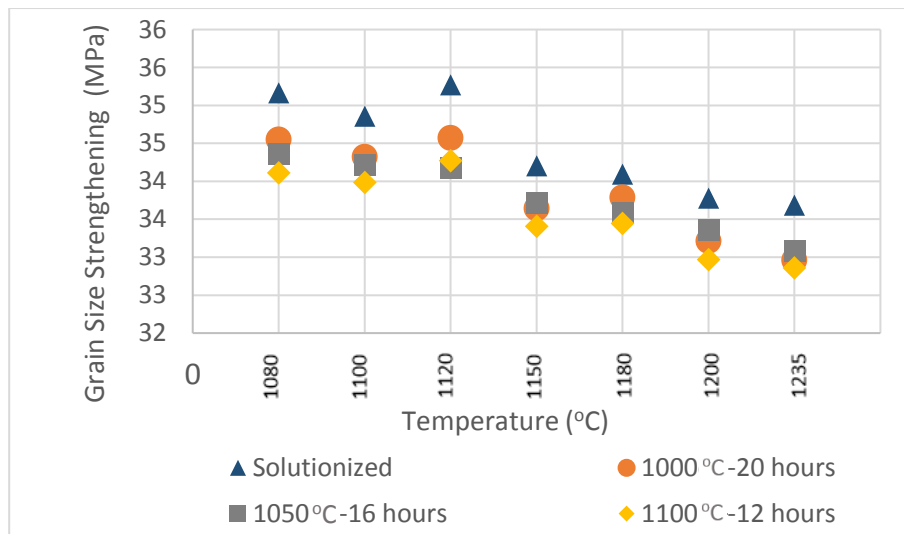


Figure 4.5: Post-solutionizing and post-coating grain boundary strengthening of samples that were solutionized at different temperatures.

In post-solutionizing microstructure, increasing solutionizing temperature decreased grain boundary strengthening due to increase in grain size. γ' microstructure of IN 738 LC showed bimodal to unimodal transformation above 1120°C. During this change coarse primary γ' particles that block to grain boundary movement, transformed into substantially smaller γ' particles. Due to this reason, a sharp decrease in grain size was seen at solutionizing temperatures above 1120°C that decreased γ' strengthening. This effect was also mentioned in studies of Koul and Castiio, and Anurag Thakur. [20, 38]

In post-coating microstructures, grain boundary strengthening found to be lower than post-solutionizing condition. Highest grain boundary strengthening was achieved after coating performed at 1000°C-20 hours followed by 1050°C-16 hours and 1100°C-12 hours. Similar to post-solutionizing trend, samples solutionized at lower temperatures showed higher grain boundary strengthening in their post-coating microstructures.

4.3.2.1.2 Effect of Varying Solutionizing Time and Cooling Rate in Combine with Varying Aluminide Coating Temperature

The samples solutionized for different time periods and cooled with different rates and CVD aluminide coated at three different conditions were investigated for grain boundary strengthening. The experimental parameters of these processes are given in Table 4.6. The varying parameters were shown with a darker background.

Table 4.6: Parameters of solutionizing for varying time periods and cooling rates, and CVD at varying temperatures.

HIP Condition		Solutionizing Conditions		Aluminide Coating Conditions
Temperature (°C)	1200	Temperature (°C)	1120	1000 °C-20 hours 1050 °C-16 hours 1100 °C-12 hours (Furnace Cooling-7°C/min)
Time (h)	10	Time (h)	1, 2, 4	
Pressure (MPa)	150	Cooling Type and Rate (°C/min)	Ar Cooling-180 Furnace Cooling-20	

The location of these samples are given in Figure 4.6.



Figure 4.6: The location of samples that were solutionized at 1120°C for 1, 2 and 4 hours and aluminide coated.

The grain boundary strengthening calculations for samples solutionized for 1, 2 and 4 hours, cooled in Ar and furnace are given in Figure 4.7 and 4.8 respectively.

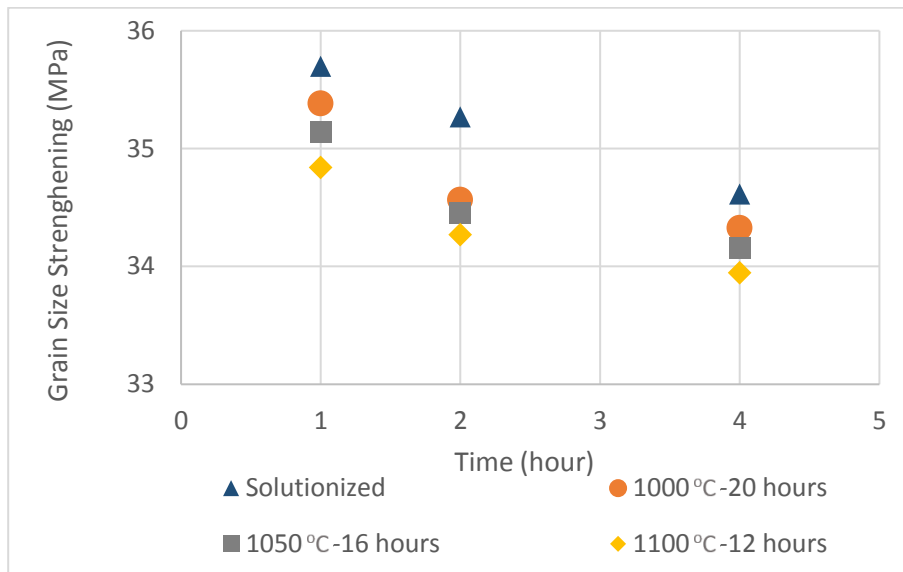


Figure 4.7: Post-coating grain boundary strengthening of samples that were solutionized for different time periods and Ar cooled.

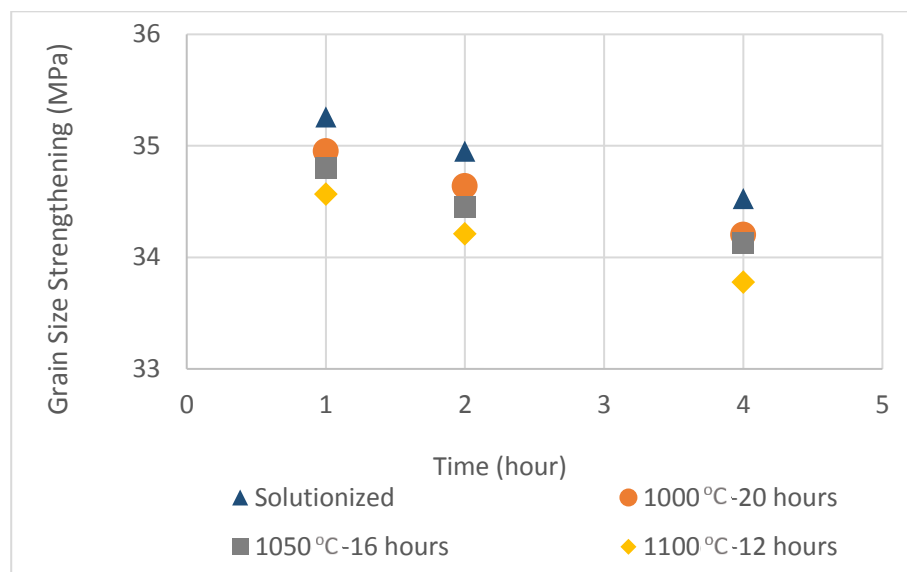


Figure 4.8: Post-coating grain boundary strengthening of samples that were solutionized for different time periods and furnace cooled.

The trend in between post-solutionizing and post-coating microstructures were obtained similarly to previous experiment group. Post-coating microstructures achieved lower grain boundary strengthening than post-solutionizing since, larger grain sizes were obtained in post-coating microstructures than post-solutionizing.

Increasing solutionizing time decreased grain boundary strengthening due to increase in grain sizes. Ar cooling achieved slightly higher grain boundary strengthening than furnace cooling due to lower grain size obtained in Ar cooling method. Furnace cooling allows grain size increase for a longer time period than Ar cooling.

The change of grain boundary strengthening in samples both during solutionizing and coating found to be less than 5 MPa which is a pretty low value compared to expected (over 500 MPa in room temperature) total yield strength of IN 738 LC.

4.3.2.2 Effect of HIP, Solutionizing, Varying Aluminide Coating Temperatures and Aging to Grain Boundary Strengthening of Thick and Thin Samples

A significant difference was seen for grain boundary strengthening between samples with different thickness. Due to inhomogeneous cooling after casting, the thick samples taken from middle section of turbine blade had considerably higher grain size than thin sample taken from the leading edge of the gas turbine blade. Therefore, thin samples acquired higher grain boundary strengthening than the thick samples. Effect of HIP, solutionizing, CVD temperature and aging to thick and thin samples was investigated with the parameters given in Table 4.7.

Table 4.7: Heat Treatment and Coating Parameters for Thick and Thin Samples.

HIP Condition		Solutionizing Conditions		CVD Conditions	Aging Condition
Temperature (°C)	1200	Temperature (°C)	1120	1000 °C-20 hours 1050 °C-16 hours 1100 °C-12 hours (Furnace Cooling-7°C/min)	845 °C-24 hours
Time (h)	10	Time (h)	2		
Pressure (MPa)	150	Cooling Type and Rate (°C/min)	Ar Cooling-180		

Additional to Table 4.7, one thick and one thin sample was directly aged after solutionizing to see the effect of aging on uncoated samples. The locations of thick and thin samples are given in Figure 4.9.

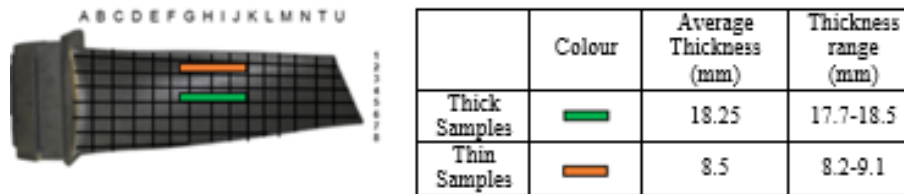


Figure 4.9: The locations of thick and thin sample group.

Grain boundary strengthening of as cast, HIPed and solutionized thick and thin samples are given in Figure 4.10.

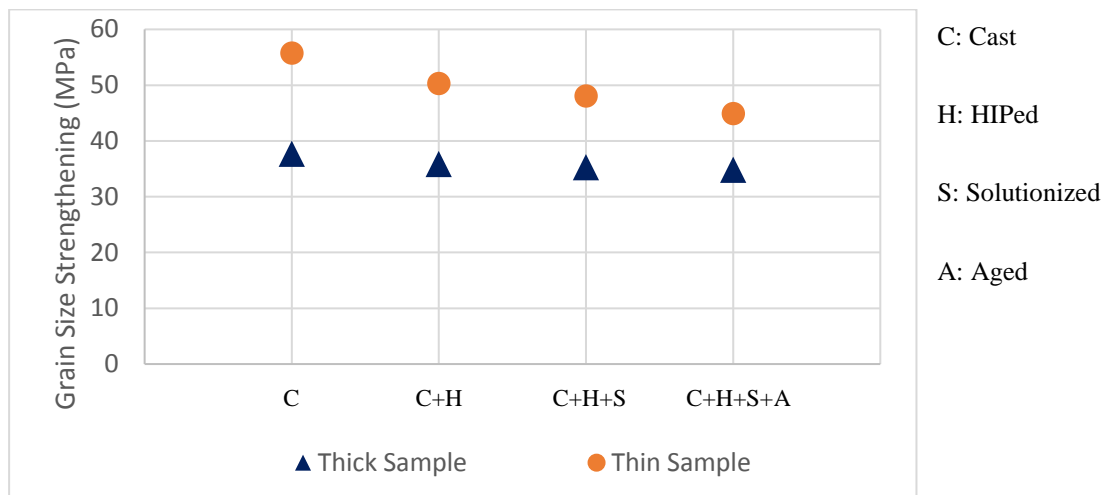


Figure 4.10: Grain boundary strengthening of the cast, HIPed, solutionized and aged thick and thin samples.

Grain boundary strengthening of the thin sample obtained to be considerably higher than thick sample since thick sample has considerably higher grain size than thin sample. This is due to inhomogeneous cooling of turbine blade during solidification. The thick samples also cooled slower cooling rate after the heat treatments and CVD process due its size.

Initially, the effect of HIP, solutionizing and aging (no coating applied) to grain boundary was investigated. HIP and solutionizing applied to these samples slightly decreased the grain boundary strengthening due to increase in grain sizes during these heat treatments.

Grain boundary strengthening decrease was slightly higher during HIP than solutionizing due to a higher temperature and a longer period of HIP process (1200°C-10 hours) than solutionizing (1120°C-2 hours). Aging did not change grain boundary strengthening greatly because of its low temperature 845°C despite the fact that it was applied for 24 hours.

The grain boundary strengthening decrease in the thin sample was slightly higher than thick sample after heat treatments and CVD, since thin sample had a significantly lower grain size (over 500 μm) that was more effected from grain size change than thick sample grain size (over 2000 μm).

Aging was also applied to samples coated at 1000°C-20 hours, 1050°C-16 hours, 1100°C-12 hours. Post-coating and post-aging grain boundary strengthening of thick and thin samples are given in Figure 4.11.

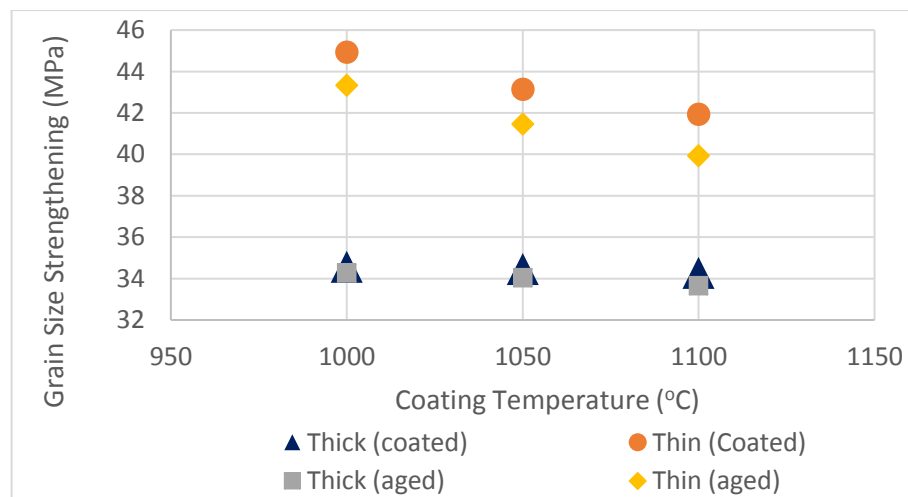


Figure 4.11: Grain boundary strengthening of post-coating and post-aging thick and thin samples.

Increase in CVD temperature resulted in decrease of grain size strengthening. Aging decreased the grain boundary strengthening slightly due to a minor increase in grain sizes during this heat treatment. The grain boundary strengthening decrease in the thin sample was slightly higher than the thick sample after CVD .

The decrease in grain boundary strengthening of directly aged samples (4.10) was slightly higher than the decrease in coated and aged samples (4.11). This was expected since coating applied prior to aging decreased the grain size strengthening and reduced the effect of aging slightly.

4.4 Precipitation Strengthening

The precipitation strengthening is derived from gamma prime (γ') and MC carbides for IN 738 LC. The MC carbides found to be Ta, Ti and Nb rich and in range of 5-50 μm . However, volume fraction of MC carbides didn't exceed 3% in samples with different heat treatment histories. Therefore, contribution of carbides to yield strength was ignored in this study.

Highest yield strength contribution is provided by γ' precipitation strengthening in Ni-based superalloys. There is a common view that this modeling can be performed by examining the interaction of dislocation pairs between small (weak pair coupling) and large (strong pair coupling) γ' particles. [86, 87] The formula for strong and weak pair coupling yield strength contribution are given below.

$$\tau_p^{strong} = 1.72M \frac{Tf^{1/2}w}{2bd} \left(1.28 \frac{\gamma_{APB}}{wT} \right)^{1/2} \quad [86] \quad (\text{Eq. 1.12})$$

$$\tau_p^{weak} = M \frac{\gamma_{APB}}{2b} \left[\phi \left(\frac{\gamma_{APB}fd}{\mu} \right)^{1/2} - f \right] \quad [86] \quad (\text{Eq. 1.13})$$

In these formula, M is Taylor equation factor, f is γ' volume fraction, w is elastic repulsion which is the order of unity, γ_{APB} is anti-phase boundary energy, μ is shear modulus. Volume fraction and radius of γ' particles were measured using the method given under section 3.2.4.2.5 Gamma Prime Size and Volume Fraction Determination.

ϕ is a constant depending on the morphology of γ' precipitate. For spherical particles $\phi = 0.72$ [86]. T is line tension calculated as 2.48×10^{-9} N for IN 738 LC by the formula given below.

$$T = \frac{\mu b^2}{2} \text{ [86] (Eq. 1.14)}$$

All the constants taken from the literature that was used to calculate yield strength and their reference numbers are given in Table 4.8.

Table 4.8: Strengthening Parameters Used in The Precipitation Hardening.

Parameters	Values	References
γ_{APB}	0.17 J/m ²	[20]
b	0.249 nm	[88]
μ_{Ni}	80 GPa	[89]
M	3	[90]

Maximum strength can be achieved if γ' precipitates can resist cutting and are too close to allow dislocation bypassing. The radius that maximum strength is achieved called as “critical radius”. It was calculated as $d_m = 29.2$ nm by the given formula below for IN 738 LC [86].

$$d_m = \frac{\mu b^2}{\gamma_{APB}} \text{ [86] (Eq. 1.15)}$$

In the Chapter 3, both primary and secondary γ' sizes were measured for samples with different microstructures and different heat treatment histories. All of them were found to be higher than the critical size of 29.2 nm which means strong coupling is the valid model for both primary and secondary γ' precipitates in our IN 738 LC samples.

In strong pair coupling, γ' strengthening is proportional to γ' volume fraction and inversely proportional to γ' size in the microstructure.

4.4.1.1 Effect of Solutionizing Parameters in Combine with Varying Aluminide Coating Temperature

The samples solutionized at various temperatures, times and cooling rates were all aluminide coated at 1000°C-20 hours, 1050°C-16 hours and 1100 °C-12 hours (furnace cooled 7°C/min) using chemical vapor deposition method.

CVD conditions changed the microstructure differently depending on initial microstructure that was formed by solutionizing conditions. Therefore, the effect of solutionizing in combined with CVD to grain boundary strengthening was investigated separately for solutionizing temperature, time and cooling rate variables.

4.4.1.1.1 Effect of Varying Solutionizing Temperature in Combine with Varying Aluminide Coating Temperature

HIPed IN 738 LC samples were solutionized at various temperatures to investigate the effect of solutionizing temperature on precipitation strengthening. The solutionizing temperature was changed in between 1080-1235°C and other parameters were kept constant as shown in Table 4.9 The varying parameters are shown with darker background.

Table 4.9: Parameters Used to Investigate Effect of Solutionizing Temperature.

HIP Condition		Solutionizing Conditions		Aluminide Coating Conditions
Temperature (°C)	1200	Temperature (°C)	1080, 1100, 1120, 1150, 1180, 1200, 1235	1000 °C-20 hours 1050 °C-16 hours 1100 °C-12 hours (Furnace Cooling-7°C/min)
Time (h)	10	Time (h)	2	

The location of samples used in these heat treatments and CVD processes are given in Figure 4.12.



Figure 4.12: The location of samples that were solutionized in between 1080-1235°C for 2 hours and aluminide coated.

The post-coating and post-solutionizing calculated primary and secondary γ' strengthening of these samples are given in Figure 4.13 and 4.14.

The total γ strengthening the contribution of γ' particles are given in Figure 4.15.

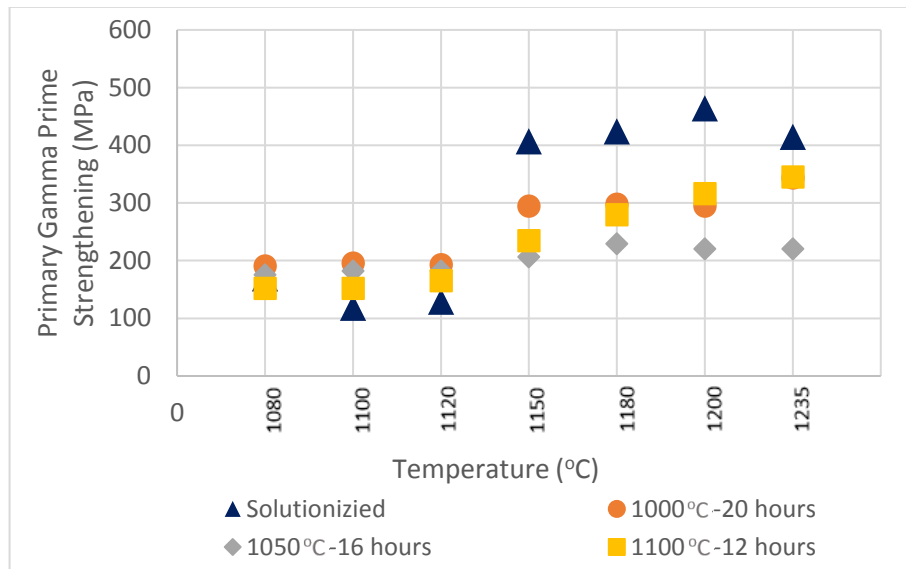


Figure 4.13: Primary γ' strengthening of post-solutionizing and post-coating samples.

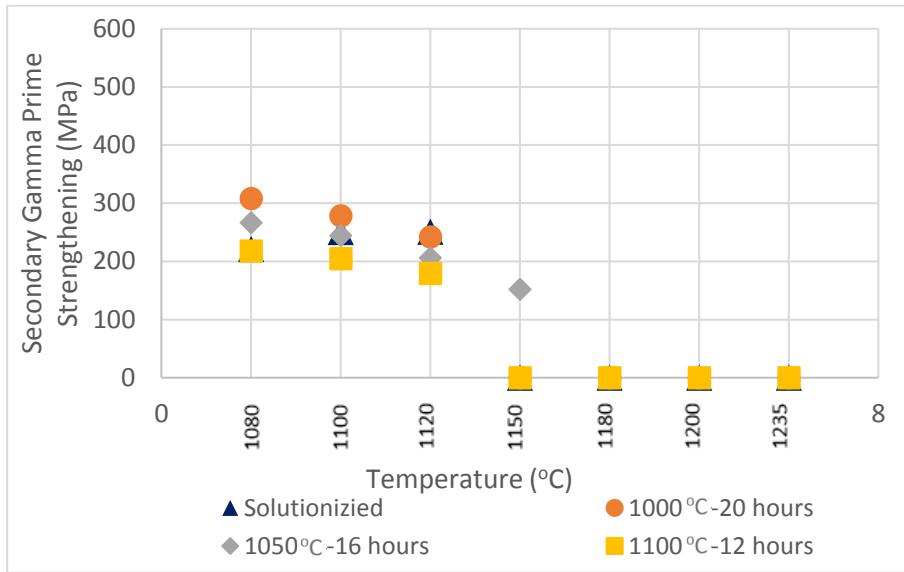


Figure 4.14: Secondary γ' strengthening of post-solutionizing and post coating samples.

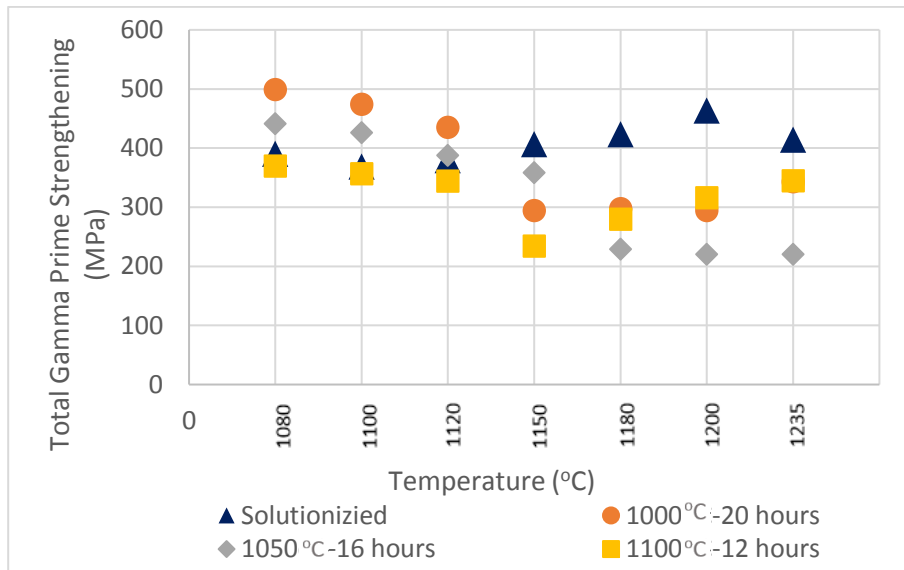


Figure 4.15: Total γ' strengthening of solutionized and post-coating samples.

As shown in Figure 4.13, primary γ' shows lower γ' strengthening contribution below 1150°C than above 1150°C in both post-solutionizing and post-coating microstructures, since bimodal microstructure was seen below 1150°C while unimodal microstructure was seen above this solutionizing temperature. Primary γ' size of the

unimodal region is considerably lower than primary γ' size of the bimodal region. Primary γ' volume fraction of the unimodal region is slightly higher than primary γ' volume fraction of the bimodal region. Due to these facts, primary γ' of the unimodal region provided higher yield strengthening contribution.

Post-coating microstructures of samples solutionized above 1150°C showed lower primary γ' strengthening than post-solutionizing. The reason for this trend was the increasing primary γ' sizes during coating. Post-coating microstructures of samples solutionized below 1150°C achieved higher primary γ' strengthening than post-solutionizing due to considerably increased primary γ' volume fraction and number of particles.

Secondary γ' strengthening was only seen at the samples solutionized below 1150°C, since solutionizing above this temperature provided unimodal structure. Increasing solutionizing temperature in between 1080-1120°C increased post-solutionizing secondary γ' strengthening and decreased post-coating secondary γ' strengthening slightly.

Secondary γ' strengthening results given in Figure 4.14 shows that after 1150°C-2 hours solutionizing, only post-coating bimodal structure was achieved with 1050°C-20 hours coating. This could be due to highest primary γ' size obtained in post-coating microstructures, after 1050°C-16 hours coating.

In the bimodal region below 1150°C solutionizing temperature, highest primary γ' strengthening was achieved after 1000°C-20 hours coating, followed by 1050°C-16 hours and 1100°C-12 hours coatings respectively. However, in the unimodal region above 1150°C solutionizing temperature, highest primary γ' strengthening was achieved after 1000°C-20 hours coating followed by 1100°C-12 hours and 1050°C-16 hours coatings respectively. The reason of this trend difference in unimodal and bimodal range is due to the different reaction of these microstructures against coating temperature. Unimodal region achieved highest γ' size after coating performed at 1050°C-16 hours while bimodal region achieved highest γ' size after coating performed

at 1100°C-12 hours. Since γ' strengthening is inversely proportional to γ' size, these conditions provided lowest yield strength for these different γ' structures.

Highest post-coating secondary strengthening was achieved after the coating at 1000°C-20 hours, followed by 1050°C-16 hours and 1100°C-12 hours. The secondary γ' strengthening of post-coating microstructure after 1100°C- 12 hours was lower than post-solutionizing conditions due to a considerable increase in particle size during this coating operation.

As shown in Figure 4.15, in case of post-solutionizing γ' strengthening contributions were compared, the samples solutionized above 1150°C has slightly higher γ' strengthening than samples solutionized below this temperature. The reason of this is the considerably low γ' sizes in unimodal microstructure that is seen at solutionizings above 1150°C.

In post-coating and post-solutionizing microstructures of samples solutionized below 1150°C bimodal structure was achieved. In bimodal structures, secondary γ' strengthening was calculated to be higher than primary γ' strengthening as shown in Figure 4.13 and 4.14 mainly due to lower size of secondary gamma primes.

In post-coating microstructures, highest total γ' strengthening was achieved after the coating performed at 1000°C-20 hours, followed by 1050°C-16 hours and 1100°C-12 hours respectively for the samples solutionized below 1150°C (bimodal region).

The post-coating microstructure of samples solutionized above 1150°C, and coated at 1000°C-20 hours and 1100°C-12 hours showed similar total γ' strengthening that was higher than the total γ' strengthening of coating performed at 1050°C-16 hours. This is due to high γ' size and low γ' volume fraction of the microstructure coated at 1050°C-16 hours.

4.4.1.1.2 Effect of Varying Solutionizing Time and Cooling Rate in Combine with Varying Aluminide Coating Temperature

The samples solutionized for different time periods and cooled with different rates in combined with CVD aluminide coating at three different conditions were investigated for precipitation strengthening. The experimental parameters of these processes are given in Table 4.10. The varying parameters were shown with a darker background.

Table 4.10: Parameters of solutionizing for varying time periods and cooling rates, and CVD at varying temperatures.

HIP Condition		Solutionizing Conditions		Aluminide Coating Conditions
Temperature (°C)	1200	Temperature (°C)	1120	1000 °C-20 hours 1050 °C-16 hours 1100 °C-12 hours (Furnace Cooling-7°C/min)
Time (h)	10	Time (h)	1, 2, 4	
Pressure (MPa)	150	Cooling Type and Rate (°C/min)	Ar Cooling-180 Furnace Cooling-20	

The location of these samples are given in Figure 4.16.



Figure 4.16: The location of samples that were solutionized at 1120°C for 1, 2 and 4 hours and aluminide coated.

The post-solutionizing and post-coating yield strength contribution of primary, secondary and total γ' strengthening contributions of these samples are given in Figure 4.17.

In post-solutionizing and post-coating microstructures, Ar cooling achieved lower γ' strengthening. Furnace cooling provided more time to γ' precipitation during cooling that increased total γ' volume fraction and γ' strengthening more than Ar cooling. However, as stated in Chapter 3, furnace cooling resulted in relatively disordered γ' precipitate shapes.

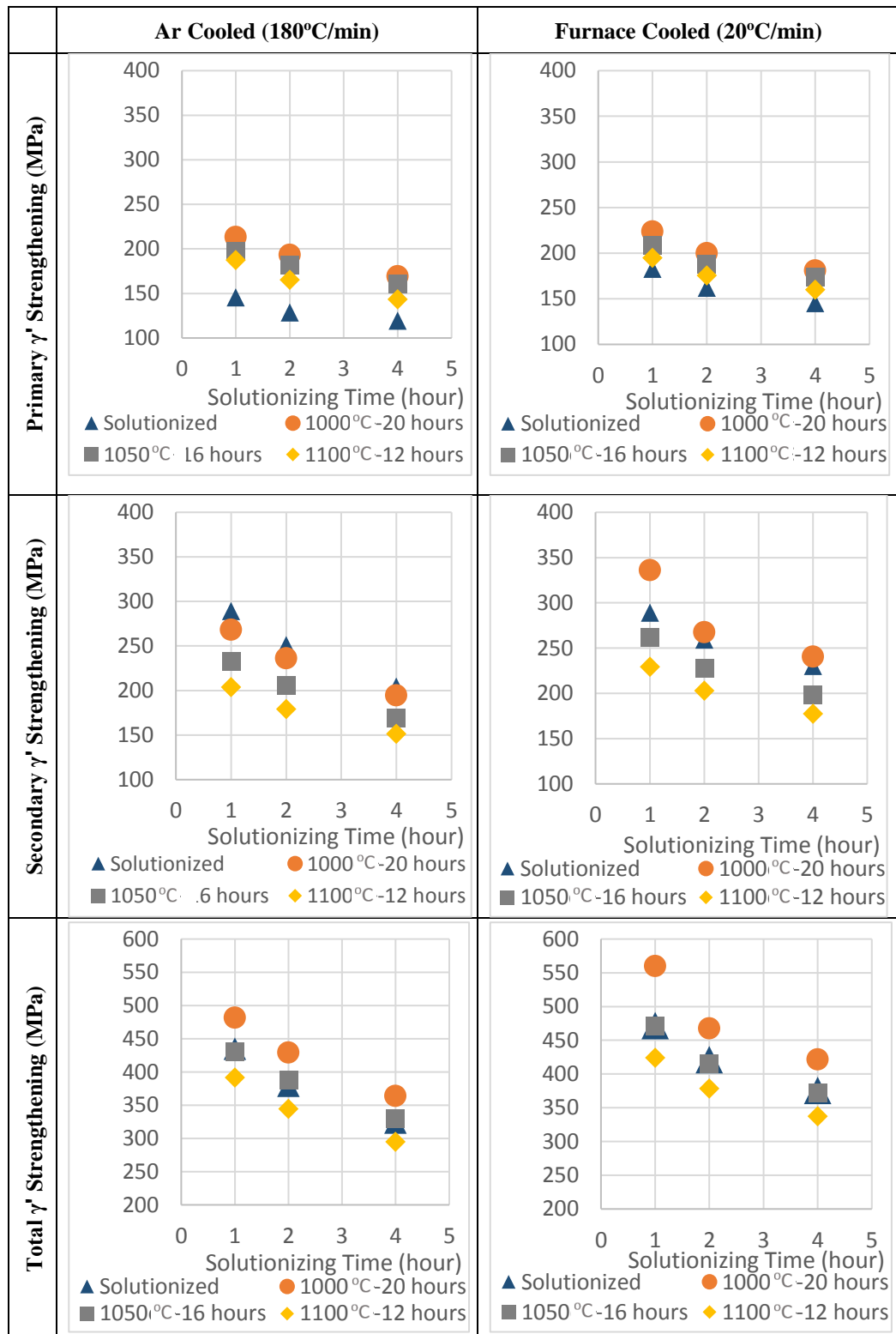


Figure 4.17: Post-solutionizing and post-coating, primary and secondary γ' strengthening for samples Ar and furnace cooled.

In the case of post-coating microstructure, both furnace and Ar cooled samples achieved higher primary γ' yield strengthening contribution than post-solutionizing microstructure. In secondary γ' strengthening group, only the sample furnace cooled after solutionizing and coated at 1000°C-20 hours achieved higher post-coating secondary γ' strengthening than post-solutionizing. The post-coating secondary γ' strengthening performed with Ar cooled samples was below the post-solutionizing due to lower volume fraction of secondary γ' particles. Furnace cooling allows a higher volume of secondary γ' fraction to form during cooling.

In the case of overall γ' strengthening, higher γ' strengthening results were achieved with the samples furnace cooled after solutionizing in both post-solutionizing and post-coating microstructures. Highest post-coating yield strength was achieved after 1000°C-20 hours coating, that is followed by 1050°C-20 hours and 1100°C-12 hours coatings respectively. Only coating condition that achieved higher γ' strengthening in post-coating condition than post-solutionizing condition was 1000°C-20 hours in both cooling types.

Shorter coating periods at high temperature achieved lower γ' volume fraction and higher γ' size, accordingly lower yield strength. Longer coating periods at low temperatures achieved higher γ' volume fraction and lower γ' size, accordingly higher yield strength.

Increasing solutionizing time decreased γ' strengthening in post-solutionizing and post-coating microstructures. This trend was seen in both Ar and furnace cooled samples. The reason of this trend is the increase of γ' sizes and decrease of γ' volume fraction when solutionizing time was increased. Additionally, γ' sizes and precipitate free zone area were increased in microstructure when the solutionizing time was increased. This resulted in decrease of the γ' strengthening.

4.4.1.2 Effect of HIP, Solutionizing, Varying Aluminide Coating Temperatures and Aging to Precipitation Strengthening of Thick and Thin Samples

Effect of HIP, solutionizing, CVD temperature and aging to thick (taken from the thick middle section) and thin (leading edge of the turbine blade) samples was investigated with the parameters given in Table 4.11.

Table 4.11: Heat Treatment and Coating Parameters for Thick and Thin Samples.

HIP Condition		Solutionizing Conditions		CVD Conditions	Aging Condition
Temperature (°C)	1200	Temperature (°C)	1120	1000 °C-20 hours 1050 °C-16 hours 1100 °C-12 hours (Furnace Cooling-7°C/min)	845 °C-24 hours
Time (h)	10	Time (h)	2		
Pressure (MPa)	150	Cooling Type and Rate (°C/min)	Ar Cooling-180		

The location of these samples are given in Figure 4.18.

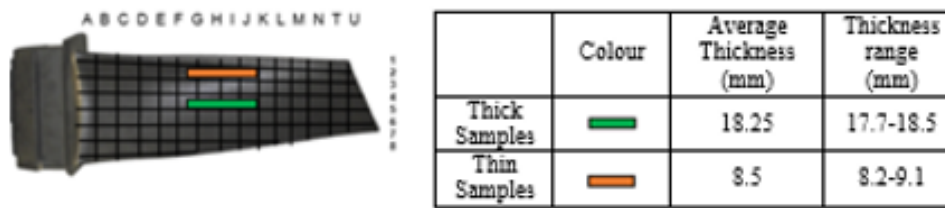


Figure 4.18: The locations of thick and thin samples.

Primary, secondary and total γ' strengthening of as cast, HIPed, solutionized and aged (no coating applied) thick and thin samples are given in Figure 4.19.

The thick and thin sample showed a similar yield strength results derived from primary and secondary γ' particles. However, due to higher volume fraction of γ' , the γ' contribution to yield strength found to be slightly higher for the thick sample. The reason of the higher γ' volume fraction of thick sample is the slower cooling after casting, following heat treatments and CVD.

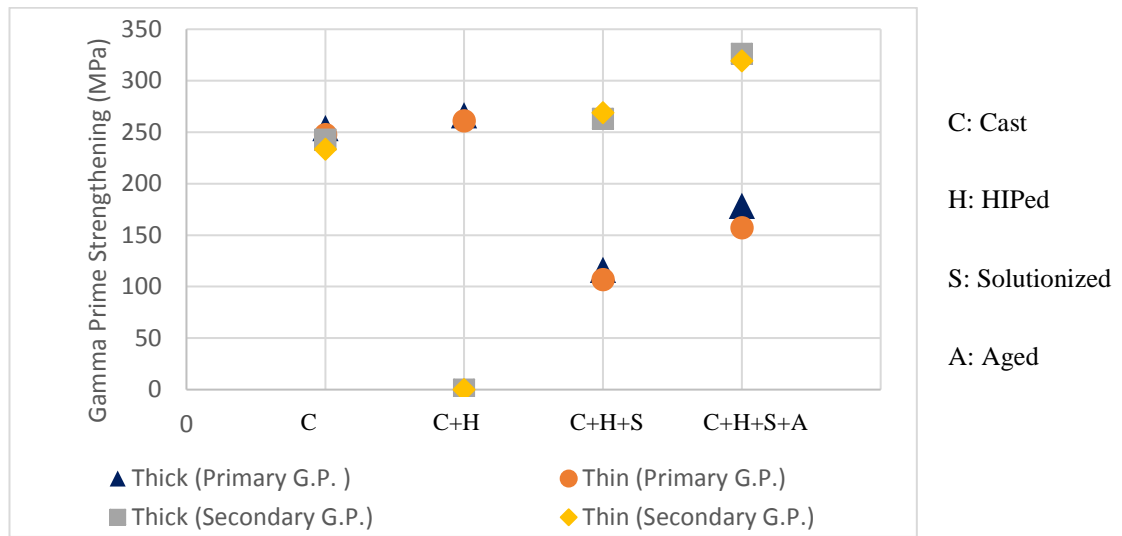


Figure 4.19: Primary, secondary and total γ' strengthening of the cast, HIPed and solutionized thick and thin samples.

There is a decrease in total γ' strengthening due to the disappearance of secondary γ' particles in the post-HIP microstructure as shown in Figure 4. 19. There is a slight increase in primary γ' strengthening after HIP operation. This result proves that secondary heat treatments are necessary to recover microstructure after HIP.

Solutionizing recovered the secondary γ' precipitates partially and increased the secondary γ' strengthening. However, during solutionizing an important part of primary γ' particles dissolved into matrix that decreased the yield strength contribution of primary γ' particles.

Aging increased both primary and secondary γ' volume fraction. Therefore, there was an increase in contribution of both primary and secondary γ' particles to yield strength.

Post-coating and post-aging primary, secondary and total γ' strengthening of both thick and thin samples are given in Figure 4.20.

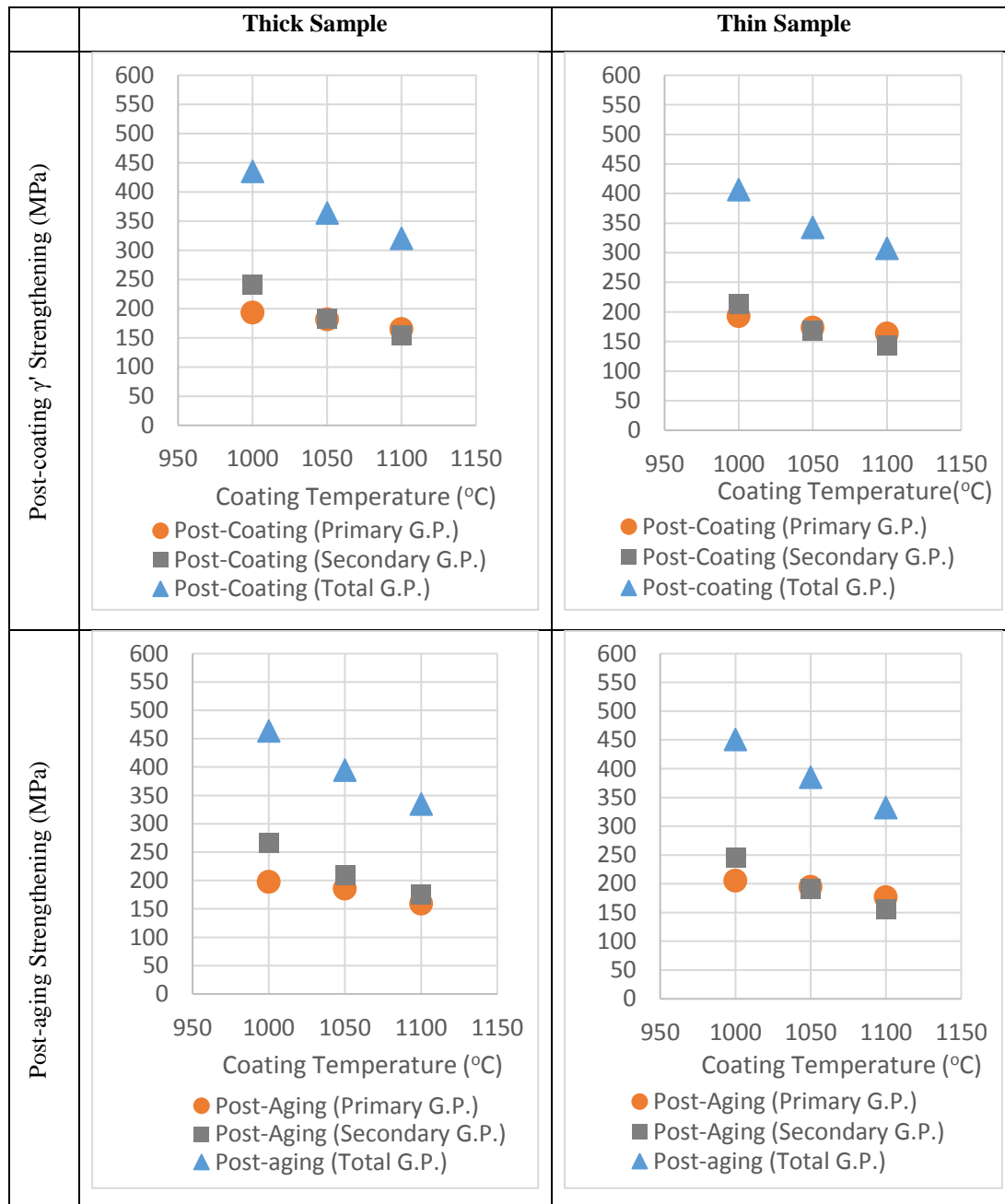


Figure 4.20: Post-coating and post-aging primary and secondary γ' strengthening of thick and thin samples.

As shown in Figure 4.20, aging increased primary and secondary γ' strengthening slightly due to increase in volume fraction these precipitates. This could be due to stabilized microstructures of samples after coatings applied above 1000°C for more

than 12 hours. Thick sample had slightly higher γ' strengthening than thin sample in both post-coating and post-aging microstructures.

Total γ' strengthening comparison of thick and thin samples is given in Figure 4.21. There is a slight difference between the results of thick and thin samples. Due to slower cooling of thick sample, γ' volume fraction of this sample was found to be higher in both post-coating and post-aging microstructures. Due to this reason γ' strengthening of thick sample was slightly higher than thin sample.

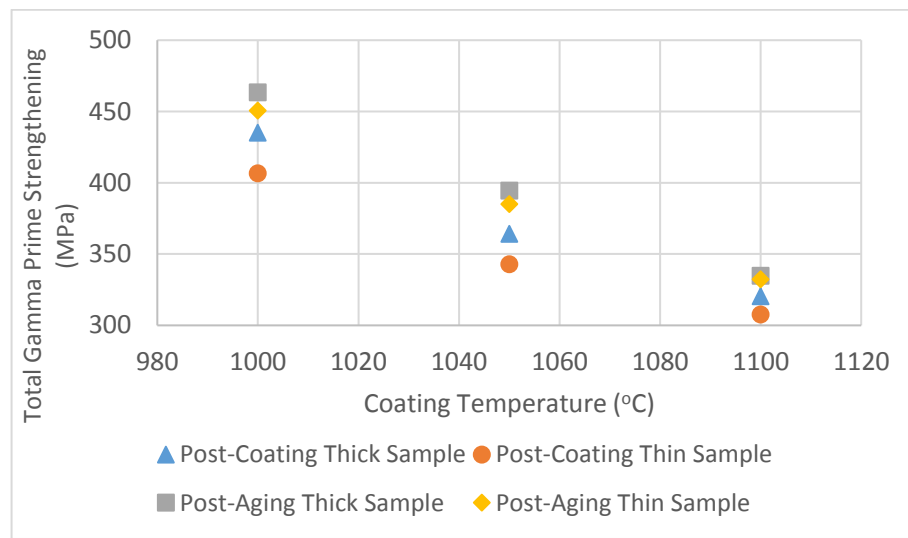


Figure 4.21: Post-coating and post-aging γ' derived yield strength of samples.

Increasing coating temperature decreased both post-coating and post-aging γ' strengthening. However, this decrease is higher in secondary γ' strengthening than primary.

This gap between primary and secondary strengthening is increased due to an increase of secondary γ' volume fraction after aging at 845°C-24 hours. The coatings performed at 1050°C-16 hours and 1100°C-12 hours showed closer primary and secondary yield strength due to higher secondary γ' size. A similar trend was seen in post-aging microstructures of these coatings.

In both of the samples, aging was found to be more effective to increase the yield strength provided by the secondary γ' particles than primary since the increase in secondary volume fraction increased yield strength more due to lower secondary γ' size than primary γ' size.

Direct aging at 845°C-24 hours provided a sharp increase in both primary and secondary γ' strengthening. This is due to high γ' volume fraction achieved with low γ' size in post-coating microstructure. Thick sample taken from middle section of turbine blade achieved higher yield strength than the thin sample taken from leading edge, in post-aging microstructure. This is due to slower cooling and accordingly obtained higher γ' volume fraction of thick sample.

4.5 Total Yield Strength

In this section, the sum of calculated solid solution strengthening, grain boundary strengthening, and γ' strengthening is given for the IN 738 LC samples with different microstructures and different heat treatment histories.

4.5.1.1 Effect of Solutionizing Parameters in Combine with Varying Aluminide Coating Temperature

The samples solutionized at various temperatures, times and cooling rates were all aluminide coated at 1000°C-20 hours, 1050°C-16 hours and 1100 °C-12 hours (furnace cooled-7°C/min) using chemical vapor deposition method.

CVD conditions changed the microstructure differently depending on initial microstructure that was formed by solutionizing conditions. Therefore, the effect of solutionizing in combined with CVD to grain boundary strengthening was investigated separately for solutionizing temperature, time and cooling rate variables

4.5.1.1.1 Effect of Varying Solutionizing Temperature in Combine with Varying Aluminide Coating Temperature

HIPed IN 738 LC samples were solutionized at various temperatures to investigate the effect of solutionizing temperature on total yield strength. The solutionizing temperature was changed in between 1080-1235°C and other parameters were kept constant as shown in Table 4.12. The varying parameters are shown with a darker background.

Table 4.12: Parameters Used to Investigate Effect of Solutionizing Temperature.

HIP Condition		Solutionizing Conditions		Aluminide Coating Conditions
Temperature (°C)	1200	Temperature (°C)	1080, 1100, 1120, 1150, 1180, 1200, 1235	1000 °C-20 hours 1050 °C-16 hours 1100 °C-12 hours (Furnace Cooling-7°C/min)
Time (h)	10	Time (h)	2	

The location of these samples are shown in Figure 4.22.

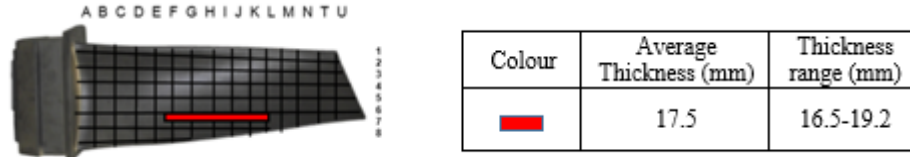


Figure 4.22: The location of samples that were solutionized in between 1080-1235°C for 2 hours and aluminide coated.

The sum of solid solution, grain boundary, and precipitation strengthening of these samples are given in Figure 4.23. The yield strength contributions and total yield strength results are given in Table 4.13.

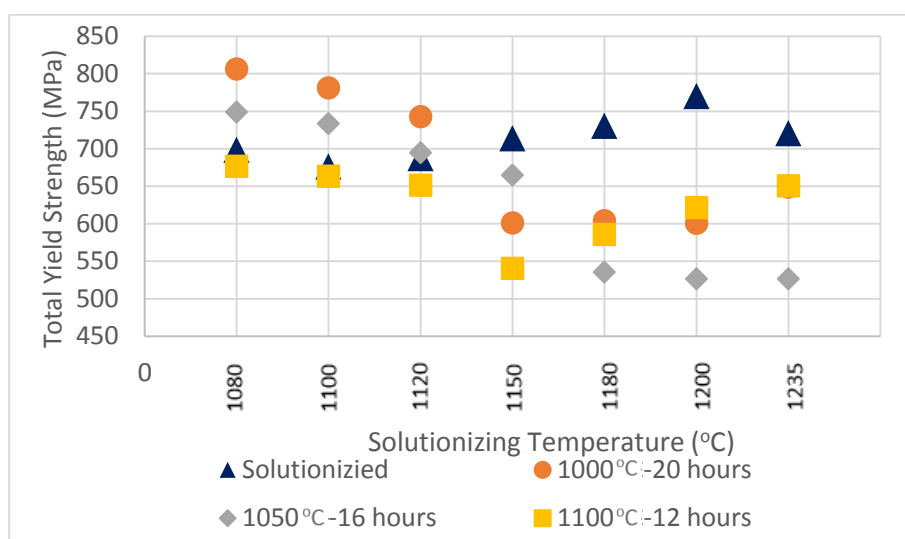


Figure 4.23: Post-solutionizing and post-coating total yield strength of samples that were solutionized and coated at different temperatures.

Table 4.13: Post-solutionizing and post-coating total yield strength of samples that were solutionized and coated at different temperatures.

Solutionizing Conditions	Post-solutionizing Total Yield Strength (MPa)				Post- coating Total Yield Strength Depending on Aluminide Coating Conditions (MPa)											
					1000°C-20 hours				1050°C-16 hours				1100°C-12 hours			
	P.	S.S.	G.B.	Total	P.	S.S.	G.B.	Total	P.	S.S.	G.B.	Total	P.	S.S.	G.B.	P.
1080 °C -2 hours-Ar C.	390	273	35	698	499	273	35	807	441	273	34	749	370	273	34	677
1100 °C -2 hours-Ar C.	369	273	35	677	474	273	34	781	426	273	34	733	357	273	34	664
1120 °C -2 hours-Ar C.	379	273	35	688	435	273	35	743	388	273	34	695	345	273	34	652
1150 °C -2 hours-Ar C.	407	273	34	714	295	273	34	601	358	273	34	665	235	273	33	541
1180 °C -2 hours-Ar C.	424	273	34	731	298	273	34	604	229	273	34	536	280	273	33	586
1200 °C -2 hours-Ar C.	464	273	34	770	295	273	33	601	220	273	33	527	316	273	33	622
1235 °C -2 hours-Ar C.	414	273	34	721	343	273	33	649	220	273	33	527	345	273	33	651

The definition of abbreviations used in Table 4.13 are given in Table 4.14.

Table 4.14. Abbreviations and Related Definitions.

Abbreviation	Definition
P.	Precipitation Strengthening
S.S.	Solid Solution Strengthening
G.B.	Grain Boundary Strengthening

In post-solutionizing microstructures, the samples solutionized above 1150°C with unimodal microstructure showed slightly higher yield strength than samples solutionized below this temperature with bimodal microstructure. This is due to lower γ' size obtained for the samples solutionized above 1150°C (unimodal region) than below this temperature (bimodal region).

In post-coating microstructures, highest total yield strength was achieved after coating at 1000°C-20 hours followed by 1050°C-16 hours and 1100°C-12 hours for the samples solutionized below 1150°C. In the same region, the coatings performed at 1000°C-20 hours and 1050°C-16 hours achieved higher yield strength than post-solutionizing condition while 1100°C-12 hours achieved lower yield strength. This was due to considerably high γ' size obtained at 1100°C-12 hours that decreased yield strength greatly.

In post-coating microstructures, the samples that were solutionized above 1150°C obtained to be unimodal and calculated yield strength of these samples were below the post-solutionizing condition. This was due to increase in primary γ' size that decreased yield strength and lack of relatively smaller secondary γ' particles that provides high strengthening contribution. After the total γ' strengthening was investigated for the samples that were solutionized at different temperatures, same investigation was performed for the samples solutionized for different time periods and cooled with different rates.

4.5.1.1.2 Effect of Varying Solutionizing Time and Cooling Rate in Combine with Varying Aluminide Coating Temperature

The samples solutionized for different time periods and cooled with different rates and CVD aluminide coated at three different conditions were investigated for total yield strength. The experimental parameters of these processes are given in Table 4.15. The varying parameters were shown with a darker background.

Table 4.15: Parameters of solutionizing for varying time periods and cooling rates, and CVD at varying temperatures.

HIP Condition		Solutionizing Conditions		Aluminide Coating Conditions
Temperature (°C)	1200	Temperature (°C)	1120	1000 °C-20 hours 1050 °C-16 hours 1100 °C-12 hours (Furnace Cooling-7°C/min)
Time (h)	10	Time (h)	1, 2, 4	
Pressure (MPa)	150	Cooling Type and Rate (°C/min)	Ar Cooling-180 Furnace Cooling-20	

The location of these samples are given in Figure 4.24.



Figure 4.24: The location of samples that were solutionized at 1120°C for 1, 2 and 4 hours and aluminide coated.

The post-solutionizing and post-coating total yield strength of Ar and furnace cooled samples are given in Figure 4.25 and 4.26. The yield strength contributions and total yield strength results are given in Table 4.16. The abbreviations used in Table 4.16 was given in Table 4.14.

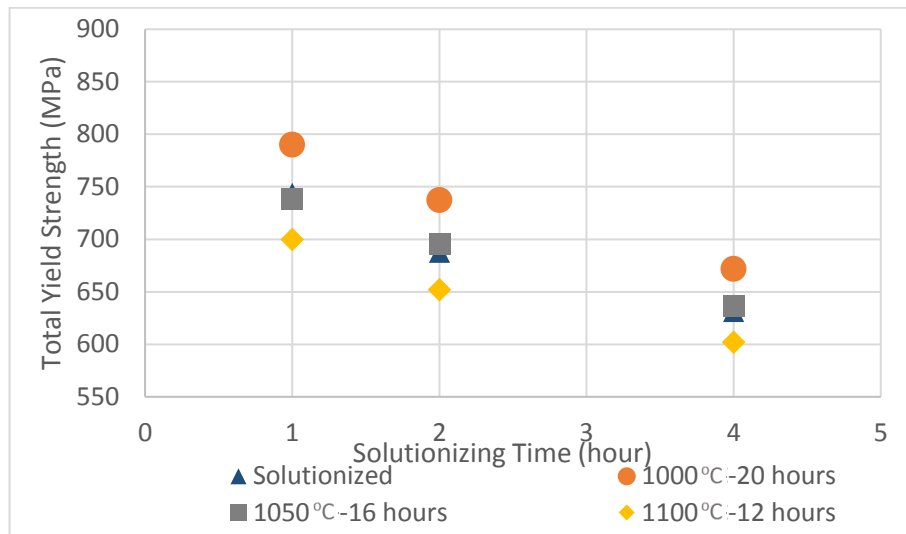


Figure 4.25: Post-solutionizing and post-coating total yield strength of samples that are solutionized for different time periods and Ar cooled.

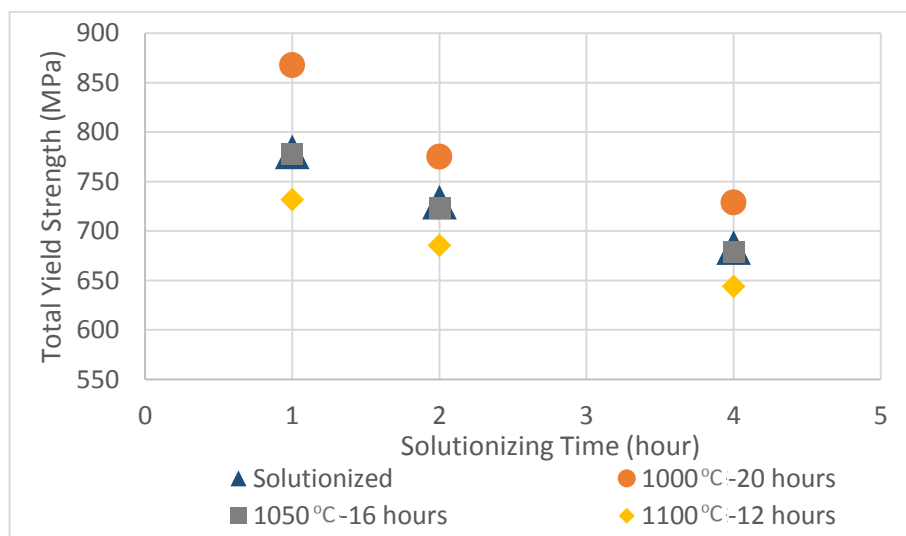


Figure 4.26: Post-solutionizing and post-coating total yield strength of samples that are solutionized for different time periods and furnace cooled.

Table 4.16: Post-solutionizing and post-coating total yield strength of samples that are solutionized for different time periods, Ar or furnace cooled.

Cooling Method	Time (hour)	Post-solutionizing Total Yield Strength (MPa)				Post- coating Total Yield Strength Depending on Aluminide Coating Conditions (MPa)											
						1000°C-20 hours				1050°C-16 hours				1100°C-12 hours			
		P.	S.S.	G.B.	Total	P.	S.S.	G.B.	Total	P.	S.S.	G.B.	Total	P.	S.S.	G.B.	Total
Ar C. (180°C/min)	1	435	273	36	744	482	273	35	790	430	273	35	739	392	273	35	700
	2	379	273	35	688	429	273	35	737	388	273	35	695	345	273	34	652
	4	324	273	35	631	364	273	35	672	330	273	34	637	295	273	34	602
Cooling Method	Time (hour)	P.	S.S.	G.B.	Total	P.	S.S.	G.B.	Total	P.	S.S.	G.B.	Total	P.	S.S.	G.B.	Total
F.C. (20°C/min)	1	472	273	35	780	560	273	35	868	471	273	35	779	424	273	35	732
	2	421	273	35	729	467	273	35	775	416	273	34	723	378	273	34	686
	4	376	273	35	683	422	273	34	729	372	273	34	679	337	273	34	644

Furnace cooling achieved higher yield strength than Ar cooling due to higher γ' volume fraction. In both cooling types, only the coating at 1000°C-20 hours achieved higher yield strength than the post-solutionizing condition. This was due to relatively small γ' size and higher volume fraction achieved at this specific condition.

Increasing solutionizing time decreased total yield strength in both post-solutionizing and post-coating microstructures due to a decrease in both precipitate and grain boundary strengthening.

4.5.1.2 Effect of HIP, Solutionizing, Varying Aluminide Coating Temperatures and Aging to Total Yield Strength of Thick and Thin Samples

Effect of HIP, solutionizing, CVD temperature and aging to thick (taken from the thick middle section) and thin (leading edge of the turbine blade) samples was investigated with the parameters given in Table 4.17 for total yield strength.

Table 4.17: Heat Treatment and Coating Parameters for Thick and Thin Samples.

HIP Condition		Solutionizing Conditions		CVD Conditions	Aging Condition
Temperature (°C)	1200	Temperature (°C)	1120	1000 °C-20 hours 1050 °C-16 hours 1100 °C-12 hours (Furnace Cooling-7°C/min)	845 °C-24 hours
Time (h)	10	Time (h)	2		
Pressure (MPa)	150	Cooling Type and Rate (°C/min)	Ar Cooling-180		

The location of these samples are given in Figure 4.27.

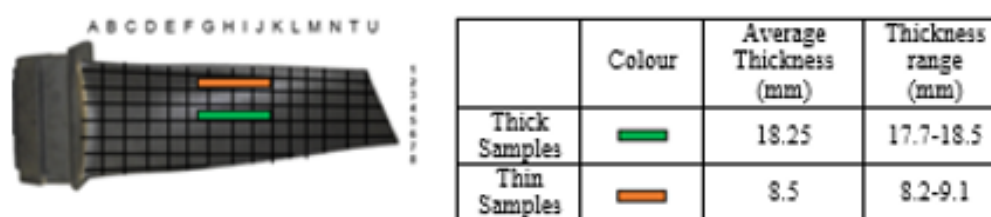


Figure 4.27: The locations of as cast, HIPed, solutionized, coated and aged thick and thin samples.

Calculated yield strength of as cast, HIPed, solutionized and aged (no coating applied) IN 738 LC thick and thin samples are given in Figure 4.28 and Table 4.18. The definition of abbreviations used in Table 4.18 were given in Table 4.14.

The thick sample have higher γ' strength contribution, however, the thin sample has higher grain boundary strengthening. These two factors are balancing each other that results in similar total yield strength in both thick and thin parts.

As shown in Figure 4.28 and Table 4.18 due to the disappearance of secondary γ' strengthening, there is a sharp yield strength decrease in the HIPed microstructures.

Solutionizing increased total yield strength due to precipitation of secondary γ' particles. Aging increased the total yield strength further mainly due to increase in primary and secondary γ' volume fraction.

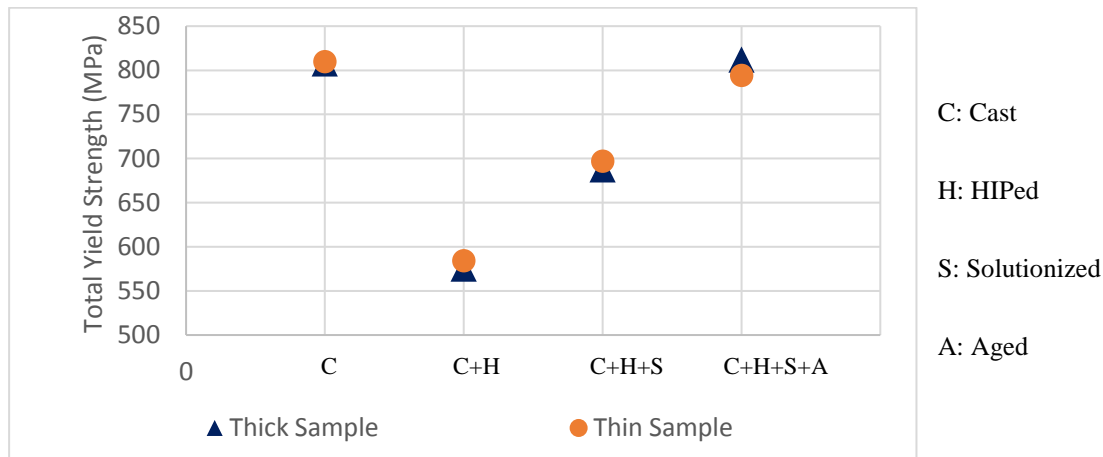


Figure 4.28: Calculated yield strength of as cast, HIPed, solutionized and aged thick and thin samples.

Table 4.18: Calculated yield strength of as cast, HIPed, solutionized and aged thick and thin samples.

Process	Thick Sample (18.25 mm)				Thin Sample (8.5 mm)			
	P.	S.S.	G.B.	Total	P.	S.S.	G.B.	Total
Casted	497	38	273	808	481	56	273	810
HIPed	266	36	273	575	261	50	273	584
Solutionized	379	35	273	688	376	48	273	697
Aged	504	35	273	812	476	45	273	794

The post-coating and post-aging yield strength of thick and thin samples are given in Figure 4.29. The yield strength contributions and total yield strength results are given in Table 4.19. The abbreviations used in Table 4.19 was given in Table 4.14. Both thick and thin samples showed similar yield strength. The thick sample have higher precipitate strength contribution, however, the thin sample has higher grain boundary strengthening. These two factors are balancing each other that results in similar total yield strength in both thick and thin parts. Aging applied after coating operations increased yield strength slightly due to highly stabilized microstructure after coating.

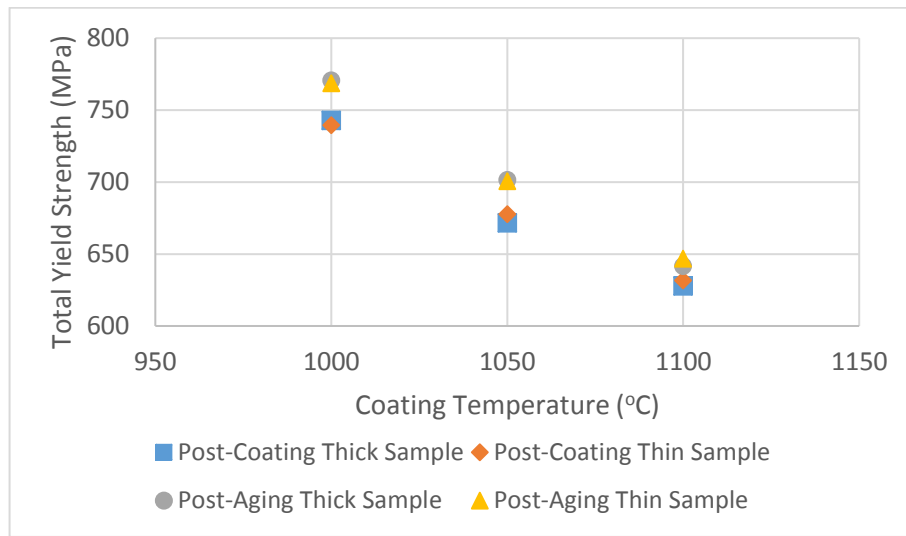


Figure 4.29: Post-coating and post-aging total yield strength of thin and thick samples.

Table 4.19: Post-coating and post-aging total yield strength of thin and thick samples.

Aluminide Coating Conditions	Total Yield Strength of Thick Sample (18.25 mm)							
	Post-coating (MPa)				Post-aging (MPa)			
	P.	S.S.	G.B.	Total	P.	S.S.	G.B.	Total
1000°C-20 hours	435	273	35	743	463	273	34	771
1050°C-16 hours	364	273	34	672	395	273	34	702
1100°C-12 hours	321	273	34	628	335	273	34	642
Aluminide Coating Conditions	Total Yield Strength of Thin Sample (8.5 mm)							
	Post-coating (MPa)				Post-aging (MPa)			
	P.	S.S.	G.B.	Total	P.	S.S.	G.B.	Total
1000°C-20 hours	418	273	48	739	451	273	45	769
1050°C-16 hours	357	273	47	678	385	273	42	701
1100°C-12 hours	314	273	45	632	332	273	42	647

When solutionized and aged (no coating applied) samples are compared to solutionized, coated and aged samples, aging had a higher effect of increasing yield strength when aging is applied directly after solutionizing. The coating operation

already effects as primary high temperature aging or replaces the actual aging operation. Therefore, the coating applied before aging decreases the effect of aging to increase γ' precipitation and accordingly volume fraction.

In the case of solutionized-aged and solutionized-coated samples compared, the aging had a better effect of increasing yield strength than coating since aging is applied at lower temperatures and for longer time periods than chemical vapour deposition. The reason post-coating microstructures achieves lower yield strength is due to high temperature of CVD aluminide coating operation. The CVD aluminide coatings achieve higher γ' size and lower γ' volume fraction due to high operation temperature above 1000°C.

The closest yield strength achieved to aging by coating is after the coating applied at 1000°C-20 hours. This coating condition is the closest condition regarding time and temperature to aging applied at 845°C-24 hours when it is compared to coating operations at 1050°C-16 hours and 1100°C-12 hours.

4.6 Yield Strength Simulation Comparison

JMAT PRO was used to simulate microstructure evolution during heat treatment and coating operations. In the previous chapter, microstructure evolution simulation results were given, and they were compared with experimental microstructure findings obtained after heat treatment and coating operations. In this section, JMAT PRO yield strength estimation for post-solutionizing, post-coating and post-aging microstructures were compared with the yield strength model results. The JMAT PRO simulation method and assumptions are given under section 3.2.3 Simulation Method.

The JMAT PRO simulation and yield strength model results for solutionizing at 1080, 1100, 1120, 1150, 1180, 1200 and 1235°C for 2 hours (Ar cooled) and coating at 1000°C-20 hours, 1050-16 hours and 1100°C- 20 hours (Furnace cooled) are given in Figure 4.30.

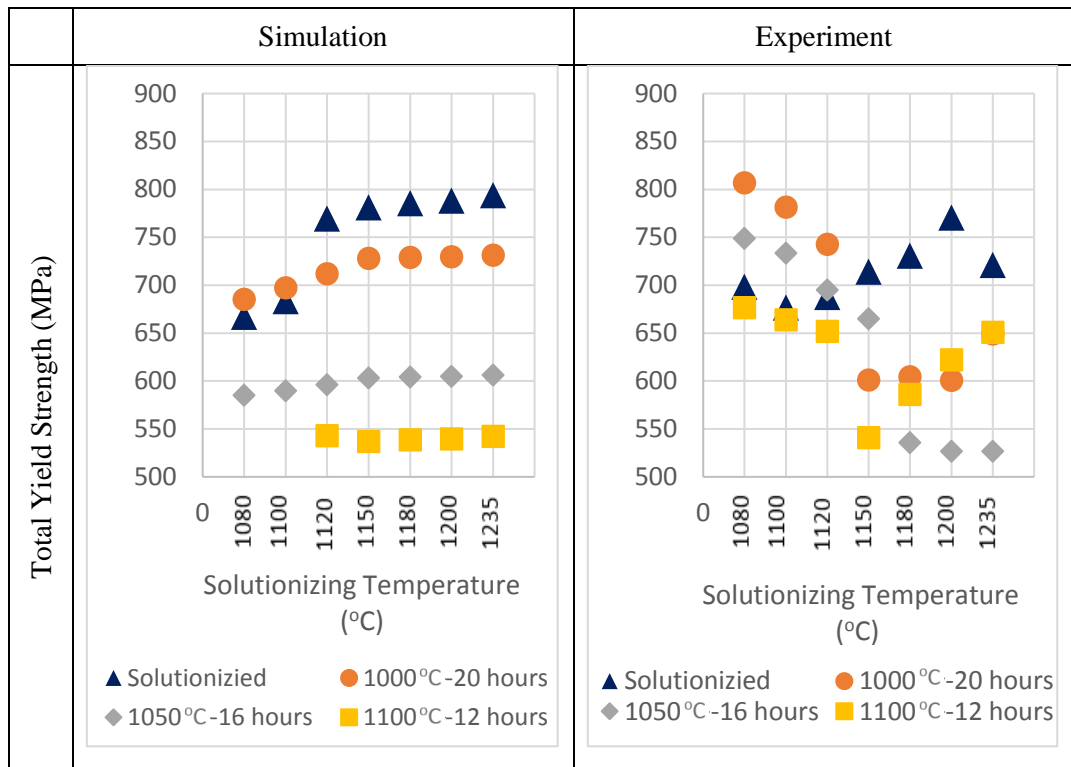


Figure 4.30: Yield strength estimation results of JMAT PRO and yield strength model for IN 738 LC samples solutionized at different temperatures.

Except few trends, results are found to be quite different. Initially, post-solutionizing microstructures were compared. The yield strength of samples that were solutionized above 1120°C was found to be higher than the samples solutionized below this temperature in yield strength model results. A similar trend was seen in JMAT RPO. However, the solutionizing temperature that yield strength started to increase in simulations was slightly higher than the experiments.

In JMAT PRO simulations yield strength result of 1000°C-20 hours coating found to be higher than post-solutionizing microstructure's yield strength for the samples that were solutionized up to 1100°C. On the other hand, in yield strength model, 1000°C-20 hours and 1050 °C-16 hours of coating results found to be higher than post-solutionizing microstructure for the samples that are solutionized up to 1120°C. The post-solutionizing microstructure yield strength was found to be higher than post-coating for the samples solutionized above 1120°C in yield strength model. Similarly,

the post-solutionizing microstructure yield strength was found to be higher than post-coating for the samples solutionized above 1150°C in JMAT PRO simulations.

The highest yield strength obtained for post-coating microstructure in JMAT PRO was achieved by 1000°C-20 hours of coating, followed by 1050°C-16 hours and 1100 °C-12 hours of coatings respectively. However, in yield strength model this trend is only valid for the bimodal region below 1150°C solutionizing temperature. Above this temperature, highest post-coating yield strength was achieved at 1000°C-20 hours, followed by, 1100-12 hours and 1050°C-16 hours. Since highest γ' size achieved in post-coating microstructure condition was 1050°C-16 hours, this coating provided the lowest γ' strengthening and accordingly lowest yield strength.

The JMAT PRO simulation and yield strength model results for samples solutionized at 1120°C for 1, 2 and 4 hours, Ar (180°C/min) or furnace cooled and coated at 1000°C-20 hours, 1050-16 hours and 1100°C- 20 hours (furnace cooled) are given in Figure 4.31. Unfortunately, it was not possible to type in solutionizing duration to JMAT PRO. The software assumes the solutionizing microstructure in equilibrium at given temperature without the interference of time duration. So the JMAT PRO simulation results for 1, 2 and 4 hours are accepted to be the same value as shown in Figure 4.31.

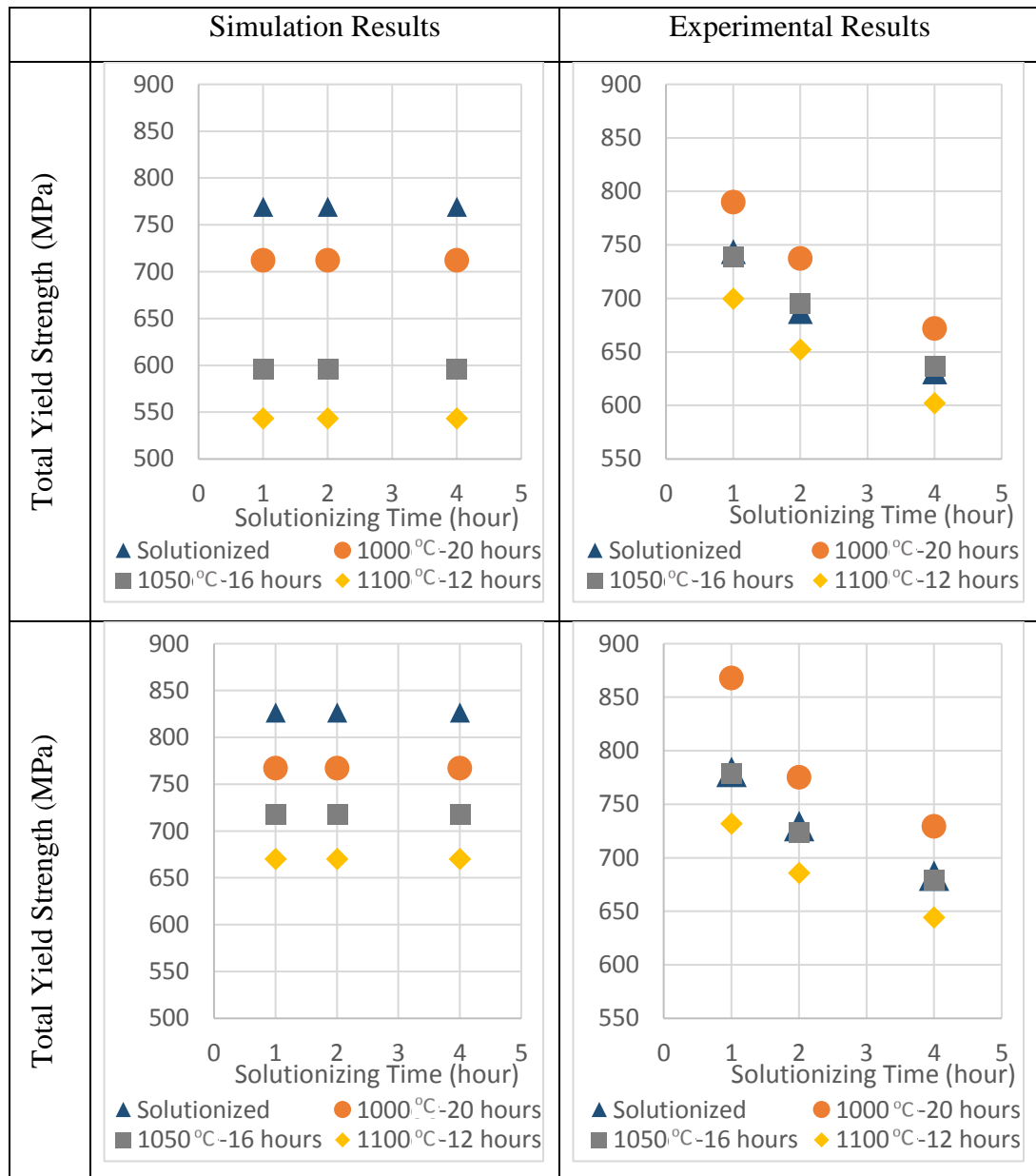


Figure 4.31: JMAT PRO yield strength estimation and yield strength model results for IN 738 LC samples solutionized for different time periods followed by Ar or furnace cooling.

In JMAT PRO results all post-coating microstructures achieved lower yield strength than post-solutionizing microstructure. However, in yield strength model results, the post-coating performed at 1000°C-20 hours achieved higher yield strength than post-solutionizing microstructure.

The post-coating and post-solutionizing JMAT PRO simulation and yield strength model total yield strength results for thick and thin samples solutionized at 1120°C for 2 hours (Ar cooled-180°C/min), coated at 1000°C-20 hours, 1050-16 hours and 1100°C- 20 hours (furnace cooled-7°C/min) and aged at 845°C-24 hours (Ar cooled 180°C/min) are given in Figure 4.32.

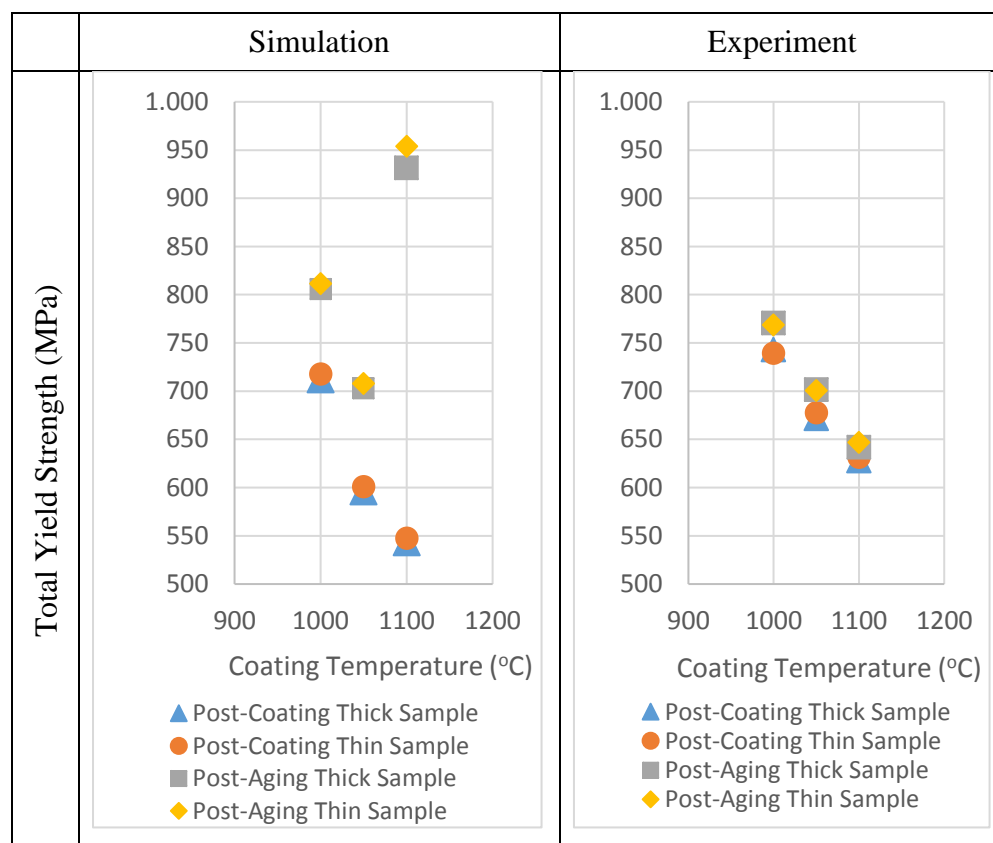


Figure 4.32: Yield strength estimation of JMAT PRO and yield strength model results for total yield strength of thick and thin IN 738 LC samples.

Post-coating microstructures of both samples showed a similar trend in both JMAT PRO and yield-strength model results. Increasing coating temperature decreased yield strength of post-coating microstructures.

Increasing coating temperature decreased the post-aging yield strength in the yield strength model results. Highest post-aging yield strength was achieved after the coating at 1000°C-20 hours in yield strength model. However, highest post-aging yield

strength was achieved at 1100°C-12 hours coating condition in JMAT PRO results. The JMAT PRO may be assuming that this coating temperature achieves partial solutionizing during coating that allows the following aging operation to be more effective. Aging process performed after this coating, increased the γ' volume fraction of solutionized microstructure and considerably the yield strength in simulation.

The JMAT PRO simulation and yield strength model results for thick and thin samples solutionized at 1120°C- 2 hours (Ar cooled-180°C/min) and directly aged (no coating applied) at 845°C-24 hours (Ar cooled-180°C/min) are given in Figure 4.33. No coating was applied to these samples.

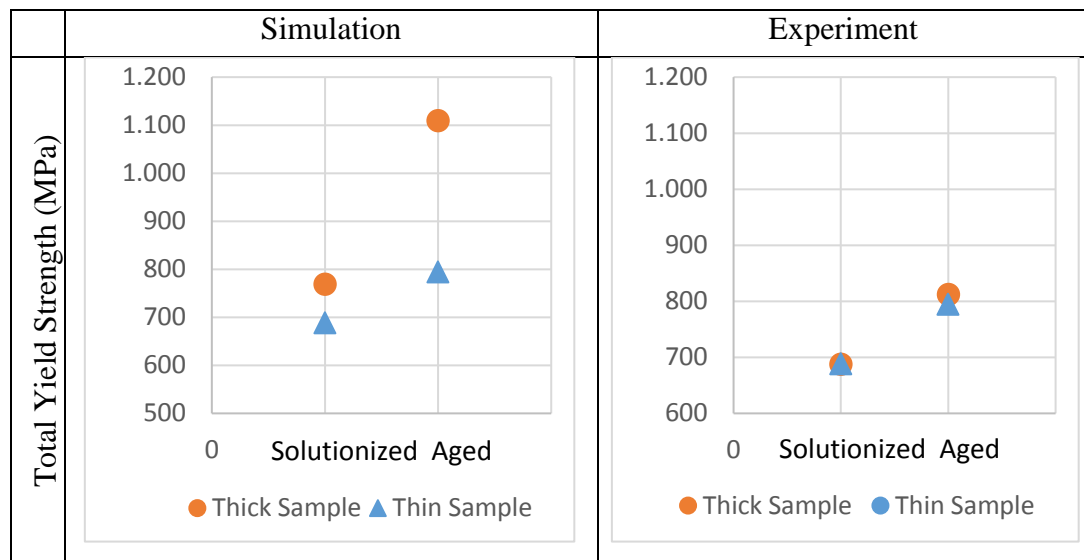


Figure 4.33: Yield strength model and JMAT PRO simulation yield strength estimation results for total yield strength of thick and thin IN 738 LC samples.

Similar trends were obtained in between JMAT PRO simulation and yield strength model results for the thin sample for both post-solutionizing and post-aging yield strength. However, the thick sample shows a much higher increase after aging in JMAT PRO results than yield strength results.

4.7 Literature Comparison

Calculated yield strength results were compared with tensile test results of IN 738 LC samples with similar microstructures obtained in literature.

E. Balikci, R. Mirshams and A. Raman has performed a tensile test for IN 738 LC samples of various microstructures under two different strain rate. The tensile test samples was solutionized at 1200°C for 4 hours and water quenched. Then samples were aged in between 1120°C-1200°C for different time periods that were not specifically pointed out. [93]

Similar microstructures were chosen from our experimental set to tensile test samples of E. Balikci, R. Mirshams and A. Raman. JMAT PRO software yield strength estimation and calculated yield strength model results were compared with tensile test results taken from literature as given in Table 4.20. [93]

The SEM images that are taken from literature and our SEM images, average γ' sizes of γ' particles in SEM images, heat treatment and coating conditions of samples are also provided in Table 4.20.

As input to JMAT PRO, the input data given in Table 3.1 and experimental conditions used in this study given in Table 4.20 were used.

Table 4.20: Literature tensile test, yield strength model, and JMAT PRO calculation results [93].

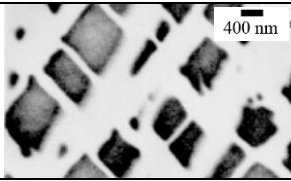
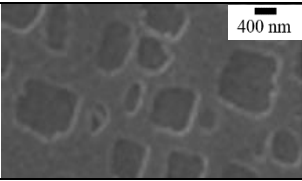
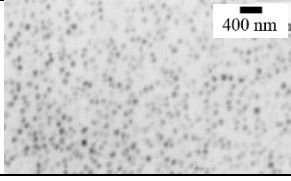
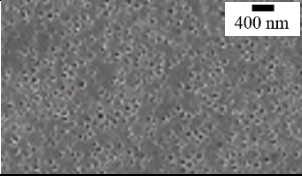
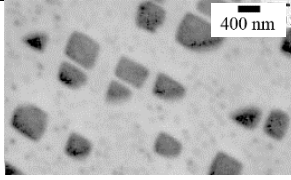
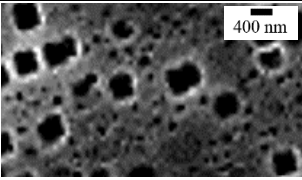
N u m b e r	Literature SEM Images	Literature Tensile Test Results (MPa)		IN 738 LC SEM Images	Yield Strength Model Results (MPa)	JMAT PRO Results (MPa)
		Low Strain 10^{-3} s^{-1}	High Strain $5 \times 10^{-5} \text{ s}^{-1}$			
1		710	697		644	670
	γ' size: 700 nm			γ' size: 702 nm-251 nm		
	Solutionizing 1200°C-4h -WQ+Aging (1120-1200 °C)			Solutionizing 1120°C-4 h-F.C.+Coating 1000°C-20 hours-F.C.		
2		853	857		721	788
	γ' size: 70 nm			γ' size: 62 nm		
	Solutionizing 1200°C-4h -WQ+Aging (1120-1200 °C)			Solutionizing 1235°C-2 h-Ar C.		
3		861	833		812	1110
	γ' size: 450-50 nm			γ' size: 437-109 nm		
	Solutionizing 1200°C-4h -WQ+Aging (1120-1200 °C)			Solutionizing 1120-2 h-Ar C.+ Aging 845°C-24 hours-Ar.C.		

Figure 4.34 shows the results of literature tensile test results with yield strength model and JMAT PRO software results in a better view for each comparison. The sample numbers in Table 4.15 and Figure 4.34 are identical.

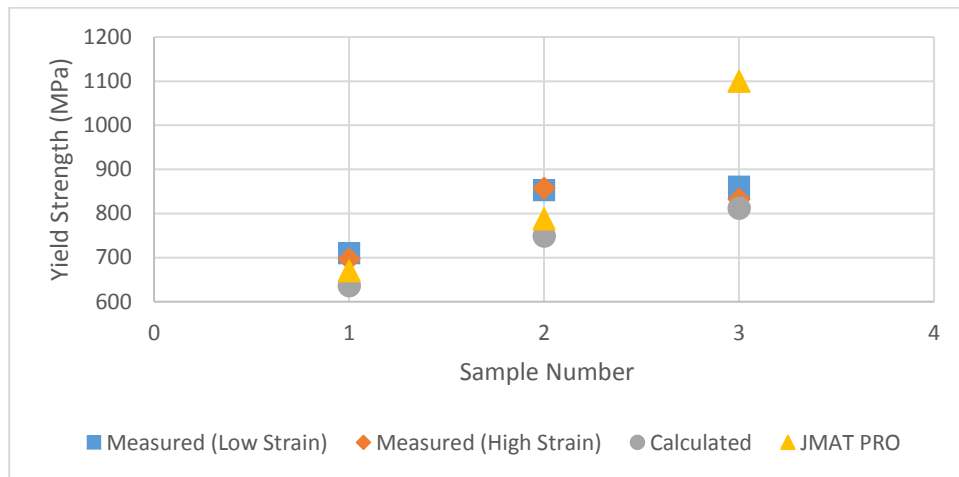


Figure 4.34: Literature tensile test (measured), yield strength model (calculated), and JMAT PRO calculation results. [93]

Yield strength model results were found to be slightly lower than actual tensile test results for both bimodal and unimodal structures. This could be due to several reasons:

- Literature study samples were 1 mm thick bars. However, grain profile of samples was not pointed out. It is highly possible that these bars don't have any grains or have limited number of grain boundaries due to a low surface area that increased the yield strength during tensile test.
- Yield strength contribution of carbides that were precipitated in grains and grain boundaries were ignored in this model due to a low fraction of carbides (below %3) in IN 738 LC.
- γ' particles below 10 nm would be hard to detect and precisely measure in SEM images. These particles have a strong contribution to yield strength due to their low size close to the critical size of γ' (24 nm) that achieves maximum yield strength.

Even though the yield strength model provides slightly lower results than actual tensile test results, the trend that is seen in between the different microstructures are the strongly similar as shown in Figure 4.34.

JMAT PRO yield strength estimation results for Sample 1 and 2 found to be relatively closer to calculated yield strength model and tensile test results found in literature. However, JMAT PRO yield strength estimation result for Sample 3 found to be considerably higher than calculated yield strength model and tensile test results found in literature.

4.8 Conclusion

Yield strength estimation was performed for as cast, HIPed, solutionized, aluminide coated and aged samples that were investigated in this chapter. A model was formed including solid solution, grain size and γ' strengthening of samples that have different microstructures. The microstructure results obtained in Chapter 3 were used as input. The results were compared with JMAT PRO estimations for yield strength and experimental tensile test results from the literature. The conclusion of these studies is listed as given below.

- Solid solution strengthening was calculated and assumed to be constant for all IN 738 LC samples. Highest contribution to yield strength was obtained from with Cr, Mo and W elements in IN 738 LC chemical composition.
- Grain size strengthening was calculated for each sample separately. Samples with higher grain size achieved relatively lower grain size strengthening. Due to grain size increase of samples during HIP, solutionizing, aluminide coating and aging, the yield strength contribution was constantly decreasing after each step applied. However, due to coarse grain size of IN 738 LC samples these changes were not greater than 20 MPa. The thick samples that were taken from middle section of turbine blade showed significantly lower grain size strengthening than samples taken from leading edge of turbine blade due to inhomogeneous cooling after casting.

- Phase boundary strengthening was calculated for a relatively small sample group. Since the strengthening contribution of dendrites found to be relatively lower they were not considered in calculation of total yield strength.
- γ' strengthening was performed for IN 738 LC samples depending on their γ' size and volume fraction. γ' strengthening found to be proportional to γ' volume fraction and inversely proportional to γ' size of the samples.
- Due to the disappearance of secondary γ' particles during HIP, yield strength was significantly decreased in post-HIPed microstructures.
- In post-solutionizing microstructures, the samples solutionized above 1150°C (unimodal region) showed slightly higher γ' strengthening than samples solutionized below this temperature (bimodal region) due to their dramatically lower size of γ' particles.
- In post-solutionizing microstructures, increasing solutionizing time decreased γ' strengthening due to lower γ' volume fraction obtained at longer solutionizing times. Additionally, furnace cooling achieved slightly γ' strengthening due to higher γ' volume fraction obtained in furnace cooled samples. Aging at 845°C-24 hours increased γ' strengthening of coated samples on a small scale since it only increased γ' volume fraction slightly.
- Highest post-coating total yield strength was achieved after 1000°C-20 hours for the samples solutionized below 1150°C (bimodal region) while samples solutionized above this temperature (unimodal region) achieved highest post-coating yield strength after coatings performed at both 1100°C-12 hours and 1000°C-20 hours.
- Aging provided only a slight increase of total yield strength of coated samples since it only increased γ' volume fraction slightly. The aluminide coating process acted as a main or primary aging for these samples and reduced the effect of aging. However, samples that were only solutionized and not coated showed dramatic yield strength increase after aging process.
- The thick sample taken from middle section of turbine blade showed higher γ' strengthening than thin sample taken from leading edge of turbine blade due to

slower cooling after casting. However, due to the same reason, grain size strengthening of the thin sample was higher than the thick sample. These two factors roughly balanced each other. Thick (middle section) and thin part (leading edge) showed quite a similar yield strength.

- The solutionizing performed 1120°C-2 hours Ar cooled (180°C/min) followed by aluminide coating at 1000°C-20 hours and aging at 845°C-24 hours found to be achieving highest total yield strength. However since the aluminide coating performed at 1000°C-20 hours didn't provide the desired coating thickness as mentioned in Chapter 3, aluminide coating performed at 1050°C-16 hours can be used since it provided the second highest total yield strength.
- Compared to tensile test results taken from literature, yield strength model and JMAT PRO yield strength estimation results showed relatively similar trends.
- The JMAT PRO simulations performed better for post-solutionizing than post-coating and post-aging yield strength estimations. In general, the simulation results were not satisfactory except the few characteristic results it estimated that were similar to yield strength modeling results.

•

CHAPTER 5

FUTURE WORK

Some suggestions for future work and development of this study are given below:

- Aluminide coating simulations can be performed over different superalloys. Phase types obtained from composition diagrams and accordingly coating properties can be determined.
- The operation conditions of a gas turbine blade can be simulated for coating region. The change in coating composition profile and Al depletion in the coating can be estimated for different initial coating structures.
- TEM (Transmission Electron Microscope) analysis can be performed to follow dislocation activity at the interfaces and in the matrix and precipitates in IN 738 LC microstructure. Additionally, TEM can provide better visualization, and thus a better determination of size and morphology of precipitates can be used to reveal very fine precipitates (if they exist) especially in the solution treated samples.
- The addition of reactive elements to aluminide coatings can be studied. Effect of these elements to a coating composition profile and phase structures can be investigated.
- Tensile strength can be performed to IN 738 LC samples with different microstructures and results can be compared with yield strength model results in this study.



REFERENCES

- [1] A. Gultekin, "Evolution of Precipitate Microstructure in the Superalloy IN 738 LC During Compression Creep (Master's Thesis)," *Boğazici University*, pp. 9, 142-143, 2008.
- [2] D. Erdeniz, "The Precipitate Evolution in the Nickel-Based Superalloy IN 738 LC (Master's Thesis)," *Boğazici University*, pp. 8-9, 2005.
- [3] J. Davis, *ASM Specialty Handbook: Heat-Resistant Materials*, ASM International, 1997, pp. 26-27, 225-226.
- [4] E. Balıkcı and D. Erdeniz, "Precipitate Formation and Evolution in the Superalloy IN 738 LC," *Rare Metal Materials and Engineering*, vol. 38, no. 3, pp. 142-146, 2009.
- [5] P. Splitte, "Gas turbine technology," *Physics Education*, vol. 38, no. 6, pp. 509-511, 2003.
- [6] L. S. Langston, "Introduction to Gas Turbines for Non-Engineers, Global Gas Turbine News," *Global Gas Turbine News*, vol. 37, no. 2, pp. 1-2, 1997.
- [7] "GT13E2 Gas Turbine (50 Hz)," General Electrics, [Online]. Available: <https://powergen.gepower.com/products/heavy-duty-gas-turbines/gt-13e2.html>. [Accessed 07 2017].
- [8] P.C.Patnaik and J.P.Immarigeon, "High Temperature Protective Coatings For Aero Engine Gas Turbine Components," *National Aeronautical Establishment*, vol. 42, pp. 1-4, 1986.

- [9] Seth and B. B., "Superalloys-The Utility of Gas Turbine Perspective," *The Minerals, Metals & Materials society*, pp. 3-16, 2003.
- [10] "EnkaPower," [Online]. Available: <http://www.enkapower.com/>. [Accessed 22 07 2017].
- [11] "Turkish Statistical Institute," [Online]. Available: <http://www.turkstat.gov.tr/UstMenu.do?metod=temelist>. [Accessed 19 07 2017].
- [12] O. Turkyilmaz, "Türkiye'nin Enerji Görünümü," UCTEA Chamber of Mechanical Engineers, 2010.
- [13] Meetham and V. d. Voorde, *Materials for High Temperature Engineering Applications*, Delft: Springer, 2000, pp. 1-8,106.
- [14] X. Han, "Diffusion Coatings for High-Temperature Applications on Ni-base Superalloys (Doctoral dissertation)," *Politecnico Di Milano Department of Mechanical Engineering*, pp. 11-13, 2001.
- [15] T. Giampaolo, *Gas Turbine Handbook: The Principles and Practices*, 3 ed., Fairmont Press, 1997, pp. 34-35.
- [16] B. L. Koff, *Gas Turbine Technology Evolution - A Designer's Perspective*, AIAA/ICAS International Air and Space Symposium and Exposition: The Next 100 Y, p. 3.
- [17] T. Pollock and T. Sammy, "Nickel-Based Superalloys for Advanced Turbine Engines: Chemistry Microstructure and Properties," *Journal of Propulsion and Power*, vol. 22, no. 2, p. 362, 2006.

- [18] B. C.G. and J. Galka, "Cast Nickel-Base Alloy". United States Patent 3.459.545, 5 August 1969.
- [19] P. Schilke, "Advanced Gas Turbine Materials and Coatings," General Electric Company, New York, 2004.
- [20] A. Thakur, "Microstructural Responses of a Nickel Base Cast IN-738 Superalloy to a Variety of Pre-weld Heat-treatments (Master's Thesis)," *Universtiy of Manitoba*, pp. 4,13-14, 1198.
- [21] Alloy IN 738 Technical Data Sheet, The International Nickel Company, pp. 1-11.
- [22] M. Boyce, *Gas Turbine Engineering Handbook*, Woburn: Gulf Professional Publishing, 2006, pp. 5-6.
- [23] D. U. Furrer, R. Shankar and C. White, "Optimizing the heat treatment of Ni-based superalloy turbine discs," *Applied Technology High-Temperature Alloys*, vol. 55, no. 3, pp. 32-34, 2003.
- [24] B. C. Wilson, J. A. Hickman and G. E. Fuchs, "The effect of solution heat treatment on a single-crystal Ni-based superalloy," *The Journal of The Minerals, Metals & Materials Society*, vol. 55, no. 3, pp. 35-40, 2003.
- [25] S. Bose, *High Temperature Coatings*, Butterworth-Heinemann, 2007, pp. 39-156.
- [26] J. R. Davis, *ASM Specialty Handbook: Nickel, Cobalt, and Their Alloys*, ASM International, 2000, pp. 17-18.

- [27] A. K. Jena and M. Chaturverdi, "The role of alloying elements in the design of nickel-base superalloys," *Journal of Materials Science*, vol. 19, no. 10, pp. 3122-3123, 1984.
- [28] O. Shina, M. Chatterjee, V. Sarma and S. Jha, "Effect of residual elements on high performance nickel base superalloys for gas turbines and strategies for manufacture," *Bulletin of Materials Science*, vol. 28, no. 4, pp. 379-380, 2005.
- [29] J. Andersson, Weldability of Precipitation Hardening Superalloys – Influence of Microstructure, Chalmers University of Technology-Department of Materials and Manufacturing Technology, 2011, pp. 7-8.
- [30] M. Igarashi and S. Muneki, "Heat Resisting Steel Containing a Ferrite or Tempered Martensite Structure". Patent US6299704 B1, 2001.
- [31] S. S. Handa, "Precipitation of Carbides in a Ni-based superalloys (Master's Thesis)," *University West*, pp. 5-6, 2014.
- [32] H. Matysiak, M. Zagorska and J. Andersson, "Microstructure of Haynes® 282® Superalloy after Vacuum Induction Melting and Investment Casting of Thin-Walled Components," *Materials (Basel)*, vol. 6, no. 11, pp. 5017-5018, 2013.
- [33] H. Collings, "Relative Stability of Carbide and Intermetallic Phases in Ni Base Superalloys," *ASM (Amer. Soc. Metals)*, vol. 62, pp. 174-175, 1969.
- [34] L. M. Pike, "Development of a Fabricable Gamma Prime Strengthened Superalloy," *The Minerals, Metals & Materials Society*, pp. 191-200, 2008.
- [35] X.Z.Qin, J.T.Guo, C.Yuan, J.S.Hou and H.Q.Ye, "Precipitation and Thermal Instability of M₂₃C₆ Carbide in Cast Ni- Base Superalloys," *Materials Letters*, vol. 62, no. 2, pp. 258-261, 2008.

- [36] S. Farahany, M. Aghaie-Khafri, A. Ourdjini and M. H. Idris, "Influence of Heat Treatment on Properties of Hot Isostatically Pressed Turbine Blade Superalloy IN738," *Advanced Materials Research*, Vols. 264-265, pp. 502-507, 2011.
- [37] W. J.C.Beddoes, "Heat treatment of hot isostatically processed IN-738 investment castings," *Metallography*, vol. 13, no. 2, pp. 185-194, 1980.
- [38] P. Wangyao, W. Homkrajai, V. Krongtong, N. Panich and G. Lothongkum, "OM Study of Effect of HIP and Heat Treatments on Microstructural Restoration in Cast Nickel Based Superalloy, IN-738," *Journal of Metals, Materials and Minerals*, vol. 17, no. 2, pp. 51-56, 2007.
- [39] G. L. a. N. C. Panyawat Wangyao, "Microstructural restoration by hip and heat treatment processes in cast nickel based superalloy, IN738," *Chiang Mai Journal of Science*, vol. 36, no. 3, pp. 287-295, 2009.
- [40] W. P., K. V., H. W., P. S. and L. G., "Comparing Rejuvenated Microstructures After HIP Process and Different Heat Treatments in Cast Nickel Base Superalloys , IN-738 and GTD-111 After Long-Term Service," *Acta Metallurgica Slovaca*, vol. 12, no. 1, pp. 23-32, 2006.
- [41] R.J.Mitchell and S.Behrouzghaemi, "Morphological Changes of γ' Precipitates in Superalloy IN738LC at Various Cooling Rates," *Materials Science and Engineering: A*, vol. 498, no. 1-2, pp. 266-271, 2008.
- [42] H. Kim, J. F. Yang, C. H. Han, S. Thongtem and S. W. Lee, "Effect of Heat Treatment on the Microstructural Characteristics of IN738 Turbine Blade," *Materials Science Forum*, vol. 695, pp. 405-408, 2011.

- [43] J.-M. Kim, J.-S. Park, H.-S. Yun, S.-J. Lee and S.-U. An, "Effect of Solid Solution Treatment on the Microstructure and Mechanical Properties of IN 738 LC," *Advanced Materials Research*, Vols. 378-379, pp. 744-747, 2011.
- [44] I. Guzman, E. Granda, R. Mendez, G. Lopez, J. Acevedo and D. Gonzalez, "Particle Size of Gamma Prime as a Result of Vacuum Heat Treatment of INCONEL 738 Super Alloy," *Journal of Materials Engineering and Performance*, vol. 22, no. 4, pp. 1143-1148, 2012.
- [45] N.El-Bagoury, M.Waly and A.Nofal, "Effect of various heat treatment conditions on microstructure of cast polycrystalline IN738LC alloy," *Materials Science and Engineering: A*, vol. 487, no. 1-2, pp. 152-161, 2008.
- [46] W. Hoffelner, E. Kny, R. Stickler and W. J. McCall, "Effects of Aging Treatments on the Microstructure of the Ni-Base Superalloy IN-738," *Materials Science and Engineering Technology*, vol. 10, no. 3, pp. 84-92, 1979.
- [47] S. Asgari and R. Sharghi-Moshtaghin, "The influence of thermal exposure on the γ' precipitates characteristics and tensile behavior of superalloy IN-738LC," *Journal of Materials Processing Technology*, vol. 147, no. 3, pp. 343-350, 2004.
- [48] A. Miodownik and N. Saunders, CALPHAD (Calculation of Phase Diagrams): A Comprehensive Guide, vol. 1, New York: Pergamon Materials Series, 1998.
- [49] N. Saunders, U. K. Z. Guo, A. P. M. X. Li and J.-P. Schillé, "Using JMatPro to model materials properties and behavior," *The Journal of The Minerals, Metals & Materials Society*, vol. 55, no. 12, pp. 60-65, 2003.
- [50] N. Saunders, Z. Guo, A. P. M. X. Li and J.-P. Schillé, "Modelling the Material Properties and Behaviour of Ni-Based Superalloy," *The Minerals, Metals & Materials Society*, pp. 849-858, 2004.

- [51] H. Li, L. Zuo, X. Song, Y. Wang and G. Chen, "The Coarsening of γ' Particles in Nickel-Based Superalloys," *Rare Metals*, vol. 28, no. 2, pp. 197-201, 2009.
- [52] C. Coddet, "Environmental Protection of Metal Structures at High Temperature: State of the Art and Future Trends," *Mater. Sci. Forum.*, Vols. 461-464, pp. 193-212, 2004.
- [53] Y. Tamarin, *Protective Coatings for Turbine Blades*, Ohio: ASM International, 2002, pp. 1-2.
- [54] C. Walter, "Simulation of Diffusion Processes in Turbine Blades and Large Area Deposition of MAX Phase Thin Films with PVD (Doctoral dissertation)," *RWTH Aachen University*, pp. 5-35, 2005.
- [55] N. Saunders, "Phase Diagram Calculations for Ni-Based Superalloys," *Superalloys 1996*, pp. 101-110, 1996.
- [56] C. Campbell, W. Boettinger and U. Kattner, "Development of a diffusion mobility database for Ni-base superalloys," *Acta Materialia*, vol. 50, no. 4, pp. 775-792, 2002.
- [57] C. Campbell, "Assessment of the diffusion mobilities in the γ' and B2 phases in the Ni–Al–Cr system," *Acta Materialia*, vol. 56, no. 16, pp. 4277-4290, 2008.
- [58] K. Wu, "Computer Simulation of Inter diffusion Microstructures in Multi-Component and Multiphase Systems (Doctoral dissertation)," *The Ohio State University*, pp. 99-127, 2003.
- [59] A. Engström, J. Bratberg, Q. Chen, L. Höglund and Paul Mason, "Application of Thermodynamic and Kinetic Modeling to Diffusion Simulations in Nickel-

- Base Superalloy Systems," *Advanced Materials Research*, vol. 278, pp. 198-203, 2011.
- [60] K. V. Dahl, J. Hald and A. Horsewell, "Interdiffusion between Ni-based superalloy and MCrAlY coating," *Defect and Diffusion Forum*, Vols. 258-260, pp. 73-78, 2006.
- [61] K. Yuan, E. Robert, R. L. Peng and Y. Wang, "Interdiffusion and Microstructure Simulation in Ni and Co Based Overlay Coatings on a Ni Based Superalloy at High Temperatures," *Thermec 2013 Supplement*, pp. 850-855, 2013.
- [62] Y. Jinjiang, S. Xiaofeng, Z. Nairen, J. Tao, G. Hengrong and H. Zhuangqi, "Effect of Heat Treatment on Microstructure and Stress Rupture Life of DD32 Single Crystal Ni-Base Superalloy," *Materials Science and Engineering: A*, Vols. 460-461, pp. 420-427, 2007.
- [63] A.M.Ges, O.Fornaro and H.A.Palacio, "Coarsening Behaviour of a Ni-base Superalloy Under Different Heat Treatment Conditions," *Materials Science and Engineering: A*, vol. 458, no. 1-2, pp. 96-100, 2007.
- [64] F.C.Campbell, *Elements of Metallurgy and Engineering Alloys*, ASM International., 2008, pp. 567-568.
- [65] P.Feltham and M. Z. Butt, "Solid-solution hardening," *Journal of Materials Science*, vol. 28, no. 10, p. 2557–2576, 1993.
- [66] T. Suzuki, "On the Studies of Solid Solution Hardening," *Japanese Journal of Physics*, vol. 20, no. 3, pp. 449-462, 1981.
- [67] R.Labusch, "A statistical theory of solid solution hardening," *Phys. Status Sol.*, vol. 41, p. 659–669, 1970.

- [68] F.R.N.Nabarro, "The theory of solution hardening," *Philos. Mag.*, vol. 35, pp. 613-622, 1977.
- [69] E.I.Galindo-Nava, L.D.Connor and C.M.F.Rae, "On the prediction of the yield stress of unimodal and multimodal γ' Nickel-base superalloys," *Acta Materialia*, vol. 98, pp. 377-390, 2015.
- [70] P.Feltham, "Solid solution hardening of metal crystals," *J. Appl. Phys.*, vol. 1, pp. 303-308, 1968.
- [71] A.Deruyttere and L. A. Gypen, "Multi-Component Solid Solution Hardening: Part 1 Proposed Model," *Journal of Materials Science*, vol. 12, no. 5, pp. 1028-1033, 1977.
- [72] A.Deruyttere and L. A. Gypen, "Multi-Component Solid Solution Hardening: Part 2 Agreement with Experimental Results," *Journal of Materials Science*, vol. 12, no. 5, pp. 1034-1038, 1977.
- [73] Y. Mishima, S. Ochiai, N. Hamao, M. Yodogawa and T. Suzuki, "Solid Solution Hardening of Nickel -Role of Transition Metal and B-subgroup Solutes," *Transactions of the Japan Institute of Metals*, vol. 27, no. 9, pp. 656-664, 1986.
- [74] E. O. Hall, "The Deformation and Ageing of Mild Steel: III Discussion of Results," *Proceedings of the Physical Society*, vol. 64, pp. 747-753, 1951.
- [75] N. J. Petch, "The Cleavage Strength of Polycrystals," *Journal of the Iron and Steel Institute*, vol. 174, pp. 25-28, 1953.
- [76] N. Hansen, "Hall–Petch Relation and Boundary Strengthening," *Scripta Materialia*, vol. 51, no. 8, pp. 801-806, 2004.

- [77] M. Preuss, P. J. Withers, J. Pang and G. J. Baxter, "Inertia Welding Nickel-Based Superalloy: Part I. Metallurgical Characterization," *Metallurgical and Materials Transactions A: Physical Metallurgy and Materials Science*, vol. 33, no. 10, pp. 3215-3225, 2002.
- [78] R. Kozar, A. Suzuki, W. Milligan, J. Schirra, M. Savage and T. Pollock, "Strengthening Mechanisms in Polycrystalline Multimodal Nickel-Base Superalloys," *Metallurgical and Materials Transactions A*, vol. 40, no. 7, pp. 1588-1603, 2009.
- [79] A. A.W.Thompson, "Yielding in Nickel as a Function of Grain or Cell Size," *Acta Metall.*, vol. 23, pp. 1337-1342, 1975.
- [80] N. Hansen, "Boundary Strengthening in Undeformed and Deformed Polycrystals," *Materials Science and Engineering: A*, vol. 409, no. 1-2, pp. 39-45, 2005.
- [81] S. Milenkovic, M. Rahimian, I. Sabirov and L. Maestro, "Effect of Solidification Parameters on The Secondary Dendrite Arm Spacing in MAR M-247 Superalloy Determined By Noval Approach," *MATEC*, vol. 14, pp. 1-5, 2014.
- [82] G. Matache, D. M. Stefanescu and E. Alexandrescu, "Dendritic Segregation and Arm Spacing in Directionally Solidified CMSX-4 Superalloy," *Journal of Cast Metals Research*, vol. 29, no. 5, pp. 303-316, 2016.
- [83] P. Sharifi, "Structure-Property Relationships of Magnesium Alloys (Master's Thesis)," *The University of Western Ontario*, pp. 10-11, 2012.
- [84] Z. Guo, N. Saunders, P. Miodownik and J. P. Schille, "Prediction of Room Temperature Mechanical Properties in Aluminium Castings," *ICAA11*, Vols. 794-796, pp. 658-663, 2008.

- [85] Z. C. Cordero, B. E. Knight and C. A. Schuh, "Six Decades of the Hall–Petch Effect – a Survey of Grain-Size Strengthening Studies on Pure Metals," *International Materials Reviews*, vol. 61, no. 8, pp. 495-512, 2016.
- [86] M.P.Jackson and R.C.Reed, "Heat Treatment of UDIMET 720Li: the Effect of Microstructure on Properties," *Materials Science and Engineering: A*, vol. 259, no. 1, pp. 85-97, 1999.
- [87] H. Stone and D. Collins, "A Modelling Approach to Yield Strength Optimisation in a Nickel-Base Superalloy," *International Journal of Plasticity*, vol. 54, pp. 96-112, 2014.
- [88] Q. X. Tang, S. Ukai, A. Minami and S. Hayashi, "Gamma Prime Precipitation and Growth Kinetics in Mechanically Alloyed Ni–Al," *Advances in Materials Science and Engineering*, pp. 1-7, 2011.
- [89] D. R. Lide, *CRC Handbook of Chemistry and Physics*, CRC Press , 2008.
- [90] H. Mecking and U. Kocks, "Physics and phenomenology of strain hardening: The FCC case," *Progress in Materials Science*, vol. 48, no. 3, pp. 171-273, 2003.
- [91] K. B. Small, D. A. Englehart and T. A. Christman, "Guide to Etching Specialty Alloys," *Advanced Materials & Processes*, pp. 32-37, 2008.
- [92] A. Koul, J.-P. Immarigeon, C. R., P. Lowden and J. Liburdi, "Rejuvenation of Service-Exposed 738 Turbine Blades," *The Metallurgical Society*, vol. 764, p. 755, 1988.
- [93] E. Balikci, R. Mirshams and A. Raman, "Tensile Strengthening in the Ni-Base Superalloys," *JMEPEG*, vol. 9, pp. 324,329, 2000.

APPENDICES

A. DICTRA Simulation Commands for Aluminide Coating Simulation

1. goto_module
2. data
3. sw tcni8
4. def-sys
5. ni al cr co ti
6. rej-ph *
7. res-ph fcc_112 bcc_b2 bct_d022 liq ni3ti_d024
8. get
9. app
10. MOBNI4
11. def-sys
12. ni al cr co ti
13. rej-ph *
14. res-ph fcc_112 bcc_b2
15. get
16. goto_module
17. d-m
18. set_cond
19. g
20. T
21. 0 1223; * N
22. enter_region
23. BASEMETAL
24. ent_grid
25. BASEMETAL

26. 2e-4
27. lin
28. 100
29. ent_ph_in_reg
30. ACTIVE
31. BASEMETAL
32. MATRIX
33. fcc_l12#1
34. ent_ph
35. ACTIVE
36. BASEMETAL
37. sph
38. fcc_l12#2
39. ent-ph
40. ACTIVE
41. BASEMETAL
42. sph
43. bcc_b2#1
44. ent-ph
45. ACTIVE
46. BASEMETAL
47. sph
48. bcc_b2#2
49. ent-ph
50. ACTIVE
51. BASEMETAL
52. sph
53. bct_d022
54. ent-ph
55. ACTIVE

56. BASEMETAL
57. sph
58. liq
59. ent-ph
60. ACTIVE
61. BASEMETAL
62. sph
63. ni3ti_d024
64. ent_comp
65. BASEMETAL
66. fcc_l12#1
67. ni
68. MOLE_FRACTION
69. AL LINEAR 0.07 7E-2
70. CO LINEAR 0.08 8E-2
71. CR LINEAR 0.18 0.18
72. TI LINEAR 0.04 4E-2
73. ent_comp
74. BASEMETAL
75. fcc_l12#2
76. Y
77. ent_comp
78. BASEMETAL
79. bcc_b2#1
80. Y
81. ent_comp
82. BASEMETAL
83. bcc_b2#2
84. Y
85. ent_comp

86. BASEMETAL
87. bct_d022
88. y
89. ent_comp
90. BASEMETAL
91. liq
92. y
93. ent_comp
94. BASEMETAL
95. ni3ti_d024
96. y
97. set_sim_ti
98. 14400
99. YES
100. 1440
101. 1E-07
102. 1E-07
103. set_cond
104. b
105. LOWER
106. fix
107. 0 6.05e-10; * N
108. 0 0.05e-10; * N
109. 0 0.05e-10; * N
110. 0 0.05e-10; * N
111. ut
112. NO
113. NO
114. y
115. NO

116.NO
117.NO
118.y
119.NO
120.NO
121.NO
122.y
123.10
124.NO
125.NO
126.NO
127.y
128.y
129.YES
130.0.05e-10
131.NO
132.s-s-c
133.0
134.1
135.2
136.n
137.act
138.y
139.y
140.1
141.2
142.y
143.y
144.n
145.ho

146.y
147.n
148.n
149.y
150.10000
151.log
152..2
153.n
154.n
155.y
156.save_workspaces cvd Y
157.set_interactive

B. Average Cooling Rates of Different Cooling Types Available in VAKSIS Vacuum Furnace

Table B.1: Average Cooling Rates of Different Cooling Types Available in VAKSIS Vacuum Furnace.

Cooling Type	Cooling Rate (°C/min)
Ar-4500sccm+fan	180
Ar-2500sccm+fan	169
Ar-500sccm+fan	165
Ar-4500sccm+no fan	174
Ar-2500sccm+ no fan	166
Ar-500sccm+ no fan	163
Air Cooling	155
Furnace Cooling	20

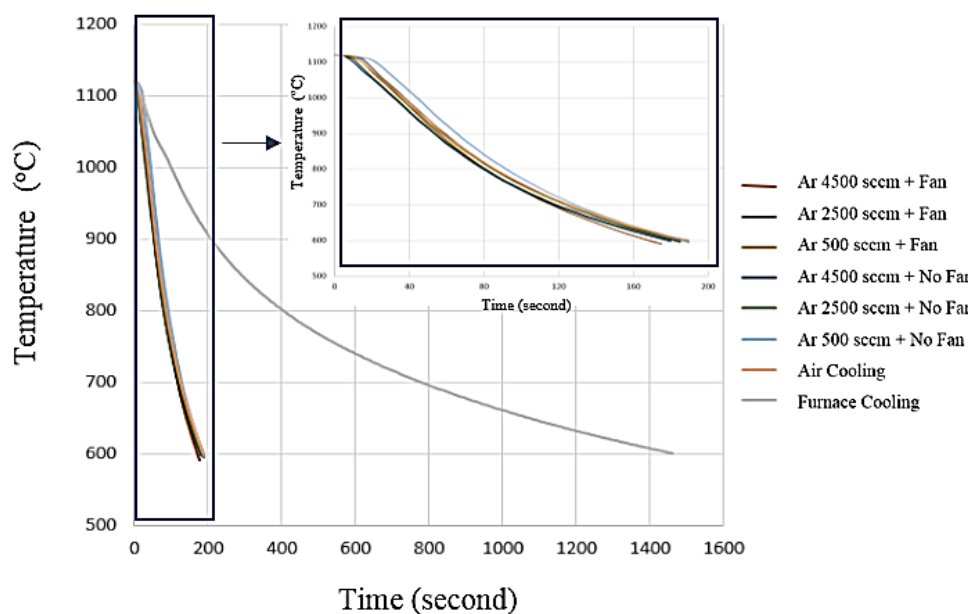


Figure B.1: Cooling Curves of VAKSIS vacuum furnace.

C. SEM Images and Composition Analysis Results of Carbides

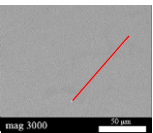
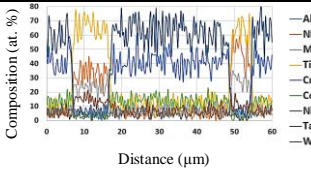
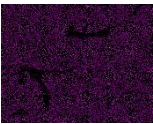
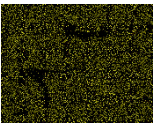
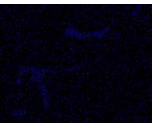
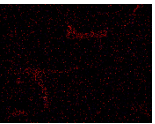
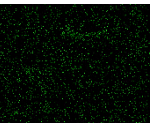
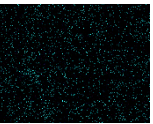
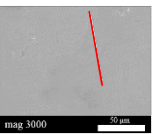
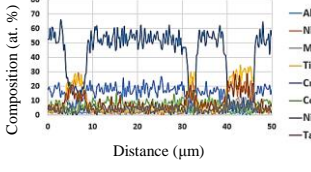
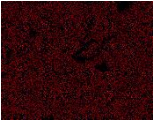
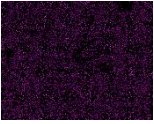
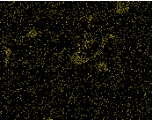
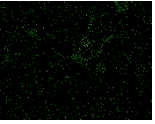
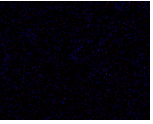
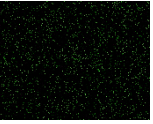
	SEM Images	Linear Composition Analysis Results	Ni	Cr	Ti	Nb	Mo	Ta
AS CAST								
HIPED (1200°C-10 h)								

Figure C.1: Composition analysis of carbides for as cast and HIPed (1200°C-10 hours-150 MPa) samples.

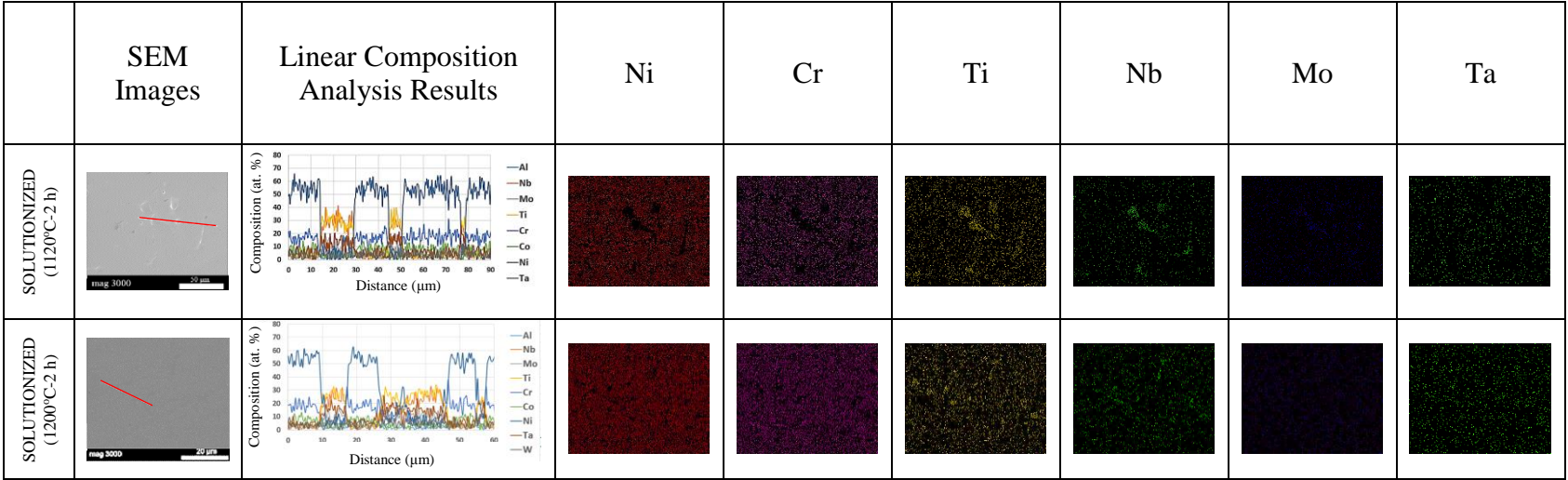


Figure C2: Composition analysis of carbides for samples that were solutionized at 1120°C and 1200°C for 2 hours (Ar cooled-180°C/min).

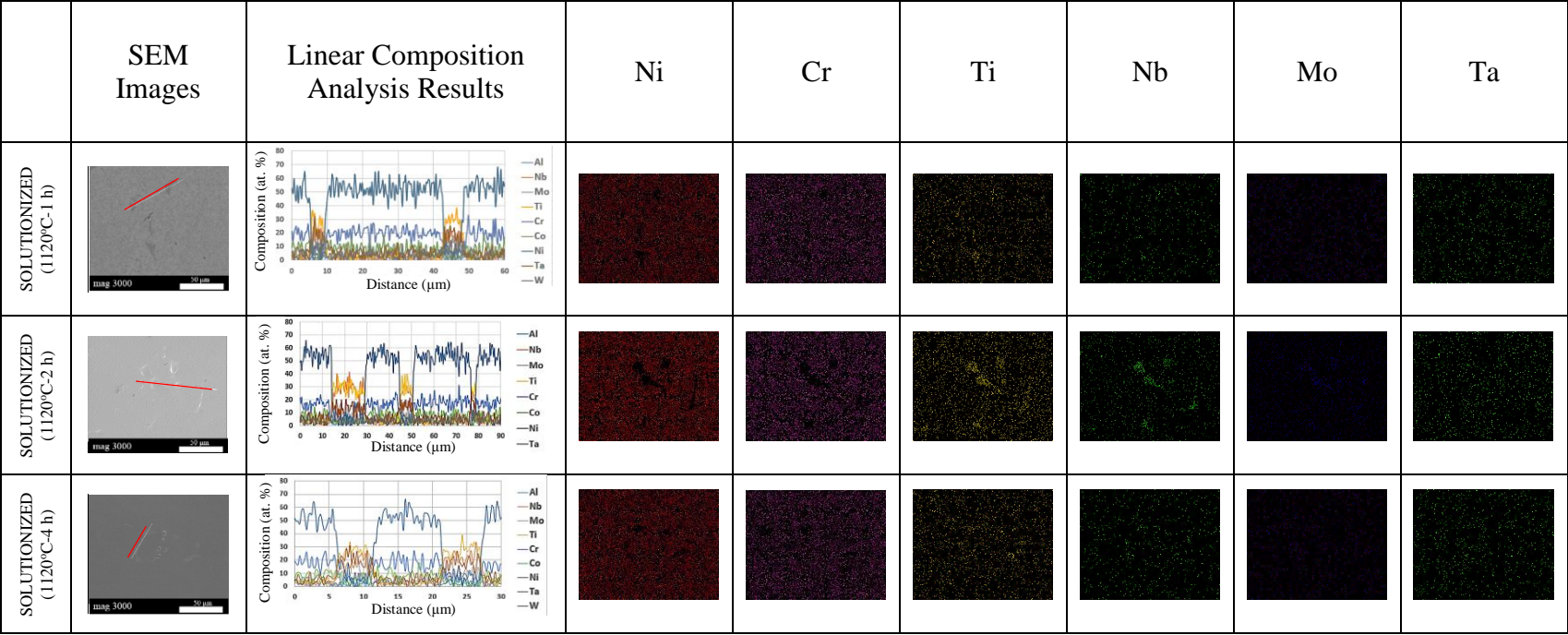


Figure C.3: Composition analysis of carbides for samples that were solutionized at 1120°C for 1, 2 and 4 hours and Ar cooled (180°C/min).

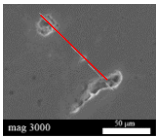
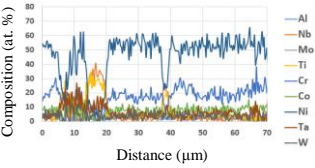
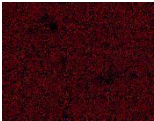
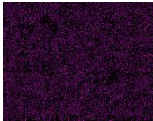
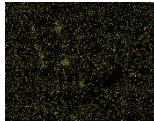
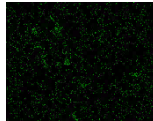
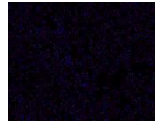
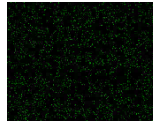
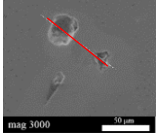
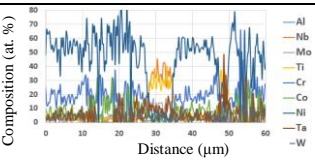
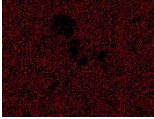
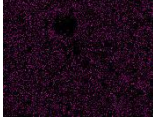
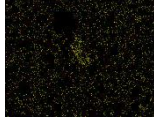
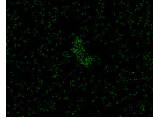

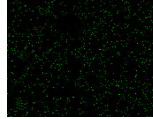
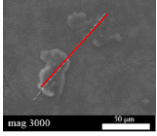
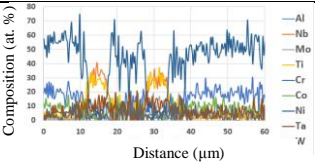

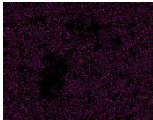
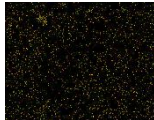
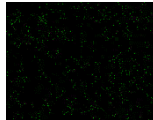

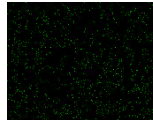
	SEM Images	Linear Composition Analysis Results	Ni	Cr	Ti	Nb	Mo	Ta
SOLUTIONIZED (1120°C-1 h)								
SOLUTIONIZED (1120°C-2 h)								
SOLUTIONIZED (1120°C-4 h)								

Figure C.4: Composition analysis of carbides for samples that were solutionized at 1120°C for 1, 2 and 4 hours and furnace cooled (20°C/min).

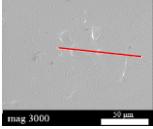
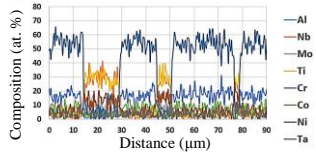
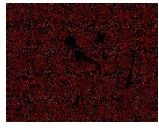
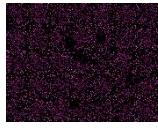
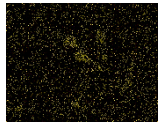
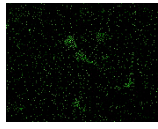
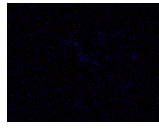
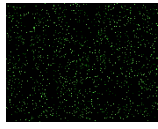
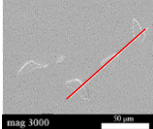
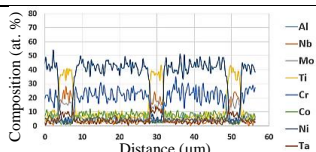
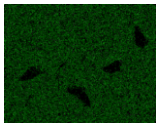
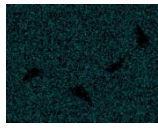
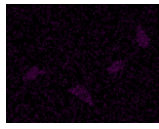



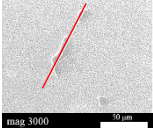
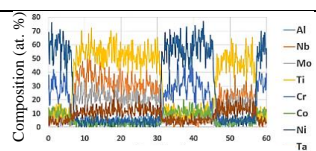
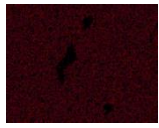
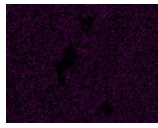
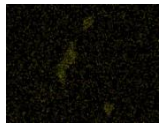
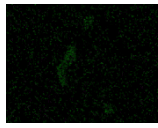
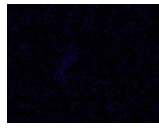
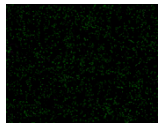
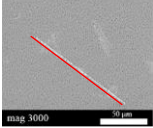
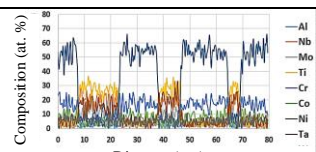
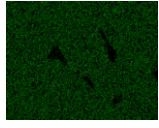

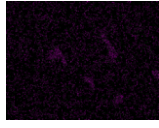
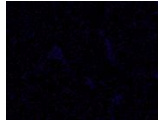


	SEM Images	Linear Composition Analysis Results	Ni	Cr	Ti	Nb	Mo	Ta
SOLUTIONIZED (1120°C-2 h)								
ALUMINIDE COATED (1000°C-20 h)								
ALUMINIDE COATED (1050°C-16h h)								
ALUMINIDE COATED (1100°C-12 h)								

Figure C.5: Composition analysis of carbides for samples solutionized at 1120°C-2 hours (Ar cooled-180°C/min), and aluminide coated at 1000°C-20 hours, 1050°C-16 hours and 1100°C-12 hours (furnace cooled-7 °C/min).

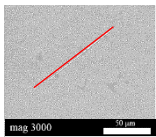
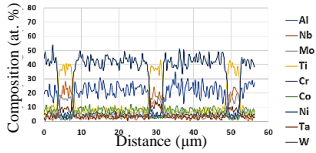

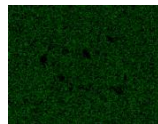
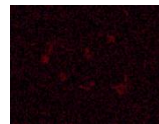
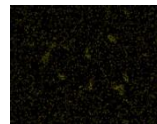
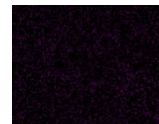
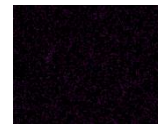
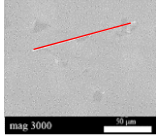
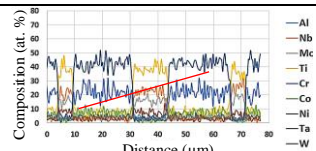
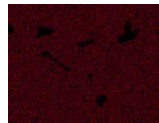
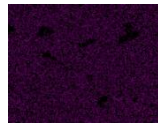
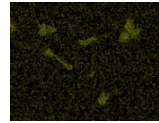
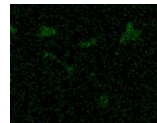
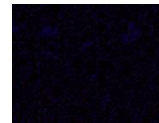
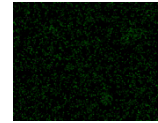
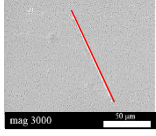
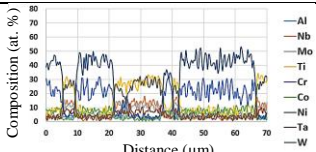
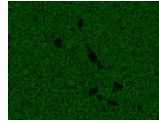
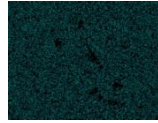
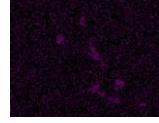
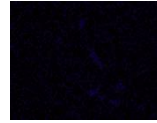


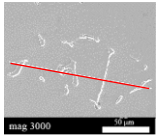
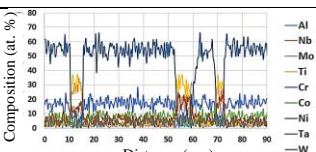
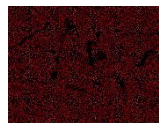
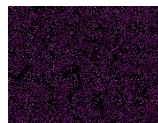
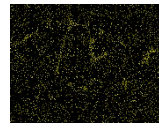
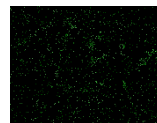
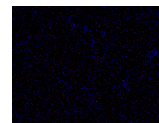
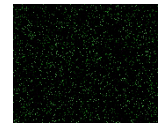
	SEM Images	Linear Composition Analysis Results	Ni	Cr	Ti	Nb	Mo	Ta
1000°C-20 h + 845°C-24 h								
1050°C-16 h + 845°C-24 h								
1100°C-12 h + 845°C-24 h								
1120°C-2 h + 845°C-24 h								

Figure C.6: Composition analysis of carbides for samples solutionized at 1120°C-2 hours (Ar cooled), coated at 1000°C-20 hours, 1050°C-16 hours (furnace cooled) and 1100°C-12 hours, and aged at 845°C-24 hours (Ar cooled), and uncoated aged sample.

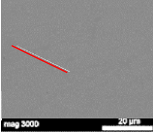
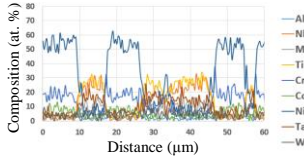

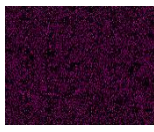
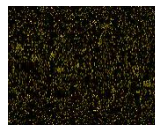
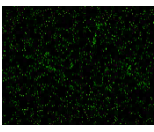
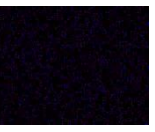
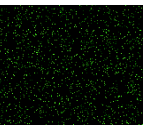
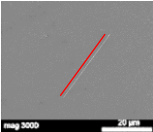
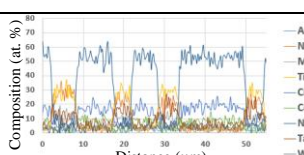
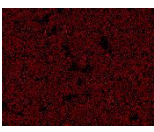
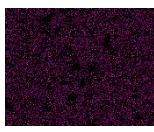
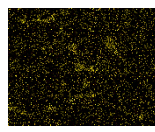
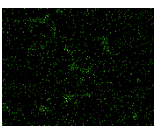
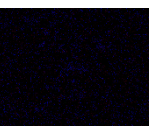
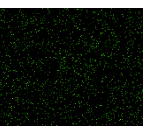
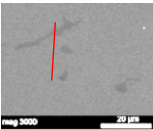
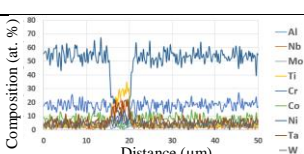
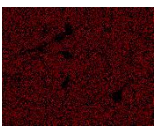
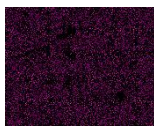
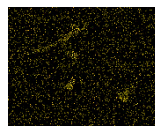
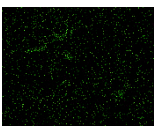

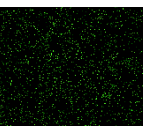
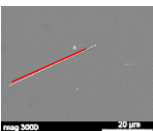
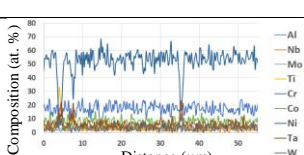
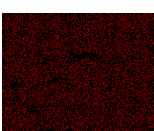

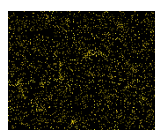
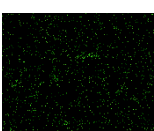
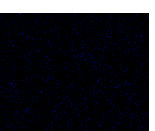
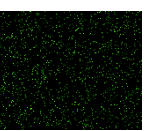
	SEM Images	Linear Composition Analysis Results	Ni	Cr	Ti	Nb	Mo	Ta
SOLUTIONIZED (1200°C-2 h)								
ALUMINIDE COATED (1000°C-20 h)								
ALUMINIDE COATED (1050°C-16 h)								
ALUMINIDE COATED (1100°C-12 h)								

Figure C.7: Composition analysis of carbides for samples solutionized at 1200°C-2 hours (Ar cooled-180°C/min), coated at 1000°C-20 hours, 1050°C-16 hours and 1100°C-12 hours (furnace cooled- 7°C/min).

